Extensional Tectonic History Of The Rhodope Metamorphic Core Complex, Greece And Geophysical Modeling Of The Halloran Hills, California

by

Peter Stanley Kaufman

B.S. Geology, Case Western Reserve University, 1989

Submitted to the Department of
Earth, Atmospheric, and Planetary Sciences
In Partial Fulfillment of the Requirements for the Degree of

Doctor of Philosophy

at the

Massachusetts Institute of Technology

February, 1995

Signature of Author: _____
Department of Earth, Atmospheric and Planetary Sciences
January, 1995

Certified by: _____
Professor Leigh H. Royden
Thesis Supervisor

Accepted by: _____
Professor Thomas H. Jordan
Department Head

Extensional Tectonic History Of The Rhodope Metamorphic Core Complex, Greece And Geophysical Modeling Of The Halloran Hills, California

by

Peter Stanley Kaufman

Submitted to the Department of Earth, Atmospheric, and Planetary Sciences at the Massachusetts Institute of Technology in partial fulfillment of the requirements for the degree of Doctor of Philosophy in Geology and Geophysics

Abstract

This thesis approaches the study of detachment faulting and core complex formation using a variety of geologic disciplines: structural geology, geochronology, geophysical modelling, and geobarometry. Two Tertiary extensional regions are examined: the Halloran Hills of the Basin and Range of southeastern California and the Rhodope metamorphic core complex of northern Greece.

In northern Greece, the Rhodope metamorphic core complex occupies a critical position between the collisional zones of the internal Hellenides and the Rhodope metamorphic province. Structural mapping in the northern Rhodope metamorphic core complex has focussed on the style and consequences of deformation related to Alpine compression and Miocene to Recent extension. The Falakron Marble Series, buried by the amphibolite-facies Serbo-Macedonian and West Thracian Gneisses during Eocene (?) Alpine thrust faulting, re-emerged in the Miocene in the footwall of the Strymon Valley detachment fault. In the northern Rhodope metamorphic core complex, the Vrondou pluton and the Elaion stock are exposed in kilometer-scale structural corrugations of the Strymon Valley detachment fault. These plutons cross-cut Alpine structural fabrics, but are strongly mylonitized by the early phase of ductile motion on the detachment fault. U-Pb and $^{40}Ar/^{39}Ar$ geochronology on the Vrondou pluton and the northern Rhodope metamorphic core complex places important constraints on the timing of pluton intrusion, the initiation of detachment faulting, the thermal evolution of the core complex during detachment faulting, and the rate of detachment faulting over time. Initiation of tectonic denudation by the Strymon Valley detachment fault is recorded by 16 Ma $^{40}Ar/^{39}Ar$ biotite cooling ages that have a closure temperature overlapping with approximate conditions of mylonitization. Continued denudation and cooling is recorded by 9 to 16 Ma K-feldspar cooling ages that overlap in age with the oldest syn-extensional sediments in the supra-detachment Serres Basin, suggesting the earliest deposits in the basin were derived from the exposed eastern part of the core complex before unroofing was complete. During the extensional period, footwall cooling between the closure temperatures of biotite and K-feldspar occurred at rates between 30° and 70° C/m.y. Spatial variations in K-feldspar cooling ages are interpreted to reflect the top-to-the-southwest denudation of the core complex at a rate between 2 and 3 km/m.y.

A set of local reconstructions of the northern Rhodope metamorphic core complex, based on general metamorphic stratigraphy, regional intrusive relationships, and the results of aluminum-in-hornblende geobarometry indicates the Strymon Valley detachment fault probably initiated at a higher angle than present-day structural fabrics would indicate. These local reconstructions also suggest significant structural relief on the detachment fault. Regional paleogeographic reconstructions developed for the entire north Aegean region strongly support a correlation between the Falakron Marble Series and the Olympos carbonate platform, implying that the tectonostratigraphic units of the Circum-Rhodope Belt and the Vardar Zone are allochthonous nappes. These regional paleogeographic

reconstructions also show that restoring extension on the Strymon Valley detachment fault realigns Alpine collisional belts around the Rhodope metamorphic province, possibly supporting a regional correlation between the Vardar Zone and the Intra-Pontide suture in Turkey. Differential displacement on the detachment fault and other, as yet unidentified extensional structures, may account for paleomagnetic rotations observed throughout the northwest Aegean region and Hellenic Arc.

Postextensional uplift and tilting of Quaternary lake sediments in the Halloran Hills, eastern Mojave desert, California, suggest that regional-scale flow within the lower crust is occurring in response to tectonic loads created during upper crustal extension in late Miocene time. The concept that significant flow within the lower crust may occur for millions of years after the cessation of extension indicates that topographic gradients can be modified by regional-scale flow within the lower crust and that direct constraints on lower crustal flow can be obtained by quantitative analysis of rates of postextensional surface tilting. An analytic solution, developed here, combines viscous flow in the lower crust, flexural bending within the midcrust, and isostasy into an invertible linear differential equation that describes the topographic response to upper crustal extension. Assuming that there was no topographic relief across the Halloran Hills region prior to extension, inversion of modern topographic data indicates that crustal thinning above the Halloran Hills detachment increases westward with an overall listric geometry and that little crustal thinning has occurred east of the western flank of the Clark Mountains, in good agreement with the known geometry of the fault and the location of its breakaway zone. Incorporation of Quaternary tilting data into the model indicates that the modern viscosity beneath the Halloran Hills (assuming a 10-km lower crustal channel) is a maximum of 10^{19} Pa s and that the viscosity of the lower crust has decreased by at least 1 to 2 orders of magnitude since 8 Ma. This corresponds to a temperature increase of at least 75° to 100°C at the Moho. A probable source of this temperature increase is a regional-scale thermal event within the underlying mantle and diffusion of heat upward into the lower crust. If correct, these results have important implications for the way in which crustal extension is linked to mantle heating within the Basin and Range Province.

Thesis advisor: Professor Leigh H. Royden

ACKNOWLEDGEMENTS

Anyone who has completed a thesis realizes that the work that has been done could not be completed without the assistance, support, and love of many people. This thesis is no exception. I would like to thank those individuals who made the completion of this work possible, and at times, even fun. It is to their credit that this thing ever got done. I had never heard of the Rhodope Mountains, the flexure equation, retsina, or *Ζαχαροπλαστειον* when I entered graduate school. Little did I imagine that I would soon find myself in the "Blue Albatross", a deteriorating VW microbus, tearing around the Balkan peninsula learning about these things and more.

Professors Jim Aronson, Phil Banks, and Peter McCall were my earliest geologic mentors at Case Western Reserve University. Professor Joe Prahl of the Mechanical Engineering department encouraged me to aim high in my pursuit of graduate programs. Without his encouragement, I would never have considered MIT. My thesis advisor, Leigh "Wiki" Royden deserves acknowledgement for her support, supervision, and encouragement. I still remember the excitement I felt when she first called me and let me know that I had been admitted to MIT. Over the past five and a half years her willingness to let me dive into uncharted waters provided me with an excellent opportunity to learn geology and geophysics and gain valuable life experiences. Her suggestion to "Take the van to Bulgaria and register it there..." started a series of adventures that are unforgettable.

Once in Bulgaria, numerous people helped me to learn about Balkan geology and circumvent Former East Block bureaucracy. Without their assistance, I would probably still be in Sofia trying to accumulate the necessary stamps and signatures to register the microbus. *"Благодаря":* Tsanko Tsankov, Radoslav Nakov, Mitko Paskalev, Blagoe Ivanov, Petar Gochev, Ian Zagorchev, Alexandra Harkovska, Jivko Ivanov, Christo Dabovski, and Slavcho Yanev. Radoslav, Mitko, Tsanko, and Blagoe are especially thanked for including me in their personal lives while I was trying to register the Blue Albatross. Petros and his family at the Hotel Petros Beach on the Aegean coastline are thanked for making their hotel a "home away from home", or at least a good place to get a swim and a shower.

My field assistants in the Rhodopes and the Halloran Hills deserve special commendation for dealing with long, seemingly pointless walks in the sun, venomous snakes, savage dogs, Balkan politics, and my own personal idiosyncrasies. Paula Waschbusch, co-"MIT stud mapper", is remembered for her tuneful rendition of Foreigner songs while under the influence of too many margaritas. Dave Root taught me that cribbage is not a game and it is possible to survive as a vegetarian. Robert Dively, co-

"Master of Menoikion", cheerfully joined me in my adventures on the Balkan peninsula spending what was "a wonderful time to be alive". Julia Sankey-Georgiev is thanked for her patience while I dealt with Bulgarian bureaucracy. Her own exploits while I was otherwise occupied culminated in her marriage to our Bulgarian ski instructor.

Numerous graduate students provided inspiration, advice, and amusing playmates during my tenure at MIT. My co-workers on the 8th floor have been a source of stimulating conversation, constructive criticism, and invaluable assistance. Carolyn Ruppel's computer savvy, geological and geophysical experience, and dogged determination have been an invaluable source of information and assistance. Matt "RTFM" Cordery and Paul Filmer demonstrated the dark side of the graduate experience. Cecily Wolfe was a cheerful office mate and a great pal. Shen Feng, Emilie Hooft, Garett Ito, Yu Jin, Mousumi Roy, Jessica Sunshine, D'Arcy Straub, Helen Webb, and Zhou Yu rounded out the floor, providing a critical social outlet and intramural opportunities. Jess is especially thanked for the use of her Mac as a platform from which to write, tabulate, and draw my thesis. Jim Gahrety, Peter Puster, and Mark Simons helped with programming issues and geophysical questions. The geology crew on the 10th and 11th floor accepted me as one of their own (sort of) for which I am grateful. Thanks go to Roy Adams, Dave Applegate, Meg Coleman, Dave Dinter, Julio Freidmann, Dave Hawkins, Martha House, Linda Kah, Allison Macfarlane, Dave McCormick, C.J. Northrup, Shane Pelechaty, Beverly Saylor, Dawn Sumner, and Deb Zervas. Dave Applegate and Meg Coleman are especially thanked for critically reading early versions of Chapters 4 and 5. Dave Dinter paved my way into the Rhodopes and has served as a source of knowledge and guidance throughout my work in Greece. Doubtless, this would not have been possible without his advice and assistance. The folks on the 11th and 12th floor walked me through the details of geochronology and microprobe analysis. Without the technical assistance of Sam Bowring, Nilanjan Chatterjee, Drew Coleman, Bill Hames, Dave Hawkins, Clark Isachser, and Bill Olszewski, the fourth and fifth chapters of my thesis would not have been possible. Bruce Cabral and Carol Gibbs provided critical administrative support.

I would like to acknowledge and thank my thesis committee, B. Clark Burchfiel, Brad Hager, Kip Hodges, Leigh Royden, and Elizabeth Schermer, for wading through a bunch of diverse chapters. Clark is thanked for his role as an unofficial advisor and for his insight into "the big picture". Kip patiently walked me through my argon data. Both Kip and Liz gave my thesis the meticulous reading and editing that it needed. John Grotzinger, although he was not on my committee, served as a source of valuable information and encouragement throughout my tenure.

My house-mates have made my life away from the institute interesting and enjoyable. Jim Bales demonstrated that it was possible to get a Ph.D. from MIT if you tried hard enough, reminding me "If it becomes necessary, you can find a pen that writes on camel dung..." Scott Lundquist provided inspiration to take advantage of the outdoor opportunities available in New England. Jivko Ivanov and Radoslav Nakov complemented the apartment by providing "the Bulgarian connection". I thank Gretchen Grozier, Emilie Hooft, Megan Jamison, Eric Parks, and Ann Tweedie for making me an honorary member of the CYA group at 400 Broadway. "*Ευχαριστω πολυ, φιλοι μου!*". Nightly "family" dinners made my penultimate year at MIT go by all too fast. Gretchen's organizational skill and maternal instinct provided the glue that kept us all together. Her knowledge of Balkan politics helped me understand the complex situations in "the powder-keg of Europe". Emilie taught me important Greek phrases (*"δεν ειμαι παντρεμενος"*) and introduced me to the whole CYA crowd. Eric's unique sense of humor and skill at boffing were much appreciated when I had thesis angst to work out. Ann's studies of Greek anthropology formed an interesting counterpoint to my own experiences.

Robert Dively spent two field seasons working as my assistant, sharing in the daily excitement of life in Greece. Our first field season together is remembered for unparalleled views from Menoikion Oros, a slow-moving red pepper truck in the Drama Basin, a midnight visit by the heavily armed border patrol, the Brits (Pam, Andy, and Barney) in Siderokarsto, and an unforgettable death march on Mt. Pangaion for my 25th birthday. Our second field season is remembered for its excellent birding which included an accidental chukar, a flock of flamingos, and the ubiquitous corn bunting (deep-deep-deep-deeble-deeble-deeble), weekly hangovers at Petros Beach, the Greek plastic chair man, and a protracted sampling mission on the Vrondou spine. Both trips included the consumption of far too much retsina, olives, and baklava, exciting interactions with native shepherds (including Nikos and his cows) and villagers, brutal games of cribbage and rock-paper-scissors, exciting excursions to the agora on Tuesdays, and daily reminders of why it is good to be alive.

I have no doubt that I never would have completed this thesis without the support, encouragement, and friendship of Paula Waschbusch. Throughout our time at MIT, we celebrated when times were good and commiserated when times were bad. No matter how busy either of us were, there was always time to squeeze in a coffee and doughnut or ice cream break. Her role in the Halloran Hills went beyond that of a field assistant, acting as a stabilizing influence that guided me through one of the most difficult times in my life. Through our friendship, I feel I have grown not only as a scientist, but more importantly as a person.

I would finally like to thank my parents, Stan and Sue Kaufman, who encouraged my endeavors and enthusiastically listened to my adventures. Although they may not fully comprehend what I do, they never stopped trying to understand, which is the important thing. Their letters while I was abroad and willingness to accept collect calls at all hours of the day and night kept my spirits up and inspired me to keep going. I also thank my fiancé, Megan Jamison who tolerated my moody disposition during the final writing stages and forced me to take time out from work to enjoy life. I hope that one day we will be able to return to Greece together and share our different perspectives of a remarkable country.

To my parents, Stan and Sue Kaufman

TABLE OF CONTENTS

CHAPTER 1. INTRODUCTION

Since the recognition in the early 1980's of low angle normal (detachment) faults in the Basin and Range [*Wernicke*, 1981], they have been identified in orogenic belts around the world. Metamorphic core complexes, also recognized in the late 1970's and early 1980's (e.g., *Davis and Coney* [1979]; *Coney* [1980]; *Armstrong* [1982]), are commonly exposed in the footwalls of regional detachment faults; a genetic relationship between detachment faulting and the formation of metamorphic core complexes is commonly accepted (e.g., *Davis and Lister* [1988]; *Lister and Davis* [1989]). Because detachment faults can accommodate a great deal of extension, effectively shuffle tectonostratigraphic units, and commonly unroof rocks from mid-crustal depths, their identification is critical; the reinterpretation of sub-horizontal structures as detachment faults usually has significant consequences for tectonic interpretations in any setting.

This thesis approaches the study of detachment faulting and core complex formation using a variety of geologic disciplines: structural geology, geochronology, geophysical modelling, and geobarometry. Two Tertiary extensional regions are examined: the Halloran Hills of southeastern California and the Rhodope metamorphic core complex of northeastern Greece. The emphasis in this thesis is intended to be on an interdisciplinary approach to solving geologic problems, using multiple geological techniques and geophysical modelling. In an integrated approach, field and laboratory work form the basic data set which may be interpreted qualitatively or quantitatively. Quantitative modelling often affords a better understanding of the underlying physical forces driving a particular geological phenomena. Numerical models allow rapid calculation of the outcome of a physical process; geologic time scales are unnecessary. However, the output of a numerical model is only as good as the assumptions that go into it. To properly use a model, it is necessary to evaluate the geologic data, observe how the model fits the data,

determine what geologically meaningful predictions it can make, and decide what the limitations of a particular model are.

OVERVIEW

The Halloran Hills, the subject of the second chapter of the thesis, are not a metamorphic core complex *sensu stricto*, but do owe their genesis to extension on the low-angle Halloran Hills-Kingston Range detachment fault. Recent workers at the University of Southern California has studied the structural geology of the Halloran Hills, the interaction between the Halloran Hills and Kingston Range detachment faults, and the development of the supradetachment Shadow Valley Basin [*Fowler*, 1992; *Friedmann and Burbank*, 1992; *Davis et al.*, 1993]. Chapter 2 contributes to that study by examining the implications of the extensional process on a crustal scale, namely the response of a viscous, ductile lower crust to topographic loads emplaced in the upper crust by extension. Using knowledge of the detachment fault geometry, Pliocene basalt flows, and post-extensional tilting data provided by Quaternary lake sediments, this study calculates the range of lower crustal densities and viscosities and the flexural strength of the crust that satisfactorily explain the observed post-extensional tilting. Analytical expressions derived in Appendix 2 of this chapter, removed in the published version of the paper, strongly emphasize the role of isostatic uplift in the footwalls of detachment faults, indicating that sub-horizontal to shallowly dipping faults observed today probably have been rotated from originally steeper dips.

Recently workers in the Aegean region have recognized that much of the extension in the Hellenic back arc has occurred on detachment faults, forming metamorphic core complexes (e.g. *Lister et al.* [1984]; *Schermer* [1989]; *Dinter and Royden* [1993]; *Sokoutis et al.* [1993]; *Dinter* [1994]). Perhaps the largest and best exposed of these is the late Tertiary Rhodope metamorphic core complex in northern Greece, formed when motion on the Strymon Valley detachment fault opened a tectonic window into an Alpine collisional

zone. Structural mapping in the northern Rhodope metamorphic core complex, discussed in Chapter 3, has focussed on the style and consequences of deformation related to Alpine compression and Miocene to Recent extension. The consequences of extension on the Strymon Valley detachment fault are explored in a series of regional paleogeographic reconstructions. In Chapter 4, U-Pb and $^{40}Ar/^{39}Ar$ geochronology are applied to the Vrondou pluton and the northern Rhodope metamorphic core complex to constrain the timing of pluton intrusion, the initiation of detachment faulting, the thermal evolution of the core complex during detachment faulting, and the rate of detachment fault motion over time. Chapter 5 explains the technical details of aluminum-in-hornblende geobarometry on samples from a transect of the Vrondou pluton and from the Elaion stock. This barometry is used to constrain the pre-extensional geometry of the core complex.

An interdisciplinary approach to the study of detachment faulting emphasizes the importance of integrating crustal-scale models of geologic behavior with geologic data. Chapter 6 ties together the analytical models of lower crustal flow and isostatic uplift developed in Chapter 2 with the geologic study of the Rhodope metamorphic core complex. Features in the Rhodope metamorphic core complex directly attributable to flexural isostatic uplift include the domal geometry of the detachment fault, probable rotation of pre- and syn-detachment structural fabrics, and suppression of large-scale, along-strike structural relief on the detachment fault. While there is little direct evidence for lower crustal flow, syn- and post-detachment footwall uplift is indicated by shallow marine formations now exposed at high elevations throughout the Rhodope metamorphic core complex. Furthermore, the modern topographic expression of the severely extended Rhodope crust precludes compensation by dense mantle material and suggests that the flexural strength of the Rhodope crust is low. By qualitatively applying the results of models developed for use in the Basin and Range, a better understanding of extension in the north Aegean has emerged, underscoring the common genesis of these regions in extensional tectonics.

REFERENCES

Armstrong, R.L., 1982, Cordilleran metamorphic core complexes – From Arizona to southern Canada, *Annual Reviews of Earth and Planetary Sciences*, v. 10, p. 129-154.

Coney, P.J., 1980, Cordilleran metamorphic core complexes: An overview, *in* Cordilleran Metamorphic Core Complexes, M.D. Crittenden Jr., P.J. Coney, and G.H. Davis, eds., Boulder, CO, Geological Society of America Memoir 153, p. 7-31.

Davis, G.H., and P.J. Coney, 1979, Geologic development of the Cordilleran metamorphic core complexes, *Geology*, v. 7, p. 120-124.

Davis, G.A., and G.S. Lister, 1988, Detachment faulting in continental extension: Perspectives from the Southwestern U.S. Cordillera, *in* S.P. Clark, B.C. Burchfiel, and J. Suppe, eds., Processes in Continental Lithospheric Deformation, Boulder, CO, Geological Society of America Memoir 218, p. 133-159.

Davis, G.A., T.K. Fowler, K.M. Bishop, T.C. Brudos, S.J. Friedmann, D.W. Burbank, M.A. Parke, and B.C. Burchfiel, 1993, Pluton pinning of an active Miocene detachment fault system, eastern Mojave Desert, California, *Geology*, v. 21, p. 627-630.

Dinter, D.A., and L. Royden, 1993, Late Cenozoic extension in northeastern Greece: Strymon Valley detachment and Rhodope metamorphic core complex, *Geology*, v. 21, p. 45-48.

Dinter, D.A., 1994, Tectonic evolution of the Rhodope metamorphic core complex, Northeastern Greece [Ph.D. Thesis], Massachusetts Institute of Technology, Cambridge, MA, 320 pp.

Fowler, T.K., 1992, Geology of the Shadow Mountain and the Shadow Valley Basin: Implications for Tertiary tectonics of the eastern Mojave Desert [M.S. Thesis], University of Southern California, Los Angeles, 160 pp.

Friedmann, S.J., and D.W. Burbank, 1992, Active footwall uplift recorded in a supra-detachment basin: The Miocene Shadow Valley Basin, *Eos Transactions, AGU*, v. 73, p. 549.

Lister, G.S., G. Banga, and A. Feenstra, 1984, Metamorphic core complexes of Cordilleran type in the Cyclades, Aegean Sea, Greece, *Geology*, v. 12, p. 221-225.

Lister, G.S., and G.A. Davis, 1989, The origin of metamorphic core complexes and detachment faults formed during Tertiary continental extension in the northern Colorado River region, U.S.A., *Journal of Structural Geology*, v. 11, p. 65-94.

Schermer, E.R., 1989, Tectonic evolution of the Mt. Olympos region, Greece, [Ph.D. Thesis], Massachusetts Institute of Technology, Cambridge, MA, 272 p.

Sokoutis, D., J.P. Brun, J. van den Driessche, and S. Pavlides, 1993, A major Oligo-Miocene detachment in southern Rhodope controlling north Aegean extension, *Journal of the Geological Society, London*, v. 150, p. 243-246.

Wernicke, B., 1981, Low angle normal faults in the Basin and Range Province: Nappe tectonics in an extending orogen, *Nature*, v. 291, p. 645-648.

CHAPTER 2: LOWER CRUSTAL FLOW IN AN EXTENSIONAL SETTING: CONSTRAINTS FROM THE HALLORAN HILLS REGION, EASTERN MOJAVE DESERT, CALIFORNIA

ABSTRACT

Postextensional uplift and tilting of Quaternary lake sediments in the Halloran Hills, eastern Mojave desert, California, suggest that regional-scale flow within the lower crust is occurring in response to tectonic loads created during upper crustal extension in late Miocene time. The concept that significant flow within the lower crust may occur for millions of years after the cessation of extension indicates that topographic gradients can be modified by regional-scale flow within the lower crust and that direct constraints on lower crustal flow can be obtained by quantitative analysis of rates of postextensional surface tilting. An analytic solution, developed in this paper, combines viscous flow in the lower crust, flexural bending within the midcrust, and isostasy into an invertible linear differential equation that describes the topographic response to upper crustal extension. Assuming that there was no topographic relief across the Halloran Hills region prior to extension, inversion of modern topographic data indicates that crustal thinning above the Halloran Hills detachment increases westward with a listric geometry and that little crustal thinning has occurred east of the western flank of Clark Mountain, in good agreement with the known geometry of the fault and the location of its breakaway zone. Incorporation of Quaternary tilting data indicates that the modern viscosity beneath the Halloran Hills (assuming a 10-km lower crustal channel) is a maximum of 10^{19} Pa s and that the viscosity of the lower crust has decreased by at least 1 to 2 orders of magnitude since 8 Ma. This corresponds to a temperature increase of at least 75° to 100°C at the Moho. In our opinion, the most likely source of this temperature increase is a regional-scale thermal event within the underlying mantle and diffusion of heat upward into the lower crust. If correct, these

results have important implications for the way in which crustal extension is linked to mantle heating within the Basin and Range Province.

INTRODUCTION

Studies of postglacial uplift suggest that the time required for upper crustal loads to be isostatically compensated by flow in the mantle aesthenosphere is relatively short, on the order of 10^4 to 10^5 years [e.g., *Turcotte and Schubert*, 1982; *Fjedskaar and Cathels*, 1991; *Hager*, 1991]. The timescales over which the compensation for these upper crustal loads is transferred to the lower crust has been less well examined. Many authors have suggested that in regions where the lower crust is hot, the weak lower crust flows in response to the imposition of upper crustal loads, effectively decoupling the upper crust and mantle [*Gans*, 1987; *Block and Royden*, 1990; *Bird*, 1991; *Kruse et al.*, 1991; *Spencer and Reynolds*, 1991; *Wdowinski and Axen*, 1992]. Recently, a number of authors have shown that flow within the lower crust may result from tectonic loading produced by extension [*Kusznir and Matthews*, 1988; *Block and Royden*, 1990; *Buck*, 1991; *Wdowinski and Axen*, 1992; see also *Allmendinger et al.*, 1987]. Numerical models of lower crustal flow have produced viscosity estimates of 10^{18} to 10^{21} Pa s for lower crustal flow beneath the Basin and Range Province [*Kruse et al.*, 1991; *Wdowinski and Axen*, 1992]. However, geologic timing constraints for lower crustal flow are, in general, lacking, and lower crustal parameters are not well known.

Direct constraints on lower crustal flow in regions of young extension can be obtained from rates of postextensional surface tilting. Unfortunately, precise estimates of postextensional tilting are rare within the Basin and Range Province because almost all of the young sediments are nonmarine. In this respect, the Halloran Hills extensional region, eastern Mojave Desert, California, presents an excellent opportunity to study rates and timing of lower crustal flow in response to late Tertiary extension because preservation of tilted Quaternary lake beds provides a quantitative measure of surface tilting and lower

crustal flow. The concept that significant flow within the lower crust may occur for millions of years after the cessation of extension is relevant to our understanding of many broadly extended regions and indicates that topographic gradients can be modified not only by tectonism, erosion and lithospheric heating, but also by regional-scale flow within the lower crust.

This paper develops a simple analytic model examining the relation between lower crustal flow and systematic changes in topography during and after extension, with application to the Halloran Hills region.

GEOLOGIC SETTING

The Halloran Hills region is located in the eastern Mojave desert, California. Recent mapping by *Davis et al.* [1990, 1993] indicates that rocks exposed within the Halloran Hills region are tilted and faulted blocks contained within the hanging wall of a regionally extensive, late Tertiary normal detachment fault, the Halloran Hills-Kingston Peak detachment (Figures 1 and 2). The breakaway zone for the Halloran Hills detachment is exposed in the Clark Mountains and the Mescal Range [*Davis et al.*, 1990; *Brudos and Davis*, 1992; *Davis et al.*, 1993]. This extended region is bounded on the east by the unextended zone of the Spring and Clark Mountains [*Wernicke et al.*, 1988]. Rock units exposed in the Halloran Hills region include Proterozoic plutonic and metamorphic rocks, Precambrian and Paleozoic miogeoclinal sequences, the Mesozoic Teutonia Quartz Monzanite, and a sequence of Tertiary volcanics, fanglomerates, siltstones, lake sediments, breccia sheets, and spectacularly developed glide blocks [*Parke and Davis*, 1990; *Bishop et al.*, 1991; *Fowler*, 1992; *Davis et al.*, 1993].

The topographic surface within the Halloran Hills region forms an arched morphologic surface with a northwest trending axis [*Sharp*, 1957]. Within the Halloran Hills region, the detachment fault has not been identified in surface exposures, although the large exposures of granite south of the Halloran Hills (Cima Dome area) suggest that the

detachment is probably exposed at the surface south of the Halloran Hills (G. Davis, personal communication, 1992). Based on the apparent width of tilted hanging wall blocks, *Bishop et al.* [1991] and *Davis et al.* [1993] argue that the basal detachment fault is present at several kilometers depth beneath the Halloran Hills (Figure 1c).

The earliest motion on the Halloran Hills detachment fault was probably coeval with hanging wall-to-the-west motion on the Kingston Range detachment fault, which formed the northern extension of the Halloran Hills detachment until about 12.5 Ma (Figure 2 [*Davis et al.*, 1993]). After motion ceased on the Kingston Range segment of the detachment fault, continued hanging wall-to-the-west motion on the Halloran Hills detachment (after 12.5 Ma and before 5 Ma) was accommodated by motion on an east-west trending, right-lateral strike-slip fault zone south of the Kingston Range (Blacksmith Hills fault [*Davis et al.*, 1993]), and this strike-slip fault formed the northern boundary of the region of active extension.

The cessation of motion on the Halloran Hills detachment fault can be fairly well constrained. Rocks as young as 11 Ma are deformed within the hanging wall [*Reynolds*, 1990; *Friedmann and Burbank*, 1992], and the hanging wall is overlain by basalt flows dated between 4.5 and 5.1 Ma [*Turrin et al.*, 1985]. Basalt flows as old as 7.5 Ma are found in the Cima volcanic field south of the Halloran Hills, but have an unknown relationship to extensional faulting. Thus extension on the Halloran Hills detachment fault ended between 11 Ma and 5 Ma, and probably ended before 7.5 Ma.

Fowler [1992] estimates a maximum bound on upper plate extension of about 40% in the Shadow Valley basin to the north of the Halloran Hills. If the Halloran Hills detachment fault had an original westward dip of 30° from its breakaway in the Clark Mountains, this suggests a maximum of about 5 km of upper plate thinning beneath the Halloran Hills (Figure 1). A similar estimate of maximum crustal unroofing can be extrapolated from the Kingston Range to the north, where unroofing due to detachment and/or erosion is limited to 4 km [*Davis et al.*, 1993]. Without evidence for deeper

structures, we believe that upper crustal thinning beneath the Halloran Hills is limited to a maximum of approximately 5 km relative to the unextended zone to the east. However, additional crustal extension may have occurred on deeper, unexposed structures, so that the total amount of crustal extension might be somewhat larger.

Little erosion or deposition has occurred in the Halloran Hills-Valley Wells region since the eruption of basaltic flows at around 5 Ma. The bases of these flows are typically 100 m above the general topographic surface within a region a few kilometers wide at the crest of Halloran Hills. Elsewhere the bases of the flows are only a few tens of meters above the topographic surface. Thus there has been little erosion and no deposition in these areas since 5 Ma. Thin (<10 m), partially eroded seqences of Quaternary lake beds in the Shadow Valley region (Figure 1) indicate minor Quaternary deposition and erosion in these areas.

The Quaternary lake beds exposed within and adjacent to the Halloran Hills indicate significant late Quaternary surface tilting. In particular, lacustrine sediments as young as ~0.5 Ma are found at Valley Wells [*Reynolds and Jefferson*, 1988]. Similar, probably correlative, lake beds are also exposed 60 m higher on the eastern flank of the Halloran Hills. In addition, flat-lying postextensional lake beds of unknown age are exposed 170 m lower in Kingston Wash (approximately 40 km north of Valley Wells (J. Friedmann, personal communication, 1994)). These deposits indicate that in Quaternary time a lake filled the Valley Wells-Shadow Valley region. Note on Figure 1d that the modern drainage is from the Valley Wells-Shadow Valley region westward into an areally extensive drainage basin that is nearly 1000 m lower in elevation. Thus a lake could not exist in the Valley Wells-Shadow Valley region today without filling most of the Basin and Range with water, which has not been the case. We infer that the Quaternary lake must have been bounded to the west by a paleotopographic sill extending from the Kingston Range to the Halloran Hills. At present, this inferred paleosill is 150 m lower than the lake sediments at Valley Wells. Because evidence for significant late Quaternary erosion of this topographic sill is

lacking (except for in Kingston Wash), we infer that Valley Wells has been uplifted by at least 150 m relative to the topographic sill since ~0.5 Ma. This interpretation suggests that the lake beds exposed in Kingston Wash are correlative with the Quaternary lake beds at Valley Wells, and have subsided 170 m relative to Valley Wells since about 0.5 Ma.

Another measure of late Quaternary tilting may be given by the difference in elevation of Quaternary lake sediments at Valley Wells and on the eastern flank of the Halloran Hills. Because of the facies similarities and consistent thicknesses of the middle units in both localities [*Reynolds and Jefferson*, 1988], it is likely that at the time of deposition, these sediments were deposited at approximately the same water depth and hence at the same topographic elevation. If so, then the observed offset of these Quaternary lake sediments is due to tilting of a paleohorizontal surface.

Used together, these two constraints on late Quaternary tilting are much stronger than either used in isolation. The evidence strongly suggests that the western outcrop of Quaternary lake beds and the age equivalent beds at Valley Wells were deposited at approximately the same elevation, but we cannot unequivocally demonstrate that these strata represent a paleohorizontal surface. We can unequivocally demonstrate that since 0.5 Ma, Valley Wells has been uplifted by at least 150 m relative to the paleotopographic sill ~30 km to the north. However, this is only a minimum estimate, and the total magnitude of relative uplift could be much greater.

These geologic data from the Halloran Hills, summarized schematically in Figure 3, provide a good opportunity to test models that describe the formation and evolution of topographic features in response to crustal processes. Bounds on the time of faulting, knowledge of the modern topography, and estimates of late Quaternary surface tilting provide constraints that may be used to answer questions such as (1) what range of fault geometries can produce the modern topography that exists across the Halloran Hills, and (2) can postextensional lower crustal flow explain the sense of motion and magnitude of uplift observed across the Halloran Hills?

DUCTILE FLOW IN THE LOWER CRUST

Strength profiles of the continental lithosphere suggest that the lower part of the crust is significantly weaker than the upper crust and upper mantle and that ductile flow may occur in the lower crust. This result follows directly from the equations that govern deformation of crustal materials in which flow is a nonlinear function of temperature and deviatoric stress. For one-dimensional flow, strain rate is related to deviatoric stress and temperature by

$$\dot{\varepsilon} = \frac{1}{2}\frac{du}{dy} = A\tau^n e^{-Q/R\theta} \tag{1}$$

where y is vertical distance (above the base of the crust), $\dot{\varepsilon}$ is strain rate, u is flow velocity in the horizontal direction, τ is shear stress, θ is temperature, and A, Q, and n are empirically determined constants for a given rheology. (Definitions and values for these and other variables are tabulated in Table 1.) Although these empirical parameters are based on laboratory measurements at high strain rates, it is probable that similar behavior occurs at the much lower strain rates for crustal deformation.

Flow within the lower crust with a power law dependence can be derived by combining equation (1) with the force balance equation, where P is pressure:

$$\frac{d\tau}{dy} = -\frac{dP}{dx} = \frac{d}{dy}\left[\left(\frac{du}{dy}\frac{1}{2A}e^{Q/R(\theta_o - \zeta y)}\right)^{1/n}\right]. \tag{2}$$

Temperature θ has been replaced by $\theta = \theta_o - \zeta y$, where θ_o is temperature at the base of the crust and ζ is the geothermal gradient, assumed to be linear with depth. This equation may be rearranged to form an expression for flow velocity, u:

$$u(y') = 2A\left(-\frac{dP}{dx}\right)^n \int_0^{y'} (y - C_1)^n e^{-Q/R(\theta_o - \zeta y)}\, dy + C_2 \qquad (3)$$

where C_1 and C_2 are arbitrary constants of integration. Although empirically derived values of n are material dependant and usually noninteger (Table 1), n is often close to 3. Setting n=3, this expression can be numerically integrated for different values of θ_o and ζ to solve for the flow velocity within the lower crust for a given total crustal thickness (taken here to be 30 km). The constants C_1 and C_2 are determined from the boundary conditions that $u = 0$ at the top and bottom of the region of interest, in this case at $y = 0$ (base of the crust) and $y = 20$ km (assumed base of the upper crustal brittle layer).

Figure 4a shows that, for a linear geothermal gradient, flow is confined to a lower crustal channel by the inherent viscosity structure of the crust and upper mantle. The channel thickness is approximately 8 to 12 km in depth for a quartzite or Westerly granite rheology. Changing the geothermal gradient has only a minor effect on the channel thickness and the normalized flow profile through the crust (Figure 4b), although it has a large effect on the total magnitude of the flow. Flow velocities drop to zero at the upper part of the lower crust because the effective viscosity increases upwards with decreasing temperature. The exact position of the base of the upper crustal brittle layer is not important, and nearly identical results are obtained if the upper boundary is set at the surface ($y = 30$ km). A narrower channel results for the Westerly granite rheology because it has a higher activation energy than quartz, yielding a stronger dependence of effective viscosity on temperature.

We can use this result, that flow in the lower crust develops in a narrow channel, to approximate the rheology of the lower crust as an upper region in which no flow occurs and a lower region in which flow is confined to a channel of specified thickness, probably between 8 and 12 km. Figure 4a also shows the flow profile for a lower crustal channel 10

km thick with a uniform Newtonian viscosity and no flow at the top and base of the channel. Provided that an appropriate viscosity is chosen for this 10-km-thick channel, the integrated flux through the channel will be the same as for the power law based rheology (note that appropriate viscosity will also depend on the pressure gradient dP/dx). We will refer to this uniform Newtonian viscosity as the equivalent viscosity μ_{eq} because it produces a total integrated flux equal to that of the power law rheology for a specified pressure gradient and a specified geothermal gradient (see appendix for further discussion).

The equivalent viscosity can be related to the geothermal gradient and material properties within the crust. Figure 4c shows total integrated flux, U, for power law flow as a function of geothermal gradient . (In constructing Figure 4c, we have assumed a pressure gradient of dP/dx = 1000 Pa/m, equivalent to about a 3% topographic slope.) For a quartzite rheology there is an approximately exponential dependence of integrated flux on geothermal gradient. There is also an increase in the total integrated flux by about 1 order of magnitude for each 3°C/km increase in geothermal gradient.

For a channel with Newtonian viscosity, the total integrated flux in the channel is linearly related to viscosity. Thus in approximating channel flow due to power law rheology by an equivalent viscosity, the equivalent viscosity will be exponentially dependent on geothermal gradient. For a quartzite rheology there is an increase in the equivalent viscosity by about one order of magnitude for each 3°C/km increase in geothermal gradient (Figure 4c). This result is essentially independent of the pressure gradient assumed. For a pressure gradient of 1000 Pa/m, a quartzite rheology with a geothermal gradient of 20°C/km corresponds to a viscosity of about 10^{20} Pa s in a 10-km-thick channel, although this relationship is highly dependent on pressure gradient and on the large uncertainties in the material properties of quartzite. If a different pressure gradient is assumed, the curves based on a power law rheology will be shifted up or down by a constant value on Figure 4c but will maintain their shape.

The results of this section show that power law flow in the lower crust can be approximated, to first order, by Newtonian flow in a lower crustal channel with uniform thickness. The equivalent Newtonian viscosity will be strongly (exponentially) dependent on geothermal gradient and less strongly (quadratically) dependent on pressure gradient. This result will be used in the next section to develop an analytical model combining lower crustal flow, flexure, and isostasy. In the next sections we will ignore the effect of pressure gradient on viscosity, but importance of this assumption is addressed in the appendix.

ANALYTICAL SOLUTION: CRUSTAL FLOW, FLEXURE, AND ISOSTASY

Figure 5 shows a simplified model for the large-scale behavior of the crust during deformation. The crust is divided into a brittle upper crust and a ductile lower crust separated by an "elastic core", which provides flexural support for loads. The base of the lower crust is treated as a viscous channel of thickness, H, bounded below by the Moho. The channel thickness is assumed to be uniform in space and constant in time (although its viscosity may change through time). The thickness of the lower crust, $h(x,t)$, is allowed to vary in time and space. No horizontal flow is allowed to occur at the Moho because the uppermost mantle is assumed to be strong. The asthenosphere is treated as an inviscid body responding to crustal loads on timescales on the order of 10^4 to 10^5 years [e.g., *Hager*, 1991; *Fjeldskaar and Cathels*, 1991], effectively instantaneous relative to the rate at which geologic processes occur (e.g., crustal loading).

Deformation in the upper crust produces tectonic loads that initiate flow in the lower crust and asthenosphere. During deformation (loading) of the upper crust, the mantle responds with virtually instantaneous flow that, together with the flexural bending of the crust, supports thickness variations within the upper crust. With time, flow occurs within the lower crust, gradually shifting the region in which tectonic loads are isostatically

compensated from the mantle to the lower crust. The lower crust thickens under areas of tectonically thinned upper crust while flowing away from regions of thicker upper crust. Because the density of the lower crust is less than that of the mantle, topographic gradients caused by isostatic compensation in the dense mantle are gradually reduced (except for short wavelength features that are elastically supported). The deflection of the Moho also decreases with time, and the Moho ultimately becomes flat as the lower crust completely compensates for tectonic loading in the upper crust.

Analytic Solution for Lower Crustal Flow With Newtonian Rheology

The behavior of this system that incorporates flow within the lower crust and mantle and flexural bending of the crust can be described by combining the flexure, continuity, and the Navier Stokes equations with regional isostasy in the mantle. The equation that governs the flexural bending of the crust is

$$D \frac{\partial^4 w(x,t)}{\partial x^4} = f(x)\rho_c g + [h(x,t) - H]\,\rho_o g + P_t(x) \tag{4}$$

where $f(x)$ is the thickness of the upper crustal load, $w(x,t)$ is the time dependent vertical displacement in response to tectonic loads, and $P_t(x)$ is the pressure at the top of the lower crustal channel. Isostasy in the mantle requires no lateral pressure gradients at some arbitrary depth of compensation c_o, giving

$$P_t(x) + H\,\rho_o g + (c_o - w_o - w - h)\,\rho_m g = \text{const} \tag{5a}$$

or equivalently,

$$\frac{\partial P_t}{\partial x} = \frac{\partial (w+h)}{\partial x} \rho_m g. \tag{5b}$$

Flow within a gently inclined lower crustal channel may be mathematically described with the continuity equation and the Navier-Stokes equation for low Reynolds number flow:

$$\frac{\partial u}{\partial x} + \frac{\partial v}{\partial y} = 0 \tag{6}$$

$$\rho_o g \sin(\beta) - \frac{dP_t}{dx} + \mu(t) \left(\frac{\partial^2 u}{\partial x^2} + \frac{\partial^2 u}{\partial y^2} \right) = 0 \tag{7a}$$

$$\rho_o g \cos(\beta) - \frac{dP_t}{dy} + \mu(t) \left(\frac{\partial^2 v}{\partial x^2} + \frac{\partial^2 v}{\partial y^2} \right) = 0 \tag{7b}$$

where u is the fluid velocity in the x direction as above, v is the fluid velocity in the y direction, β is the angle of inclination of the channel, and $\mu(t)$ is the time dependent viscosity of the lower crustal channel. We assume that the spatial dependence of viscosity is small, especially compared to changes in viscosity through time. Because we are also assuming a Newtonian rheology, we are ignoring any dependence of the viscosity on pressure gradient (see appendix for discussion). For small angles β,

$$\sin(\beta) \approx \tan(\beta) \approx \frac{d(w+h)}{dx} \tag{8a}$$

$$\cos(\beta) \approx 1. \tag{8b}$$

For Newtonian flow in a gently inclined channel with velocity equal to zero at upper and lower boundaries (Poiseuille flow) and with a time dependent viscosity $\mu(t)$, u and v are given by

$$u = \frac{1}{2\mu(t)}\left[\frac{dP_t}{dx} - \rho_o g\left(\frac{dh}{dx} + \frac{dw}{dx}\right)\right] y\,(y-H) \tag{9a}$$

$$v = -\frac{1}{2\mu(t)}\left[\frac{d^2P_t}{dx^2} - \rho_o g\left(\frac{d^2h}{dx^2} + \frac{d^2w}{dx^2}\right)\right]\left(\frac{y^3}{3} - \frac{Hy^2}{2}\right) \tag{9b}$$

provided that the third and higher derivatives of P, h, and w with respect to x are small compared to lower derivatives. The change in thickness of the lower crust through time is then simply given by the difference in the vertical flow at the top and bottom boundaries:

$$\frac{dh(x,t)}{dt} = v\Big|_0^H = \frac{H^3}{12\mu(t)}\left[\frac{d^2P_t}{dx^2} - \rho_o g\left(\frac{d^2h}{dx^2} + \frac{d^2w}{dx^2}\right)\right]. \tag{10}$$

Combining equations (4), (5b), and (10) to solve for the deflection of the crust through time gives

$$\frac{\partial}{\partial t}\left(D\frac{\partial^4 w(x,t)}{\partial x^4} - f(x)\rho_c g + \rho_m g w(x,t)\right) =$$

$$\frac{(\rho_m-\rho_o)\,g\,H^3}{12\mu(t)}\,\frac{d^2}{dx^2}\left(D\frac{\partial^4 w(x,t)}{\partial x^4} - f(x)\rho_c g + \rho_o g w(x,t)\right). \tag{11}$$

(A similar relationship, expressed in a different form, has also been derived by *Kusznir and Matthews* [1988].)

In this paper, we assume faulting occurs instantly with no thickness changes within the upper crust after the initial faulting event, giving $df/dt = 0$. (If faulting is taken to be noninstantaneous, then some finite amount of lower crustal flow will occur during extension. However, the topography at the end of faulting would look approximately the same as if instantaneous faulting had occurred followed by lower crustal flow over a time period somewhat less than the duration of extension.)

Several special cases of equation (11) are worth noting. First, when the crust has no flexural strength ($D=0$), equation (11) reduces to a simple diffusion equation. Second, if lower crustal flow has gone to completion, such that $t = \infty$, then the left-hand side of equation (11) is zero and the equation reduces to the flexure equation with compensation in the lower crust. Third, if there is no flow in the lower crust (μ is infinite) the right-hand side of equation (11) equals zero; there is no time dependent behavior, and loads are compensated in the mantle. For $t=0$, when crustal flow has not yet occurred, the latter geometry will also be present. This is consistent with all compensation being in the mantle at $t=0$.

Equation (11) is most easily solved by taking its Fourier transform. A solution that satisfies the initial conditions and conditions at $t = \infty$ is

$$\tilde{w}(k,t) = \tilde{f}(k)\rho_c g\left[\frac{1}{Dk^4 + \rho_o g} + \left(\frac{1}{Dk^4 + \rho_m g} - \frac{1}{Dk^4 + \rho_o g}\right)e^{-\gamma(k,t)}\right] \qquad (12)$$

where $\tilde{w}(k,t)$ and $\tilde{f}(k)$ are the Fourier transforms of $w(x,t)$ and $f(x)$, respectively, and k is the wave number (1/wavelength).

The decay constant $\gamma(k,t)$ is defined by

$$\gamma(k,t) = \left[\frac{(\rho_m - \rho_o)\, g\, H^3}{12}\right]\left[k^2\, \frac{Dk^4 + \rho_o g}{Dk^4 + \rho_m g}\right] \int_0^t \frac{dt'}{\mu(t')} \quad . \tag{13}$$

The variable $\gamma(k,t)$ controls the rate at which crustal thickness variations are compensated by flow within the lower crust. For short wavelength features, k and $\gamma(k,t)$ are large, and flow occurs rapidly; for long wavelength features, k and $\gamma(k,t)$ are small, and flow occurs slowly. Thus short wavelength features are rapidly smoothed over, while longer wavelength features take longer to come to a final equilibrium state. Note that $\gamma(k,t)$ is linearly dependent on the density contrast between lower crust and mantle and, for constant μ, on $[H^3/\mu]$. Thus lower viscosities, greater channel thicknesses, and greater density contrasts all serve to increase the rate at which flow occurs in the lower crust. The parameter $[H^3/\mu]$ combines two unknown lower crustal quantities that we aim to determine together by examining time dependent evolution of the Halloran Hills. However, arguments from the preceding section suggest that H is likely to be around 8 to 12 km.

Inverse Method

One of the powerful features of the mathematical model developed here is the linear nature of equation (11). This permits us to formulate an inverse problem, where we can use observed topography to solve for $f(x)$ and $w(x,t)$. This has obvious advantages over forward modeling, where one must guess $f(x)$ and proceed by trial-and-error to match the observed topography. In our opinion, errors in assuming a constant channel thickness for flow and spatially invariant viscosity are more than compensated by the derivation of a invertible linear equation. (Because we do not know how channel thickness and viscosity might vary laterally, models that incorporate lateral variations in these parameters are not

only more complex, but are likely to introduce errors as large or larger than those arising from assuming that these parameters are constant.)

The surface topography $T(x,t)$ is related to the thickness of the upper crustal material removed during faulting, $f(x)$, and the deflection of the elastic core due to flexure, $w(x,t)$:

$$T(x,t)=f(x)+w(x,t). \tag{14}$$

It is possible to calculate the predicted topography for an arbitrarily complicated fault geometry by assuming that the fault is composed of N planar segments. Figure 5b schematically shows such a detachment fault geometry with N planar segments, where the ith fault segment is located between x_i and x_{i+1} and corresponds to removal of a section of upper crustal material with geometry $d_i f_i(x)$. The f_i are defined to have unit thickness between $x=0$ and $x=x_i$, and the d_i are dimensionless constants such that $d_i f_i(x)$ gives the thickness of each fault wedge between $x=0$ and $x=x_i$ (Figure 5). In this simple geometry we assume for $x>x_N$ there is no thinning of the crust. For $x<x_0$ the fault is a horizontal decollement. The predicted topography $T(x,t)$ is

$$T(x,t) = T_o + \sum_{i=1}^{N} d_i f_i(x) + \sum_{i=1}^{N} d_i w_i(x,t) \tag{15}$$

where T_o is a constant and $d_i f_i(x)$ and $d_i w_i(x,t)$ are the upper crustal thinning and the flexural response, respectively, to removal of the ith upper crustal block. If M observations of topography are made at positions $x=x_i$, then M equations may be set up for the topography $T(x_i,t)$:

$$T(x_j,t) = T_o + \sum_{i=1}^{N} d_i f_i(x_j) + \sum_{i=1}^{N} d_i w_i(x_j,t) \qquad 1 \le j \le M . \tag{16}$$

Combining Equations (12) and (16) gives

$$T(x_j,t) = T_o + \sum_{i=1}^{N} d_i f_i(x_j) +$$

$$\sum_{i=1}^{N} d_i F^{-1} \left\{ \tilde{f}_i(k)\, \rho_c g \left[\frac{1}{Dk^4 + \rho_o g} + \left(\frac{1}{Dk^4 + \rho_m g} - \frac{1}{Dk^4 + \rho_o g} \right) e^{-\gamma(k,t)} \right] \right\} \Bigg|_{x=x_i} \tag{17}$$

where F^{-1} signifies the inverse Fourier transform of the function in the braces, evaluated at $x=x_j$. This set of equations is linear with respect to the thicknesses of the removed crustal blocks, d_i. If $M = N$ and the values for x_i are specified, then a matrix can be formed which can be inverted to determine values of T_o and the d_i, thereby solving for the amount of crustal material that is removed by extension. (Or if $M > N$, then the values of the d_i can be found that minimize the misfit between the observed and computed topography.) Thus, given an observed topography at a specified time t after crustal deformation and assumptions about values of D, ρ_o, and $\mu(t)$, one can use equation (17) to solve for the initial crustal geometry $(d_i f_i)$ that exactly reproduces the observed topography (Figure 5a). This is not possible with the numerical methods usually used to model flow, nor for numerical or analytical techniques that assume non-Newtonian flow.

INVERSE MODELING OF HALLORAN HILLS REGION

Computed Fault Geometries

From the equations derived in the preceding section, one can derive the amount of crustal thinning necessary to reproduce a given topographic profile, provided that the lower crustal viscosity, lower crustal density, flexural rigidity, timing of extension and preextensional topography are known. The same pieces of information can be used to calculate postextensional surface tilting in response to lower crustal flow through time. In order to understand the evolution of the Halloran Hills through time, we need to understand the effects of these parameters on the calculated magnitude of crustal thinning and the calculated tilting rate.

For the inverse model presented in this paper, we used topographic data from an east-northeast trending cross section across the crest of the Halloran Hills (Figure 1). Topographic data east of the breakaway zone in the Clark Mountains were also included within the data set. For simplicity, the locations of the M topographic data points (x_j) were taken to be the endpoints for N individual planar segments along the denudation profile (x_i), with $M=N$, giving an exactly invertible $(N \times N)$ matrix. Flow in the lower crust is assumed to occur for 8 m.y., roughly corresponding with the time since the end of major extensional faulting within the Halloran Hills. The lower crustal channel thickness, H, was held constant at 10 km. Because no data are available on preextensional topography in this region, we make the assumption that the preextensional topographic surface had no relief.

In this section, we examine the effects of lower crustal density, lower crustal viscosity, and flexural rigidity on the computed geometry of crustal material removed during extensional faulting. (For clarity, we will refer to the geometry of all the material removed during faulting, or the net crustal thinning, as the "denudation profile." If all of the material above a detachment fault is removed during extension, then the denudation profile is equivalent to the initial fault geometry prior to extension, assuming no footwall deformation. If not all of the material above the detachment fault is removed during

extension, then the denudation geometry and the initial fault depth do not correspond. The upper crustal geometry $f(x)$ is then taken to be the total upper crustal load, or the total thickness of crustal material removed during faulting; it should not be interpreted as a detachment fault surface.)

The three curves in Figure 6a correspond to lower crustal densities ρ_o of 0.5%, 1%, and 10% greater than that of the upper crust (mantle density is 22% greater). All three curves show a geometry that is listric in character. When the density of the lower crust increases, there is a decrease in the amount of upper crustal thinning required to produce the present topography. Depending on flexural wavelength chosen, lower crustal densities consistent with the observed topography can be as low as the density of the upper crust and still produce less than 5 km of crustal thinning beneath the Halloran Hills.

The three curves in Figure 6b correspond to flexural wavelengths α of 8 km, 16 km, and 32 km (α is computed as defined in Table 1). All three curves are approximately listric in character. The crustal thinning geometry is a complex function of flexural wavelength and lower crustal density, but increasing the flexural wavelength decreases the amounts of crustal thinning computed. Small flexural wavelengths predict greater thinning and a less smooth geometry. This occurs as surface topography begins to directly reflect the crustal thinning, ultimately resulting in Airy compensation.

The three curves in Figure 6c correspond to time-averaged lower crustal viscosities μ_{av} of 2×10^{20}, 2×10^{19}, and 2×10^{18} Pa s. Increasing the viscosity of the lower crust decreases the amount of thinning across the Halloran Hills. As viscosity increases, less flow can occur over 8 Ma, and more of the crustal load must be supported in the mantle. In the limit of lower crustal viscosity going to infinity, flow does not occur, and the predicted initial upper crustal geometry is equivalent to that for a lower crustal density approaching that of the mantle.

Note that all of the denudation profiles shown in Figure 6 show little crustal thinning on the east flank of the Clark Mountains, consistent with the observation that the

breakaway for the west dipping Halloran Hills detachment lies on the western flank of the Clark Mountains. In addition, all profiles show a westward increase in the amount of crustal thinning consistent with what one would expect above a west dipping detachment fault. Note too, that all denudation profiles are roughly listric in shape, also consistent with what one might expect above a low angle normal fault.

Although constraints on total thinning are not sufficient to distinguish among curves, the broad range of denudation profiles and crustal parameters that are compatible with the modern topography across the Halloran Hills can be greatly reduced by requiring the temporal evolution of the topographic profiles to be consistent with the record of surface tilting within the Halloran Hills.

Constraints Placed by Quaternary Tilting

Occurrences of Quaternary lake beds place the best constraints on the recent uplift of Halloran Hills relative to the surrounding areas. Because our model calculations are two-dimensional, they are strictly applicable only to problems in two-dimensional flow. However, in the Halloran Hills region, lower crustal flow following extension probably occurred both from the north and from the east. This geometry is shown schematically in Figure 2, in which Kingston Wash is shown to define a zone separating a northern region which did not experience extension after 12.5 Ma from a southern region which experienced later extension. If we make the simplistic assumption that the rate of lower crustal flow from the north is approximately the same as the rate of lower crustal flow from the east, then the rate of north-south tilting at Valley Wells should be about the same as the rate of east-west tilting at Valley Wells. This allows us to project the amount of relative vertical motion between Valley Wells and a point lying approximately 30 km to the north along the paleolake sill (Figure 1d) onto the approximately east-west topographic profile through Valley Wells. This point on the cross section will be called the projected northern sill. We estimate that in simplifying this three-dimensional flow problem to a simple two-

dimensional cross-sectional geometry, we are incorporating uncertainties of perhaps a factor of 2 in the magnitude of tilting and uplift.

Figure 7 shows predicted topography as a function of time for the crustal parameters corresponding to curve B in Figure 6. Initially steep topographic gradients between the Clark Mountains and Baker are rapidly subdued by rapid flow within the lower crust, while the region which is to become the Halloran Hills is uplifted relative to regions to its east. By 2 Ma, crustal flow proceeds slowly, and the rates of surface uplift and subsidence are much slower than at earlier times. Near Halloran Hills the computed direction of tilting is consistent with the observed tilting of Quaternary lake beds, but the computed magnitude of tilting is too small by at least 1 order of magnitude (Figure 8). This result cannot be improved significantly by changing the lower crustal viscosity; viscosities between 2×10^{18} and 2×10^{19} Pa s yield the greatest magnitude of computed Quaternary tilting. For very low viscosities, flow is completed by 2 Ma and there is no significant tilting after 2 Ma. For very high viscosities, very little flow occurs between 8 Ma and the present, and there is no significant tilting between 2 Ma and the present. High viscosities also predict initial postextensional topographic gradients that are very gentle, and the total amount of tilting is much less than for lower viscosities (for example, Figure 6c). For average viscosities above about 2×10^{20} Pa s, the total uplift of the western lake beds relative to Valley Wells is less than 60 m. For average viscosities above about 2×10^{19} Pa s, the total uplift of Valley Wells relative the projected northern sill is less than 150 m. These provide an upper bound on the average viscosity for the entire 8 m.y. period.

One way in which the observed magnitude of Quaternary tilting might be explained by lower crustal flow is with a significant decrease in channel viscosity between 8 Ma and the present. Note that, if viscosity is a function of time, any viscosity function that satisfies

$$\frac{1}{(t_2-t_1)}\int_{t_2}^{t_1}\frac{dt'}{\mu(t')}=\frac{1}{\mu_{av}} \qquad (18)$$

will produce the same amount of lower crustal flow and surface tilting between $t=t_1$ and $t=t_2$. For simplicity, we identify an average viscosity prior to the deposition of the Quaternary lake beds (μ_{early}) and an average viscosity after the deposition of the Quaternary lake beds (μ_{late}). Then, if the average viscosity (μ_{av}) for the interval 0 to 8 Ma is specified, μ_{early} and μ_{late} can be uniquely determined by requiring the computed tilting to match the observed Quaternary tilting.

For example, using curve B from Figure 6 ($\mu_{av} = 2 \times 10^{19}$ Pa s) and the requirement that the western lake beds and Valley Wells be at the same elevation at 0.5 Ma gives $\mu_{early} = 1.3 \times 10^{20}$ Pa s and $\mu_{late} = 1.5 \times 10^{18}$ Pa s (Figure 9 and Table 2). These values of μ_{early} and μ_{late}, which yield 60 m of post 0.5 Ma uplift of the western lake beds relative to Valley Wells, also yield about 150 m of uplift of Valley Wells relative to the projected northern sill over the same time interval. Thus both estimates of late Quaternary vertical motion, which have different sources of uncertainty, give consistent estimates of late Quaternary tilting near Valley Wells and consistent estimates of lower crustal viscosity as a function of time. The minimum viscosity change from μ_{early} to μ_{late} is about 1 to 2 orders of magnitude (Table 2). Note that μ_{early} and μ_{late} are average viscosities before and after deposition of the Quaternary lake beds and probably reflect a gradual change in viscosity through time rather than an abrupt change of viscosity at 0.5 Ma. It is not possible to place an upper bound on the viscosity decrease and we have selected as most reasonable those models which produce the smallest change in viscosity from 8 Ma to the present (see discussion below).

Additional Evidence for Tilting and Uplift

Because tilting constraints from Quaternary lake beds are applicable only to regions within a few tens of kilometers of Valley Wells, this tilting might reflect local processes active during late Quaternary time (for example, magma inflation). However, other geologic data indicate that paleotopographic gradients of regional extent were created at the time of extension, and that these paleogradients were probably steeper than those present in the same regions today. This is an important point because it indicates that regional changes in topographic gradients were temporally linked to extension and that regional topographic gradients have probably decreased since the time of extension.

Evidence for steep paleotopographic gradients created during extension include spectacularly developed gravity glide blocks, breccia sheets, and boulder conglomerates shed westward from the Clark Mountains [*Parke and Davis*, 1990]; (Friedmann et al., Basin geometry, paleodrainage, and geologic rates from the Shadow Valley supradetachment system, Eastern Mojave, California, submitted to *Reconstructing Cenozoic History of the Basin and Range with the Stratigraphic Record*, edited by K. Beratan and J. Smith, *Geol. Soc. Am. Spec. Pap.*, 1994) (herein after referred to as Friedmann et al., submitted manuscript). In addition, late Miocene coarse clastic synextensional sediments were shed southward off of the Kingston Range (Figure 3 [*Friedmann and Burbank*, 1992; *Davis et al.*, 1993]). Transport and deposition of these sediments postdate motion on the northern segment of the Kingston Range-Halloran Hills detachment fault and probably coincided with continuing or renewed motion on the southern portion of the Halloran Hills detachment fault [*Davis et al.*, 1993; Friedmann et al., submitted manuscript]. At this time the right-lateral Blacksmith Hills fault formed the northern boundary of the region of active extension, so that steep topographic gradients seem to have been formed along both margins of the actively extending region.

Moderately extensive basalt flows were erupted along the crest of the Halloran Hills antiform and in the Cima volcanic field between 8 Ma and the present [*Dohrenwend et al.*,

1984]. Flow directions for 5.1 to 3.6 Ma basalts erupted from centers along the crest of the Halloran Hills indicate that an antiformal geometry was present by at least 5 Ma (older flows are restricted to the Cima volcanic field south of the Halloran Hills). (In this study, all of the acceptable model runs reproduced this antiformal geometry by 5 Ma, for example, Figure 7.) These basalts also provide circumstantial evidence that bending of the Halloran Hills antiform occurred progressively from 8 Ma to the present. For example, a northwest trending dike swarm near the crest of the Halloran Hills [*Wilshire*, 1988] indicates that during intrusion the axis of least horizontal compression was perpendicular to the axis of the Halloran Hills antiform. This suggests that basaltic volcanism was localized along the crest of the Halloran Hills antiform because the axis of the antiform coincided with the axis of greatest extensional bending. If this interpretation is correct, then the eruption of basalts from 8 Ma until the present is consistent with progressive flexing of the Halloran Hills antiform over this time interval. The presence of very young (Holocene) flows to the south in the Cima volcanic field suggests that this flexural bending process is continuing today and is consistent with observations of young tilting as deduced from the Quaternary lake sediments.

DISCUSSION

In this paper we have developed an analytical method for computing rates of lower crustal flow from observations of surface topography and postdeformational surface tilting. Application of this method to the Halloran Hills and adjacent areas indicates that the maximum average lower crustal viscosity between 8 Ma and the present is no more than 10^{20} Pa s (for a 10-km-thick channel) and that the channel viscosity decreased by at least 1 to 2 orders of magnitude over this time interval. If correct, these results have important implications for the geological and thermal evolution of the Halloran Hills region (and probably other parts of the Basin and Range province) and provide constraints on the

deformation properties of crustal rocks at lower crustal temperatures and at geological strain rates.

Regional Geological Implications

It is generally assumed that the uplifted ranges within the Basin and Range Province are faulted, tilted, and rotated crustal blocks found in the hanging walls of major detachment faults. However, much of the topographic relief in the Clark Mountains and the Kingston Range may have been created by a very different mechanism: by flexural uplift of the footwall adjacent to a regional detachment fault [e.g. *Weisel and Karner*, 1989; Vening Meinesz, 1950]. For example, the western flank of the Clark Mountains appears to be formed by the denuded Halloran Hills detachment fault, somewhat modified by erosion, while the eastern slope of the Clark Mountains appears to be largely the result of flexural uplift of a previously horizontal or gently dipping surface. Because the flexural strength of the Basin and Range Province is very low, the flexurally uplifted Clark Mountain and Kingston ranges that have dimensions similar to those of faulted crustal blocks found in the hanging walls of major detachment faults.

It may be that other uplifted ranges within the Basin and Range Province have been created by flexural footwall uplift (see also discussion by *Wernicke and Axen* [1988]). A possible candidate for a flexurally uplifted range is the Spring Mountain Range, which lies east of the Kingston Range detachment fault. If so, then the breakaway zone for the Kingston Range detachment may occur farther east than has been recognized previously (see discussion by *Fowler* [1992]; T.K. Fowler and J.P. Calzia, manuscript in preparation, 1994).

Implications for Crustal Flow Properties at Geological Strain Rates

Our study suggests that the modern viscosity of the lower crust beneath the Halloran Hills region is a maximum of about 10^{20} Pa s (assuming a 10-km-thick channel).

This gives a bound on the material properties of the lower crust at geological strain rates and lower crustal temperatures and should provide a useful addition to laboratory data measured at strain rates many orders of magnitude faster. However, before this result is useful, the equivalent Newtonian channel viscosities must be interpreted in terms of temperature, pressure gradient, and power law flow.

The absolute value of equivalent viscosity depends on the geothermal gradient and on the pressure gradient driving the flow. Figure 10 shows a plot of lateral pressure gradient versus equivalent channel viscosity (μ_{late}) for model runs that produced acceptable fits to the topographic, geologic, and Quaternary tilting data from the Halloran Hills region. Lateral pressure gradients correspond to computed present-day lower crustal pressure gradients for each of the model runs and the channel viscosity is the viscosity computed for 0.5 Ma to the present (μ_{late}). Using a nominal temperature at the base of the crust of 600°C and assuming a linear geothermal gradient, the relationship between lateral pressure gradient and equivalent viscosity for quartzite and Westerly granite has also been computed. (The equivalent viscosity is that which produces the same integrated flow within a 10-km-thick channel as is produced by power law flow for a specified pressure gradient and temperature, or geothermal gradient.)

Figure 10 indicates that present-day flow within the lower crust beneath the Halloran Hills region is proceeding at a rate well within the uncertainty range of predicted flow rates for quartzite as extrapolated from laboratory to geological strain rates. Because we cannot place a lower bound on the modern viscosity beneath the Halloran Hills region, we cannot preclude the possibility that flow is occurring at rates much faster than that predicted from a quartzite rheology, but many of the model runs, and our preferred results, indicate that flow rates are within the bounds predicted by the flow properties of quartzite.

Thermal Implications

Paleotopography predicted by the flow models and Quaternary tilting data indicate that the equivalent viscosity within the lower crust must have decreased by at least one to two orders of magnitude since the time of extension. The most likely cause for a viscosity decrease of this magnitude is an increase in the temperature of the lower crust. Figure 4c shows the relation between equivalent viscosity and temperature at the base of the crust (for a linear geothermal gradient) for quartzite rheology. An order of magnitude decrease in equivalent viscosity is equivalent to an increase in Moho temperature of about 75°C. This result is independent of pressure gradient driving the flow because changing the pressure gradient simply shifts the curves up and down on the plot without changing their shape.

There are several mechanisms by which heat may be added to the lower crust during extension. For example, magmatic intrusion into the lower crust can raise the temperature of the lower crust significantly, but requires enormous volumes of magma to do so. For example, a magmatic sill 5 km thick at the Moho at a temperature 300°C hotter than the surrounding rocks would be required to produces a temperature increase of 75°C after 4 m.y. However, the total volume of magma erupted within the Halloran Hills is quite small. We feel that it is unlikely that such large volumes of magma could have been emplaced in the lower crust on a regional scale without a much greater volume and areal extent of surface volcanism. However, we cannot rule out the possibility that magmatic intrusion contributes to some of the temperature increase within the lower crust [*Gans and Miller*, 1983; *Miller et al.*, 1983; *McCarthy and Thompson*, 1988].

Another mechanism for increasing the temperature of the lower crust is a regional-scale thermal event within the mantle and diffusion of heat from the mantle into the lower crust. If the inferred temperature increase within the lower crust is due to diffusion of heat from the mantle, mantle heating must predate or partially predate the temperature increase within the lower crust because of the timescale over which thermal diffusion occurs. (For example, it takes 5 to 10 m.y. for significant increases in temperature to occur if diffusion

occurs over a distance of several tens of kilometers.) This suggests that heating within the mantle may be coeval with or even predate crustal extension (although it is possible that heating within the mantle continued after extension was complete). We feel that a regional heating event within the mantle is the most likely mechanism for heating of the lower crust beneath the Halloran Hills because it explains the magnitude and regional scale of the inferred crustal heating, as well as the continued heating of the lower crust for millions of years after the end of crustal extension.

CONCLUSIONS AND IMPLICATIONS

Postextensional uplift and tilting of Quaternary lake sediments in the Halloran Hills, eastern Mojave desert, California, suggest that regional-scale flow within the lower crust is occurring in response to tectonic loads created during upper crustal extension in late Miocene time (at approximately 8 Ma). Constraints on paleotopography and tilting rates from Quaternary lake beds indicate that the viscosity of the lower crust beneath the Halloran Hills has decreased by at least one to two orders of magnitude since 8 Ma, corresponding to a temperature increase of at least 75° to 100°C at the Moho.

Although this paper specifically describes the evolution of the Halloran Hills region, the method developed in this paper, whereby lower crustal flow rates can be constrained from surface topography and rates of surface tilting, is generally applicable to regions that have experienced crustal extension. Because it is difficult to be sure that surface tilting in any one area is due to lower crustal flow, analyses of postextensional surface tilting are needed in several areas of young extension. In particular, we need to address whether postextensional surface tilting and lower crustal flow commonly occur over a timescale of millions of years, as is inferred in this study of the Halloran Hills. In addition, it is important to establish whether there is generally a decrease in the effective viscosity of the lower crust on the same timescale. If the latter can be established, it has important implications for the way in which crustal extension is linked to mantle heating

and perhaps for the way in which the Basin and Range Province has acquired its high geothermal gradient.

APPENDIX 1: MAJOR UNCERTAINTIES ASSOCIATED WITH USE OF UNIFORM NEWTONIAN CHANNEL VISCOSITIES

There are two major sources of uncertainty associated with development of the inverse model presented in the paper; both sources of uncertainty are fundamentally related to the need to keep equations linear in terms of $w(x,t)$. First, the assumption that channel thickness and viscosity within the channel are spatially invariant (although viscosity may vary with time) and, second, the assumption that flow can be adequately described by Newtonian viscosity rather than by a higher order power law rheology.

Lateral Variations in Viscosity

Lateral variations in lower crustal viscosity almost certainly occur beneath the Basin and Range Province, primarily as a result of temperature differences at the Moho but perhaps also because of rheological differences in lower crustal rocks. Factors that influence lower crustal temperatures include mantle heat flow, magmatism and lateral advection of flowing lower crustal material. Yet despite extensive modeling by many authors, we have little idea of the degree to which these processes affect lower crustal temperatures in regions of extension nor do we have any information about lateral temperature variations at the Moho beneath the Halloran Hills and adjacent regions. Therefore, models that include lateral variations in lower crustal viscosity will provide little insight into crustal flow beneath the Halloran Hills region because we have no idea how viscosities (temperatures) vary spatially. Indeed, the uncertainties introduced by the estimates of lateral variations in lower crustal viscosities are probably as large as the uncertainties inherent in ignoring the lateral viscosity variations. We have concluded that the benefits inherent in keeping the mathematical analysis linear in viscosity (e.g., allowing

no lateral variations in viscosity) far outweigh the dubious benefits of incorporating lateral variations in lower crustal viscosities.

For linear geothermal gradients, channel thickness is nearly independent of Moho temperature (Figure 3), so than variations in channel thickness may be fairly small. In addition, variations in channel thickness through time trade off against variations in viscosity through time and can be reasonably ignored (equation (11)).

Newtonian Versus Power Law Channel Flow

Ductile deformation of crustal rocks on geological timescales is generally assumed to occur by power law flow, where strain rate is linearly proportional to stress raised to some exponent (see equation (1)). Laboratory measurements at strain rates many orders of magnitude faster than geological strain rates give exponents between about n=2 and n=4, and it is usually assumed that n=3 provides a good description of ductile deformation of crustal rocks. In this paper we have assumed throughout that lower crustal flow can be approximated by n=1 (Newtonian) flow, and mimic the temperature dependence of the flow by choosing an appropriate equivalent viscosity (see text for discussion). In this section we address the magnitude of the errors that we may have introduced through using Newtonian flow rather than than n=3 power law flow for the lower crust.

The most important way in which n=1 and n=3 flows differ from one another is in the decay of flow rate through time. As lateral pressure gradients driving the flow decrease through time, the rate of n=1 flow will decrease linearly with dP/dx, while the rate of n=3 flow will decrease as the cube of dP/dx. Thus the rate of n=3 flow will decrease much faster than the rate of n=1 flow. Because the rate of surface tilting is closely related to flow rate (it is the rate of change of lateral crustal thickness gradients and of lateral pressure gradients), this has important implications for the computations that compare the expected rate of tilting at Valley Wells to the computed rate of tilting and hence to our inferences about the effective lower crustal viscosities beneath the Halloran Hills. In this section we

examine the differences in present-day rates of surface tilting for n=1 and n=3 flows that produce similar present-day denudation profiles (and topography) for the same amount of instantaneous crustal thinning.

Figure A1 shows the computed crustal thickness 0 and 8 m.y. after instantaneous faulting on a detachment fault similar in geometry to that inferred for the Halloran Hills detachment fault (a planar fault between x=-40 and x=40 km, intersecting the surface at x=-40 km and flattening out at a depth of 8 km at x=40 km). For simplicity, the flexural rigidity is assumed to be zero in this computation, and the equivalent viscosity within a 10-km-thick lower crustal channel is assumed to be $=2 \times 10^{19}$ Pa s for n=1 flow, similar to that inferred for the Halloran Hills region. Also shown is the computed crustal thickness 8 m.y. after faulting for the same initial fault geometry, but with n=3 flow. For n=3 flow, strain rate is assumed to be related to lateral pressure gradient by

$$\frac{1}{A}\left\{\frac{\partial}{\partial y}\left[\left(\frac{du}{dy}\right)^{\frac{1}{3}}\right]\right\}^3 = -\left(\frac{\partial P}{\partial x}\right)^3 \qquad \text{(A1.1)}$$

where A was chosen such that, over the region $-100<x<100$ km, the crustal geometry around x=0 after 8 m.y. of n=3 flow was approximately the same as for n=1 case (in this case $A=10^{-31}$ Pa^{-3} s^{-1} with a channel thickness of 10 km). Note that the crustal thickness across the profile, after 8 m.y. of flow, is nearly the same for the n=1 and n=3 flow, despite the differing dependence on dP/dx and the fact that dP/dx is clearly not uniform across the profile.

Figure A1 also shows the rate of tilting as a function of time at the position x=0, which is midway along the sloping portion of the normal fault and roughly analogous to the position of the Quaternary lake beds at Valley Wells with respect to the Halloran Hills detachment fault. There is a much greater decrease in the tilting (and flow) rates through time for n=3 flow than for n=1 flow. However, n=1 and n=3 flow that produce the same

crustal geometry 8 m.y. after faulting have tilting rates at 8 m.y. that differ by only a factor of 2. This difference in tilting rate by about a factor of 2 is present for about the last 6 m.y. of flow, and it is only in the first 1 to 2 m.y. after faulting that the tilting (and flow) rates for n=3 flow are greater than for n=1 flow. This result indicates that the use of Newtonian, rather than n=3, flow for the Halloran Hills region probably introduces errors in the computed Quaternary tilting rates of about a factor of 2, hence giving rise to uncertainties in the inferred viscosity by about a factor of 2. Since we cannot constrain the bounds on viscosity to better than an order of magnitude, the uncertainties that arise from using Newtonian, rather than n=3 power law, flow to constrain Quaternary tilting rates, are not significant.

The calculations in this appendix are designed to show that the linear, Newtonian model of crustal flow used in this paper is useful in that, in addition to being invertible, it yields a gross, average viscosity, fault shape, and tilting rate. If so desired, these results can be used to infer nonlinear rheologic properties (as is done in the discussion section of this paper) or as a preliminary to conducting nonlinear forward calculations in which the parameter values are approximately known. The latter is beyond the scope of this paper and, in our opinion, is not warranted because many factors, such as temporal and spatial variations in temperature at depth, are not known in any detail.

APPENDIX 2: FLEXURE OF SIMPLE FAULT GEOMETRIES

The model developed in this paper allows the evaluation of the effects of complex extensional geometries, flexural rigidity of the crust, and time dependent rheological behavior of the lower crust on topographic evolution through time. It has been shown that the viscous lower crust responds nonlinearly over time to extension in the upper crust. Using a limiting case of a simple extensional geometry with no flow (or flow to completion) in the lower crust, the basic geometric characteristics of an extended region can be quantified. If time dependent crustal behavior is ignored (e.g. no lower crustal flow,

erosion, or sedimentation) the response of the crust to tectonic unroofing is a function of the geometry of the removed allochthon, the flexural rigidity of the crust, and the density of the compensating material. It is mathematically described by setting the left hand side of equation (11) to zero.

For a simple antisymmetric fault geometry shown in Figure A2a, the topography resulting from the removal of all material above the fault is given by the sum of the crustal deformation and the flexural response of the crust to that deformation:

$$T(x)= -\frac{d}{2}\left(\frac{\rho_o-\rho_c}{\rho_o}\right)+\frac{\alpha}{4}\frac{d}{2x_o}\frac{\rho_c}{\rho_o}\left[\cos\left(\frac{x-x_o}{\alpha}\right)\exp\left(\frac{x-x_o}{\alpha}\right)-\cos\left(\frac{x+x_o}{\alpha}\right)\exp\left(\frac{x+x_o}{\alpha}\right)\right.$$

$$\left.-\sin\left(\frac{x+x_o}{\alpha}\right)\exp\left(\frac{x+x_o}{\alpha}\right)+\sin\left(\frac{x-x_o}{\alpha}\right)\exp\left(\frac{x-x_o}{\alpha}\right)\right] \qquad -\infty < x < -x_o \qquad \text{(A2.1a)}$$

$$T(x)= x\frac{d}{2x_o}\left(\frac{\rho_o-\rho_c}{\rho_o}\right)+\frac{\alpha}{4}\frac{d}{2x_o}\frac{\rho_c}{\rho_o}\exp\left(-\frac{x_o}{\alpha}\right)\left[\cos\left(\frac{x-x_o}{\alpha}\right)\exp\left(\frac{x}{\alpha}\right)-\cos\left(\frac{x+x_o}{\alpha}\right)\exp\left(-\frac{x}{\alpha}\right)\right.$$

$$\left.+\sin\left(\frac{x+x_o}{\alpha}\right)\exp\left(-\frac{x}{\alpha}\right)+\sin\left(\frac{x-x_o}{\alpha}\right)\exp\left(\frac{x}{\alpha}\right)\right] \qquad -x_o< x < x_o \qquad \text{(A2.1b)}$$

$$T(x)=\frac{d}{2}\left(\frac{\rho_o-\rho_c}{\rho_o}\right)+\frac{\alpha}{4}\frac{d}{2x_o}\frac{\rho_c}{\rho_o}\left[\cos\left(\frac{x-x_o}{\alpha}\right)\exp\left(-\frac{x-x_o}{\alpha}\right)-\cos\left(\frac{x+x_o}{\alpha}\right)\exp\left(-\frac{x+x_o}{\alpha}\right)\right.$$

$$\left.+\sin\left(\frac{x+x_o}{\alpha}\right)\exp\left(-\frac{x+x_o}{\alpha}\right)-\sin\left(\frac{x-x_o}{\alpha}\right)\exp\left(-\frac{x-x_o}{\alpha}\right)\right] \qquad x_o< x < \infty \qquad \text{(A2.1c)}$$

Variables specific to this appendix are given in Table A1.

Figure A2b compares the predicted topography for two different values of lower crustal density, ρ_o: one corresponding to mantle density (3300 kg/m^3) (curve M) and a second corresponding to a value only slightly greater (2%) than that of the upper crust (2754 kg/m^3) (curve LC). All other variables are held constant. The regional difference in

topographic elevation between the unextended region ($x > x_o$) and the fully extended region ($x < -x_o$) is much greater when the lower crustal density is closer to that of the mantle. In addition, the shape of fault surface after flexure is different for the two densities. When ρ_o is close to mantle density, the first term of equation (A2.1b) dominates the solution and the resulting fault geometry is nearly planar. When ρ_o is close to the density of the upper crust, the first term is relatively small and the fault surface is gently warped, displaying a local topographic maximum and minimum between the unextended zone ($x > x_o$) and the fully extended zone ($x < -x_o$). Because the topography across the Halloran Hills and other extended regions have a profile similar to that produced for lower crustal densities close to those of the upper crust, it is worth examining under what conditions these local extrema form along the fault surface for a simplistic fault geometry.

Equation (A2.1b) places constraints on the flexural wavelength α and compensating density ρ_o which allow the formation of a local topographic maxima at $-x_b$ in an unroofed, originally planar, fault surface. In order for local extrema to occur, the slope of the fault plane must be less than or equal to 0 at $x = 0$:

$$\left.\frac{dT}{dx}\right|_{x=0} = \frac{\rho_o - \rho_c}{\rho_c}\left(\frac{x_o}{\alpha}\right) + \cos\left(\frac{x_o}{\alpha}\right) \leq 0 \qquad \text{(A2.2)}$$

Equation (A2.2) indicates that formation of local topographic extrema depends only on the density contrast between upper crust and the compensating material and on the ratio of the length of the dipping section of the "fault plane" to the flexural wavelength α. It does not depend on the thickness of the material removed or the dip of the detachment fault. The crust must have a non-zero flexural rigidity for a local topographic maxima to form; in the limit of zero flexural rigidity, an initially planar fault remains planar (e.g. *Spencer*, [1984]; *Wernicke and Axen*, [1988]). The formation of local maxima also requires that $\pi/2 <$

$(x_o/\alpha) < 3\pi/2$ and that $[(\rho_o-\rho_c)/\rho_c]$ be less than about 0.07. For an upper crustal density of 2700 kg/m^3, the density of the lower crust must be less than about 2900 kg/m^3.

The positions of the local topographic maximum and minimum along the flexed fault surface (at $x=-x_b$ and $x=x_b$, respectively) depend on the density contrast and the flexural wavelength. Figure A3a shows contours of the ratio (x_b/x_o). Increasing the density contrast between upper and lower crust (larger values of $[(\rho_o-\rho_c)/\rho_c]$ decreases x_b. Increasing the ratio (x_o/α) generally increases x_b.

The amplitude of the topographic minimum and maximum at $\pm x_b$ is linearly dependent on d and $(1/x_o)$ and in a more complex manner on flexural wavelength α and lower crustal density ρ_o. Although amplitude is linearly related to decollement depth, which may be unknown, the ratio of the height of the bulge to the maximum uplift at the "breakaway", $[T(-x_b)/T(x_o)]$, is independent of d. Figure A3b shows contours of this ratio. Increasing $[(\rho_o-\rho_c)/\rho_c]$ or decreasing (x_o/α) decreases $[T(-x_b)/T(x_o)]$.

Figure A3c shows contours of $[T(x_o)/d]$, the ratio of maximum elevation of the uplifted footwall at the breakaway to the initial depth of the decollement surface. Decreasing (x_o/α) increases $[T(x_o)/d]$, producing a greater uplift $T(x_o)$ for a given decollement depth. Increasing the value of $[(\rho_o-\rho_c)/\rho_c]$ also increases this ratio.

Because the topography across the Halloran Hills is not perfectly antisymmetric, it can not be fit with such a simple model of detachment geometry. However, the position and elevation of the topographic bulge relative to the location and elevation of the breakaway zone can be used to estimate approximate bounds on lower crustal density and flexural wavelength beneath the Halloran Hills. A reference point halfway between Valley Wells and the summit of the Halloran Hills is assumed and corresponding values for x_o, x_b, $T(x_o)$, $T(x_b)$ and their ratios are given in Table A2. The corresponding values and uncertainty range of x_b/x_o and $T(-x_b)/T(x_o)$ are plotted on Figure A3d and the region of overlap is shaded. Figure A3d suggests topography in the Halloran Hills can be best fit with $[(\rho_o-\rho_c)/\rho_c]$ less than 0.03 ($\rho_o < 2780$ kg/m^3). Using the range of x_o values given in

Table A2, α is constrained to be between 7 and 18 km, corresponding to an effective elastic plate thickness of 1 to 4 km. Similar low effective elastic plate thicknesses and lower crustal densities have been predicted under the Whipple and Snake Range core complexes and elsewhere in the Basin and Range (e.g. *Block and Royden*, [1991]; *Spencer and Reynolds*, [1991]). The limits placed on (x_o/α) and $[(\rho_o-\rho_c)/\rho_c]$ by the ratios of (x_b/x_o) and $[T(x_b)/T(x_o)]$ suggest $[T(x_o)/d]$ is about 0.13, giving a maximum tectonic thinning between 6 and 14 km west of Baker. These decollement depths suggest tectonic removal of approximately 2 to 5 km of material at the location of the Halloran Hills, consistent with the estimates of maximum crustal thinning based on geologic constraints.

The asymmetry of the Halloran Hills limits the amount of information that may be gained from modeling the detachment fault as a simple planar feature. However the results determined by modeling simple extensional geometries are similar to more complex analytic models, such as the one developed in this paper, which accurately predict the topography across the Halloran Hills.

Rotation of structures by flexure and isostatic uplift

It is possible to use the equations derived in this appendix to determine the amount of rotation which will accompany flexure and isostatic uplift of extended regions. From examining Figure A2b, it is clear that geologic structures in the footwall of major extensional structures are rotated by flexural uplift following extension. It is possible to determine the amount of rotation by taking the derivative of the difference between the final topography and the pre-rotational geometry:

$$\text{Rotation} = \frac{d}{dx}[T(x)-f(x)] \qquad \text{(A2.3)}$$

For the simple geometry shown above in Figure A2a, the angular rotation is:

$$\text{Rotation} = \tan^{-1}\left\{\frac{\rho_c}{\rho_o}\frac{d}{4x_o}\left[\cos\left(\frac{x-x_o}{\alpha}\right)\exp\left(\frac{x-x_o}{\alpha}\right) - \cos\left(\frac{x+x_o}{\alpha}\right)\exp\left(\frac{x+x_o}{\alpha}\right)\right]\right\}$$

$$(-\infty < x < -x_o) \qquad \text{(A2.4a)}$$

$$\text{Rotation} = \tan^{-1}\left\{-\frac{\rho_c}{\rho_o}\frac{d}{2x_o} + \frac{\rho_c}{\rho_o}\frac{d}{4x_o}\left[\cos\left(\frac{x+x_o}{\alpha}\right)\exp\left(-\frac{x+x_o}{\alpha}\right) + \cos\left(\frac{x-x_o}{\alpha}\right)\exp\left(\frac{x-x_o}{\alpha}\right)\right]\right\}$$

$$(-x_o < x < x_o) \qquad \text{(A2.4b)}$$

$$\text{Rotation} = \tan^{-1}\left\{\frac{\rho_c}{\rho_o}\frac{d}{4x_o}\left[\cos\left(\frac{x+x_o}{\alpha}\right)\exp\left(-\frac{x+x_o}{\alpha}\right) - \cos\left(\frac{x-x_o}{\alpha}\right)\exp\left(-\frac{x-x_o}{\alpha}\right)\right]\right\}$$

$$(x_o < x < \infty). \qquad \text{(A2.4c)}$$

Figure A4 shows the amount of rotation that results from the removal of upper crustal material with the simple geometry described above. For this geometry, flexural uplift produces negative values for rotation because the derivative of the difference between the final topography and the original geometry is always negative. The two curves show the rotation resulting from different values of ρ_o. Curve M corresponds to mantle density (3300 kg/m^3) and curve LC corresponds to a density of 2754 kg/m^3. Because the rotation depends on the ratio of the density contrast between the upper crust and the compensating material, decreasing ρ_o produces a greater magnitude of rotation.

Several other features of equation A2.4 are worth noting. Because rotation is linearly related to the slope of the fault plane, $\tan^{-1}(d/2x_o)$, steeper faults and greater tectonic denudation produce more rotation. In the limits of zero flexural rigidity of the crust (Airy isostasy, $\alpha = 0$), rotation occurs only where the fault is dipping $(-x_o < x < x_o)$. Interestingly, for all values of α and ρ_o, the greatest magnitude of structural rotation does not occur at the breakaway zone, but at the inflection point, x=0. The magnitude of the angular rotation at x=0 is

$$\text{Rotation}_{x=0} = \tan^{-1}\left\{\frac{\rho_c}{\rho_o}\frac{d}{2x_o}\left[\cos\left(\frac{x_o}{\alpha}\right)\exp\left(-\frac{x_o}{\alpha}\right) - 1\right]\right\}. \qquad \text{(A2.5)}$$

This value is reaches its maximum magnitude when $x_o/\alpha = 3\pi/4$. In general, for any portion of the dipping fault plane to be flexed and rotated to or beyond horizontal, x_o/α and ρ_c/ρ_o must be within the bounding curve shown on Figure A3. As long as the density of the compensating medium (ρ_o) is not less than that of the crust, the amount of the rotation can only exceed the original dip of the fault by small amount . Setting $x_o/\alpha = 3\pi/4$ and $\rho_c/\rho_o = 1$, the angular rotation (in radians) of a fault initially dipping at angle β is

$$\text{Rotation}_{x=0} = \tan^{-1}\left(1.067\tan\beta\right) = \tan^{-1}\left(\tan\beta + 0.067\tan\beta\right) \approx \beta + \frac{0.067\tan\beta}{1+\tan^2\beta}. \qquad \text{(A2.6)}$$

The second term in the expansion reaches its maximum value when $\beta = 45°$, producing a rotation beyond the horizontal of only 2°.

Although the calculations derived in this appendix are for a very simple extensional geometry, the results point to some basic generalizations that may be made about zones of continental extension where lower crustal material of density comparable to that of the upper crust may be compensating loads produced in the upper crust. First, extension will produces footwall uplift in essentially all cases, unless the flexural rigidity of the crust is zero or infinite. Second, in order to produce the domal geometry observed in many core complexes from an originally planar fault, the density of the lower crust (or region where loads are being isostatically compensated) must be very close to that of the upper crust. Third, pre-existing geologic structures in the footwall of an extended region are flexurally rotated by extension. However, the maximum rotation occurs in the central portion of the fault, not at the breakaway zone. Finally, except under unusual conditions where the density of the compensating region is less than that of the crust, the rotated footwall cannot be rotated more than 2° beyond the horizontal.

REFERENCES

Allmendinger, R. W., T. A. Hauge, E. C. Hauser, C. J. Potter, S. L. Klemperer, K. D. Nelson, P. Knuepfer, and J. Oliver, Overview of the COCORP 40°N transect, western United States: The fabric of an orogenic belt, *Geol. Soc. Am. Bull.*, *98*, 308-319, 1987.

Bird, P., Lateral extrusion of lower crust from under high topography, in the isostatic limit, *J. Geophys. Res.*, *96*, 10,275-10,286, 1991.

Bishop, K. M., G. A. Davis, T. K. Fowler, and M. L. Parke, Late Tertiary geology of the Halloran Hills area, SE California: Problems in deciphering the geometric evolution of an extended terrane, *Geol. Soc. Am. Abstr. Programs*, *23*, 82, 1991.

Block, L., and L. H. Royden, Core complex geometries and regional scale flow in the lower crust, *Tectonics*, *9*, 557-567, 1990.

Brudos, T.C., and G. A. Davis, Geology of a Tertiary extensional breakaway zone, eastern Mojave Desert, California, *Geol. Soc. Am. Abstr. Programs*, *24*, 10, 1992.

Buck, W.R., Modes of continental lithospheric extension, *J. Geophys. Res.*, *96*, 20,161-20,178, 1991.

Carter, N.L., and M. C. Tsenn, Flow properties of continental lithosphere, *Tectonophysics*, *136*, 27-63, 1987.

Davis, G.A., B. C. Burchfiel, and M. Parke, Late Miocene detachment fault tectonics in the greater Halloran Hills-Shadow Valley area, eastern San Bernadino County, California, *Geol. Soc. Am. Abstr. Programs*, *22*, 17, 1990.

Davis, G.A., T. K. Fowler, K. M. Bishop, T. C. Brudos, S. J. Friedmann, D. W. Burbank, M. A. Parke, and B. C. Burchfiel, Pluton pinning of an active Miocene detachment fault system, eastern Mojave Desert, California, *Geology*, *21*, 627-630, 1993.

Dohrenwend, J.C., L. D. McFadden, B. D. Turrin, and S. G. Wells, K-Ar dating of the Cima volcanic field, eastern Mojave Desert, California: Late Cenozoic volcanic history and landscape evolution, *Geology, 12*, 163-167, 1984.

Fjeldskaar, W., and L. Cathels, Rheology of mantle and lithosphere inferred from post-glacial uplift in Fennoscandia, in *Glacial Isostasy, Sea-Level and Mantle Rheology*, edited by R. Sabadini et al., pp. 1-19, Kluwer Academic, Norwell, Mass., 1991.

Fowler, T.K., Geology of the Shadow Mountain and the Shadow Valley Basin: Implications for Tertiary tectonics of the eastern Mojave Desert, M.S. thesis, 160 pp., Univ. of Southern Calif., Los Angeles, 1992.

Friedmann, S.J., and D.W. Burbank, Active footwall uplift recorded in a supra-detachment basin: the Miocene Shadow Valley Basin, *Eos Trans. AGU, 73*, 549, 1992.

Gans, P.B., An open-system two-layer crustal stretching model for the eastern Great Basin, *Tectonics, 6*, 1-12, 1987.

Gans, P.B., and E.L. Miller, Style of mid-Tertiary extension in east-central Nevada, in *Geologic Excursions in the Overthrust Belt and Metamorphic Core Complexes of the Intermountain Region*, edited by K.D. Gurgel, pp. 107-139, Utah Geological Mining Survey, Salt Lake City, 1983.

Hager, B.H., Mantle viscosity: A comparison of models from postglacial rebound and from the geoid, plate driving forces, and advected heat flux, in *Glacial Isostasy, Sea-Level and Mantle Rheology*, edited by R. Sabadini et al., pp. 493-513, Kluwer Academic, Norwell, Mass., 1991.

Kruse, S.E., M.K. McNutt, J. Phipps-Morgan, L.H. Royden, and B. Wernicke, Lithospheric extension near Lake Mead, Nevada: A model for ductile flow in the lower crust, *J. Geophys. Res., 96*, 4435-4456, 1991.

Kusznir, N.J., and D.H. Matthews, Deep seismic reflections and the deformational mechanics of the continental lithosphere, *J. Petrol., Spec. Lithosphere Issue*, 63-87, 1988.

McCarthy, J., and G.A. Thompson, Seismic imaging of extended crust with emphasis on the western United States, *Geol. Soc. Am. Bull., 10*, 1361-1374, 1988.

Miller, E.L., P.B. Gans, and J. Garing, The Snake Range decollement: An exhumed mid-Tertiary ductile-brittle transition, *Tectonics, 2*, 239-263, 1983.

Parke, M., and G.A. Davis, Gravity gliding in the eastern Mojave desert? Only the Shadows know..., *Geol. Soc. Am. Abstr. Programs, 22*, 74, 1990.

Reynolds, R.E., Erosion, deposition, and detachment: The Halloran Hills sequence in *At the End of the Mojave: Quaternary Studies in the Eastern Mojave Desert*, edited by J. Reynolds, pp. 101-103, Special Publication of the San Bernadino County Museum Association, Redlands, Calif., 1990.

Reynolds, R.E., and G.T. Jefferson, Timing of deposition and deformation in Pleistocene sediments at Valley Wells, eastern San Bernadino County, California, in *This Extended Land, Geological Journeys in the Southern Basin and Range* , edited by D.L. Weide and M.L. Faber, pp. 218-220, Department of Geoscience, University of Nevada, Las Vegas, 1988.

Sharp, R.E., Geomorphology of Cima Dome, Mojave Desert, California, *Geol. Soc. Am. Bull., 68*, 273-290, 1957.

Spencer, J.E., and S.J. Reynolds, Tectonics of mid-Tertiary extension along a transect through west central Arizona, *Tectonics, 10*, 1204-1221, 1991.

Turcotte, D.L., and G. Schubert, *Geodynamics: Applications of Continuum Physics to Geological Problems*, 450 pp., John Wiley, New York, 1982.

Turrin, B.D., J.C. Dohrenwend, R.E. Drake, and G.H. Curtis, K-Ar ages from the Cima volcanic field, eastern Mojave desert, California, *Isochron West, 44*, 9-16, 1985.

Vening Meinesz, F.A., Les grabens Africans resultant de compression ou de tension dans la crôute terrestre?, *Inst. R. Kolonial Belge Bull., 21*, 539-552, 1950.

Wdowinski, S., and G.J. Axen, Isostatic rebound due to tectonic denudation: A viscous flow model of a layered lithosphere, *Tectonics, 11*, 303-315, 1992.

Weisel, J.K., and G.D. Karner, Flexural uplift of rift flanks due to mechanical unloading of the lithosphere during extension, *J. Geophys. Res., 94*, 13,919-13,950, 1989.

Wernicke, B., and G.J. Axen, On the role of isostasy in the evolution of normal fault systems, *Geology, 16*, 848-851, 1988.

Wernicke, B., G.J. Axen, and J.K. Snow, Basin and Range extensional tectonics at the latitude of Las Vegas, Nevada, *Geol. Soc. Am. Bull., 100*, 1738-1757, 1988.

Wilshire, H.G., Geology of the Cima volcanic field, San Bernadino County, California, in *This Extended Land, Geological Journeys in the Southern Basin and Range*, edited by D.L. Weide and M.L. Faber, pp. 210-213, Department of Geoscience, University of Nevada, Las Vegas, 1988.

Table 1. Definitions of Variables

Variable	Definition	Value or Units	Comments
$\dot{\varepsilon}$	strain rate	s^{-1}	
τ	shear stress	Pa	
u	horizontal flow velocity	m/s	
v	vertical flow velocity	m/s	
U	integrated flux in lower crustal channel	m^2/s	
A	empirically determined material constant	$10^{-5.7}$ $MPa^{-n}s^{-1}$	Westerly Granite rheology*
		$10^{-6.9}$ $MPa^{-n}s^{-1}$	Quartzite rheology*
n	empirically determined material constant	3.3	Westerly Granite rheology*
		2.72 ± 0.4	Quartzite rheology*
Q	empirically determined material constant	186.5 kJ	Westerly Granite rheology*
		134 ± 64 kJ	Quartzite rheology*
R	universal gas constant	R = 8.314 J/mol K	
θ	temperature	°C	θ_o is temperature at Moho
ζ	geothermal gradient	°C/km	
dP/dx	pressure gradient	Pa/m	
P_t	pressure at top of lower crustal channel	Pa	
$T(x,t)$	topography	m	T_o is reference topography determined in inversion
$f(x)$	thickness of upper crust	m	
$w(x,t)$	deflection of upper/lower crustal boundary	m	w_o is reference boundary depth
$h(x,t)$	thickness of lower crustal region	m	
H	thickness of lower crustal channel in which flow is occurring	m	
D	flexural rigidity	N m^3	$D = (8.89 \times 10^9$ Pa$) \times T_e^3$
T_e	effective elastic plate thickness	m	
α	flexural wavelength	m	$\alpha^4 = 4D\rho_o g$
ρ_c	upper crustal density	ρ_c = 2700 kg/m^3	
ρ_o	lower crustal density	kg/m^3	
ρ_m	mantle density	ρ_m = 3300 kg/m^3	
g	gravitational acceleration	g = 9.8 m/s^2	
β	inclination of lower crustal channel	degrees	
$\mu(t)$	viscosity of lower crust	Pa s	
$\gamma(k,t)$	decay constant for crustal loads	s^{-1}	
df_i	geometry of removed allochthon segment i	m	see Figure 4 and text

*From Carter and Tsenn [1987].

Table 2. Computed Viscosities and Lateral Pressure Gradients Within the Lower Crust

$\frac{(\rho_o-\rho_c)}{\rho_c}$	α, km	μ_{av}, Pa s	μ_{early}, Pa s	μ_{late}, Pa s	$\frac{\mu_{early}}{\mu_{late}}$	dP/dx†, Pa/m
0.01	8	2×10^{17}	1.9×10^{18}	1.4×10^{16}	135	0
0.01	16	2×10^{17}	3.8×10^{18}	1.3×10^{16}	292	0
0.02	8	2×10^{17}	3.0×10^{18}	1.3×10^{16}	231	0
0.02	16	2×10^{17}	7.5×10^{18}	1.3×10^{16}	577	0
0.01	8	2×10^{18}	4.1×10^{18}	2.3×10^{17}	18	656
0.01	16	2×10^{18}	8.8×10^{18}	1.6×10^{17}	55	350
0.02	8	2×10^{18}	6.3×10^{18}	1.8×10^{17}	35	479
0.02	16	2×10^{18}	1.4×10^{19}	1.5×10^{17}	93	301
0.01	8	2×10^{19}	5.2×10^{19}	2.0×10^{18}	26	1342
0.01	16	2×10^{19}	1.3×10^{20}	1.5×10^{18}	87	917
0.02	8	2×10^{19}	6.0×10^{19}	1.8×10^{18}	33	1202
0.02	16	2×10^{19}	1.5×10^{20}	1.4×10^{18}	107	865
0.01	8	2×10^{20}	9.4×10^{20}	1.6×10^{19}	59	2058
0.01	16	2×10^{20}	–	–	–	–
0.02	8	2×10^{20}	–	–	–	–
0.02	16	2×10^{20}	–	–	–	–

*Determined for Quaternary lake beds deposited on a horizontal surface at 0.5 Ma.
†Pressure gradient in lower crust beneath Valley Wells after 8 m.y. of flow.

Table A1. Additional variables used in Appendix 2

Variable	Definition	Units
$\pm x_o$	Location of breakaway and horizontal decollement plane	m
$\pm x_b$	Location of topographic minima and maxima formed such that - $x_o<x<x_o$	m
$\pm T_o$	Elevation (depression) at $x = x_o$ ($-x_o$)	m
$\pm T_b$	Elevation (depression) at $x = -x_b$ (x_b)	m
d	Maximum thickness of removed allochthon	m
β	Angle of fault dip equal to $\tan^{-1}(d/2x_o)$	°

Table A2. Topographic characteristics across the Halloran Hills[a]

	East of "anti-symmetry" axis	West of "anti-symmetry" axis
x_b	5.8 km	5.8 km
x_o	17.6 km	34.0 km
x_b/x_o	0.33	0.17
T_b	59 m	253 m
T_o	388 m	895 m
T_b/T_o	0.15	0.28
$T_{b\ east}/T_{o\ west}$	0.066	
$T_{b\ west}/T_{o\ east}$	0.65	

[a]See Table A1 for a list of variables.

FIGURE CAPTIONS

Figure 1a. Regional map showing location of Baker (BA), the Blacksmith Hills Fault (BHF), Cima Dome (CD), the Cima volcanic field (CV), the Clark Mountain Range (CM), the Halloran Hills (HH), the Kingston Range (KR), the Kingston Range-Halloran Hills detachment fault (KR-HHD), the Mescal Range (MR), the Shadow Mountains (SM), Shadow Valley (SV), the Spring Mountains (SP), and Valley Wells (VW). Stipple pattern is ~12.5 Ma Kingston Peak Pluton. Quaternary lake beds are shown in black (aereal distribution of the northern lake beds (NLB) greatly exaggerated). Line AA' indicates line of geologic cross section and topographic profile used for inversion. Box indicates location of geologic map in Figure 1b.

Figure 1b. Simplified geologic map of the Halloran Hills region.

Figure 1c. Schematic cross section through the Halloran Hills (modified after *Davis et al.* [1993]).

Figure 1d. Generalized topography of the Halloran Hills and Shadow Valley region showing locations of Quaternary lake sediments in black and regions above 4000' elevation in gray. Contour interval is 200'.

Figure 2. Schematic diagram of Halloran Hills and surrounding regions showing structural elements of detachment and transfer (strike-slip) faults. Barbed lines show location of the Kingston Range-Halloran Hills detachment fault. Dotted region undergoes extension after 12 Ma. Arrows in shaded lower crust indicate inferred direction of lower crustal flow after extension. See text for details.

Figure 3. Schematic diagram showing the evolution of the Halloran Hills region through time, beginning during the waning stages of extension. (a) Late extensional phase to early postextensional phase showing major pathways for synextensional sedimentation (arrows) and localization of eruptive basalts on the crest of the Halloran Hills (black). (b) Quaternary lake basin bounded on the west by a paleotopographic sill. (c) Modern drainage pattern from Shadow Valley through Kingston Wash. Remnants of Quaternary lake shown in black. CM, Clark Mountains; HH, Halloran Hills; KR, Kingston Range; SM, Shadow Mountains; VW, Valley Wells.

Figure 4. (a) Normalized flow velocity, u/u_{max}, as a function of depth for power-law flow with quartzite (Qu) and Westerly Granite (Wg) rheologies (material parameters given in Table 1). Geothermal gradient ζ =20°C/km, flow is constrained to zero at H =20 km above the Moho, and total crustal thickness equals 30 km. Dotted line is normalized flow velocity for a 10-km-thick channel at the base of the crust with a uniform Newtonian viscosity. (b) Normalized flow velocity as a function of depth for power law flow with quartz rheology for geothermal gradient ζ = 10, 15, 20, and 25°C/km. (c) Total flux (flow integrated over depth) for quartzite rheology as a function of geothermal gradient. Dashed lines are uncertainty range based on uncertainties in activation energy for quartzite (Table 1). Horizontal lines show flux for flow in a 10-km-thick channel with uniform Newtonian viscosities of 10^{18} and 10^{20} Pa s. Pressure gradient (dP/dx) driving flow is 1000 Pa/m.

Figure 5. Schematic diagram of crust and upper mantle showing brittle upper crust (with zero strength) deformed by extension, flexurally strong middle crust, viscous lower crust, and rigid upper mantle. (a) Sample topographic data used to generate the denudation profile in Figure 5b through the inversion procedure described in the text. Solid circles indicate topographic points used in the inversion. (b) Sample "denudation profile" shows how complex denudation profiles are calculated from topographic data as the sum of many

planar fault segments (ends of planar segments shown by solid circles). Material shown in gray is removed instantaneously.

Figure 6. Denudation profiles across the Halloran Hills (location of profile in Figure 1) calculated for different values of ρ_o (lower crustal density), α (flexural wavelength), and μ_{av} (average lower crustal viscosity). Curve B in each panel is a reference curve with ρ_o = 2727 kg/m^3 (1% greater than the density of the upper crust), α = 16 km ($T_e \approx$ 4 km), and $\mu_{av} = 2 \times 10^{19}$ Pa s. Shaded box indicates maximum estimate of 5 km of crustal thinning under the Halloran Hills. Topography data used for inversion are shown by solid circles on upper curve in each panel. (a) Effect of ρ_o on calculated denudation profiles. (b) Effect of α on calculated denudation profiles. (c) Effect of μ_{av} on calculated denudation profiles. BA, Baker; CM, Clark Mountain Range; HH, Halloran Hills; VW, Valley Wells.

Figure 7. Topography computed through time for profile across the Halloran Hills, plotted at 2 m.y. intervals from the time of cessation of faulting (8 Ma) to the present and assuming a constant lower crustal viscosity. Crustal parameters and initial upper crustal geometry correspond to reference curve B in Figure 6 (α = 16 km, ρ_o = 2727 kg/m^3, and $\mu_{av} = 2 \times 10^{19}$ Pa s). Solid circles indicate location of topographic data used for the inversion. BA, Baker; CM, Clark Mountain Range; HH, Halloran Hills; VW, Valley Wells.

Figure 8. Detail of profile across Halloran Hills and the Clark Mountain Range showing the computed change in topographic elevation relative to Valley Wells for lower crustal viscosities of 2×10^{20}, 2×10^{19}, and 2×10^{18} Pa s. Flexural wavelength α is 16 km and lower crustal density ρ_o is 2727 kg/m^3. CM, Clark Mountains; HH, Halloran Hills; PNS, the projection of the northern drainage region onto the profile; VW, Valley Wells; WLB, western lake beds. (a) Relative change in elevation between 0.5 Ma and the present. (b) Relative change in elevation between 8.0 Ma and the present.

Figure 9. Detail of profile across Halloran Hills and the Clark Mountain Range showing the computed change in topographic elevation between 0.5 Ma and the present relative to Valley Wells for time-dependent viscosity. Parameters are the same as for reference curve B in Figure 6 (α = 16 km, ρ_o = 2727 kg/m^3, and average viscosity $\mu_{av} = 2 \times 10^{19}$ Pa s). Viscosity changes stepwise at 0.5 Ma from $\mu_{early} = 1.3 \times 10^{20}$ Pa s to $\mu_{late} = 1.5 \times 10^{18}$ Pa s. Solid circles indicate observed change in topographic elevation relative to Valley Wells since deposition of Quaternary lake beds. CM, Clark Mountains; HH, Halloran Hills; PNS, the projection of the northern drainage region onto the profile; VW, Valley Wells; WLB, western lake beds.

Figure 10. Relationship between pressure gradient and equivalent viscosity for power law flow (see text for discussion). Solid curves correspond to best estimates of activation energy for quartzite (Qu) rheology (at a nominal Moho temperature of 600°C). Also shown are the computed present-day pressure gradients and equivalent viscosities for the profile across the Halloran Hills. The equivalent viscosity is taken to be μ_{late} for a viscosity that changes stepwise at 0.5 Ma (Table 2). The corresponding pressure gradient is the computed present-day lateral pressure gradient within the lower crust under the Halloran Hills.

Figure A1. Comparison of crustal thickness and flow rates for n=1 (Newtonian) flow with $\mu = 2 \times 10^{20}$ Pa s (solid lines) and n=3 power law flow with $A = 10^{-31}$ Pa^{-3} s^{-1}. (Top) Comparison of crustal thickness after 8 m.y. of flow (initial crustal thickness was 30 km before faulting). Complete removal of upper plate for a fault that is planar between x=-40 and x=40 km, intersecting the surface at x=-40 km and flattening out at a depth of 8 km at x=40 km. Curves for n=1 and n=3 are virtually indistinguishable. (Bottom) Comparison of tilting rates at x=0 as a function of time.

Figure A2. (a) Diagram of extensional geometry used in models. Fault dips between $-x_o$ and x_o and a thickness d = 10 km of upper plate material is completely removed. Inset shows schematic fault geometry. (b) Resultant topography for extensional geometry shown in (a). Curves are for compensation by mantle density material (M) and lower crustal density material (2754 kg/m^3). $-x_o$ and x_o are end points of dipping fault segment as above. $-x_b$ and x_b are locations of local topographic maxima and minima respectively.

Figure A3. (a) Contours of the ratio x_b/x_o. (b) Countours of the ratio $T(x_b)/T(x_o)$. (c) Contours of the ratio $T(x_b)/d$. (d) Estimates of x_b/x_o and $T(x_b)/T(x_o)$ for the Halloran Hills.

Figure A4. Magnitude of rotation resulting from flexural isostatic rebound for a fault dipping 15° between -20 and 20 km. Curves are for compensation by mantle density (M) and lower crustal density (LC) material.

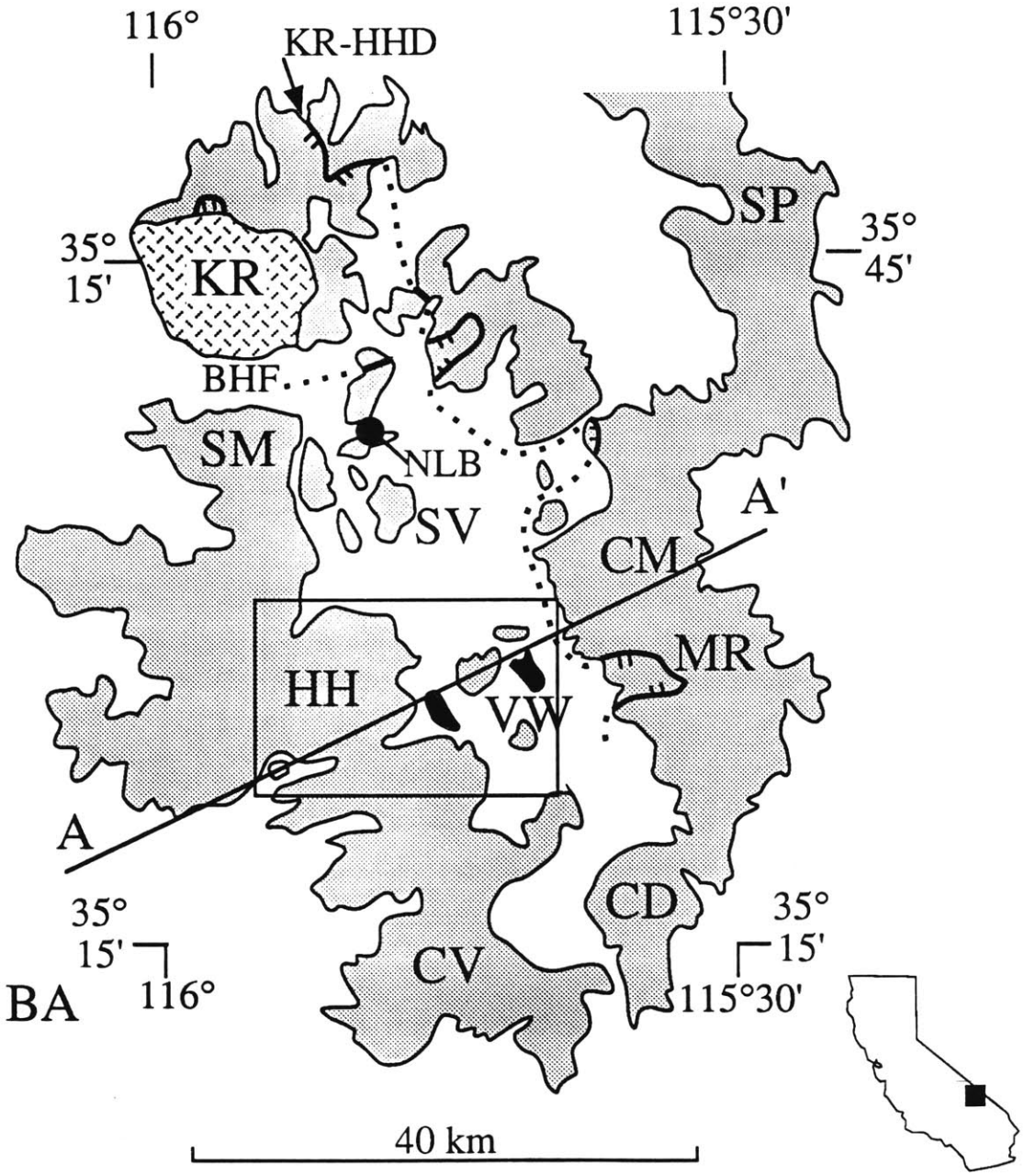

Figure 1a. Regional map showing locations of Baker (BA), the Blacksmith Hills fault (BHF), Cima Dome (CD), the Cima volcanic field (CV), the Clark Mountains (CM), the Halloran Hills (HH), the Kingston Range (KR), the Kinston Range-Halloran Hills detachment fault (KR-HHD), the Mescal Range (MR), the Shadow Mountains (SM), Shadow Valley (SV), the Spring Mountains (SP), and Valley Wells (VW). Stipple pattern is ~12.5 Ma Kingston Peak Pluton. Quaternary lake beds are shown in black (aereal distribution of the northern lake beds (NLB) greatly exaggerated). Line AA' indicates line of geologic cross section and topographic profile used for inversion. Box indicates location of geologic map in Figure 1b.

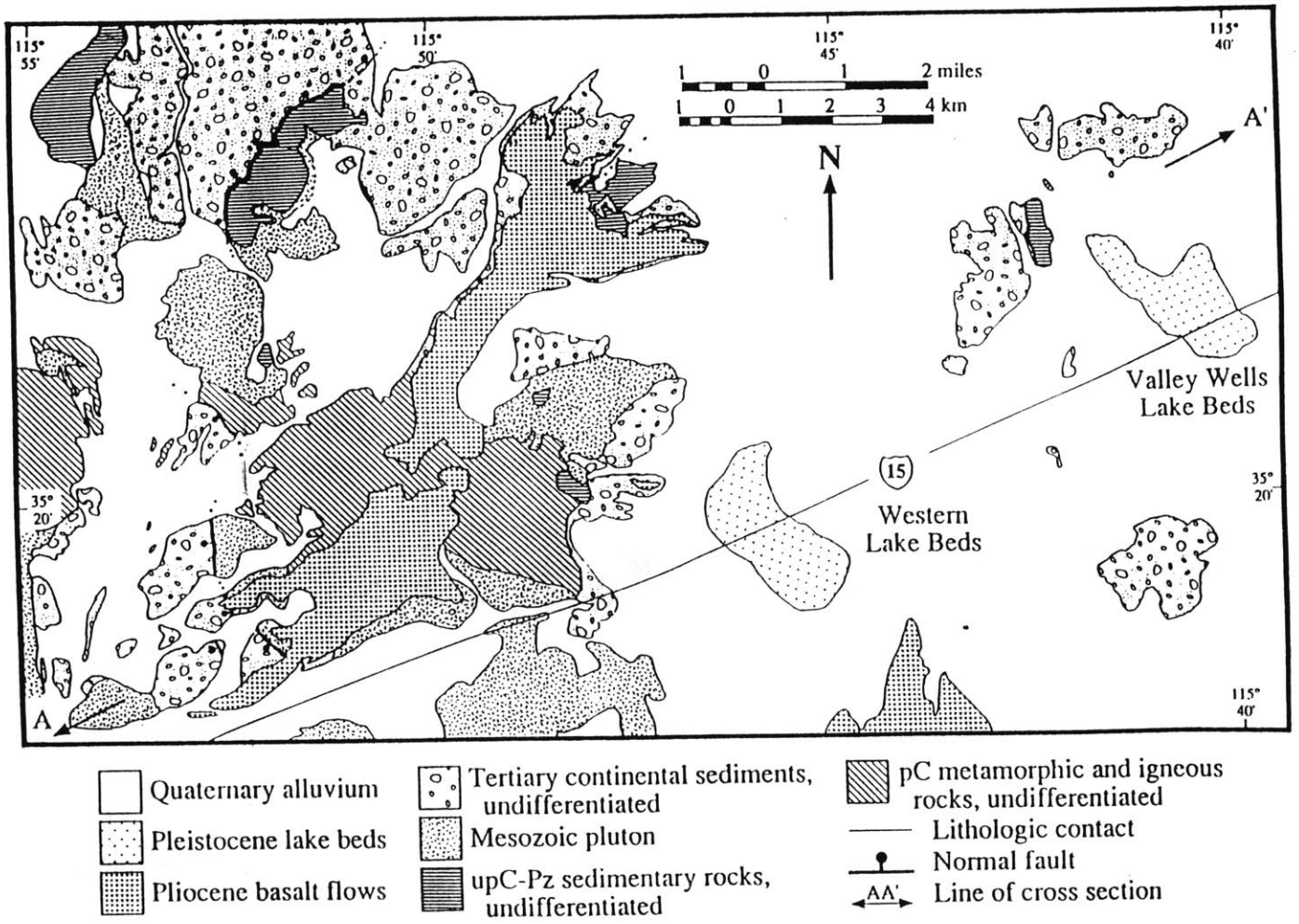

Figure 1b. Simplified geologic map of the Halloran Hills region.

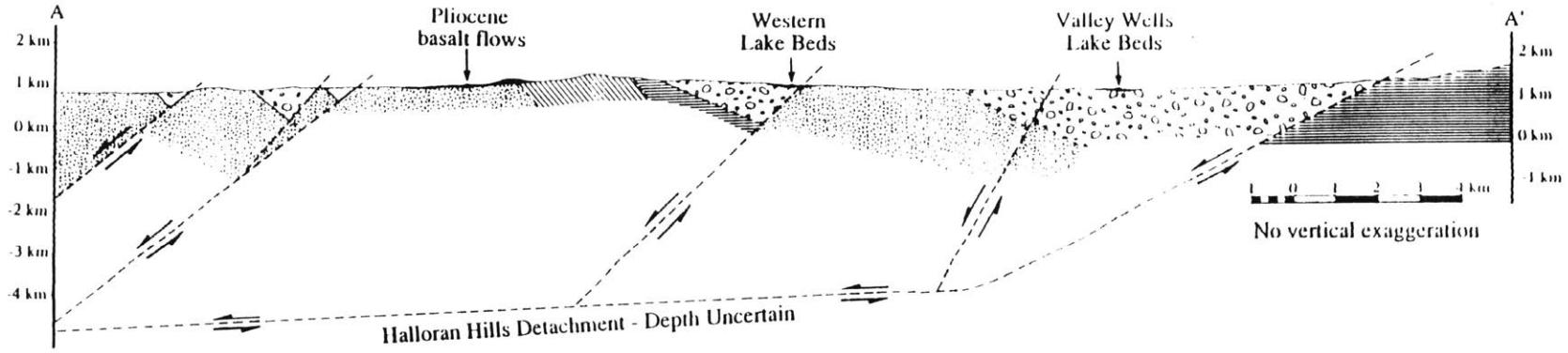

Figure 1c. Schematic cross section through the Halloran Hills (modified after *Davis et al.* [1993]).

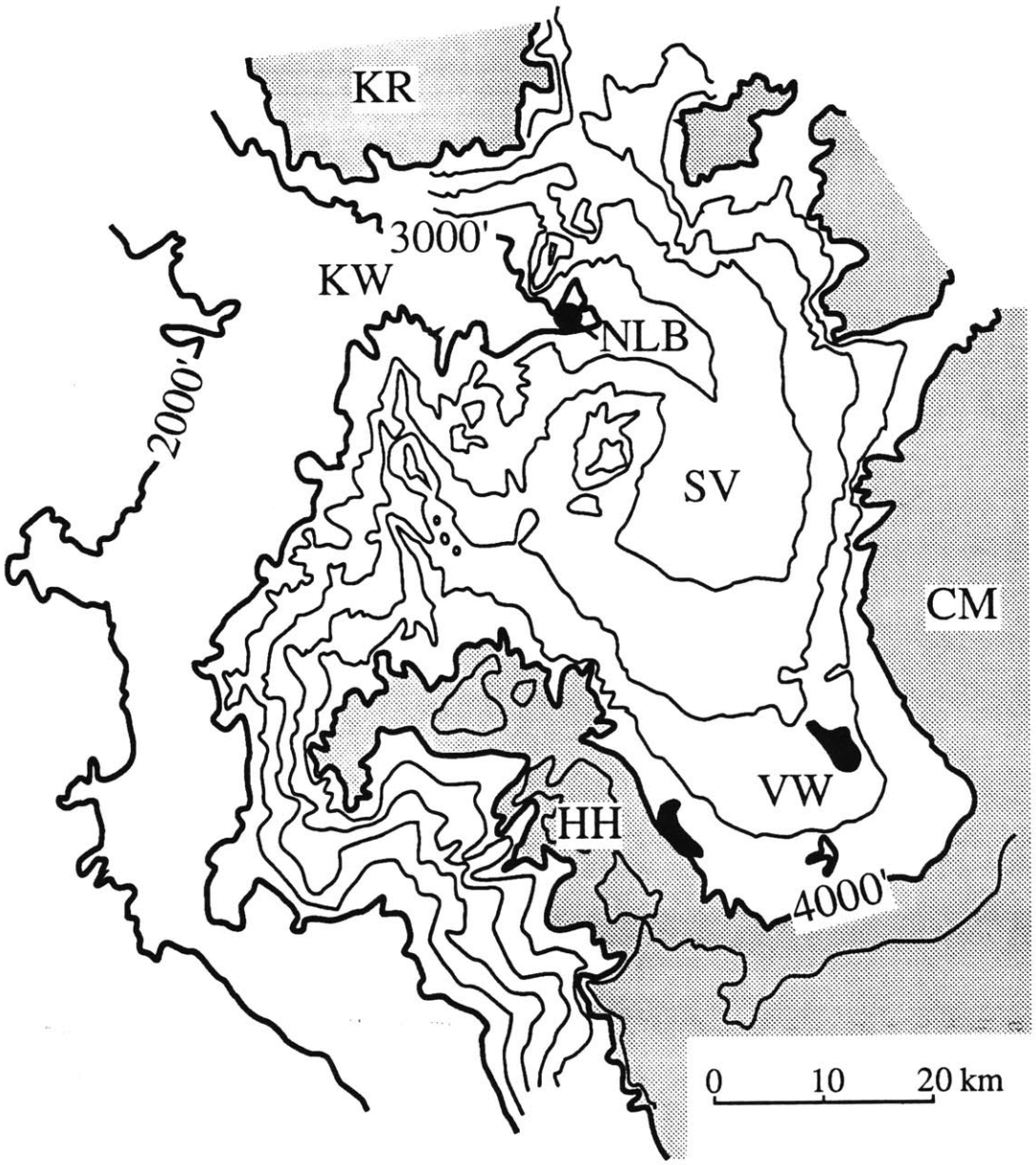

Figure 1d. Generalized topography of the Halloran Hills and Shadow Valley region showing locations of Quaternary lake sediments in black and regions above 4000' in gray. Contour interval is 200'.

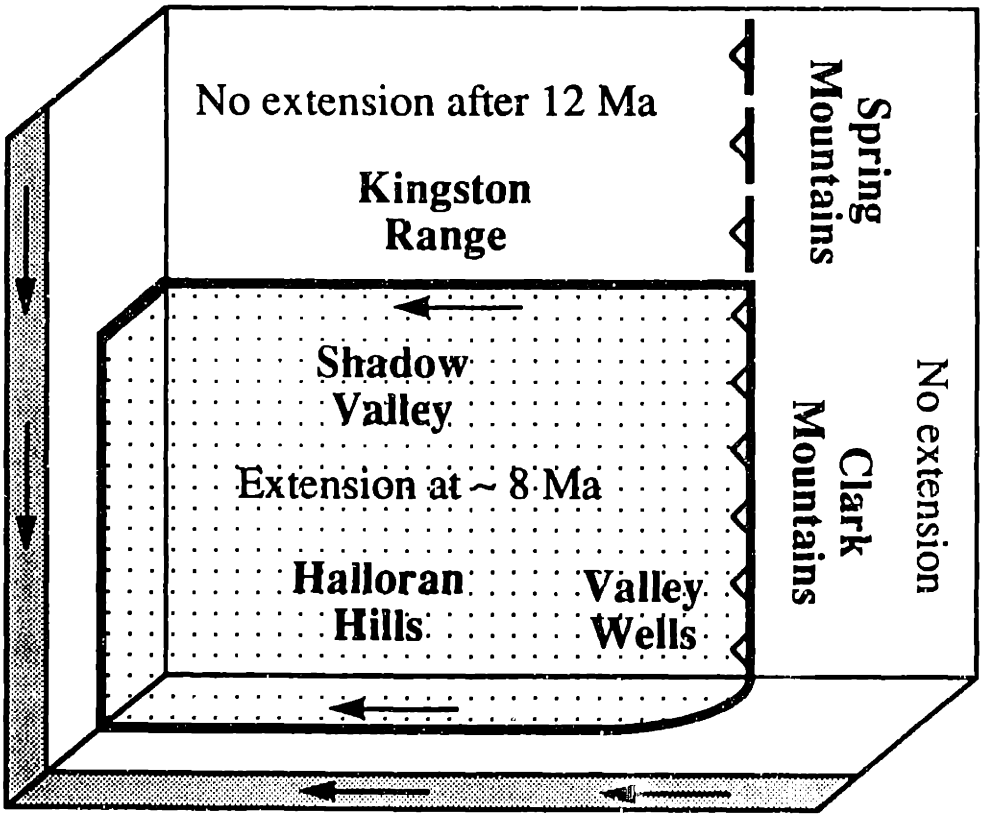

Figure 2. Schematic diagram of Halloran Hills and surrounding regions showing structural elements of detachment and transfer (strike-slip) faults. Barbed lines show location of the Kingston Range-Halloran Hills detachment fault. Dotted region undergoes extension after 12 Ma. Arrows in shaded lower crust indicate inferred direction of lower crustal flow after extension. See text for details.

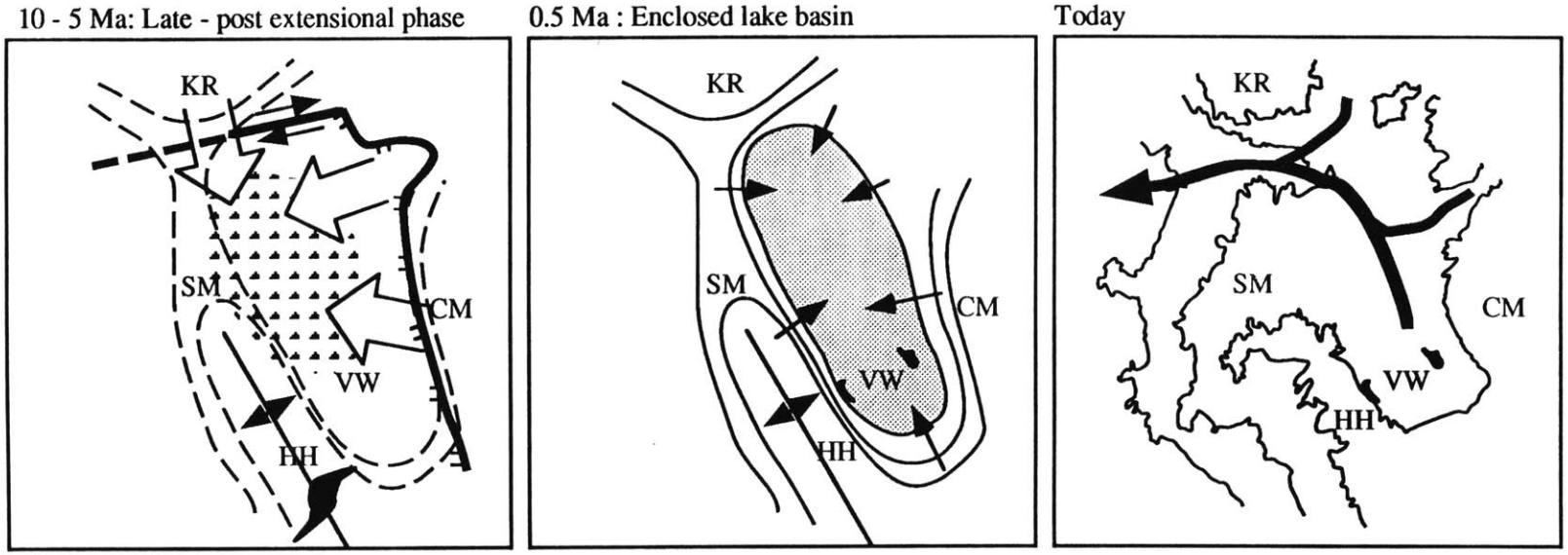

Figure 3. Schematic diagram showing the evolution of the Halloran Hills region through time, beginning during the waning stages of extension. (a) Late extensional phase to early postextensional phase showing major pathways for synextensional sedimentation (arrows) and localization of eruptive basalts on the crest of the Halloran Hills (black). (b) Quaternary lake basin bounded on the west by a paleotopographic sill. (c) Modern drainage pattern from Shadow Valley through Kingston Wash. Remnants of Quaternary lake shown in black. CM, Clark Mountains; HH, Halloran Hills; KR, Kingston Range; SM, Shadow Mountains; VW, Valley Wells.

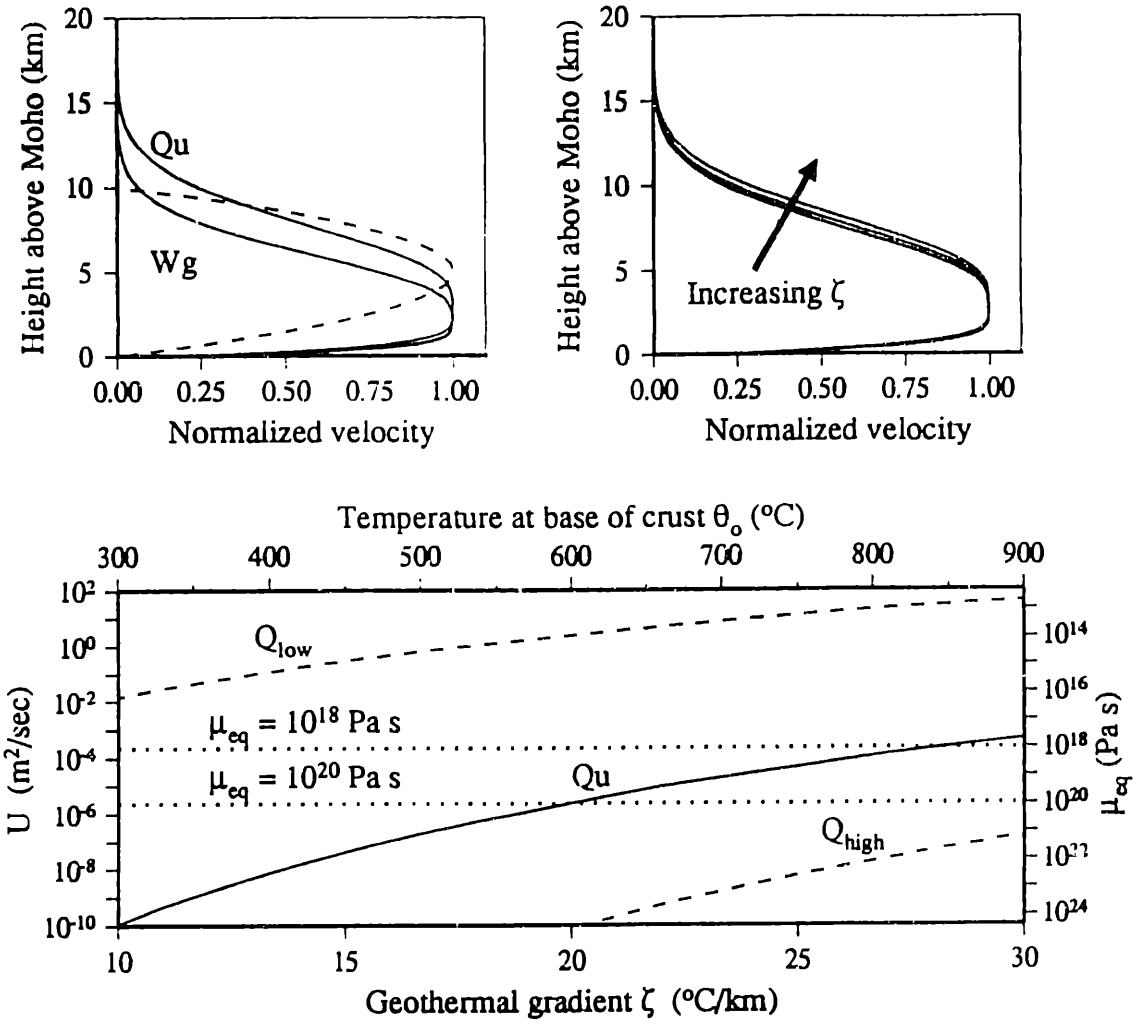

Figure 4. (a) Normalized flow velocity, u/u_{max}, as a function of depth for power-law flow with quartzite (Qu) and Westerly Granite (Wg) rheologies (material parameters given in Table 1). Geothermal gradient ζ =20°C/km, flow is constrained to zero at H =20 km above the Moho, and total crustal thickness equals 30 km. Dotted line is normalized flow velocity for a 10-km-thick channel at the base of the crust with a uniform Newtonian viscosity. (b) Normalized flow velocity as a function of depth for power law flow with quartz rheology for geothermal gradient ζ = 10, 15, 20, and 25°C/km. (c) Total flux (flow integrated over depth) for quartzite rheology as a function of geothermal gradient. Dashed lines are uncertainty range based on uncertainties in activation energy for quartzite (Table 1). Horizontal lines show flux for flow in a 10-km-thick channel with uniform Newtonian viscosities of 10^{18} and 10^{20} Pa s. Pressure gradient (dP/dx) driving flow is 1000 Pa/m.

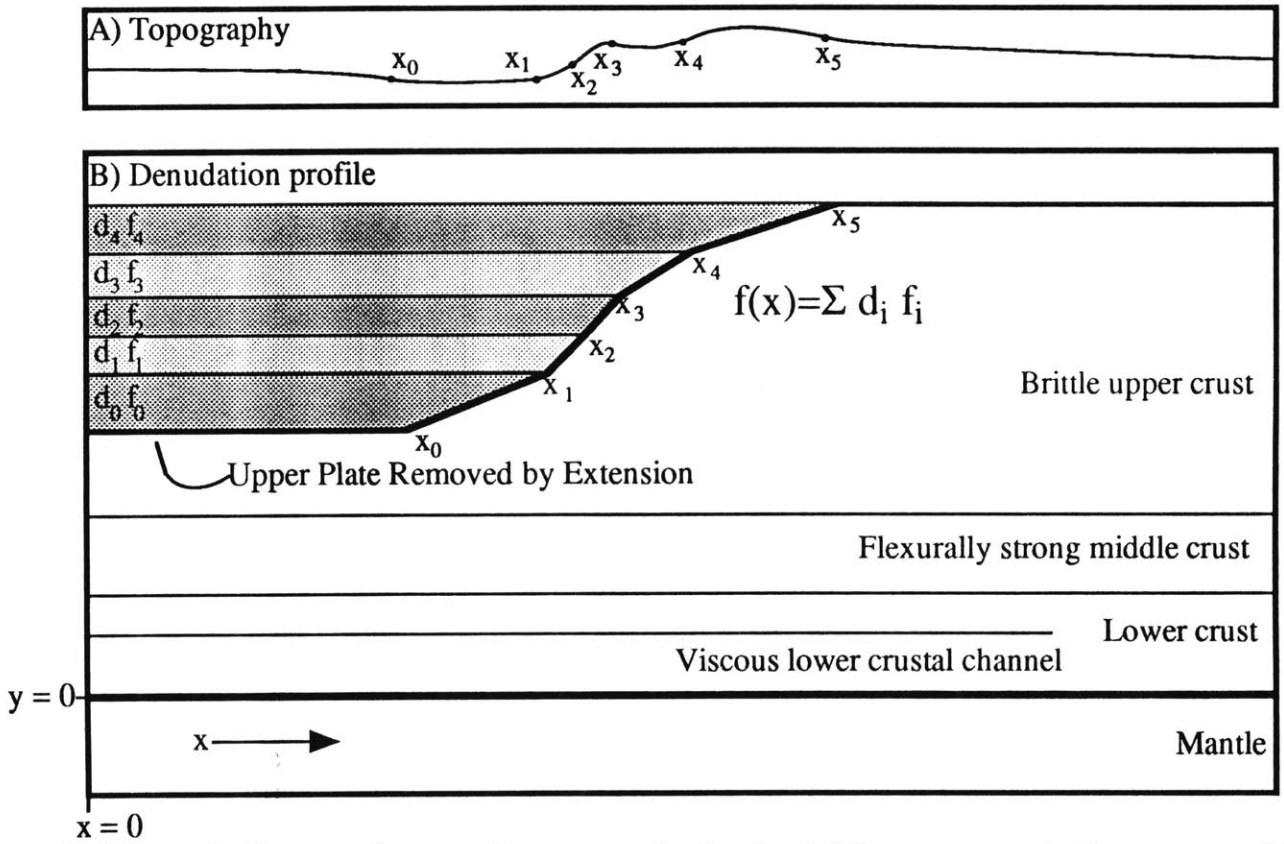

Figure 5. Schematic diagram of crust and upper mantle showing brittle upper crust (with zero strength) deformed by extension, flexurally strong middle crust, viscous lower crust, and rigid upper mantle. (a) Sample topographic data used to generate the denudation profile in Figure 5b through the inversion process described in the text. Solid circles indicate topographic points used in the inversion. (b) Sample "denudation profile" shows how complex denudation profiles are calculated from the topographic data as the sum of many planar fault segments (ends of planar segments shown by solid circles). Material shown in gray is removed instantaneously.

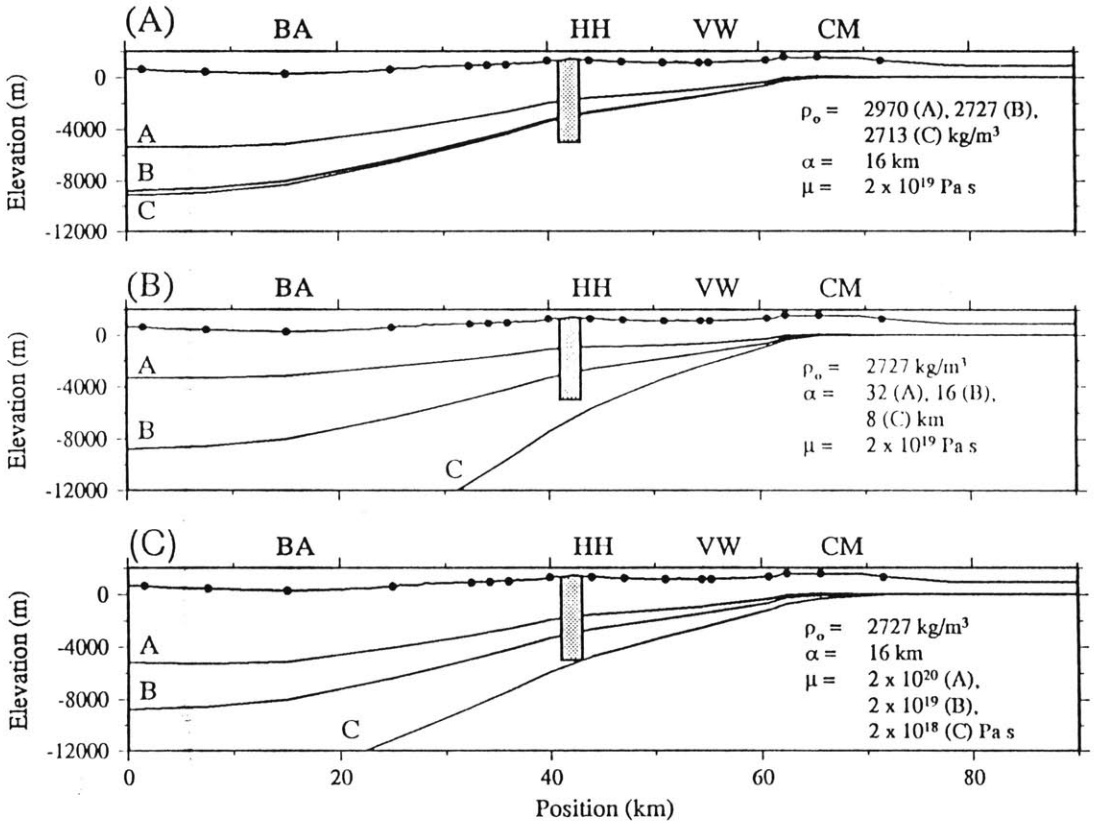

Figure 6. Denudation profiles across the Halloran Hills (location of profile in Figure 1) calculated for different values of ρ_o (lower crustal density), α (flexural wavelength), and μ_{av} (average lower crustal viscosity). Curve B in each panel is a reference curve with $\rho_o = 2727$ kg/m^3 (1% greater than the density of the upper crust), $\alpha = 16$ km ($T_e \approx 4$ km), and $\mu_{av} = 2 \times 10^{19}$ Pa s. Shaded box indicates maximum estimate of 5 km of crustal thinning under the Halloran Hills. Topography data used for inversion are shown by solid circles on upper curve in each panel. (a) Effect of ρ_o on calculated denudation profiles. (b) Effect of α on calculated denudation profiles. (c) Effect of μ_{av} on calculated denudation profiles. BA, Baker; CM, Clark Mountain Range; HH, Halloran Hills; VW, Valley Wells.

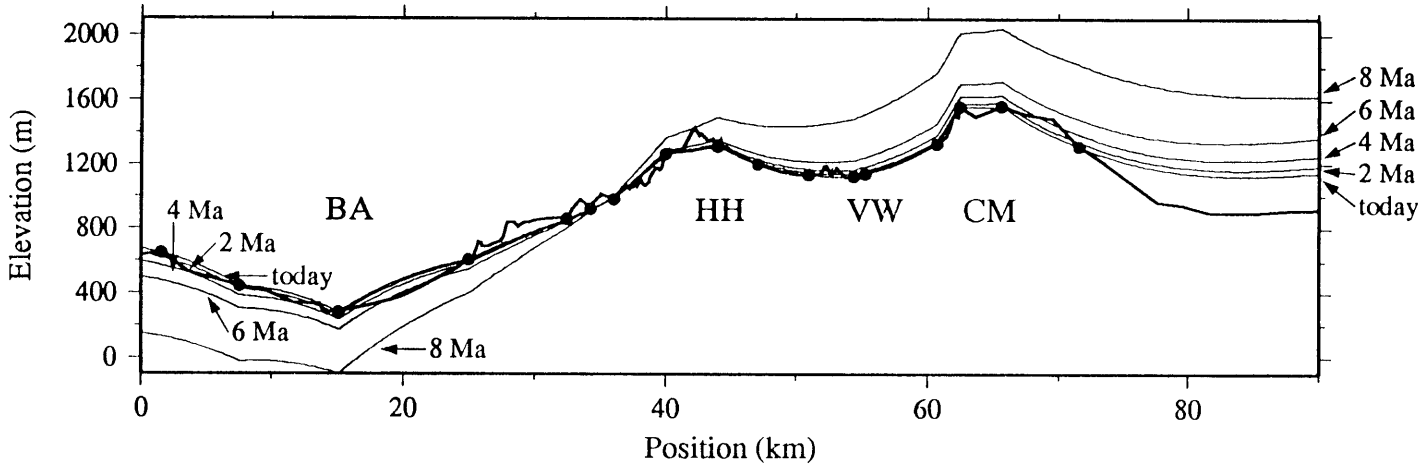

Figure 7. Topography computed through time for profile across the Halloran Hills, plotted at 2 m.y. intervals from the time of cessation of faulting (8 Ma) to the present and assuming a constant lower crustal viscosity. Crustal parameters and initial upper crustal geometry correspond to reference curve B in Figure 6 ($\alpha = 16$ km, $\rho_o = 2727$ kg/m^3, and $\mu_{av} = 2 \times 10^{19}$ Pa s). Solid circles indicate location of topographic data used for the inversion. BA, Baker; CM, Clark Mountain Range; HH, Halloran Hills; VW, Valley Wells.

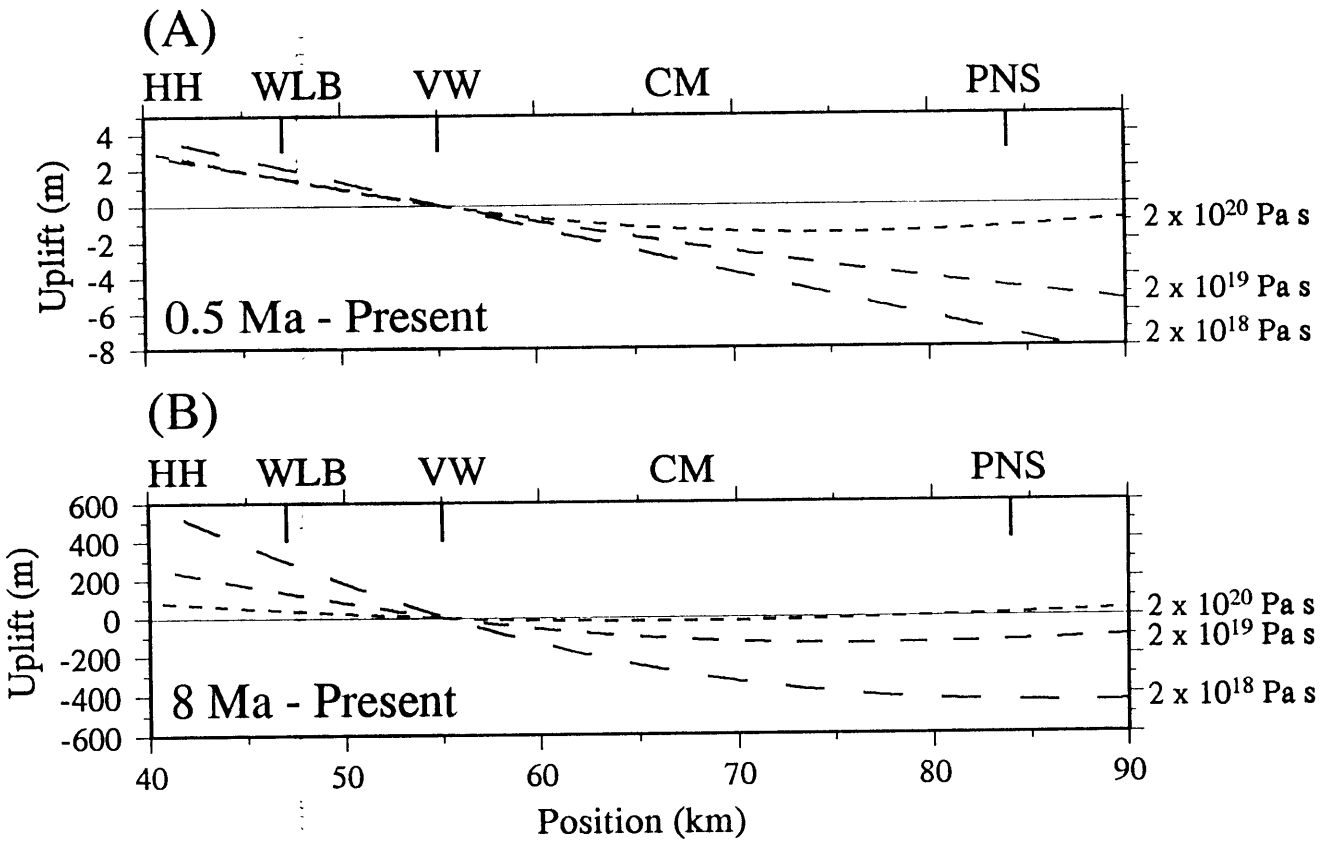

Figure 8. Detail of profile across Halloran Hills and the Clark Mountain Range showing the computed change in topographic elevation relative to Valley Wells for lower crustal viscosities of 2×10^{20}, 2×10^{19}, and 2×10^{18} Pa s. Flexural wavelength α is 16 km and lower crustal density ρ_o is 2727 kg/m³. CM, Clark Mountains; HH, Halloran Hills; PNS, the projection of the northern drainage region onto the profile; VW, Valley Wells; WLB, western lake beds. (a) Relative change in elevation between 0.5 Ma and the present. (b) Relative change in elevation between 8.0 Ma and the present.

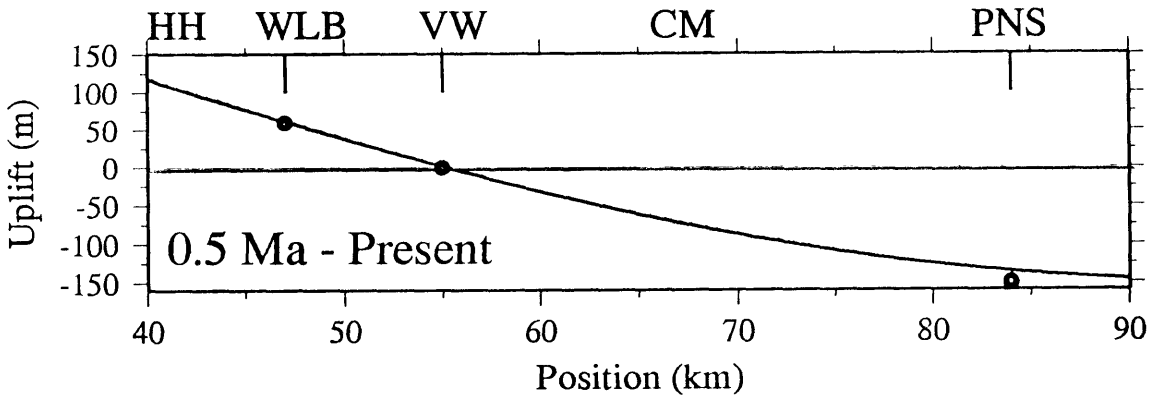

Figure 9. Detail of profile across Halloran Hills and the Clark Mountain Range showing the computed change in topographic elevation between 0.5 Ma and the present relative to Valley Wells for time-dependent viscosity. Parameters are the same as for reference curve B in Figure 6 (α = 16 km, ρ_o = 2727 kg/m^3, and average viscosity $\mu_{av} = 2 \times 10^{19}$ Pa s). Viscosity changes stepwise at 0.5 Ma from $\mu_{early} = 1.3 \times 10^{20}$ Pa s to $\mu_{late} = 1.5 \times 10^{18}$ Pa s. Solid circles indicate observed change in topographic elevation relative to Valley Wells since deposition of Quaternary lake beds. CM, Clark Mountains; HH, Halloran Hills; PNS, the projection of the northern drainage region onto the profile; VW, Valley Wells; WLB, western lake beds.

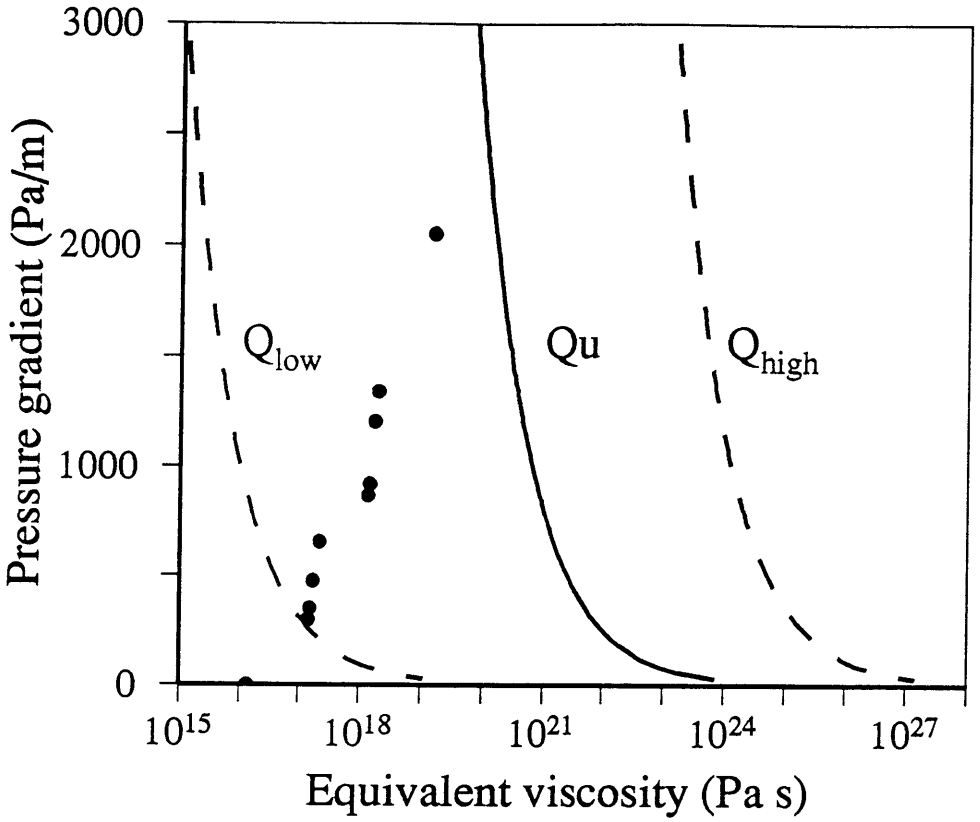

Figure 10. Relationship between pressure gradient and equivalent viscosity for power law flow (see text for discussion). Solid curves correspond to best estimates of activation energy for quartzite (Qu) rheology (at a nominal Moho temperature of 600°C). Also shown are the computed present-day pressure gradients and equivalent viscosities for the profile across the Halloran Hills. The equivalent viscosity is taken to be μ_{late} for a viscosity that changes stepwise at 0.5 Ma (Table 2). The corresponding pressure gradient is the computed present-day lateral pressure gradient within the lower crust under the Halloran Hills.

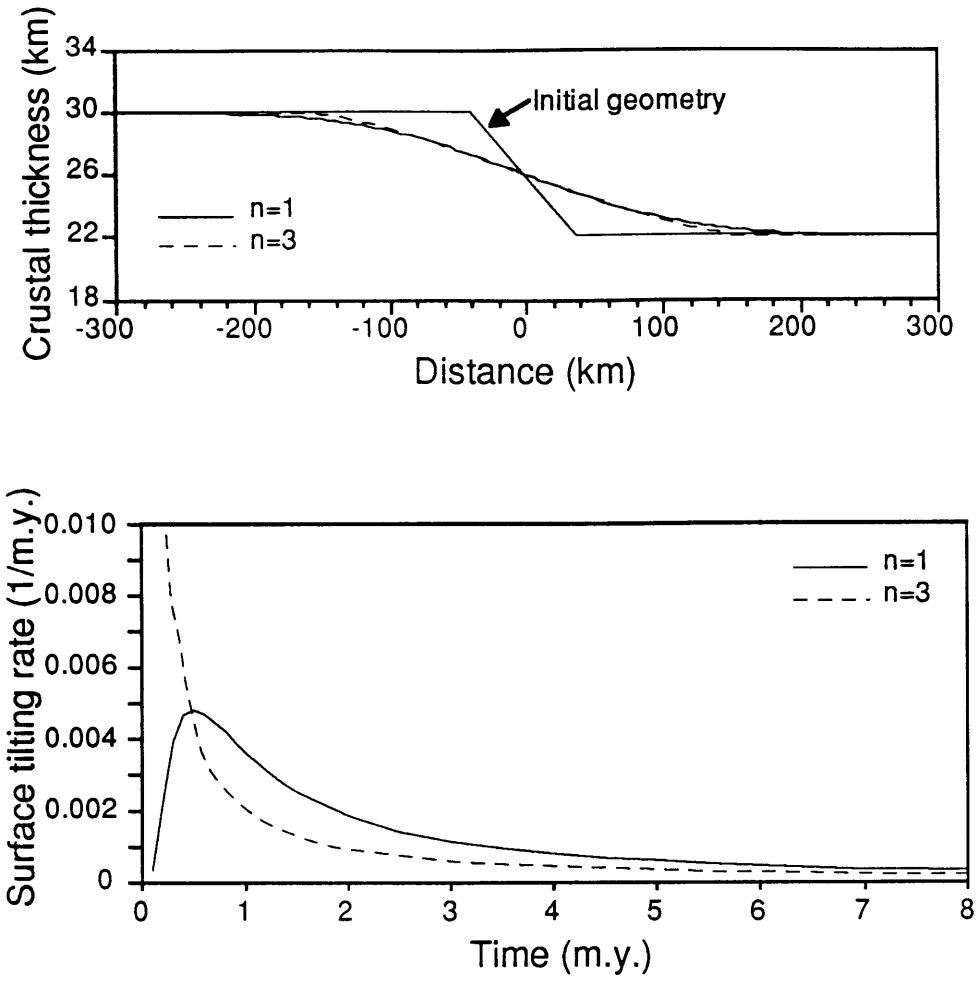

Figure A1. Comparison of crustal thickness and flow rates for n=1 (Newtonian) flow with $\mu = 2 \times 10^{20}$ Pa s (solid lines) and n=3 power law flow with $A = 10^{-31}$ Pa^{-3} s^{-1}. (Top) Comparison of crustal thickness after 8 m.y. of flow (initial crustal thickness was 30 km before faulting). Complete removal of upper plate for a fault that is planar between x=-40 and x=40 km, intersecting the surface at x=-40 km and flattening out at depth of 8 km at x=40 km. Curves for n=1 and n=3 are virtually indistinguishable. (Bottom) Comparison of tilting rates at x=0 as a function of time.

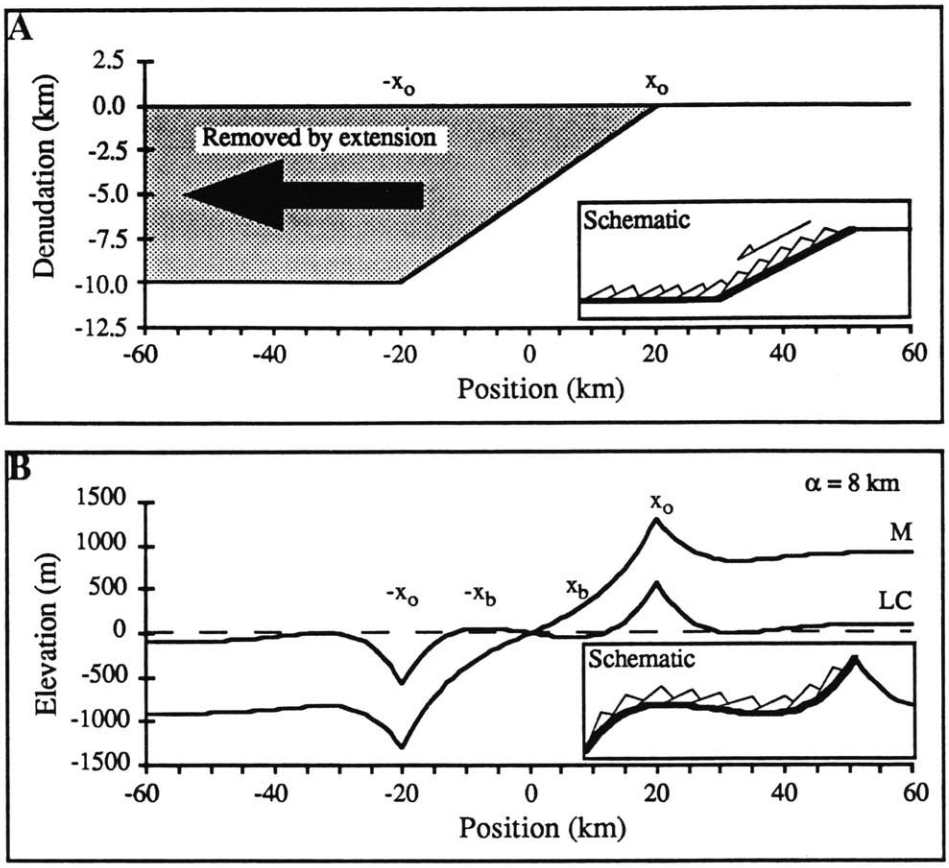

Figure A2. (a) Diagram of extensional geometry used in models. Fault dips between $-x_o$ and x_o and a thickness d = 10 km of upper plate material is completely removed. Inset shows schematic fault geometry. (b) Resultant topography for extensional geometry shown in (a). Curves are for compensation by mantle density material (M) and lower crustal density material (2754 kg/m^3). $-x_o$ and x_o are end points of dipping fault segment as above. $-x_b$ and x_b are locations of local topographic maxima and minima respectively.

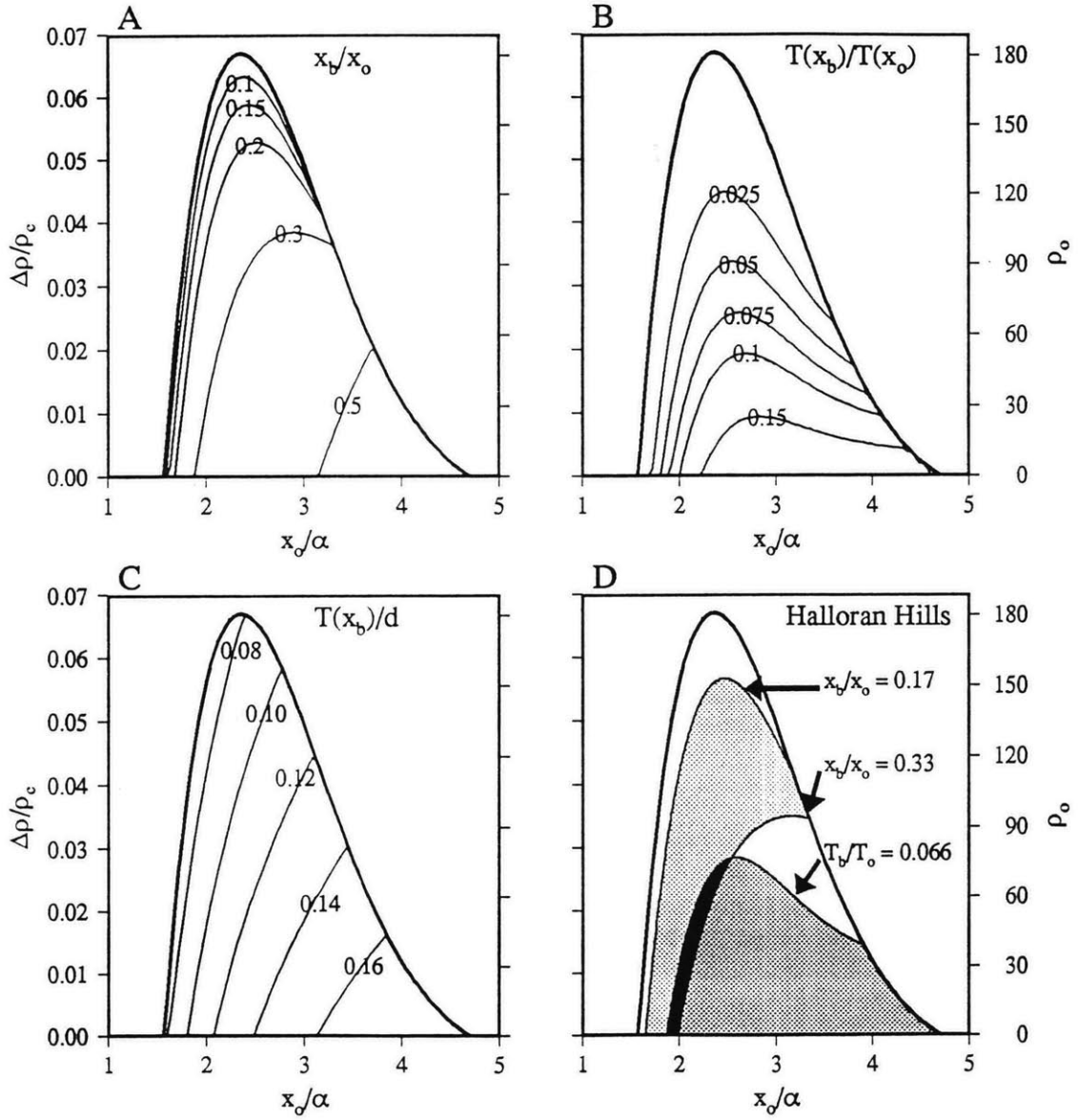

Figure A3. (a) Contours of the ratio x_b/x_o. (b) Contours of the ratio $T(x_b)/T(x_o)$. (c) Contours of the ratio $T(x_b)/d$. (d) Estimations of x_b/xo and $T(x_b)/T(x_o)$ for the Halloran Hills.

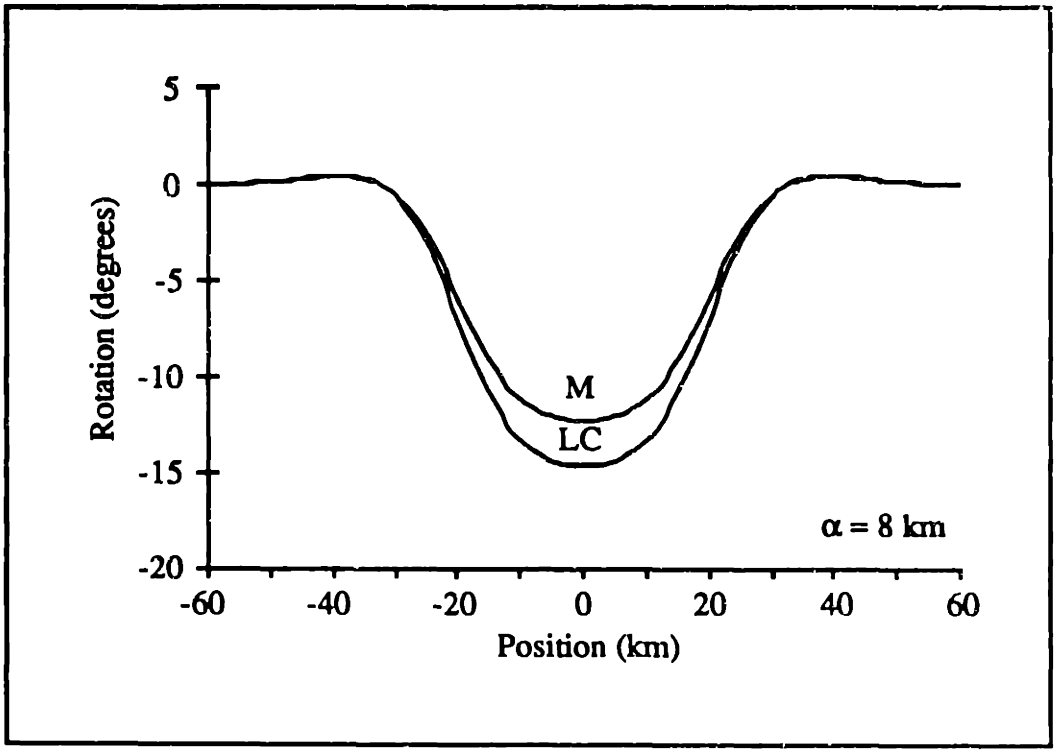

Figure A4. Magnitude of rotation resulting from flexural isostatic rebound for a fault dipping 15° between -20 and 20 km. Curves are for compensation by mantle density (M) and lower crustal density (LC) material.

CHAPTER 3: STRUCTURAL EVOLUTION OF THE NORTHERN RHODOPE METAMORPHIC CORE COMPLEX, MACEDONIA, GREECE

ABSTRACT

In northern Greece, the Rhodope metamorphic core complex occupies a critical location between the collisional zones of the internal Hellenides and the Rhodope metamorphic province. Structural mapping in the northern Rhodope metamorphic core complex has focussed on the style and consequences of deformation related to Alpine compression and Miocene to Recent extension. The Falakron Marble Series, buried during Eocene (?) thrust faulting beneath the Serbo-Macedonian and West Thracian Gneisses, reemerged in the Miocene in the footwall of the Strymon Valley detachment fault, a regionally developed, low-angle normal fault characterized by a progression from ductile to brittle structural fabrics. The re-interpretation of the Strymon Valley detachment fault as an extensional structure requires re-evaluation of the tectonic history of the north Aegean region, which is explored in a series of regional paleogeographic reconstructions. These regional reconstructions strongly support a correlation between the Falakron Marble Series and the Olympos carbonate platform, implying that the tectonostratigraphic units of the Circum-Rhodope Belt and the Vardar Zone are allochthonous nappes. These reconstructions also imply that restoring extension on the Strymon Valley detachment fault realigns Alpine collisional belts around the Rhodope metamorphic province, ultimately supporting a regional correlation between the Vardar Zone and the Intra-Pontide suture in Turkey.

INTRODUCTION

Structural, paleomagnetic, and GPS studies in the Hellenic Arc and Aegean Sea have shown that outward bowing of the Hellenic Arc and retreat of the Hellenic trench is accompanied by extension in the back-arc Aegean Sea (Figure 1) [*Le Pichon and Angelier*,

1979; *Kissel and Laj*, 1988; *Kastens et al.*, 1993; *Oral*, 1994]. Recent workers in the Aegean region have recognized that much of the early extension in the Aegean Sea occurred on low-angle normal (detachment) faults, forming metamorphic core complexes (e.g., *Lister et al.* [1984]; *Schermer* [1989]; *Dinter and Royden* [1993]; *Sokoutis et al.* [1993]). Because detachment faults typically accommodate large magnitudes of extension, effectively shuffle tectonostratigraphic units, and commonly unroof rocks from mid-crustal depths, their identification is critical; the reinterpretation of sub-horizontal structures as a detachment faults usually has significant consequences for tectonic interpretations in any setting. Perhaps the largest and best exposed of the Aegean core complexes is the Miocene Rhodope metamorphic core complex in northern Greece, exposed in the footwall of the Strymon Valley detachment fault (Figure 2). The understanding of extension in the Rhodope metamorphic core complex is critical for two reasons: 1) linear northwest-trending tectonic belts are disrupted where they wrap around the Rhodope metamorphic province (e.g., *Kockel* [1986]) and 2) Tertiary formations east of the Strymon Valley detachment fault do not show evidence for clockwise paleomagnetic rotations that are observed west of the detachment fault [*Kissel and Laj*, 1988]. These two factors suggest the Strymon Valley detachment fault forms a critical tectonic boundary that must be assessed to understand the tectonic evolution of the north Aegean region.

In the Rhodope metamorphic core complex, continuous excellent exposures of the Strymon Valley detachment fault for over 100 km along strike make it an excellent setting to study detachment faulting and its effect on an Alpine collisional belt. Unlike other core complexes in the Aegean region, the Rhodope metamorphic core complex has been only minimally affected by post-detachment faulting and is submerged only at its southern end. In order to better understand its role in the development of the northern Rhodope metamorphic core complex, the Strymon Valley detachment and adjacent hanging-wall and footwall rocks were mapped around the margins of Menoikion Oros and the Vrondou pluton at a scale of 1:25,000 on a topographic base during four field seasons from 1991 to

1993 (Plates 1 and 2). Several complex regions were mapped at a scale of 1:12,500. Where detailed topographic coverage was unavailable, 1:50,000 satellite photos were used in conjunction with topographic constraints provided by enlargements of WW II vintage 1:200,000 topographic maps. In addition to delineating the northern trace of the Strymon Valley detachment fault, this study recognizes and quantifies the sequence of structural events in the northern Rhodope metamorphic core complex and places them in a regional context to unravel the Tertiary tectonic history of the north Aegean region.

GEOLOGIC FRAMEWORK OF THE NORTH AEGEAN REGION

In the north Aegean region, tectonostratigraphic units juxtaposed by Alpine thrust faulting and Tertiary detachment faulting form northwest-trending belts, traditionally termed "isopic zones" (Figure 2) [*Aubouin*, 1959]. The most internal of these is the Rhodope metamorphic province, a mountainous region in Greece and Bulgaria bounded on the west by the Strymon (Struma) River, on the south by the Aegean Sea, and to the north and east by the Thracian depression of central Bulgaria. The Rhodope metamorphic province is separated on its western boundary from the Serbo-Macedonian province by the late Tertiary Strymon Valley detachment fault. Two amphibolite-facies gneiss units, the Kerdilion and Vertiskos Gneiss Series comprise the Serbo-Macedonian province. On its western boundary, the Vertiskos Gneiss is thrust over the units of the Circum-Rhodope Belt, a series of east-dipping, thrust fault-bound packages [*Kockel*, 1986, *De Wet et al.*, 1989]. From east to west these are (A) the *Melissochori-Cholomon* unit, a sequence of Triassic to Middle Jurassic marbles, quartzites, and phyllites, (B) the *Aspro-Vrissi-Chortiatis* unit, composed of Upper Triassic to Middle Jurassic phyllites and marbles overlying a sequence of gneisses, schists, and weakly schistose intrusives, (C) a sequence of ultramafic rocks, considered to be part of a dismembered ophiolite sequence, and (D) the *Peonia* unit, a weakly metamorphosed sequence of Upper Jurassic to Lower Cretaceous carbonate rocks unconformably overlying Hercynian (?) basement intruded by Upper

Jurassic plutons [*Kockel et al.*, 1971]. West of the Circum-Rhodope Belt, the Vardar Zone contains Middle Jurassic ophiolite sequences and has traditionally been thought to represent the suture between the European and Apulian plate (e.g., *Bernoulli and Laubscher* [1972]). Three tectonostratigraphic units comprise the Vardar Zone. From east to west they are the (A) *Guevguelije* unit, composed predominantly of ophiolites intruded by Upper Jurassic Granites and overlain by deep water Upper Jurassic carbonates, (B) the *Paikon* unit, composed of pre-Alpine crystalline basement overlain by thick Triassic to Lower Eocene platform carbonates, metavolcanics, turbidites, and flysch, and (C) the *Almopias* unit, composed mainly of ophiolites overlain by Cretaceous conglomerates and carbonates grading into Upper Cretaceous flysch [*Kockel*, 1986]. On its western margin, the Vardar Zone is thrust over the Pelagonian Zone, which in the Mt. Olympos area is composed of a series of thrust nappes. From the top to bottom they are (A) the *Flambouron* unit, composed of a pre-Alpine continental basement and Triassic to Jurassic cover sequences, (B) the *Ambelakia* unit, consisting of continental margin carbonate and siliciclastic rocks and basic to intermediate volcanics, and (C) the *Olympos* unit, a carbonate platform sequence of Triassic and Lower Cretaceous to Eocene age overlain by Eocene flysch. The tectonostratigraphy of the entire north Aegean region from the Rhodope metamorphic province to Mt. Olympos is summarized in Figure 3.

The Rhodope metamorphic core complex forms the southwestern portion of the Rhodope metamorphic province. Its eastern geographic boundary is defined as the Eocene (?) southwest-vergent Nestos Thrust which places the amphibolite-facies West Thracian Gneiss Complex over the greenschist-facies Falakron Marble Series during Alpine thrust faulting (Figure 4) [*Papanikolaou and Panagopoulos*, 1981; *Kilias and Mountrakis*, 1990]. On the west, the core complex is bounded by the Miocene Strymon Valley detachment fault, which is responsible for unroofing the footwall from mid-crustal depths and re-exposing the Falakron Marble Series. The Strymon Valley detachment fault, originally mapped as the Strimonüberschiebung (Strymon overthrust) [*Kockel and Walther*, 1965],

has recently been shown to be regional low-angle detachment fault which extends over 100 km from the Aegean coastline to the Greek-Bulgarian border and probably farther north [*Dinter and Royden*, 1993]. The hanging wall of the detachment fault contains the amphibolite-facies Kerdilion and Vertiskos Gneisses and Tertiary supradetachment basins formed during motion on the detachment fault.

TECTONOSTRATIGRAPHY

The northern Rhodope metamorphic core complex can be divided into three general tectonostratigraphic sequences, based on their relationship in time and space to the Strymon Valley detachment fault. The oldest units are those found in the footwall of the detachment fault and include the Falakron Marble Series and Tertiary granitic bodies intruded into the older metamorphic units. The second sequence is composed of supradetachment basin sediments deposited synchronously with motion on the detachment fault. The youngest sequence is a relatively undisrupted Pliocene-Quaternary overlap sequence that overlies the detachment fault and syndetachment sediments.

Footwall units: Falakron Marble Series and the Vrondou pluton

Three metamorphic units within the Falakron Marble Series (Oreini Gneiss, Menoikion Marble, and Dafnoudi Schist) and one granitic intrusive (the Vrondou pluton) were mapped as separate units in the footwall of the Strymon Valley detachment fault (Figure 5, Plate 1). These units are part of the lower tectonic unit of *Papanikolaou and Panagopoulos* [1981]. The Falakron units correspond to the upper schist-gneiss sequence, the marble sequence, and the lower schist-gneiss sequence of *Kronberg* [1969].

Oreini Gneiss (Lower schist-gneiss sequence)

The Oreini Gneiss, a sequence of interfoliated ortho- and paragneisses forming the lowest unit of the Falakron Marble Series is found on the southeastern margin of the

Vrondou pluton near the town of Oreini and on the western nose of the Vrondou pluton (Figure 5, Plate 1). It is characterized by interfoliated quartzofeldspathic gneisses, biotite schists and gneisses, biotite-garnet schists, marbles, and amphibolites. Foliations are concordant with the overlying Menoikion Marble. South of the Vrondou pluton, its structural thickness is approximately 3 km. *Kronberg* [1969] estimates the thickness of the lower schist-gneiss sequence (Oreini Gneiss) to be greater than 1500 m.

Two types of quartzofeldspathic gneiss are common within the Oreini Gneiss: a fine-grained mylonitic orthogneiss (?) composed almost exclusively of recrystallized quartz and feldspar grains and a quartzofeldspathic gneiss with large sigmoidal feldspar porphyroclasts in a matrix of fine-grained quartz and biotite. The mylonitized orthogneisses contain quartz, plagioclase, K-feldspar, and muscovite with accessory zircon and fibrolitic sillimanite. They appear to be mylonitized aplite dikes. The foliation is defined by recrystallized quartz ribbons and aligned muscovite grains. Quartz ribbons as long as 25 mm are present. Sigmoidal feldspar porphyroclasts up to 3 mm in length are elongated parallel to the foliation and commonly show undulose extinction. Deformation twins are common and many large feldspar porphyroclasts are broken. Smaller (0.1 mm) subhedral quartz and feldspar grains (neoblasts ??) comprise the matrix between larger quartz ribbons and feldspar porphyroclasts.

The porphyroclastic quartzofeldspathic gneiss contains quartz, plagioclase, biotite, and minor amounts of garnet and sillimanite. Foliation surfaces are defined by aligned biotite grains and compositional layering. Sigmoidal feldspar porphyroclasts are typically 1 to 2 mm across but reach 1 cm in size. Quartz grains typically do not exhibit undulose extinction. Myrmekitic intergrowth of quartz and feldspar commonly occurs along their mutual grain boundaries. Garnet porphyroblasts grow across the foliation defined by aligned biotite crystals.

Marble within the Oreini Gneiss is found in irregular outcrops of generally small size which were not separated during the course of mapping. Generally marbles are more

coarsely crystalline than those in the overlying Menoikion Marble, with calcite grains as large as 5 mm across.

Garnet-biotite schists are composed of quartz, plagioclase, K-feldspar, biotite, garnet, and muscovite with minor amounts of sillimanite, epidote, and chlorite. Quartz occurs as anhedral subgrains up to 0.25 mm across and as ribbons up to 3 mm in length and seldom exhibits undulose extinction. Plagioclase is of intermediate (oligoclase to andesine) composition. Aligned biotite laths, approximately 0.5 mm in length define the main foliation. Garnet occurs as fractured euhedral porphyroblasts and poikiloblasts up to 2.5 mm across. Quartz and biotite are common inclusions in garnet, in some cases comprising a significant amount of the grain. Fractures in garnet are filled by biotite, muscovite, and chlorite. In one thin section, large, strain-free muscovite grains (up to 2 mm across) grow across a poorly defined biotite foliation. Sillimanite occurs as small, aligned needles and as fibrolitic mats.

Amphibolites are composed of hornblende and anorthite-rich plagioclase with subordinate diopside, quartz, epidote, biotite, and titanite and accessory apatite, opaques, and zircon. The foliation surface is defined by compositional layering in the rock. Amphibole grains form elongate crystals up to 1 mm in length aligned within the foliation. Plagioclase forms porphyroblasts up to 1 mm across. Quartz grains are annealed and do not show undulose extinction.

Reconnaissance mapping northeast of the Siderokastro Basin suggests that a comparable unit to the Oreini Gneiss crops out near the Bulgarian border. The Oreini Gneiss is correlated across the Bulgarian border to the Lower Proterozoic (?) Sitovska Group [*Kozhoukharov*, 1988].

Menoikion Marble (Marble sequence)

The Menoikion Marble is a thick sequence composed mainly of marble with minor interfoliations of muscovite schist, biotite-muscovite schist, biotite gneiss, and

quartzofeldspathic gneiss. Marbles are fine to coarsely crystalline, white to dark grey, and well foliated to massive. Foliations are defined by alternating dark and light bands of calcite, small amounts of impurities within the marble, and minor variations in grain size. Lineations are formed by coarse calcite grains and quartz impurities. Layering is tectonic, with ubiquitous isoclinal folds transposing original bedding. Original sedimentary features are completely obliterated. Foliations are concordant with those in the Oreini Gneiss and the Dafnoudi Schist. The thickness of the marble series varies greatly. Because this unit is intensely deformed by isoclinal folding, thicknesses must be considered as structural thicknesses. It reaches a maximum thickness of about 7000 m in the Falakron Mountains (Figure 4) [*Kronberg*, 1969]. Its thickness on Menoikion Oros is approximately 2000 m (Figure 5) [*de Boer*, 1970]. It is severely tectonically attenuated to 0 m thickness over the Elaion stock.

The Menoikion Marble is the most resistant basement unit in the Rhodope metamorphic core complex. Karst formation is prevalent where marbles have been exposed for long periods of time with the development of sink holes, caves, and poljes. Several generations of joints with different orientations affect the Menoikion Marble [*Dinter*, 1994]. Deeply weathered joints (~1 m in depth) locally give it a "cyclopean block" texture.

Thin section analysis of pelitic schists interfoliated with the Menoikion Marble shows textural evidence for peak metamorphic conditions occurring pre- to syn-kinematic to the earliest structural deformation. Interfoliated pelitic schists typically contain quartz, plagioclase (albite), K-feldspar, muscovite, biotite, chlorite, zoisite, epidote, calcite, and garnet. Muscovite and biotite define the main foliation surface. Plagioclase forms sigmoidal to elliptical porphyroclasts aligned parallel to foliation surfaces. Often, poikiloblastic albite grains contain euhedral epidote and muscovite inclusions. Epidote and zoisite crystals that are not included within plagioclase cores form elongate crystals aligned parallel to the foliation. Garnets are typically euhedral and contain minor inclusions.

Calcite grains are sutured together with a granoblastic texture and typically have no preferred crystallographic orientation.

Dafnoudi Schist (Upper gneiss-schist sequence)

The Dafnoudi Schist forms the upper part of the Falakron Marble Series (Figure 5, Plate 1). It is composed mainly of muscovite and calcareous schists with interfoliations of marble, biotite-muscovite schist, and quartzofeldspathic gneiss. Large marble interfoliations are mapped separately on Plate 1. It has a total structural thickness of about 1500 m. Foliations between the Dafnoudi Schist and the Menoikion Marble are typically concordant.

Muscovite schists are comprised of quartz, muscovite, albite, and K-feldspar. Foliations are defined by compositional layering, sigmoidal feldspar porphyroclasts, quartz ribbons, and long axes of muscovite laths. Type II S-C fabrics [*Lister and Snoke*, 1984] are typically well developed. Albite is commonly poikiloblastic with subhedral epidote crystals preserved in the cores of porphyroclasts. Calcareous schists have similar textures and mineral assemblages with the addition of varying fractions of calcite. Quartz "augen" up to 3-5 cm in size are common in the Dafnoudi Schist and appear to be formed from highly attenuated isoclinal fold hinges. These "augen" typically behave as large sigmoidal porphyroclasts forming a type II S-C mylonitic fabric.

Age and metamorphism of the Falakron Marble Series

The age of the protolith of the Falakron Marble Series is unknown. A single poorly preserved coral specimen suggests a post-Cambrian age [*Meyer et al.*, 1963]. The Falakron Marble Series is intruded by Upper Oligocene plutons, and must consequently be of Oligocene age or older. Structural relations discussed below indicate a pre-Eocene age. Rb-Sr isochrons for paragneisses and orthogneisses from the lowest part of the Falakron Series in the southern Rhodope metamorphic core complex and on Thassos give late

Paleozoic ages [*Del Moro et al.*, 1990; *Wawrzenitz et al.*, 1994]. Paleozoic inheritance is also indicated by U-Pb zircon dates from the Vrondou and Symvolon plutons [*Kokkinakis*, 1980; *Dinter et al.*, 1995; Chapter 4]. These late Paleozoic isotopic ages may reflect regional Hercynian deformation and metamorphism that may be restricted to the lowest part of the Falakron Marble Series.

The units of the Falakron Marble Series are characterized as being metamorphosed in the quartz-albite-epidote-biotite subfacies of greenschist-facies metamorphism [*Kronberg*, 1969; *Kronberg et al.*, 1970; *deBoer*, 1970]. The metamorphic grade increases down section in the Falakron Marble Series. In the northern Rhodope metamorphic core complex, uppermost greenschist to lower amphibolite facies is attained in the middle and lower Falakron Marble Series, as evidenced by ubiquitous garnet in the Oreini Gneiss and pelitic schists interfoliated with the Menoikion Marble.

The metamorphic grade of the Oreini Gneiss is higher than the overlying Menoikion Marble and Dafnoudi Schist. Sillimanite is the stable aluminum silicate, requiring temperatures above ~500° C; its fibrolitic habit suggests conditions are close to the sillimanite-kyanite phase boundary. Myrmekitic textures in quartzofeldspathic gneisses indicates temperatures of at least 450° to 500°C [*Simpson and De Paor*, 1991]. It is possible that some of the foliated aplitic dikes in the Oreini Gneiss are formed from minimum melt magmas. The muscovite breakdown reaction is not attained. Co-existence of hornblende, plagioclase, and epidote in amphibolites places conditions in the epidote-amphibolite facies [*Spear*, 1993]. The higher metamorphic grade in the Oreini Gneiss may result from a regional northward increase in metamorphic grade in the Falakron Marble Series (as observed by *Kronberg and Raith* [1977]), lower position in the tectono-stratigraphic section, an early metamorphic event which is unique to the Oreini Gneiss, thermal metamorphism in the contact aureole of the Vrondou pluton, or some combination of these factors.

Tertiary intrusive rocks

The Vrondou pluton is one of several Mid Tertiary intrusive rocks emplaced in the Rhodope metamorphic province following Alpine deformation. It is an I-type, mesozonal, metaluminous, medium-grained, granitic intrusive body which intrudes the Oreini Gneiss and the Menoikion Marble. Compositionally, it ranges from granite and granodiorite to monzonite with gradational contacts between the various phases [*Theodorikas*, 1983]. Previous studies indicate that the area shown on Plate 1 is quartz monzonite [*Theodorikas*, 1983]. Minor enclaves of gabbro and dioritic xenoliths are present in the eastern Vrondou pluton [*Theodorikas*, 1983]. Because of its proximity and similar character, the Elaion stock is thought to be closely associated with the Vrondou pluton. Although their physical connection cannot be conclusively demonstrated at the current level of exposure, major and trace element geochemistries of the two bodies are indistinguishable, suggesting that they formed from the same magma body [*Kolocotroni and Dixon*, 1991].

Recent geochronologic work suggests that the Vrondou pluton and the Elaion stock may form a composite intrusive body, perhaps composed of at least two magmatic pulses [Chapter 4]. Although the boundary between these pulses was not observed during the course of this study, geochronology and earlier petrographic work [*Theodorikas*, 1983] suggest that the eastern Vrondou pluton and the Elaion stock are an Oligocene intrusive phase (biotite and hornblende K-Ar and $^{40}Ar/^{39}Ar$ cooling ages of 29 to 33 Ma [*Marakis*, 1969; *Dürr*, 1978; N. Kolocotroni, pers. comm., 1992; Chapter 4]). Similar major element geochemistries and Upper Oligocene ages for the Panorama and Granitis stocks (exposed 2 and 5 km east of the main Vrondou pluton respectively, Figure 5) suggests they may be part of the early phase of the composite intrusive complex [*Meyer*, 1968; *Jones et al.*, 1992]. Samples from the central and western Vrondou pluton yield U-Pb titanite and $^{40}Ar/^{39}Ar$ hornblende cooling ages that are significantly younger (23.7 ± 0.1 Ma and 22 ± 2 Ma, respectively [Chapter 4]). These data are interpreted to indicate a younger second pulse of magmatism, although slow cooling of a single Oligocene intrusive cannot be ruled

out [Chapter 4] Biotite and K-feldspar yield $^{40}Ar/^{39}Ar$ cooling ages between 16.4 ± 0.6 Ma and 9.4 ± 0.2 Ma. K-Feldspar cooling ages decrease from northeast to southwest, possibly reflecting the progressive tectonic unroofing of the Vrondou pluton by the Strymon Valley detachment fault [Chapter 4].

Aluminum-in-hornblende barometry [*Hammarstorm and Zen*, 1986; *Hollister*, 1987; *Schmidt*, 1992] indicates that the central portion of the Vrondou pluton was emplaced between 5 and 6 kbar pressure [Chapter 5]. A southwest emplacement gradient of approximately 0.15 kbar/km exists between the central and eastern portions of the pluton [Chapter 5]. Aluminum-in-hornblende barometry on the Elaion stock indicates it was emplaced at a shallower level (3.8 ± 0.4 kbar [Chapter 5]).

Granitic dikes and sills considered to be synchronous with the Vrondou pluton intrude the Oreini Gneiss. Although a mylonitic fabric is often developed within these dikes, different cross-cutting dikes show variable degrees of deformation ranging from unmylonitized to mylonite. Some dikes show limited evidence for syn-intrusional extension as small-scale, normal-sense shear zones offsetting intrusive dikes are in turn cross-cut by later dikes. This phenomenon is not observed to be widespread, and may reflect local conditions during dike intrusion or may result from late dike intrusion during motion on the Strymon Valley detachment fault.

Hanging wall units

The hanging wall of the Strymon Valley detachment fault is composed of the Serbo-Macedonian Gneisses and Upper Miocene to Pliocene syn-extensional sediments in the supradetachment Sandanski, Siderokastro, Serres, Angitis, Akropotamos, and Prinos-Kavala basins (Figure 4). These tilted and disrupted supradetachment sediments fill southwest-trending corrugations in the Strymon Valley detachment fault. Sediments are generally coarse, terrigenous deposits derived mainly from the footwall of the Strymon Valley detachment fault. The oldest sedimentary formation in the hanging wall of the

Strymon Valley detachment fault is found in the Sandanski Graben and has yielded the middle Miocene (~15.5 Ma) fossil rodent *Micromeryx flourensianus* Lartet [*Kojumdgieva et al.*, 1982]. The oldest faunal assemblage found in the Serres Basin is 9.8 Ma [*Armour-Brown et al.*, 1977].

Two boreholes in the Strymon Basin, Strymon 1 and 2 (Figure 5), have penetrated thicknesses of 3631 m and 2677 m of Neogene sediments, respectively, before drilling into metamorphic basement [*Erki et al.*, 1984]. It is unclear whether the contact between Neogene sediments and basement is an unconformity formed on top of metamorphic basement in the hanging wall of the Strymon Valley detachment fault or is the down-dip continuation of the detachment fault.

Much of this study focussed on the southeastern margin of the Serres Basin in order to understand the interaction between the Strymon Valley detachment fault, syn-tectonic sedimentation, and post-detachment deformation. Stratigraphic descriptions are largely based on observations from this area, and are compared to published descriptions from elsewhere in the basin.

Lefkon Conglomerate

The oldest Tertiary unit observed in the Serres Basin, the Lefkon Conglomerate, is a polymictic conglomerate with monolithologic marble breccia-conglomerate sheets intercolated near its base. Thicker marble breccia-conglomerate sheets are shown separately on Plate 1. The Lefkon Conglomerate corresponds to the fanglomerate member of the Lefkon formation [*Armour-Brown et al.*, 1977], the subsidence conglomerates of Lefkon Group [*Karistineos and Georgiades-Dikeoulia*, 1985], and the lowest part of the Liegendfolge [*Freyberg*, 1952]. The formation is observed only in fault contact with the basement units and its base is not exposed. The Lefkon Conglomerate varies laterally in thickness and composition around the basin. Because no fossils have been reported from

the Lefkon Conglomerate, its minimum age must be that of oldest fossils (9.8 Ma) in the overlying Lefkon Sands [*Armour-Brown et al.*, 1977].

The basal marble breccia-conglomerate is composed exclusively of sub-angular to rounded marble clasts up to 50 cm in diameter with an interlocking breccia to conglomeratic texture. Coarse calcite crystals are often found in veins within the member. The total thickness of the basal marble breccia-conglomerate cannot be determined due to structural dismemberment, but a minimum thickness of approximately 100 m is present in the southeastern Serres Basin. These breccia-conglomerate sheets appear to thin westward and this probably represents a maximum thickness.

Overlying the basal marble breccia-conglomerate is a thick package of coarse conglomerates with interbeds of crossbedded coarse sand and gravel. Cobble to boulder sized clasts are composed of lithologies found in the footwall of the Strymon Valley detachment fault. In the southeastern Serres Basin, well-rounded clasts up to 50 cm in diameter are composed of marble, quartzofeldspathic gneiss, biotite schist and gneiss, granite, mylonitized granite, and amphibolite. Fractured and re-cemented marble cobbles are occasionally found. The conglomerate clast composition varies from at least 80% marble at the base of the formation to less than 15% marble near the top of the formation, perhaps reflecting the unroofing history of the core complex or a fundamental change in paleo-depositional patterns. Several brick-red soil weathering horizons approximately 2 m thick are present in the southeastern Serres Basin. Along the southern margin of the Vrondou pluton, cobbles and boulders (up to 1 m) are comprised predominantly of Vrondou granite and units of the Oreini Gneiss with rare marble clasts. The thickness of the Lefkon Conglomerate varies around the Serres Basin. A structural thickness of approximately 150 m is present in the southeastern Serres Basin. Its total thickness is estimated to be 200 to 300 m [*Freyberg*, 1952; *Armour-Brown et al.*, 1977].

Lefkon Sands

Gradationally overlying the Lefkon Conglomerate is a thick package of interbedded siltstones, sandstones, and granule to pebble conglomerates, termed here the Lefkon Sands formation after *Karistineos and Georgiades-Dikeoulia* [1985]. It is equivalent to the sandy members of the Lefkon formation [*Armour-Brown et al.*, 1977] and the upper sandy part of the Liegendfolge [*Freyberg*, 1952]. Beds are generally cross bedded and fairly well sorted. Several coal seams are present within the formation [*Karistineous and Ioakim*, 1989]. The thickness of the Lefkon Sands in the southeastern Serres Basin is approximately 150 m. Its total thickness is estimated to be approximately 200 m [*Freyberg*, 1952; *Armour-Brown et al.*, 1977].

Rodent fossils from the lower part of the Lefkon Sands are latest Vallesian (9.8 Ma [*Armour-Brown et al.*, 1977]). Additional rodent fossils recovered from higher stratigraphic levels in this unit are of late Turolian age (~6 Ma, [*Armour-Brown et al.*, 1977]). Palynologic studies of the coal from this also formation indicate a Late Miocene age [*Psilovikos and Karistineos*, 1986; *Karistineos and Ioakim*, 1989].

St. George Formation

The St. George Formation is the most resistant Tertiary unit in the Serres Basin and forms high cliffy outcrops. Its resistance to weathering and distinctive ashy color generally make it easy to identify. It is composed of fossiliferous, well-cemented, fine-grained, calcareous sandstones and marls deposited in a shallow water, brackish to marine environment. Algal structures are common and spherical oncolites up to 2 cm in diameter are present. On weathered surfaces it is light grey to ashy colored and often can be distinguished from marble only by its light tan color on fresh surfaces. Several authors have described breccia lenses of lineated granite within the St. George Formation [*Armor-Brown et al.*, 1977, *Karistineos and Georgiades-Dikeoulia*, 1985], but none were observed during this study. It was first thoroughly described by *Freyberg* [1952] and included as

the "hauptmergl" (main marl) unit of his Liegendfolge. It is equivalent to the Dafni and the lower part of the Choumnikon of *Gramann and Kockel* [1969] exposed 30 to 40 km to the south, west of Mt. Pangaion (Figure 4). It is equivalent to the Georgios Formation of *Armor-Brown et al.* [1977]. Its thickness is variable within the Serres Basin, reaching a maximum thickness of approximately 200 m in the southeastern Serres Basin and thinning dramatically to west and south [*Karistineos and Georgiades-Dikeoulia*, 1985]. A 375 m thick marl unit recognized in the Strymon boreholes [*Erki*, 1984] is tentatively correlated to the St. George Formation.

Faunal assemblages in overlying and underlying units indicate the St. George Formation is of Late Miocene to Early Pliocene age [*Armor-Brown et al.*, 1977]. *Karistineos and Georgiades-Dikeoulia* [1985] attribute the deposition of the St. George Formation to a marine incursion at the end of the Messinian salinity crisis associated with a rise in sea-level at the Pliocene-Miocene boundary [*Haq et al.*, 1988].

Spilia Formation

Gradationally overlying the St. George Formation, are the coal-bearing sandstones, siltstones, and mudstones of the Spilia Formation [*Karistineos and Georgiades-Dikeoulia*, 1985]. This formation is equivalent to the lower part of the Spilia Formation of *Armour-Brown et al.* [1977] and the Flözfolge of *Freyberg* [1952]. These poorly consolidated, fine-grained yellowish sandstones and siltstones are extremely disrupted by faulting in the southeastern Serres Basin. Gypsum crystals are locally present, suggesting evaporitic conditions during deposition. Thin gravel lenses are also locally present. Mammal fossils and palynologic studies of the Spilia Formation indicate a Lower Pliocene age (3.4 to 5.4 Ma, [*Armour-Brown et al.*, 1977; *Karistineos and Georgiades-Dikeoulia*, 1985]).

Menoikio Breccia-Conglomerate

Forming a klippe south of Menoikion Oros is a resistant marble cobble conglomerate, known as the Menoikio Breccia-Conglomerate (Figure 5, Plate 1) [*de Boer*, 1970; *Dinter*, 1994]. Clasts are spherical to slightly elliptical, sub- to well rounded, and consist almost entirely of cobble-sized marble clasts cemented together with white to light grey calcite cement. The matrix is composed of sand- to granule-sized marble fragments. Bands of limestone have been reported in this formation [*Kouris*, 1988]. This unit has been disrupted by normal faulting and its base and top are not exposed in the area of Plate 1. It is estimated to be several hundred meters thick, although this probably varies significantly laterally.

The age of this formation is poorly constrained. Its coarse nature and its position as a structural klippe immediately above the Strymon Valley detachment fault suggests that it was one of the earliest deposits formed syn-extensionally with the Strymon Valley detachment fault. Upper Miocene fauna found in overlying units [*Gramann and Kockel*, 1969; *Kouris*, 1988] support this argument. It is tentatively considered to be a lateral time equivalent of the Lefkon Conglomerate.

Post-detachment sediments and geomorphologic surfaces

Continued normal faulting following cessation of motion on the Strymon Valley detachment fault has resulted in the deposition of thick sequences of Quaternary sediments within the modern Strymon Basin. Two boreholes, Strymon 1 and Strymon 2 have penetrated approximately 900 m of Quaternary silts, sands, and marls [*Erki et al.*, 1984]. Different post-detachment sedimentary deposits were generally not differentiated during the course of this study.

Quaternary terrace conglomerates

Well-developed Quaternary terrace conglomerates are present along the southern margin of Menoikion Oros. These terraces form a well-cemented, resistant terra rosa surface dipping shallowly (5° to 9°) basinward and cutting across older structural features, including the Strymon Valley detachment fault. The conglomerates are composed almost exclusively of sub-angular to sub-rounded marble pebbles, cobbles, and rare boulders (up to 75 cm in diameter) within a rusty orange matrix of sand sized grains cemented together with calcite cement. Quartz pebbles and schist and gneiss cobbles derived from lenses within the Falakron Marble Series comprise approximately 1 to 2% of the clasts. The erosional contact with the underlying marble, schist, and Tertiary units is sharp with little erosional relief. Where the unit overlies marble, a karst zone is formed and small solution veins filled with the rusty orange matrix material are found extending up to 10 meters into the underlying marble. Thickness of this unit varies with distance from the mountain front, but typically does not exceed 10 to 20 m. Because these units form a young aggregational surface, they help to identify the most recent fault motions and form a base level with which to compare modern surfaces.

Quaternary geomorphic stream terraces

Although not strictly a sedimentary deposit, erosional terraces provide considerable information about post-detachment faulting and modification and were observed along the southern margin of the Vrondou pluton and east of the Serres Basin. Along the southern margin of the Vrondou pluton several levels of terrace are cut onto the sediments of the Serres Basin at elevations between 920 and 840 m, 760 and 720 m, and 680 and 580 m. The highest erosional terraces are found in the northeastern corner of the basin and their elevations gradually decrease to the southwest. These terraces may represent the dissected remnant of a single southwest-dipping erosional surface formed on top of the Serres Basin sediments after the cessation of detachment faulting. A profile connecting these erosional

surfaces along the southern margin of the Vrondou pluton forms a gentle west-dipping gradient of approximately 2°.

STRUCTURAL DEFORMATION IN THE NORTHERN RHODOPE METAMORPHIC CORE COMPLEX

The structural deformation of the Rhodope metamorphic core complex can be divided into three main phases: ductile Alpine (Mesozoic to Early Tertiary) and pre-Alpine (?) deformation, ductile and brittle Neogene deformation along the Strymon Valley detachment fault, and late brittle Neogene deformation. Within this framework, seven separate deformational phases have been distinguished in the northern part of the Rhodope metamorphic core complex and Serres Basin. Earlier workers identified the main structural features associated with Alpine convergence and late Neogene extension (e.g., *Freyberg* [1952]; *Kronberg* [1966]; *Kronberg* [1969]; *deBoer* [1970]) but the parallel nature of successive deformational events prevented the recognition of the extensional nature of the Strymon Valley detachment fault until only recently [*Dinter and Royden*, 1993; *Dinter*, 1994]. Sub-horizontal northeast-southwest trending lineations formed under ductile conditions have been attributed by *Dinter* [1994] to three distinct structural events: Eocene (?) Alpine compression, Lower Miocene pure-shear extension, and Middle Miocene to Pliocene extension on the Strymon Valley detachment fault. This study recognizes two of these structural events (Alpine compression and detachment faulting) as part of the sequence of deformational events that have affected the northern Rhodope metamorphic core complex.

D_0: Pre-Alpine (?) deformation

The earliest deformational events affecting the units of the Rhodope metamorphic core complex are not differentiable due to overprinting by later structural deformation. All early events are grouped here into a single D_0 event. It is locally possible to determine the

character of this early deformation where it affects the Oreini ortho- and paragneisses. Mylonitic quartzofeldspathic gneisses and amphibolites show an early compositional differentiation and formation of strain heterogeneities and S_0 foliation surfaces. Thin aplitic dikes have been sheared into parallelism with the primary foliation, strongly mylonitized, and boudinaged. S_0 surfaces are defined by compositional differentiation, alignment of mica grains, and elongated quartz grains and ribbons. D_0 structural features in amphibolites include compositional zonation and alignment of the long axes of hornblende crystals. Lenses of amphibolite are ductiley strained and boudinaged. Structures attributed to Eocene (?) Alpine deformation (D_{1-2}) fold S_0 surfaces. There are no constraints on the maximum age of this deformation. D_0 has not been recognized in the Menoikion Marble and Dafnoudi Schist; it is suspected that D_0 deformation occurred before the deposition of their sedimentary protoliths.

D_{1-2}: Isoclinal folding about a northeast-southwest sub-horizontal axis

The first deformation phase attributed to Alpine convergence in the Rhodope metamorphic core complex develops tight to isoclinal recumbent folds with sub-horizontal northeast and southwest trending axes. Isoclinal folds are extensively developed throughout the Falakron Marble Series (e.g., *Kronberg* [1969]; *Meyer* [1969], *deBoer* [1970]; *Papanikalou and Panagopoulous* [1981]) and are observed at all scales (Figure 6). Two generations of coaxial isoclinal folds (F_1 and F_2) have been recognized during this study. The first folds S_0 foliation surfaces (and original sedimentary bedding??) and develops an axial planar foliation (S_1) in mica-bearing schists and a strong intersection lineation (L_1) in quartzofeldspathic gneisses. The second folds S_1 foliations into tight to isoclinal folds but does not develop an axial planar foliation. F_1 and F_2 folds probably developed during progressive deformation under declining temperature conditions. A composite stereonet diagrams of all F_{1-2} fold axes and L_1 lineations is shown on Figure 7. The mean fold axis is 49°/2°. Corrugations and minor fold axes associated with a large F_2

fold between the Menoikion Marble and the Dafnoudi Schist define a mean fold axis of 50°/5° (Figure 8).

D_{1-2} deformation in the Rhodope metamorphic core complex is regionally associated with quartz-albite-epidote-bioite sub-facies greenschist-facies metamorphism [*deBoer*, 1970; *Kronberg*, 1966]. Peak conditions in the northern part of the core complex are at uppermost greenschist-facies to lower amphibolite facies as evidenced by ubiquitous garnet in the Menoikion Marble and Oreini Gneiss. Textural relations in mica-bearing schist interfoliated with the Menoikion Marble indicate peak metamorphic conditions are pre- to synkinematic with D_1. These include alignment of biotite and muscovite parallel to S_1, elliptical feldspar porphyroclasts, elongated epidote crystals oriented parallel to S_1, and the preservation of unoriented mica and epidote inclusions shielded within feldspar porphyroclasts. No metamorphic assemblages are observed to cross-cut S_1 fabrics. D_2 deformation tightly folds S_1 surfaces without developing an axial planar cleavage, producing muscovite grains with unresolved strain concentrated in F_2 fold hinges (Figure 6d).

D_3: Open to close folding about a northwest-southeast sub-horizontal axis

Following the isoclinal folding event, a locally developed folding phase (D_3) affected the units of the Falakron Marble Series, forming open to close folds with northwest and southeast trending fold axes and inclined axial planes (Figures 9 and 10). These folds are more gentle at the map scale (cross sections EE′ and FF′). This folding does not form an axial planar foliation. Where it affects coarse aplitic sills in the Oreini Gneiss, it forms centimeter-scale corrugations (parasitic folds?) along the folded S_0 or S_1 surfaces parallel to F_3 fold axes. The irregular character of this deformation and later structural deformation make it difficult to define a meaningful mean fold axis. Folds with northwest and southeast-trending axes have been recognized throughout the Rhodope metamorphic core complex [*Meyer*, 1969; *Kronberg et al.*, 1970; *Kronberg and Raith*,

1977; *Koukouvelas and Doutsos*, 1990]. However, previous workers have not distinguished these folds from a second folding phase with northwest-trending fold axes (D_{6f}) nor recognized the regional implications of either event.

D_4: Open folding about a southwest axis

Southwest-trending open folds were rarely observed at the outcrop scale but are significant on a regional scale. These large-scale open folds with southwest-trending axes were considered by earlier workers to represent the main structural features in this region (e.g., *deBoer* [1970]; *Kronberg* [1969]). A stereonet plot of open folds with southwest-trending fold axes is shown in Figure 11a. On Menoikion Oros this folding is expressed by a bimodal distribution of marble foliations (Figure 11b, Plate 1, cross section HH').

D_5: Deformation associated with the intrusion of the Vrondou pluton

During the Late Oligocene and Early Miocene, the Vrondou, Xanthi, and Symvolon plutons and several smaller calc-alkaline bodies were intruded into the Rhodope metamorphic core complex. The nature of the contact between the Vrondou pluton and the units of the Falakron Marble Series varies significantly around the pluton. Where the pluton intrudes the Falakron Marble Series along its northeastern margin, a sharp, sub-horizontal intrusive contact is formed with a 10 to 20-m thick zone of hornblende hornfels grade skarn composed predominantly of garnet and epidote. Sharp intrusive contacts (Figure 12a) and skarn mineralization are commonly observed at deeper structural levels of the Elaion stock; ductile and brittle shearing during later detachment faulting deformed the contact at shallow structural levels.

In contrast, the southern contact of the Vrondou pluton with the Oreini Gneiss is characterized by a thick zone of dikes that intrude the country rock. Migmatites are locally developed with minor interfolding of granite and amphibolite gneiss. A weak planar fabric, S_5, possibly genetically linked to pluton emplacement, is locally developed in the granitic.

Sub-angular amphibolite xenoliths within the foliated granite dikes are aligned sub-parallel to the foliation plane, but pre-intrusional fabrics within the xenoliths are not disturbed (Figure 12b).

There is some limited evidence for syn-intrusional extension associated with the Vrondou pluton. Locally, dikes intruded into the Oreini Gneiss are cut by small shear zones which have shallowly dipping, top-to-the-south, normal sense displacement (Figure 12c). These brittle shears are in turn cross-cut by younger dikes. Because the cumulative offset observed on these shear zones is small and they were seldom observed, this brittle syn-intrusional extension is thought to be of limited magnitude.

In one locality on the southern margin of the Vrondou pluton, a southwest-trending, open to close fold affects L_1 lineations and S_5 cleavage surfaces. Aplitic dikes intruded parallel to the axial plane of this fold contain a weak fabric subparallel to the axial plane. Fold vergence and dike fabrics indicate top-to-the-northeast sense of motion. Dikes do not show evidence for chilled margins or baked contacts suggesting that their intrusion was into warm country rock. The limited areal extent of this deformation suggests that it may be causally related to the intrusion of the Vrondou pluton.

D_6: Strymon Valley detachment fault

The Strymon Valley detachment fault is a regionally developed, corrugated low-angle normal fault which juxtaposes the amphibolite-facies Serbo-Macedonian Gneisses and syn-extensional supradetachment basins against footwall marbles and schists of the Falakron Marble Series and the Upper Oligocene to Lower Miocene (?) Vrondou pluton. The earliest structures associated with the fault are ductile shear fabrics formed at elevated temperatures at mid-crustal levels. Footwall rocks are affected in a heterogeneous manner. In general, marble and the Tertiary intrusive rocks are the most strongly deformed footwall units; felsic granites are more intensely mylonitized than mafic-rich granites and gneisses. Pre-existing metamorphic foliations, lineations, and fold axes in the footwall are warped

into parallelism with the detachment fault to a depth of several hundred meters below the fault plane. The southern, western, and northwestern margins of the Vrondou pluton and the Elaion stock are sheared to form granite proto-mylonite, mylonite, and ultramylonite. An S-C fabric *[Berthé et al.*, 1979] is generally well defined (Figure 13a and 13b). The contact between undeformed granite and mylonitized granite is gradational and the degree of mylonitization generally decreases structurally downward below the Strymon Valley detachment fault. Dikes and sills intruded into the Oreini Gneiss are mylonitized to varying strength. As displacement on the fault continued, the footwall passed through the brittle-ductile transition, superimposing brittle structural fabrics over the earlier ductile ones.

The predominant style of deformation associated with the Strymon Valley detachment fault (ductile vs. brittle) varies considerably along its trace. At Elaion, the detachment fault juxtaposes the Tertiary supradetachment sequence against granite mylonite and marble along a thin, discrete brittle zone overlying a thick, well-developed zone of ductile shear. Ductile motion on the Strymon Valley detachment fault severely attenuates the Falakron Marble Series over the Elaion stock. The contact between marble and granite mylonite is typically undulatory and commonly brittlely sheared (Figure 13c). Mylonitic fabrics in the underlying granite mylonite are drawn into parallel with the contact. Marble foliations are slightly oblique to the underlying mylonitic fabrics. The detachment fault is characterized by a thin (2-10 cm) marble microbreccia carapace underlain by well-developed granite mylonite and ultramylonite with ductile fabrics subparallel to the fault plane (Figure 13d). Chloritization in the footwall is prevalent only near the fault. Subvertical brittle shears with centimeter to decimeter spacing are the only macroscopic brittle features in the footwall (Figure 6b). These brittle shears typically have minor normal-sense offset, but their cumulative displacement is negligible. Sediments near the fault zone are sheared and disrupted and blocks of footwall marble are locally incorporated into the hanging wall (Figure 13d).

In contrast, on the western margin of the Vrondou pluton, a thick zone of brittle shear is superimposed on poorly developed ductile structures. Large (5,000 m^2) fault scarps dip westward and juxtapose the Tertiary supradetachment sequence against granite proto-mylonite and Oreini Gneiss (Figure 13e). Above the fault, Tertiary sediments are ground to rock flour and heavily mineralized in a zone approximately 50 cm thick (Figure 13f). The fault plane itself is defined by a 50 to 100 cm thick resistant carapace of marble microbreccia. This carapace overlies about 75 to 100 meters of less-resistant, heavily chloritized granite cataclasite. Immediately below the fault plane, a late secondary foliation is formed in the chlorite cataclasite, slightly oblique to the overlying fault plane. This cataclasite zone grades structurally downward into 75 to 100 m of shattered and brecciated granite mylonite overlying about 100 m of shattered *in situ* lineated granite. This in turn grades downward into weakly lineated granite mylonite.

Laterally northward from these excellent fault plane exposures, the core complex is characterized by a 500 m thick zone of intensely brecciated footwall with a poorly exposed overlying detachment fault plane. The brecciated footwall has been extensively leached and mineralized, often to the point that the original footwall lithology is unrecognizable (Figure 13g). A compositional layering which resembles sedimentary bedding is formed in the composite granite, marble, and gneiss breccia, reflecting original lithology and zones of mineralization. This compositional layering is locally folded. Breccias formed from granite proto-mylonite are leached white and contain abundant gypsum crystals. Mineralized marble-gneiss breccias are either dark gray or tan. The detached overlying sediments are heavily mineralized within 100 m of the detachment fault plane. This highly brecciated and mineralized detachment fault zone grades abruptly northward into a fault which is intermediate in character between the Elaion and western Vrondou segments. The character of the detachment fault along the southern margin of the Vrondou pluton is also intermediate between these end-member segments.

East of Serres, the character of the detachment fault depends mainly on footwall lithology. Where the fault overlies schist or gneiss, it is expressed as a 20-50 cm thick resistant carapace of chloritized microbreccia with a characteristic Dijon mustard color. Underlying schists and gneisses are variably brecciated and chloritized in a thin zone (on the order of tens of meters). Where the detachment fault overlies marble, a discrete fault plane is formed as at Elaion.

The Strymon Valley detachment fault is characterized along its length by well-exposed, shallowly dipping fault planes that have gently southwest-plunging local and regional corrugation axes. Like the overlying detachment fault plane, the ductile shear zone associated with the Strymon Valley detachment fault is regionally corrugated. This is most evident on the Vrondou pluton where foliations formed during the ductile phase of detachment faulting wrap gently around the pluton. Foliations formed in the granite mylonite show considerable variation in attitude, but are generally sub-parallel to the corrugations of the overlying brittle detachment fault. Stretching lineations vary as much as 30° from the mean stretching lineation, but are generally close to a well-defined, gently southwest-plunging average stretching lineation. The mean stretching lineation coincides with the mean corrugation axis defined by mylonitic foliation planes, 231°/8° (Figure 14). Within uncertainty, the mean stretching lineation observed in the Elaion stock (229°/9°) is identical to that determined for the mylonitic margins of the Vrondou pluton (233°/7°).

Gentle flutings and corrugations at all scales are ubiquitous along the detachment fault. Where developed, these corrugations define a southwest direction of transport. Slickenslides and outcrop-scale corrugations of the fault plane have an mean attitude of 225°/7° (Figure 15). This is close to the corrugation axis defined by all fault planes (241°/12°), suggesting that the sinuous map trace of the detachment fault results from regional-scale corrugations. The four segments where the fault has been most clearly identified (East of Serres, Elaion area, south of Vrondou, and west and north of Vrondou) show similar corrugation axes (Figure 16). Measurements on the fault plane south of

Vrondou between Oreini and Xirotopos match the regional corrugation, suggesting that the fault which displaces the Serres Basin against the Vrondou pluton is at least locally the Strymon Valley detachment fault (Plate 1). East of Oreini and west of Xirotopos, the detachment fault has been disrupted by post-detachment high angle faulting.

Several of the faults in the southeastern Serres Basin are attributed to motion on the Strymon Valley detachment fault (Plate 1). These include north-striking faults with normal sense offset and northeast-striking, high-angle, right-lateral tear faults. Low-angle normal faults are both antithetic and synthetic to the Strymon Valley detachment. Fault planes are poorly exposed except where they cut marble breccia or calcareous sandstone. Extremely disrupted supradetachment sediments are faulted and rotated above the Strymon Valley detachment fault, faults synthetic and antithetic to it, and post-detachment faulting (Figure 17). Sedimentary bedding dips between 15° and 60°. In two locations, tilted supradetachment sediments unaffected by post-detachment faulting are preserved in klippen above poorly exposed segments of the detachment fault. Bedding planes in these klippen typically dip between 10° and 50° to the north and northeast (Figure 18).

D_{6f}: Gentle to open folding about a southeast sub-horizontal axis

A second folding phase with northwest and southeast trending axes affects the units of the Falakron Marble Series. This folding phase is characterized by outcrop scale, gentle to open folds with well-defined, shallowly southeast-plunging fold axes and upright axial planes (Figure 19). The average fold axis is 137°/14°. This deformation folds S_0 and S_1 surfaces and L_1 lineations in the Oreini Gneiss and Menoikion Marble. In marble units, small vertical joints and calcite-filled extension cracks subparallel to the axial plane of this folding are locally developed on crests of antiforms.

D7: Post-detachment brittle faulting

Post-detachment extensional faulting is expressed throughout the Rhodope metamorphic core complex by the formation of the modern Strymon and Drama Basins and the smaller Kato Nevrokopion and Akladohorion Basins (Figure 4 and 5, Plate 1). High-angle normal and strike-slip faults cut into the footwall of the Strymon Valley detachment fault and disrupt the supradetachment sediments of the Serres Basin. Where these faults juxtapose basement units, their presence is often difficult to prove with certainty. The basement is locally brecciated, but displaced footwall markers are generally scarce. The best constraints for the motion on post-detachment faults comes from offset geomorphic surfaces. Although several generations of cross-cutting faults have been recognized in the Serres Basin, all are grouped together as "post-detachment faulting".

East-northeast to northeast striking high-angle faults that disrupt the southern and northern margins of the Vrondou pluton, the southeastern Serres Basin, and the footwall of the Strymon Valley detachment fault east of Serres (Plate 1) are suspected to have a significant component of right-lateral strike-slip separation but piercing points are generally absent. A single exception to this is in the southeastern Serres Basin where a northwest-dipping fault forming the boundary between the basement and Tertiary sediments offsets the contact between the Strymon Valley detachment fault and the St. George Formation approximately 1.5 km in a right-lateral sense (Plate 1). Brittle microstructures near this fault are consistent with right-lateral displacement. This fault projects into a deep valley in the footwall where an offset geomorphologic surface indicates it is responsible for approximately 100 to 200 meters of north-side-down separation in addition to its right-lateral component. Other deep, northeast-trending valleys on Menoikion Oros may be associated with unidentified high-angle faults.

The right-lateral strike-slip fault in the southeastern Serres Basin is cut by a set of younger north-striking normal faults with approximately 750 m of cumulative normal displacement (Figure 5, Plate 1, Cross section EE′ and FF′). These faults are, in turn, cut

by the youngest faults observed in the region, the east to southeast striking normal faults which form the modern active eastern boundary of the Strymon Basin near Serres. These faults disrupt the youngest basin sediments and Quaternary stream terraces.

The Kato Nevrokopion Basin is bounded by an active northeast-striking fault on its southeastern side (Figure 5). Normal motion on this is indicated by scallops in the footwall. A minimum vertical separation of 1000 m on this fault is required to down-drop the basin relative to the surrounding highlands. Approximately 300 to 400 meters of north-side-down separation of the Menoikion geomorphologic surface occurs along the projection of this fault northwest of Menoikion Oros (Plate 1).

KINEMATICS, TIMING, AND REGIONAL IMPLICATIONS OF DEFORMATION EVENTS

D_{1-2}: The Nestos Thrust

The pervasive formation of D_{1-2} fabrics throughout the footwall of the Rhodope metamorphic core complex is generally attributed to emplacement of the West Thracian Gneiss Complex over the Falakron Marble Series on the southwest-vergent Nestos Thrust [*Papanikolaou and Panagopoulos*, 1981; *Kilias and Mountrakis*, 1990; *Koukouvelas and Doutsos*, 1990; *Dinter*, 1994]. Major and minor F_{1-2} fold axes and stretching lineations are oriented sub-parallel to the direction of shear transport, a common attribute of rock units that have accommodated large magnitudes of ductile shear strain (e.g., *Hansen* [1971]). Asymmetric folds and porphyroclasts consistently indicate a top-to-the-southwest sense of motion during D_{1-2}. Sense of shear indicators near the Nestos thrust show a well defined, top-to-the-southwest sense of ductile thrust motion [*Kilias and Mountrakis*, 1990; *Koukouvelas and Doutsos*, 1990; Dinter, pers. comm. 1994].

The timing of motion on the Nestos Thrust is poorly constrained. The Upper Cretaceous to Lower Tertiary Skaloti-Echinos granite (Rb-Sr isochron age of 86 ± 27 Ma [*Soldatos and Christofides*, 1986]) is carried in the hanging wall; the thrust fault and

fabrics associated with it are cross-cut by Oligocene plutons. A more precise, but speculative, constraint for the motion on the Nestos Thrust has been recently interpreted from cooling ages in the overriding West Thracian Gneiss Complex and Kerdilion Gneiss Series. *Dinter* [1994] reinterpreted published 47 to 36 Ma K-Ar hornblende cooling ages [*Harre et al.*, 1968; *Liati*, 1986] to represent a rapid cooling of the West Thracian Gneiss Complex in response to the underthrusting of the thick, cool Falakron protolith.

D_3: Late orogenic compression

The absolute timing of D_3 is uncertain, but it must occur after D_{1-2} and before the intrusion of Oligocene plutons. D_3 folds are cut by granite dikes that are probably associated with the emplacement of the Vrondou pluton. The timing of this deformation phase relative to D_4 is uncertain. I attribute D_3 deformation to late orogenic compression between the West Thracian Gneiss Complex and the Falakron Marble Series directed along a northeast-southwest axis. On a regional scale, reconstructions imply the eastern boundary of the incipient Rhodope metamorphic core complex was at the surface prior to the epizonal emplacement of the Xanthi pluton and the eruption of Paleogene volcanics (see below). This implies the Falakron Marble Series had a regional southwest dip at this time. I interpret this southwest dip to be the expression of a regional F_3 antiform. The present trace of the Nestos Thrust is preserved in the eastern limb of this antiform.

D_4: Southwest folding

The timing of this folding phase relative to other deformation events is uncertain. While these folds clearly affect D_{1-2} structural fabrics, their timing relative to D_3 is uncertain. Variability in F_3 fold axes could caused by this later open folding. In a single location, crenulations with west-southwest trending axes appear to be cut by the Elaion stock. However, it could not be conclusively demonstrated that these crenulations were formed during the D_4 folding phase. Cross sections DD′ and HH′ are drawn to show

southwest-trending folds are cut by the Oligocene intrusives, but this could not be clearly demonstrated in the field. It is possible that this folding post-dates intrusion of the Vrondou pluton and is associated with the detachment faulting process.

D_5: Oligo-Miocene pluton intrusion: "Symvolon Shear Zone??"

Late Oligocene to Miocene intrusives form an east-southeast trending belt through the Rhodope metamorphic province (Figure 4). Paleogene volcanics are widespread north of this belt. Based on their chemical composition, these plutons are considered to be formed in either a subduction-related or post-collisional environment [*Kotopouli and Pe-Piper*, 1989]. Recently, several workers have suggested that the emplacement of these plutons is associated with extension resulting from gravitational collapse of the over-thickened Rhodope crust [*Kolocotroni and Dixon*, 1991; *Koukouvelas and Pe-Piper*, 1991; *Jones et al.*, 1992]. Structural and geochronologic work in the southern Rhodope metamorphic core complex has shown that the intrusion of at least one of these calc-alkaline plutons, the Symvolon pluton, occurs synchronously with extension [*Dinter et al.*, 1995]. Textural relationships in the Symvolon pluton strongly suggest that crystallization occurred in the earliest Miocene (at 21-22 Ma) in a northeast-trending pure-shear extensional zone, termed the "Symvolon Shear Zone" [*Dinter et al.*, 1995]. Fabrics associated with this shear zone are cross-cut by fabrics associated with the Strymon Valley detachment fault [*Dinter*, 1994].

In the northern Rhodope metamorphic core complex, no structural features were recognized that could be unambiguously attributed to pure-shear extension on a "Symvolon Shear Zone". Unlike the Symvolon pluton, mylonitization of the Vrondou pluton is restricted to its margins and mylonitic fabrics show a consistent top-to-the-southwest sense of shear. Thermochronology indicates that approximate mylonitic conditions (300° - 350° C) occurred at least six to eight million years after the emplacement of the central Vrondou pluton [Chapter 4]. Small-scale shears cut by intrusive dikes are typically brittle features of

limited magnitude. It is suspected that the "Symvolon Shear Zone" is regionally restricted to the southern part of the Rhodope metamorphic core complex.

D_6: Strymon Valley detachment fault

Both ductile and brittle kinematic indicators along the Strymon Valley detachment fault and in the underlying S-C granite mylonites indicate a top-to-the-southwest sense of motion. Well-developed ductile sense of shear indicators (e.g., S-C fabrics, preferred grain shape orientations, brittle shears in feldspar) consistently indicate a top-to-the-southwest sense of motion during the mylonite formation. All S-C fabrics examined in the field in which a sense of shear could be established showed this sense of motion. Locally, winged δ-type porphyroclasts (sense of *Hanmer and Passchier* [1991]) are formed in marble from rigid knots of garnet skarn (Figure 13h). Thin section analyses of granite mylonite show either a clear top-to-the-southwest sense of motion or no clear motion sense at all. Brittle kinematic indicators are especially well developed on the western margin of the Vrondou pluton, and include asymmetric shear folds formed in the gouge and breccia, extensional cracks developed directly below the fault plane oriented perpendicular to the transport direction, and a late secondary foliation in chlorite microbreccia that dips more gently than the detachment fault plane which cuts it.

The Strymon Valley detachment fault is a long-lived, extensional structure, with active deformation occurring over approximately 12 to 15 million years. Tectonic denudation beginning at ~16 - 18 Ma is interpreted from $^{40}Ar/^{39}Ar$ muscovite, biotite, and K-feldspar cooling ages from the Vrondou pluton, the Elaion stock, and the Falakron Marble Series [Chapter 4]. This denudation initiated slightly earlier than in the Symvolon pluton to the south [*Dinter et al.*, 1995]. The oldest mammal fauna recovered from supra-detachment sediments in the Serres Basin are 9.8 Ma [*Armour-Brown et al.*, 1977] overlapping with K-feldspar cooling ages. Sediments as young as 3.5 Ma are disrupted by the detachment fault [*Armour-Brown et al.*, 1977; *Karistineos and Georgiades-Dikeoulia,*

1985]. Using the displacement-parallel width of the core complex at the latitude of the Vrondou pluton (~40 km), the average rate of motion on the detachment fault is 3.3 mm/yr, approximately half of that estimated at the latitude of the Symvolon pluton [*Dinter et al.*, 1995]. Comparable estimates of the rate of detachment are inferred from systematic younging of K-feldspar cooling ages in the direction of hanging wall motion [Chapter 4].

The breakaway zone for the Strymon Valley detachment fault has not been recognized. A minimum estimate for the horizontal displacement on the Strymon Valley detachment fault is constrained by the displacement-parallel width over which supradetachment deposits are tilted and disrupted, ~25 km in the Serres Basin. An equivalent minimum displacement is calculated for the Angitis Basin if the metamorphic basement recognized in boreholes Strymon 1 and 2 [*Erki et al.*, 1984] represents the down-dip projection of the detachment fault footwall (Figure 5). A better, but less certain, estimate for displacement magnitude is the present width of the Rhodope metamorphic core complex which decreases northward from ~80 km at the Aegean coastline to ~40 km at the latitude of the Vrondou pluton. This width continues to decrease northward into the Bulgarian Sandanski graben, suggesting the magnitude of displacement is less to the north.

Shallow-level Oligocene-Miocene stocks in the Serbo-Macedonia Range provide independent support for these estimates of displacement magnitude on the Strymon Valley detachment fault (Figure 2). Stocks in the southern Serbo-Macedonian Range (the Stratoni, Tsikara/Asprolakkos, and Skouries stocks) have Upper Oligocene to Lower Miocene U-Pb zircon ages between 19 and 27 Ma [*Frei*, 1992]. If these stocks are the tectonically decapitated upper portions of the Symvolon pluton, their present location requires between 40 and 80 km of southwest-directed translation since their emplacement. In the northern Serbo-Macedonian Range, the Jerakario and Vathi stocks (U-Pb zircon ages of 22 to 34 and 17 to 18 Ma, respectively [*Frei*, 1992]) could be the upper levels of the Vrondou pluton or the Teshovo pluton. Removing approximately 50 km of displacement restores these northern stocks to a position along the linear trend defined by the Teshovo,

Vrondou, and Symvolon plutons. Although these correlations are tentative, it is significant that they provide an independent estimate for displacement on the Strymon Valley detachment fault that is equivalent to the present-day width of the Rhodope metamorphic core complex.

Although the footwalls of the Strymon Valley detachment fault and the Nestos Thrust coincide, the Strymon Valley detachment fault is an independent structure which does not reactivate the Alpine thrust fault, but rather cuts indiscriminately across older structures and fabrics in its footwall. The Strymon Valley detachment fault, as recognized along the western margin of the Rhodope metamorphic core complex, is wholly constrained to the footwall of the Nestos Thrust. Significant along-strike structural relief on the Strymon Valley detachment fault is implied by the gross metamorphic stratigraphy of the Falakron Marble Series. In the northern Rhodope metamorphic core complex, the detachment fault cuts down-section to the northwest, exposing successively deeper levels of the Falakron Marble Series and ultimately the Vrondou pluton. In doing so, it cuts across structural boundaries and fabrics formed during the emplacement of the Nestos Thrust. The detachment fault reaches its shallowest structural level where it exposes the Dafnoudi Schist and cuts down section again to the southeast where it exposes the Symvolon pluton and the basal Falakron Marble Series (Figure 4). The magnitude of structural relief on the detachment is estimated to be 6 km (cross section HH') but may approach the thickness of the Falakron Marble Series, estimated to exceed 10 km [*Kronberg*, 1969]. It is possible that the Strymon Valley detachment fault took advantage of a significant strength contrast between Tertiary intrusive rocks and the Falakron Marble Series and opportunistically localized near the pluton-country rock interface.

Southwest-trending corrugations and flutings of the Strymon Valley detachment fault observed at the outcrop scale are reflected on a larger scale by regional corrugations of the Strymon Valley detachment fault. These corrugations, with a wavelength of approximately 15 km and amplitudes between 1 to 3 km (peak to trough), are reflected in

alternations of basement highs (Vrondou, Menoikion, Pangaion, and Symvolon Mountains) and lobes of supradetachment basins (Siderokastron, Serres, Angitis, and Akropotamos Basins) (Figure 4). The modern topography of the western margin of the Rhodope metamorphic core complex closely mimics the modern geometry of the Strymon Valley detachment fault. Footwall lithologies are typically more resistant than the Tertiary supradetachment basin sediments and form the highest elevations. Menoikion Oros, composed predominantly of resistant marble, forms a broad dome interpreted to be the slightly eroded remnant of the Strymon Valley detachment fault (Plates 1 and 2). If so, the Strymon Valley detachment fault becomes subhorizontal as it is gently warped over Menoikion Oros. The granites of the Vrondou pluton are less resistant to weathering and the original detachment surface is not preserved. However, the eroded surface of the Strymon Valley detachment fault is reflected by the southwest-plunging topography preserved all along the western boundary of the Rhodope metamorphic core complex.

The cause of these major corrugations of the detachment fault plane is uncertain. Large-scale corrugations observed in other core complex have been typically attributed to primary warps, or mega-mullions of the detachment fault plane (c.f., *John* [1987]). It seems counter-intuitive that km-scale primary warps of the detachment fault could be preserved as the primary topographic expression in the core complex while there is no expression of the apparent large-scale structural relief on the detachment fault. Recent work in the Alps and the Death Valley region suggests that regional-scale extensional strain occurring on low-angle normal faults may be accompanied by compression perpendicular to the extension direction in tectonic settings undergoing transpression or lateral extrusion, creating folds with axes oriented sub-parallel to the extension direction [*Mancktelow and Pavlis*, 1994; see also *Yin*, 1991]. It is possible that regional- and local-scale corrugations of the Strymon Valley detachment fault and mylonitic foliations result from such a mechanism. Folds attributed to D_4 deformation may, in fact, be formed in a similar manner. Sedimentary bedding in the supradetachment basins, although irregular, is

consistent with such a mechanism (Plate 1). There is no clear evidence, however, that the Rhodope metamorphic core complex was formed in a regional tectonic setting dominated by either transpression or lateral extrusion. A third explanation of the large-scale corrugations is that they are an interference pattern formed by the flexural isostatic rebound of a curvi-planar detachment surface that has a component of dip not only in the direction of motion but also perpendicular to the transport direction (i.e., a detachment fault with along-strike structural relief). The interplay between these three mechanisms is unclear and it is possible that some or all of them have a role in the formation of the modern corrugated detachment fault surface.

The Strymon Valley detachment fault has been correlated to a low-angle normal fault on the western side of the island of Thassos where Tertiary sediments are juxtaposed against metamorphic basement along a shallowly dipping fault plane (Figure 4) [*Soukoutis et al.*, 1993; *Dinter and Royden*, 1993]. This correlation suggests that the Prinos-Kavala Basin is a submerged, southwest-trending, supradetachment basin lobe formed in a major downward corrugation of the Strymon Valley detachment fault. Seismic reflection studies in the Prinos-Kavala Basin have imaged a west-dipping fault southwest of Thassos forming the eastern boundary of a deep half graben (Figures 4, 20) [*Martin*, 1987]. This fault has been interpreted to be the offshore manifestation of the low-angle normal fault observed on Thassos [*Soukoutis et al.*, 1993].

The displacement on this fault makes its correlation to the Strymon Valley detachment fault equivocal. Its offset is small compared to the Strymon Valley detachment fault with approximately 1.5 seconds (two-way travel time) of throw and approximately 2 km of heave, far to little to unroof Thassos from mid-crustal depths. I interpret this fault to be a post-detachment structure formed in the footwall of the Strymon Valley detachment fault during more recent Aegean extension (D_7), essentially a "submerged Drama Basin". In this interpretation, the acoustic basement imaged on seismic cross sections represents the tilted and disrupted detachment fault surface. It is also possible that the Thassos

detachment represents a second, structurally higher detachment fault in the hanging wall of the Strymon Valley detachment fault (Dinter, pers. comm., 1994). However, the juxtaposition of supradetachment sediments against the mid-crustal Falakron Marble Series still requires more displacement than the seismically imaged fault in the Prinos-Kavala basin can account for.

D_{6f}: Northwest-southeast gentle folding: isostatic uplift (?)

The timing of D_{6f} is poorly constrained and its inclusion as a component of the detachment faulting is speculative. Folds with northwest and southeast-trending fold axes have been recognized throughout the Rhodope metamorphic core complex, but as this study shows, it is probable that two phases of folding occur with this orientation. The distinction of the second folding phase from the earlier northwest-trending folding phase is based largely on their different styles. D_3 folds are open to close, have inclined to recumbent axial planes, and do not have a well-defined average fold axis. In contrast, D_{6f} folds are gentle to open, have vertical to subvertical axial planes, and have a well-defined fold axis. The two folding phases are further distinguished by the conditions under which they developed. Neither deformation forms an axial planar foliation in mica-bearing schists. Ambient conditions during D_3 folding are inferred to be below the peak metamorphic conditions during D_{1-2} deformation but above the temperature for mylonite formation, estimated to be 300° C to 350° C [Chapter 4]. The locally produced, calcite-filled, axial planar fractures in marble suggests D_{6f} occurred at a significantly lower temperature.

This gentle folding phase is interpreted to result from flexural bending and unbending accompanying isostatic uplift of the Rhodope metamorphic core complex during its tectonic denudation (i.e., the passage of a "rolling hinge" through the footwall [*Buck*, 1988; *Manning and Bartley*, 1994]). The broad domal geomorphologic surface of Menoikion Oros is interpreted to reflect the slightly eroded remnant of the Strymon Valley

detachment fault which has been gently flexed to horizontal about a northwest-trending axis. It is suspected that regional-scale warping of the detachment fault is manifested on local scales by the formation of gentle parasitic folds in the footwall of the core complex. Folds formed in this manner have their axes oriented perpendicular to the extension direction.

D_7: Post-detachment faulting

The youngest deformation that affects the Rhodope metamorphic core complex is associated with ongoing extension in the Aegean region and the westward propagation of the Northern Anatolian Fault into the Aegean Sea. The Spilia Formation is the youngest unit (3.5 Ma) in the Serres Basin disrupted by the Strymon Valley detachment fault. This places a maximum age constraint for the transition from detachment-related extension to the modern faulting regime dominated by dextral strike-slip and normal faults that disrupt both the hanging wall and footwall of the Rhodope metamorphic core complex.

The modern Strymon Basin is bounded on its eastern and western margins by active normal faults that disrupt the units of the Serbo-Macedonian Range, the Rhodope metamorphic core complex, and the supradetachment basins formed by motion on the Strymon Valley detachment fault. The Drama Basin is a half-graben formed in the footwall of the Strymon Valley detachment fault and is the largest post-detachment basin formed wholly within the geographic boundaries of the Rhodope metamorphic core complex. It is bounded on its western side by an active northwest-striking normal fault. The elevation of the basin relative to adjacent highlands requires at least 2 km of vertical separation on this western boundary fault. Such large faults have not observed on its eastern margin. The half-graben morphology suggests that the eroded remnant of Strymon Valley detachment fault should crop out on the eastern side of the basin. Although the detachment fault itself has not been recognized on the eastern side of the basin, the topography suggests that

macroscale southwest-trending basement corrugations exist and could represent the eroded remnants of the detachment fault.

The entire north Aegean region is seismically active. Focal mechanisms for major earthquakes have northeast-striking dextral strike-slip mechanisms and north to northwest striking normal mechanisms [*Jackson et al.*, 1982]. Seismicity in the Rhodope Mountains is limited and is of low magnitude relative to the rest of the Aegean region [*Scordilis et al*, 1989]. Seismic events are concentrated along the northwestern and eastern margins of the Drama Basin and the eastern and western margins of the Strymon Basin. A few scattered events have occurred elsewhere within the footwall of the Strymon Valley detachment fault, mainly along southeastern margin of the Kato Nevrokopion Basin. Recent GPS work suggests that the region is relatively stationary relative to the European continent and the Northern Aegean Trough forms the principal northern boundary between more active extension in the Aegean Sea and less active extension on-land in the Rhodope metamorphic core complex [*Oral*, 1994].

PALEOGEOGRAPHIC RECONSTRUCTIONS AND IMPLICATIONS OF THE STRYMON VALLEY DETACHMENT FAULT

The reinterpretation of the Strymon Valley detachment fault, the western tectonic boundary of the Rhodope metamorphic province, as an extensional structure has significant implications for the tectonic history of the entire north Aegean region. In order to examine these implications, a series of paleogeographic reconstructions are presented that trace the regional tectonic history through the Tertiary. The reconstructions and correlations that are developed support and elaborate on the ideas of *Dinter* [1994]. A regional northeast-southwest cross section showing the modern boundaries of major tectonic units from the West Thracian Gneiss Complex to Mt. Olympos forms the basis for all regional reconstructions (Figure 21a).

Reconstruction of post-detachment extension

During the Pliocene and Quaternary, extension in the north Aegean region is dominated by normal and right-lateral strike-slip faulting that disrupts the Rhodope metamorphic core complex and the northwest-trending tectonostratigraphic facies belts formed during Alpine collision. Although the displacement on individual Pliocene-Quaternary faults may be large (up to several kilometers), they are inferred to accommodate relatively little lateral translation of tectonostratigraphic units as compared to regional Miocene detachment faults and Alpine thrust faults. In general, boundaries between tectonostratigraphic units are shifted little by restoring the displacement on these post-detachment faults. A reconstructed cross section of the north Aegean region at the end of the Miocene is shown in Figure 21b. Over the length of the section, five to ten kilometers of extension have been removed, a conservative estimate of lateral extension. In this reconstruction, the Drama and Volvi basins are closed up and the effects of high angle normal faulting east of Mt Olympos and in the Gulf of Thermiakos are removed. The topographic surface defined by the outlines of the Rhodope metamorphic core complex roughly corresponds to the Strymon Valley detachment fault surface.

Reconstruction of detachment-related extension and late Alpine folding

The pre-detachment geometry of the Rhodope metamorphic core complex can be inferred from the regional distribution of pre-detachment Tertiary intrusive plutons and extrusive volcanics and the suspected location of the detachment fault breakaway zone (Figure 4). Along the western boundary of the core complex, the Vrondou pluton and Elaion stock are emplaced at mesozonal levels [Chapter 5]. Although the emplacement depth of the Symvolon pluton has not been studied, because it intrudes the lower Falakron Marble Series and contains ductile fabrics formed during detachment faulting [*Dinter*, 1994], it is suspected to have been emplaced at a comparable level. Near the suspected breakaway zone, the epizonal Xanthi pluton is in intrusive contact with Eocene-Oligocene

flysch and Oligocene volcanics on its eastern boundary (Figure 4) [*Koukouvelas and Pe-Piper*, 1991]. Oligocene volcanics are also present northeast of the Vrondou pluton. These intrusive relations, combined with the width of the core complex and the suspected location of the breakaway zone imply an initial low to intermediate southwest dip on the Strymon Valley detachment fault.

Restoring the displacement on the Strymon Valley detachment fault has major implications for the tectonic history of the north Aegean region. The recognition of the extensional nature of the fault prompted *Dinter* [1994] to propose a correlation between amphibolite-facies gneisses in Serbo-Macedonia and the West Thracian Gneiss Complex. This correlation implies that the present width of the Rhodope metamorphic core complex approximates the magnitude of displacement on the detachment fault; possible correlation between mesozonal plutons in the Rhodope metamorphic core complex and shallow stocks in the Serbo-Macedonian Gneiss Complex supports these estimates of extension. Restoring approximately 60 km of displacement on the Strymon Valley detachment fault juxtaposes the Serbo-Macedonian Gneiss Complex and the West Thracian Gneiss Complex in a pre-Miocene configuration as suggested by *Dinter* [1994] (Figures 21c and 22). These reconstructions show the geometry of the north Aegean region at the beginning of the Miocene, after the intrusion of the Vrondou and Xanthi plutons and the eruption of Oligocene volcanics but before extension initiated on either the Strymon Valley detachment fault or the Symvolon Shear Zone. The regional dip of the detachment fault is taken to be 15° - 20° and the breakaway zone is located near the present trace of the Nestos Thrust. In addition, a conservative 20 km of extension on the Lizadiko-Keri Ridge and Kalipevki faults [*Schermer*, 1993] was removed, effectively shifting the units of the Olympos region eastward relative to the Rhodope metamorphic core complex. Suspected additional normal shear between the Kerdilion and Vertiskos Gneisses (Dinter, pers. comm., 1994) is unquantified and has not been incorporated into the reconstruction.

The westward dip of the Falakron Marble Series in Figure 21c is attributed to late Alpine compressional folding (D_3) which has folded the nappes emplaced during Eocene thrust faulting. Late Alpine folds with northwest-trending axes are recognized in both the Rhodope metamorphic core complex (D_3 above) and in the Olympos window (D_4 of *Schermer* [1993]). In the Rhodope metamorphic core complex this folding is interpreted to fold the Nestos Thrust and bringing the Falakron Marble Series to the surface before the eruption of Oligocene volcanics and the emplacement of the Xanthi pluton. In Olympos, this deformation folds Eocene and older Alpine thrust faults [*Schermer*, 1993]. The effects of this folding are removed in the final reconstruction in Figure 21d. The depths of the Nestos and Olympos Thrusts are constrained by estimates of metamorphic pressures from their footwalls (4 to 7 kbar along the Nestos Thrust [*Kilias and Mountrakis*, 1990] and 2.5 to 3.0 kbar (or more) on the Olympos Thrust [*Schermer*, 1989; *Doutsos et al.*, 1993]).

Implications of the paleogeographic reconstruction of the Strymon Valley detachment fault

The most startling implication of the reconstruction is that not only are the Vertiskos and Kerdilion Gneisses restored on top of Falakron Marble Series, but the eastern units of the Vardar Zone are as well. This implies that the Vardar Zone, at least in Greece, is a nappe structure that must root east of the Falakron Marble Series. This conclusion is supported by geophysical evidence that ophiolites exposed in the eastern Vardar Zone are shallow allochthonous tectonic units overlying continental basement [*Kiriakidis and Brooks*, 1989; *Kiriakidis*, 1989].

Faced with the recognition that the Serbo-Macedonian Gneisses and at least the eastern Circum-Rhodope Belt are allochthonous units carried in the hanging wall of the Strymon Valley detachment and the Nestos Thrust, the critical question for tectonic reconstructions is: what forms the western boundary of the thrust plate over the Falakron Marble Series? From the reconstructions developed here, the most obvious lithologic correlation to the Falakron Marble Series are the Olympos platform carbonates as proposed

by *Dinter* [1994]. In his correlation he argued that sub-horizontal northeast-trending stretching lineations in both the Falakron Marble Series and the Olympos unit were created by top-to-the-southwest motion along a single Eocene thrust structure, effectively equating the Nestos Thrust to the Olympos Thrust.

While the reconstruction developed here strongly supports the correlation between the Falakron Marble Series and the Olympos carbonates, minor modification of the simple thrust fault geometry must be incorporated to explain structural relations in the footwall of the Olympos Thrust. Because the Olympos Thrust is observed to ramp up-section to the southwest through the Olympos carbonate platform [*Schermer*, 1993], the Nestos and Olympos Thrusts can not form single thrust structure overriding a Mesozoic carbonate platform unless that structure cuts both up-section and down-section in the direction of transport (Figure 22a). An alternative interpretation is that the Falakron Marble Series forms a crustal-scale duplex structure caught between the Olympos and Nestos Thrusts (Figure 22b). This model satisfactorily explains the apparent thrust ramp and the sub-parallel transport directions in both footwalls. In this scenario, thrust faulting propagates towards the Apulian plate, forming a series of in-sequence thrust faults. It is possible that other tectonostratigraphic units in the Circum-Rhodope Belt and the Vardar Zone are other fragments of the Apulian plate or Vardar ocean scraped off during the collisional process.

The correlation of the Falakron Marble Series and the Olympos carbonate platform implies the Rhodope metamorphic core complex forms a window into the leading edge of the subducted Apulian plate. The Serbo-Macedonian and West Thracian Gneisses and the Circum-Rhodope Belt form the margin of the European plate that has been thrust over the Apulian plate during the Eocene. The Vardar Ocean is still considered to be a strand of the Neo-Tethyan ocean which lay between the Apulian and European plates, but the ophiolites now exposed in Vardar Zone in Greece have been subsequently obducted onto the Apulian continental margin. In this interpretation, the units of the Circum-Rhodope Belt and Vardar Zone were successively accreted to the southern margin of the Rhodope continental

fragment during the Late Mesozoic. In the final stages of the convergence between Apulia and Europe, the assembled Serbo-Macedonian and West Thracian Gneisses, Circum-Rhodope Belt, and Vardar ophiolites were thrust together onto the Apulian continental margin, leading to the paleogeography shown in Figure 21d. Because the Nestos Thrust is interpreted to be younger than thrust faults in the Circum-Rhodope Belt and the Vardar Zone and ophiolites are not exposed in its hanging wall east of the Rhodope metamorphic core complex, the West Thracian and Serbo-Macedonian Gneisses must override the suture between the Apulian and European plates (Figure 22b). The extent of Apulian subduction below the Vardar ophiolites north of Mt. Olympos is uncertain, but it is likely to decrease. Where it dies out, the ophiolites in the Vardar Zone would then, in fact, represent the suture between the Apulian and European plates.

The apparent along-strike differential displacement on the Strymon Valley detachment fault explains the disruption of the northwest-trending tectonostratigraphic facies belts around the Rhodope metamorphic province and can account for some of the regional paleomagnetic rotations observed within the north Aegean region (e.g., *Kissel and Laj* [1988]). The restoration of the differential displacement on the Strymon Valley detachment fault realigns tectonostratigraphic facies belts around the Rhodope metamorphic province, correlating ophiolites of the Vardar Zone to those observed on the island of Samothraki and matching the eastern and western parts of the Circum-Rhodope Belt (Figure 23). Taking this restoration even further, it is possible that the ophiolites in the Vardar Zone are matched to those in Turkey, in particular those in the Intra-Pontide suture. While this correlation has been suggested before (e.g., *Kronberg* [1969]; *Sengor et al* [1984]), the restoration of motion on the Strymon Valley detachment fault realigns tectonostratigraphic facies belts, adding considerable support to the correlation.

Paleomagnetic studies on Tertiary intrusive and extrusive rocks in Serbo-Macedonia and the Rhodope metamorphic province indicate the Eocene Sithonia Batholith (Figure 2) has been rotated approximately 30° clockwise with respect to the relatively stable "Rhodope

block" [*Kissel et al.*, 1986; *Kondopoulou and Westphal*, 1986; *Kissel and Laj*, 1988; *Kondopoulou and Pavlides*, 1990]. Almost all of this rotation is accounted for by restoring the differential displacement on the Strymon Valley detachment fault, rotating Serbo-Macedonia and the Sithonia Batholith approximately 30° counter-clockwise about a poorly constrained pole in southwest Bulgaria (Figure 23). Although it is possible that the rotation of the Sithonia Batholith occurs on earlier structures before detachment faulting or on small-scale block rotations after detachment faulting, it is remarkable how well its rotation can be explained by differential displacement on the Strymon Valley detachment fault.

CONCLUSIONS

The reinterpretation of the Strymon Valley detachment fault as an extensional structure has important ramifications for the tectonic evolution of the north Aegean region. Restoring the extension on this fault suggests a probable correlation between the Falakron Marble Series and the Olympos carbonate platform, explains the disruption of Alpine tectonostratigraphic facies belts in the north Aegean, and possibly accounts for some of the regional-scale crustal paleomagnetic rotations recognized throughout the Aegean Sea and Hellenic Arc. The Strymon Valley detachment fault, and perhaps other unrecognized detachment faults, may account for a significant amount of the overall crustal extension in the Aegean Sea. Finally, the recognition of the Strymon Valley detachment fault and the acknowledgement that regional-scale, sub-horizonal structures effectively shuffle the tectonic units of the northern Aegean region during Tertiary extension requires re-evaluation of tectonic boundaries throughout the north Aegean. Interpretations of tectonic boundaries throughout the region are potentially suspect; unrecognized or misinterpreted extensional structures may contribute significantly to the total magnitude of extension in the north Aegean. Future work in the north Aegean region needs to concentrate on firmly establishing the nature of tectonic boundaries, recognizing potential correlations between tectonostratigraphic units, quantifying the magnitude of displacement on different

structures, and improving the chronologic framework for tectonic events. The result will be the emergence of a better understanding of the tectonic evolution of the Internal Hellenides.

REFERENCES

Armour-Brown, A., H. de Bruijn, C. Maniati, G. Siatos, and P. Neisen, 1977, The geology of the Neogene sediments north of Serrai and the use of rodent faunas for biostratigraphic control, *in* G. Kallergis, ed., Colloquium on the Geology of the Aegean Region, VI, Proceedings, Athens, Institute of Geological and Mining Research, v. 2, p. 615-622.

Aubouin, J., 1959, Contributions à l'étude géologiques de la Gréce septentrionals: les confins de l'Epire et de la Thessalie, *Annales Géologiques des Pays Helléniques*, v. 10, p. 1-525.

Bernoulli, D., and H. Laubscher, 1972, The palinspastic problem of the Hellenides, *Ecologae Geolicae Helveticae*, v. 65, p. 107-118.

Berthé, D., P. Choukroune, and P. Jegouzo, 1979, Orthogneiss, mylonite, and non coaxial deformation of granites: The example of the South Armorican Shear Zone, *Journal of Structural Geology*, v. 1, p. 31-42.

Buck, R., 1988, Flexural rotation of normal faults, *Tectonics*, v. 7, p. 959-973.

de Boer, H.U., 1970, Geologisch-petrographische Untersuchungen im Rhodope-Massiv Griechisch-Ostmazedoniens: Der Menikion-Bergzug nordöstlich Serrai, *in* F. Birk, H.U. de Boer, P. Kronberg, W. Meyer, A. Pilger, and P. Schenck, eds. Zur Geologie des Rhodopen-Kristallins im Gebiet zwischen Strimon und Neston (Griechisch-Ostmazedonien), *Beihefte zum Geologischen Jahrbuch*, Heft 88, Hannover, p. 43-79.

Del Moro, A., K. Kyriakopoulos, A. Pezzino, P. Atzori, and A. Lo Giudice, 1990, The metamorphic complex associated to the Kavala plutonites: An Rb-Sr geochronological, petrological and structural study, *Geologica Rhodopica*, v. 2, p. 143-152.

De Wet, A.P., J.A. Miller, M.J. Bickle, and H.J. Chapman, 1989, Geology and geochronology of the Arnea, Sithonia, and Ouranopolis intrusions, Chalkidiki Peninsula, northern Greece, *Tectonophysics*, v. 161, p. 65-79.

Dinter, D.A., and L. Royden, 1993, Late Cenozoic extension in northeastern Greece: Strymon Valley detachment and Rhodope metamorphic core complex, *Geology*, v. 21, p. 45-48.

Dinter, D.A., 1994, Tectonic evolution of the Rhodope metamorphic core complex, Northeastern Greece [Ph.D. Thesis], Massachusetts Institute of Technology, Cambridge, MA, 320 pp.

Dinter, D.A., A.M. Macfarlane, W. Hames, C. Isachsen, and L. Royden, 1995, U-Pb and $^{40}Ar/^{39}Ar$ geochronology of the Symvolon granodiorite: Implications for the thermal and structural evolution of the Rhodope metamorphic core complex, northeastern Greece, submitted to *Tectonics*.

Doutsos, T., G. Pe-Piper, K. Boronkay, and I. Koukouvelas, 1993, Kinematics of the central Hellenides, *Tectonics*, v. 12, p. 936-953.

Dürr, St., R. Altherr, J. Keller, M. Okrusch, and E. Seidel, 1978, The median Aegean crystalline belt: Stratigraphy, structure, metamorphism, magmatism, *in* Alps, Apennines, and Hellenides-geodynamic investigation along geotraverses by an international group of geoscientists, Inter-union Commission on Geodynamics, Scientific Report 38, H. Cloos, D. Roeder, and K. Schmidt eds., Schweizerbart, Stuttgart, p. 455-477.

Erki, I., N. Kolios, and L. Stegena, 1984, Heat flow density determination in the Strymon Basin, NE Greece, *Journal of Geophysics*, v. 54, p. 106-109.

Frei, R., 1992, Isotope (Pb, Rb-Sr, S, O, C, U-Pb) geochemical investigations on Tertiary intrusives and related mineralizations in the Serbomacedonian Pb-Zn, Sb+Cu-Mo metallogenetic province in northern Greece [Ph.D. Thesis], ETH, Zurich, Switzerland, 231 pp.

Freyberg, B., 1952, Geologie und Lagerstattenkunde des Braunkohlenreviers von Serrae (Makedonien), The Geology of Greece, Subsurface Research Department Ministry of Coordination, Athens, p. 87-154.

Gramann, von F., and F. Kockel, 1969, Das Neogen im Strimonbecken (Griechisch-Ostmazedonien, *Geologisches Jahrbuch.*, v. 87, p. 445-484.

Hammarstrom, J.M., and E. Zen, 1986, Aluminum in hornblende: An empirical igneous geobarometer, *American Mineralogist*, v. 71, p. 1297-1313.

Hanmer, S., and C. Passchier, 1991, Shear-sense indicators: A review, Geological Survey of Canada, Paper 90-17, 72 p.

Hansen, E., 1971, Strain Facies, Berlin, Springer-Verlag, 207 p.

Harre, W., F. Kockel, H. Kreuzer, H. Lenz, P. Müller, and H.W. Walther, 1968, Über Rejuvenationen im Serbo-Mazedonischen Massiv (Deutung radiometrischer Alterbestimmungen), Proceedings of the 23rd International Geological Congress, Prague, p. 223-236.

Haq, B.U., J. Hardenbol, and P.R. Vail, 1988, Mesozoic and Cenozoic chronostratigraphy and cycles of sea-level change, *in* Sea-Level Changes – an Integrated Approach, Society of Economic Paleontologists and Mineralogists Special Publication No. 42, C.K. Wilgus, B.S. Hastings, C.G.St.C. Kendall, H.W. Posamentier, C.A. Ross, and J.C. van Wagoner, eds., p. 71-109

Hollister, L.S., G.C. Grissom, E.K. Peters, H.H. Stowell, and V.B. Sisson, 1987, Confirmation of the empirical correlation of Al in hornblende with pressure of solidification of calc-alkaline plutons, *American Mineralogist*, v. 72, p. 231-239.

Jackson, J.A., G. King, and C. Vita-Finzi, 1982, The neotectonics of the Aegean: An alternative view, *Earth and Planetary Science Letters*, v. 61, p. 303-318.

John, B.E., 1987, Geometry and evolution of a mid-crustal extensional fault system: Chemehuevi Mountains, southeastern California, *in* Continental Extensional Tectonics, M.P. Coward, J.F. Dewey, and P.L. Hancock eds., Geological Society Special Publication 28, p. 313-335.

Jones, C.E., J. Tarney, J.H. Baker, and G. Gerouki, 1992, Tertiary granitoids of Rhodope, northern Greece: Magmatism related to extensional collapse of the Hellenic Orogen, *Tectonophysics*, v. 210, p. 295-314.

Karistineos, N.K., and E. Georgiades-Dikeoulia, 1986, The marine transgression in the Serres Basin, *Annales Géologiques des Pays Helléniques*, v. 33, p. 221-232.

Karistineos, N., and C. Ioakim, 1989, Palaeoenvironmental and palaeoclimatic evolution of the Serres Basin (N. Greece) during the Miocene, *Palaeogeography, Palaeoclimatology, Palaeoecology*, v. 70, p. 275-285.

Kastens, K.A., L.E. Gilbert, and K.S. Hurst, 1993, GPS evidence for arc-parallel extension along the Hellenic arc, southern Aegean Sea, Greece, *Geological Society of America, Abstracts*, v. 25, p. 242.

Kilias, A., and D. Mountrakis, 1990, Kinematics of the crystalline sequences in the western Rhodope massif, *Geologica Rhodopica*, v. 2, p. 100-116.

Kiriakidis, L., and M. Brooks, 1989, A geophysical study of the Vardar Zone ophiolite belt in Chalkidhiki, northern Greece, *Journal of the Geological Society of London*, v. 146, p. 859-865.

Kiriakidis, L.G., 1989, The Vardar ophiolite: A continuous belt under the Axios basin sediments, *Geophysical Journal International*, v. 98, p. 203-212.

Kissel C., D. Kondopoulou, C. Laj, and P. Papadopoulos, 1986, New paleomagnetic data from Oligocene formations of northern Aegea, *Geophysical Research Letters*, v. 13, p. 1039-1042.

Kissel, C., and C. Laj, 1988, The Tertiary geodynamical evolution of the Aegean arc: A paleomagnetic reconstruction, *Tectonophysics*, v. 146, p. 183-201.

Kockel, F., and H.W. Walther, 1965, Die Strimonlinie als Grenze zwischen Serbo-Mazedonischem und Ril-Rhodope-Massiv in Ost-Mazedonien, *Geologisches Jahrbuch*, v. 83, p. 575-602.

Kockel, F., H. Mollat, and H.W. Walther, 1971, Geologie des Serbo-Mazedonischen Massivs und seines mesozoischen Rahmens (Nordgriechenland), *Geologisches Jarhbuch*, v. 89, p. 529-551.

Kockel, F., 1986, Die Vardar- (Axios-) Zone, *in* Geologie von Griechenland, V. Jacobshagen ed., Gebrüder Borntraeger, Berlin, p. 150-168.

Kojumdgieva, E., I. Nikolov, P. Nedjalkov, and A. Busev, 1982, Stratigraphy of the Neogene in Sandanski graben, *Geologica Balcanica*, v. 12, p. 69-81.

Kokkinakis, A., 1980, Altersbeziehungen zwischen Metamorphosen, mechanischen, Deformationen und Intrusionen am Sudrand des Rhodope-Massivs (Makedonien, Griechenland), *Geologische Rundschau*, v. 69, p. 726-744.

Kolocotroni, C., and J.E. Dixon, 1991, The origin and emplacement of the Vrondou granite, Serres, N.E. Greece, *Bulletin of the Geological Society of Greece*, v. 25, p. 469-483.

Kondopoulou, D., and M. Westphal, 1986, Paleomagnetism of Tertiary intrusives from Chalkidiki (N. Greece), *Journal of Geophysics*, v. 59, p. 62-66.

Kondopolou, D., and S. Pavlides, 1990, Tertiary geodynamic pattern of Rhodope and surrounding areas based on paleomagnetic and neotectonic data, *Geologica Rhodopica*, v. 2, p. 25-36.

Kotopouli, C.N., and G. Pe-Piper, 1989, Geochemical characteristics of felsic intrusive rocks within the Hellenic Rhodope: A comparative study and petrogenic implications, *Neues Jarhbuch für Mineralogie, Abhandlungen.*, v. 161, p. 141-169.

Koukouvelas, I., and T. Doutsos, 1990, Tectonic stages along a traverse cross cutting the Rhodopian zone (Greece), *Geologische Rundschau*, v. 79, p. 753-776.

Koukouvelas, I., and G. Pe-Piper, 1991, The Oligocene Xanthi pluton, northern Greece: A granodiorite emplaced during regional extension, *Journal of the Geological Society, London*, v. 148, p. 749-758.

Kouris, Ch., 1988, Geological Map of Greece, Prosotsani sheet (1:50,000), Institute of Geology and Mineral Exploration, Athens, Greece.

Kozhoukharov, D., E. Kozhoukharova, and D. Papanikolaou, 1988, Precambrian in the Rhodope massif, *in* Precambrian in Younger Fold Belts, V. Zoubek ed., John Wiley and Sons, New York, p 723-778.

Kronberg, P., 1966, Petrographie und Tektonik im Rhodopen-Kristallin des Tsal Dag, Simvolon und Ost-Pangäon (Griechisch-Makedonien), *Neues Jahrbuch für Geologie und Paläontologie, Monatshefte*, v.7, p. 410-424.

Kronberg, P., 1969, Gliederung, Petrographie und Tektogenese des Rhodopen-Kristallins im Tsal-Dag, Simvolon, und Ost-Pangaon (Griechisch-Makedonien), *Geotektonische Forschungen*, v. 31, p. 1-49.

Kronberg, P., W. Meyer, and A. Pilger, 1970, Geologie der Rila-Rhodope-Masse zwischen Strimon und Nestos (Nordgriechenland), *Beihefte zum Geologischen Jahrbuch*, v. 88, p. 133-180.

Kronberg, P., and M. Raith, 1977, Tectonics and metamorphism of the Rhodope crystalline complex in Eastern Greek Macedonia and parts of West Thrace, *Neues Jahrbuch für Geologie and Paläontologie, Monatshefte*, v. 11, p. 697-704.

Le Pichon X., and J. Angelier, 1979, The Hellenic Arc and Trench system: A key to the neotectonic evolution of the eastern Mediterranean area, *Tectonophysics*, v. 60, p. 1-42.

Liati, A., 1986, Regional metamorphism and overprinting contact metamorphism of the Rhodope zone, near Xanthi (N. Greece). Petrology, geochemistry, geochronology [Ph.D. Thesis], Techn. Univ. Braunschweig, Braunschweig, Germany, 186 pp.

Lister, G.S., G. Banga, and A. Feenstra, 1984, Metamorphic core complexes of Cordilleran type in the Cyclades, Aegean Sea, Greece, *Geology*, v. 12, p. 221-225.

Lister, G.S., and A.W. Snoke, 1984, S-C mylonites, *Journal of Structural Geology*, v. 6, p. 617-638.

Mancktelow, N.S., and T.L. Pavlis, 1994, Fold-fault relationships in low-angle detachment systems, *Tectonics*, v. 13, p. 668-685.

Manning, A.H., and J.M. Bartley, 1994, Postmylonitic deformation in the Raft River metamorphic core complex, northwestern Utah: Evidence of a rolling hinge, *Tectonics*, v. 13, p. 596-612.

Marakis, G.I., 1969, Geochronologic studies of some granites from Macedonia, *Annales Géologiques des Pays Helléniques*, v. 21, p. 121-152.

Martin, L., 1987, Structure et evolution recente de la mer Egee: Apports d'une etude par sismique reflexion [Ph.D. Thesis], Universite Pierre et Marie Curie, Paris, France, 324 pp.

Meyer, W., A. Pilger, F. Birk, and H. Jordan, 1963, Zur Geologie des Gebietes zwischen Strymon und Nestos (Rhodopen-Massiv) in Griechisch-Makedonien, *Neues Jahrbuch für Geologie und Paläontologie, Abhandlungen*, v. 118, p. 272-280.

Meyer, W., 1968, Zur Alterstellung des plutonismus im Südteil der Rila-Rhodope-Masse (Nordgriechenland), *Geologica et Paleontologica*, v. 2, p. 86-96.

Meyer, W., 1969, Die Faltenachsen im Rhodopen-Kristallin ostlich des Strimon (Nordost-Griechenland), *Geotektonische Forschungen*, v. 31, p. 86-96.

Oral, M.B., 1994, Global positioning system (GPS) measurements in Turkey (1988-1992): Kinematics of the African-Arabian-Eurasian plate collision zone [Ph.D. Thesis], Massachusetts Institute of Technology, Cambridge, MA, 344 pp.

Papanikolaou, D., and A. Panagopoulos, 1981, On the structural style of Southern Rhodope, Greece, *Geologica Balcanica*, v. 11 p. 13-22.

Psilvikos, A., and N. Karistineos, 1986, A depositional sedimentary model for the Neogene uraniferous lignites of the Serres graben Greece, *Palaeogeography, Palaeoclimatology, Palaeoecology*, v. 56, p. 1-16.

Schermer, E.R., 1989, Tectonic evolution of the Mt. Olympos region, Greece [Ph.D. Thesis], Massachusetts Institute of Technology, Cambridge, MA, 272 pp.

Schermer, E.R., 1993, Geometry and kinematics of continental basement deformation during the Alpine orogeny, Mt. Olympos region, Greece, *Journal of Structural Geology*, v. 15, p. 571-591.

Schmidt, M.W., 1992, Amphibole composition in tonalite as a function of pressure: An experimental calibration of the Al-in-hornblende barometer, *Contributions to Mineralogy and Petrology*, v. 110, p. 304-310.

Scordilis, E., N. Theodoulidis, P. Hatzidimitriou, D. Panagiotopolous, and D. Hatzfeld, 1989, Microearthquake study and near-field seismic wave attenuation in the Mygdonian graben, north Greece, *Geologica Rhodopica*, v. 1, p. 84-92.

Sengor, et al., 1984, Tectonics of the Mediterranean Cimmerides: Nature and evolution of the western termination of Paleo-Tethys, *in* The Geological Evolution of the Eastern Mediterranean, J.E. Dixon and A.H.F. Robertson, eds., Geological Society of London Special Publication Number 17, Blackwell Scientific Publications, Oxford, p. 77-112.

Simpson, C., and D. De Paor, 1991, Deformation and kinematics of high strain zones, *Geological Society of America Short Course Notes*.

Sokoutis, D., J.P. Brun, J. van den Driessche, and S. Pavlides, 1993, A major Oligo-Miocene detachment in southern Rhodope controlling north Aegean extension, *Journal of the Geological Society, London*, v. 150, p. 243-246.

Soldatos, T., and G. Christofides, 1986, Rb-Sr geochronology and origin of the Elatia pluton, central Rhodope, north Greece, *Geologica Balcanica*, v. 16, p. 15-23.

Spear, F.S., 1993, Metamorphic phase equilibria and pressure-temperature-time paths, Mineralogical Society of America Monograph, 799 p.

Theodorikas, S., 1983, The mineralogy, petrology and geochemistry of the Serres-Drama granitic complex, Northern Greece, Aristotle University of Thessaloniki, Faculty of Science, School of Geology, Scientific Annals, Thessaloniki, v. 22, n. 28, 415 p.

Wawrzenitz, N., A. Baumann, and G. Nollau, 1994, Miocene uplift of mid-crustal rocks in the Rhodope metamorphic core complex, caused by late Alpine extension of

previously thickened crust (Thassos Island, Pangaeon Complex, northern Greece), 7th Congress of the Geological Society of Greece, Thessaloniki, May 25-27, 1994, abstracts, p. 74-75.

Yin, A, 1991, Mechanism for the formation of domal and basinal detachment faults: A three dimensional analysis, *Journal of Geophysical Research*, v. 96, p. 14,577-14,594.

FIGURE CAPTIONS

Figure 1. Regional map of tectonic elements in the eastern Mediterranean. RCF – Rhodope continental fragment; RMP – Rhodope metamorphic province; RMCC – Rhodope metamorphic core complex; NAT – North Aegean Trough. From *Dinter* [1994].

Figure 2. Regional map of north Aegean region. From *Dinter* [1994].

Figure 3. Generalized tectonostratigraphy of the north Aegean region.

Figure 4. Simplified geologic map of the Rhodope metamorphic core complex. Sediment thicknesses in the Aegean Sea are contoured in seconds of two-way travel time (From *Martin* [1987]). After *Dinter* [1994].

Figure 5. Simplified geologic map of northern Rhodope metamorphic core complex. Locations of bore holes in the Strymon Valley shown south of Dafnoudi.

Figure 6. D_{1-2} structures developed in the Rhodope metamorphic core complex. (a) Isoclinal recumbent folds on the top of Menoikion Oros. Cows in foreground provide scale. (b) F_{1-2} isoclinal folds in marble with superimposed detachment-related brittle deformation. (c) Corrugations developed on F_2 fold between Dafnoudi Schist and Menoikion Marble. (d) Photomicrograph of F_2 fold in pelitic schist interfoliated within Menoikion Marble. F_2 folds S_1 schistosity defined by muscovite cleavage and elongate zoisite crystals.

Figure 7. Lower hemisphere equal area stereonet plot of L_1 lineations and F_{1-2} fold axes in the northern Rhodope metamorphic core complex. (a) Solid circles – lineations and fold axes interpreted as D_{1-2} structures (n = 242). (b) Contour plot of L_1 lineations and F_{1-2} fold axes; contour interval = 5%/1% area contours.

Figure 8. Lower hemisphere equal area stereonet plot of S_1 foliation surfaces and minor F_2 fold axes on large F_2 fold southeast of Menoikion Oros. Open squares – poles to S_1 foliations (n = 15); small solid circles – F_2 fold axes (n = 10); solid square – β axis for S_1 foliations = 54°/3°; large solid circle – mean F_2 fold axis = 50°/5°.

Figure 9. F_3 fold developed in Oreini Gneiss. Width of view ~ 3 m.

Figure 10. Lower hemisphere equal area stereonet plot of fabrics attributed to D_3 deformation. (a) F_3 fold axes. (b) S_{1-2} foliations and L_1 lineations folded by D_3 folding. Solid circles – folded L_1 lineation (n = 61); open squares – poles to S_1 surfaces (n = 151); large solid circle – best fit F_3 fold axis calculated from folded L_1 lineations = 316°/5°.

Figure 11. Lower hemisphere equal area stereonet plot of F_4 folds. (a) Solid circles – F_4 fold axes (n = 7); open squares – poles to S_1 foliations on Menoikion Oros (n = 198); solid square – β axis for S_1 foliations defining average F_4 fold axis = 233°/3°. (b) Contour plot of S_1 foliations on Menoikion Oros showing two concentrations of foliation poles; contour interval = 3%/1% area contours.

Figure 12. Intrusive relationships associated with the Vrondou pluton. (a) Granitic dike intruding Menoikion Marble east of Elaion. (b) Amphibolite xenoliths in mafic granite. (c) Granite dikes cut by and cutting small-scale brittle shear zone.

Figure 13. Structures associated with the Strymon Valley detachment fault. (a) S-C granite mylonite with dextral sense of shear. (b) Thin section of granite mylonite showing dextral sense of shear. (c) Irregular contact between sheared marble and mylonitic granite east of Elaion. (d) Detachment fault near Elaion with large block of footwall marble incorporated into the hanging wall. (e) Outstanding exposure of detachment fault on western side of Vrondou pluton. (f) Gouge - rock flour zone on the western side of the Vrondou pluton. Dextral sense of shear indicated by overturned folds in gouge zone. (g) Highly brecciated footwall zone on the western side of the Vrondou pluton. (h) Garnet δ-type porphyroclast in marble showing dextral shear sense.

Figure 14. Lower hemisphere equal area stereonet plot of ductile mylonitic foliations and lineations in the margins of the Vrondou pluton and Elaion stock. (a) Solid circles – poles to foliation planes (n = 209); open squares – ductile stretching lineations (n =

135); large open circle (hidden) – corrugation axis for foliation planes = 231°/8°; large open square – mean stretching lineation = 231°/8°. (b) Contour plot of poles to mylonitic foliations and stretching lineations; contour interval = 5%/1% area contours.

Figure 15. Lower hemisphere equal area stereonet plot of brittle structures associated with the Strymon Valley detachment fault. (a) Open squares – poles to the detachment fault (n = 180); solid circles – slickenslides and mullions (n = 32); solid square – corrugation axis defined by all fault planes = 241°/12°; large solid circle – mean slickenslide and mullion azimuth = 225°/17°. (b) Contour plot of poles to detachment fault planes and slickenslides and mullions; contour interval = 5%/1% area contours.

Figure 16. Lower hemisphere equal area stereonet plot of poles to the detachment fault planes along it trace. Solid circles – poles to fault planes east of Serres (n = 49); open squares – poles to fault planes in Elaion area (n = 61); stars – poles to fault planes on the southern margin of Vrondou (n = 19); crosses – poles to fault planes west and north of Vrondou (n = 51).

Figure 17. Lower hemisphere equal area stereonet plot of poles to sedimentary bedding in the Neogene sediments in the supradetachment Serres Basin. (a) Solid circles – poles to bedding planes. Average bedding plane = 285°/14°. (b) Contour plot of poles to bedding planes; contour interval = 5%/1% area contours.

Figure 18. Lower hemisphere equal area stereonet plot of poles to sedimentary bedding in klippen directly above the detachment fault. (a) Poles to bedding in the Menoikio breccia-conglomerate (n = 17). Solid circles – poles to bedding; crosses – poles to bedding affected by D_7 normal faulting along the western margin of the Drama Basin. Average bedding plane = 319°/35°. (b) Poles to bedding in the St. George Formation in klippe on eastern margin of Serres Basin (n = 8). Average bedding plane = 305°/25°.

Figure 19. Lower hemisphere equal area stereonet plot of structures attributed to D_{6f} deformation. (a) F_{6f} fold axes. (b) $S_{1\text{-}2}$ foliations and $L_{1\text{-}2}$ lineations folded by D_{6f} folding. Solid circles – folded L_1 lineation (n = 82); open squares – poles to $S_{1\text{-}2}$

surface (n = 44); large open circle – best fit F_{6f} fold axis calculated from folded L_1 lineations = 137°/14°.

Figure 20. Line drawing of northeast-southwest seismic section of Gulf of Orphanou (after Martin, 1987). Fine lines – prominent reflectors; thick lines – normal faults; dark dashed line – base of Messinian sediments. Location of seismic line shown on Figure 4.

Figure 21. Paleogeographic reconstructions of the northern Aegean region. No vertical exaggeration. A – Almopias unit; Amb – Ambelakia unit; AP – Arnea pluton; AVC – Aspro-Vrissi-Chortiatis unit; F – Flambouron unit; G – Guevguelije unit; MC – Melissochori-Cholomon unit; O – ophiolites; O-O – Olympos-Ossa carbonate platform; P – Peonia unit; Pa – Païkon unit; SE – Skaloti-Echinos granite; Tv – Tertiary volcanics. See text and Figure 3 for additional details of individual tectonostratigraphic units. No vertical exaggeration. (a) Present-day northeast-southwest cross section of the north Aegean region. (b) Pliocene (~5 Ma) reconstruction removing late Tertiary extension. (c) Oligo-Miocene reconstruction, after D_3 but before intrusion of Oligo-Miocene plutons. Note westward dip on Nestos Thrust. (d) Oligocene reconstruction after the emplacement of the Nestos and Olympos thrusts.

Figure 22. Schematic cartoon showing alternate correlations between the Olympos and Nestos Thrusts with the requirement that the Olympos Thrust ramps up-section through the Olympos platform carbonates. (a) Single Olympos-Nestos Thrust cuts alternatively up and down section through the Olympos platform - Falakron Marble Series; (b) Falakron Marble Series is present in a large duplex. Nestos Thrust forms roof thrust and Olympos Thrust forms sole thrust. Both thrust faults may merge east of the Falakron Marble Series. Apulia – Subducted Apulian plate margin shown to indicate location of Apulian-Vardar suture below Olympos-Nestos Thrusts; CRB – Circum-Rhodope Belt; O-NT – Olympos-Nestos Thrust; SM–WTG – Serbo-Macedonian and West Thracian Gneisses; VZ – Vardar Zone;

Figure 23. Oligocene reconstruction of extension on the Strymon Valley detachment fault with ~30° of counter-clockwise rotation of Serbo-Macedonia and the Circum-Rhodope Belt. Note realignment of Circum-Rhodope Belt. Vardar Zone is realigned with ophiolites on Samothraki and the Intra-Pontide Suture. Black – ophiolites; dark lines – major tectonic boundaries; dashed light line – modern geographic boundaries; light gray – future location of Oligo-Miocene plutons intruded at depth into the incipient Rhodope metamorphic core complex. IS – Incipient Strymon Valley detachment fault; S – Samothraki; SB – Sithonia Batholith; SMG – Serbo-Macedonian Gneiss Complex; SP – Symvolon pluton; VP – Vrondou pluton; WTG – West Thracian Gneiss Complex; XP – Xanthi Pluton.

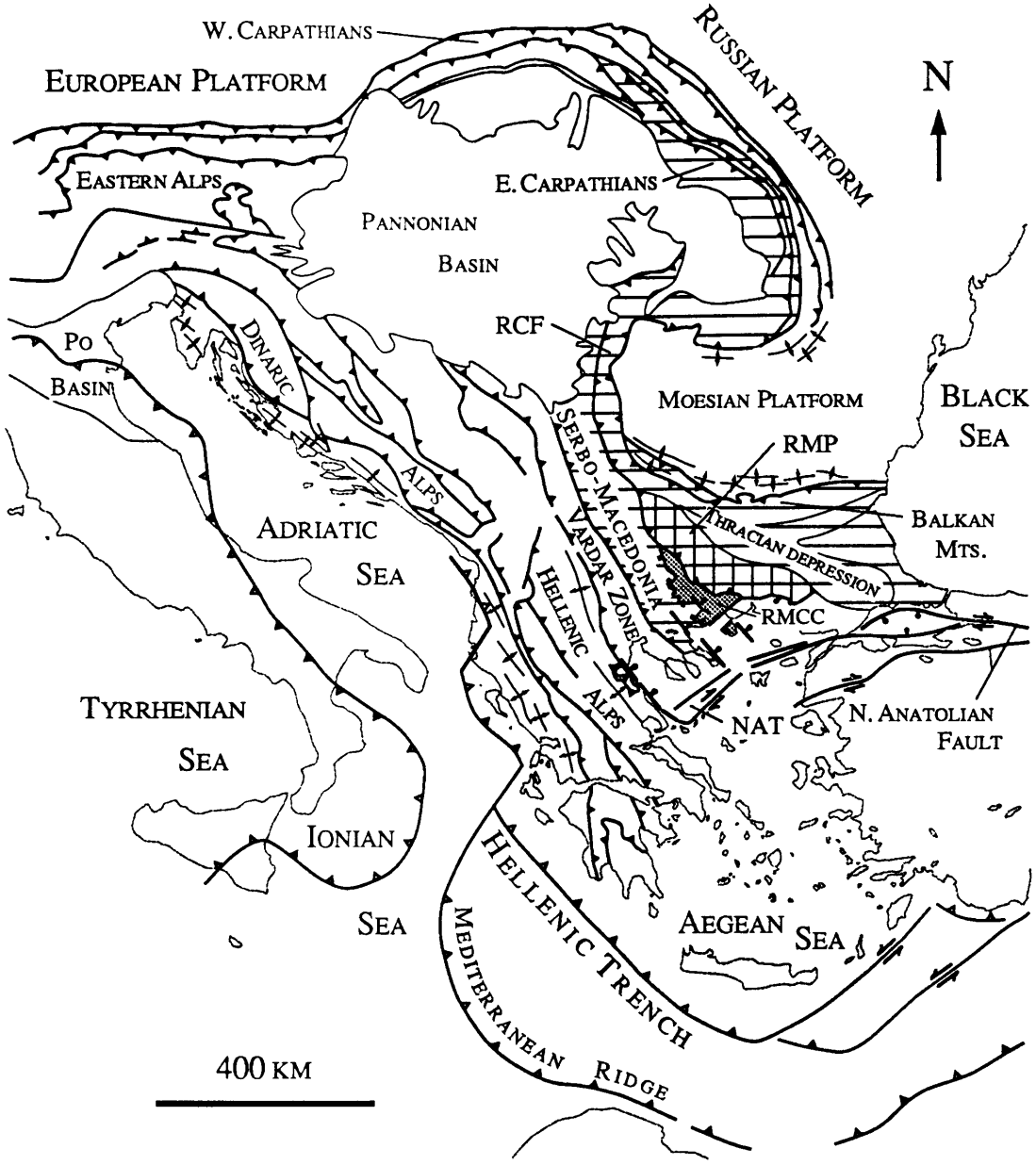
W. CARPATHIANS
EUROPEAN PLATFORM
RUSSIAN PLATFORM
N
EASTERN ALPS
E. CARPATHIANS
PANNONIAN
BASIN
RCF
PO
BASIN
DINARIC
ALPS
MOESIAN PLATFORM
BLACK
SEA
SERBO-MACEDONIA
VARDAR ZONE
RMP
BALKAN
MTS.
THRACIAN DEPRESSION
ADRIATIC
SEA
HELLENIC
ALPS
RMCC
TYRRHENIAN
SEA
NAT
N. ANATOLIAN
FAULT
IONIAN
SEA
HELLENIC TRENCH
AEGEAN SEA
MEDITERRANEAN RIDGE
400 KM

FIGURE 1

22°
23°
24°
25°
41°
40°
SERBO-
MACEDONIAN
WEST THRACIAN
GNEISS
COMPLEX
Jerakario
and Vathi
Stocks
Falakron
Nestos thrust
STRYMON BASIN
DRAMA BASIN
marble
series
RHODOPE
METAMORPHIC
CORE COMPLEX
Thasos
Strymon
Valley
detachment
Symvolon
shear zone
THASOS - SAMOTHRAKI BASIN
Samothraki
TROUGH
Ouranopolis
pluton
Figure 4
Stratoni stock
Jerissos
pluton
Sithonia
batholith
Lizadiko Ridge LANF
Olympos-Ossa unit
Kallipevki LANF
Mt. Olympos
Olympos thrust
VARDAR ZONE
PELAGONIAN ZONE
MESOHELLENIC TROUGH
AEGEAN
VARDAR-THERMAIKOS BASIN
NORTH
LARISA BASIN
TRIKALA BASIN
N
0
50 km
Late Pliocene - Quaternary sediments
Late Pliocene - Quaternary volcanics
Neogene sediments
Oligocene - Miocene volcanics
Tertiary intrusive rocks
Eocene - Oligocene sediments
Marble w/ schist, amphibolite intercalations
Gneiss, schist, amphibolite / migmatites
Ophiolites, ultrabasic rocks

Figure 2

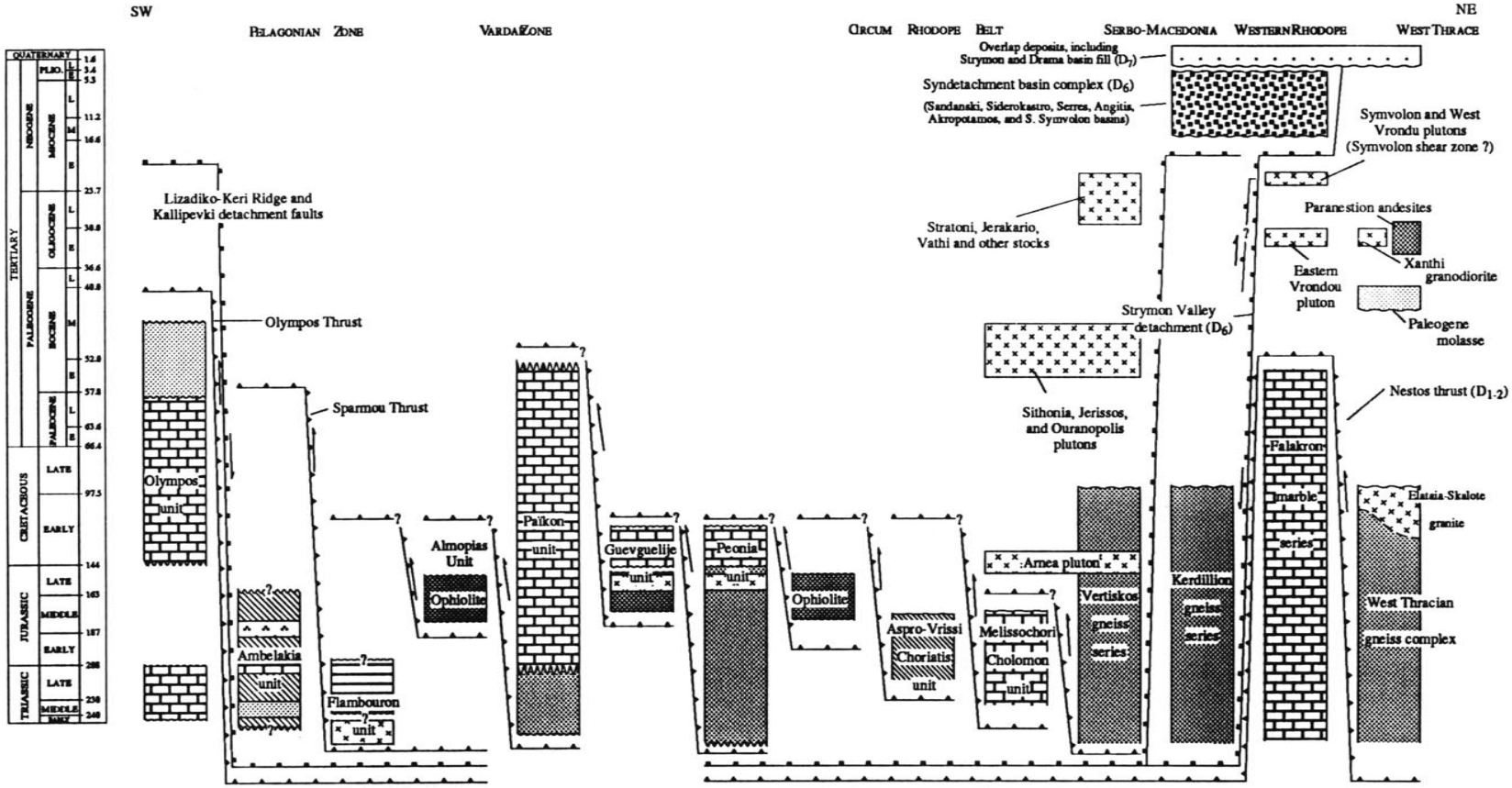
SW
NE
Pelagonian Zone
Vardar Zone
Circum Rhodope Belt
Serbo-Macedonia
Western Rhodope
West Thrace
QUATERNARY
TERTIARY
NEOGENE
PALEOGENE
PLIO.
MIOCENE
OLIGOCENE
EOCENE
PALEOCENE
CRETACEOUS
JURASSIC
TRIASSIC
LATE
EARLY
MIDDLE
Overlap deposits, including Strymon and Drama basin fill (D7)
Syndetachment basin complex (D6)
(Sandanski, Siderokastro, Serres, Angitis, Akropotamos, and S. Symvolon basins)
Symvolon and West Vrondu plutons
(Symvolon shear zone ?)
Lizadiko-Keri Ridge and Kallipevki detachment faults
Stratoni, Jerakario, Vathi and other stocks
Paranestion andesites
Xanthi granodiorite
Eastern Vrondou pluton
Paleogene molasse
Olympos Thrust
Strymon Valley detachment (D6)
Sparmou Thrust
Sithonia, Jerissos, and Ouranopolis plutons
Nestos thrust (D1-2)
Olympos unit
Almopias Unit
Ophiolite
Paikon unit
Guevguelije unit
Peonia unit
Ophiolite
Aspro-Vrissi Choriatis unit
Arnea pluton
Melissochori Cholomon unit
Vertiskos gneiss series
Kerdillion gneiss series
Palaikron marble series
Elatsia-Skalote granite
West Thracian gneiss complex
Ambelakia unit
Flambouron unit

Figure 3

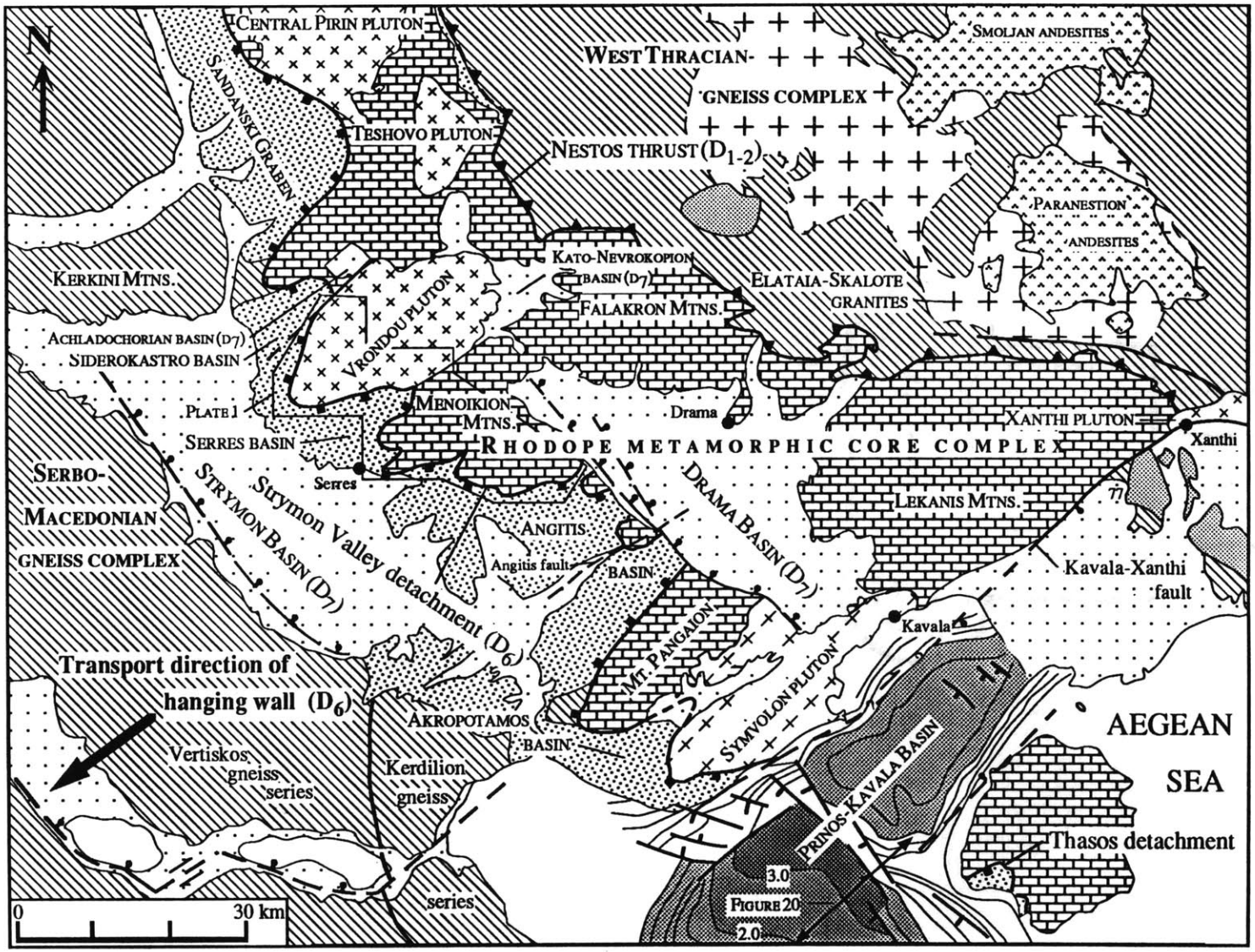
N
Central Pirin pluton
Sandanski graben
Teshovo pluton
West Thracian-
gneiss complex
Nestos thrust (D_{1-2})
Smoljan andesites
Paranestion
andesites
Kato-Nevrokopion
basin (D_7)
Falakron Mtns.
Elataia-Skalote
granites
Kerkini Mtns.
Vrondou pluton
Achladochorian basin (D_7)
Siderokastro basin
Plate 1
Menoikion
Mtns.
Drama
Xanthi pluton
Xanthi
Serres basin
Rhodope metamorphic core complex
Serbo-
Macedonian
gneiss complex
Strymon basin (D_7)
Strymon Valley detachment (D_6)
Serres
Drama basin (D_7)
Lekanis Mtns.
Angitis
Angitis fault
basin
Kavala-Xanthi
fault
Kavala
Mt. Pangaion
Symvolon pluton
Transport direction of
hanging wall (D_6)
Akropotamos
basin
Vertiskos
gneiss
series
Kerdilion
gneiss
series
Prinos-Kavala basin
AEGEAN
SEA
Thasos detachment
3.0
Figure 20
2.0
0
30 km

Figure 4

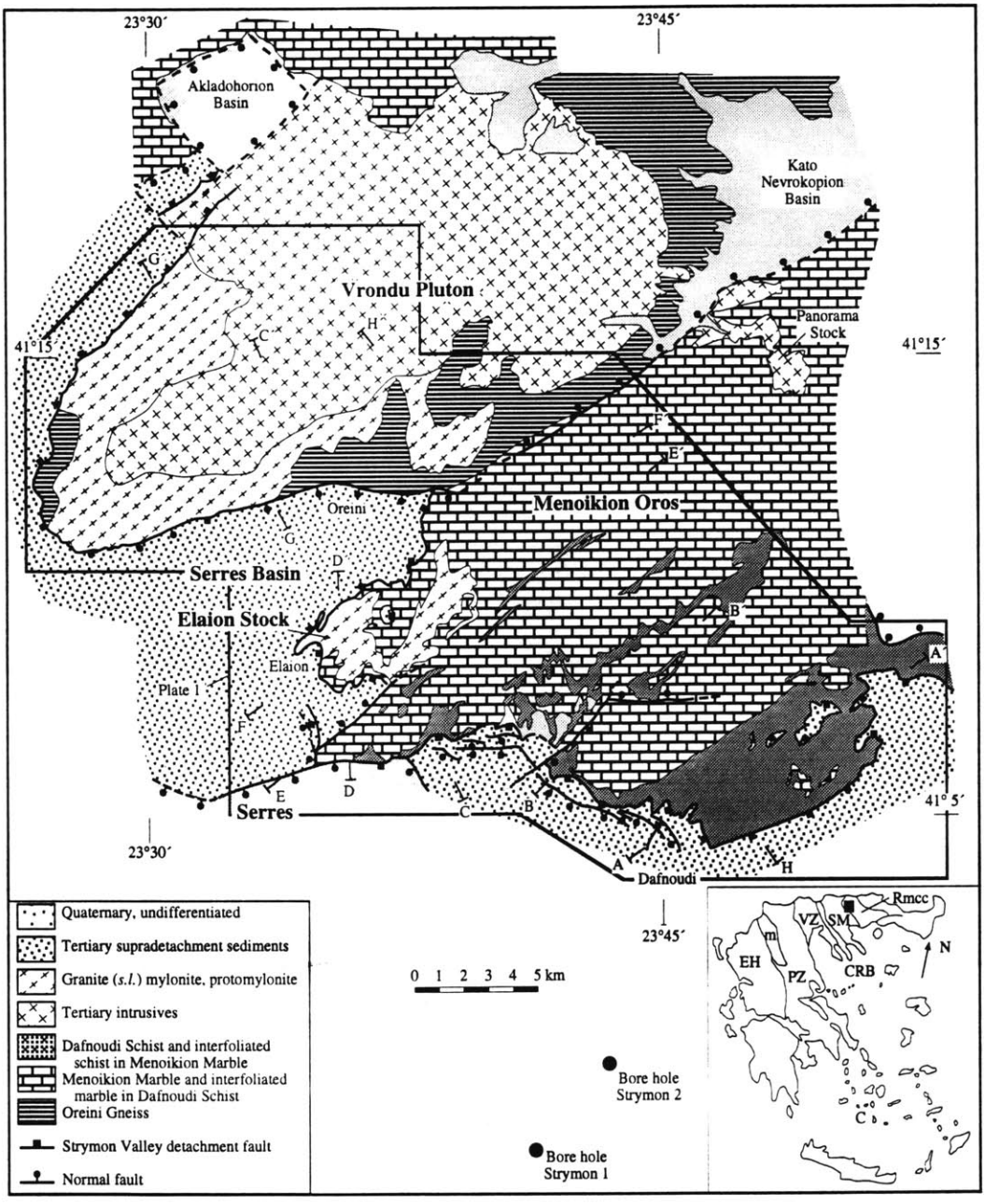
23°30′
23°45′
Akladohorion Basin
Kato Nevrokopion Basin
Vrondu Pluton
Panorama Stock
41°15′
Menoikion Oros
Oreini
Serres Basin
Elaion Stock
Elaion
Plate 1
Serres
Dafnoudi
41°5′
A
A′
B
B′
C
C′
D
D′
E
E′
F
F′
G
G′
H
H′
Quaternary, undifferentiated
Tertiary supradetachment sediments
Granite (s.l.) mylonite, protomylonite
Tertiary intrusives
Dafnoudi Schist and interfoliated schist in Menoikion Marble
Menoikion Marble and interfoliated marble in Dafnoudi Schist
Oreini Gneiss
Strymon Valley detachment fault
Normal fault
0 1 2 3 4 5 km
Bore hole Strymon 2
Bore hole Strymon 1
Rmcc
VZ
SM
m
EH
PZ
CRB
N
C

Figure 5

Figure 6a

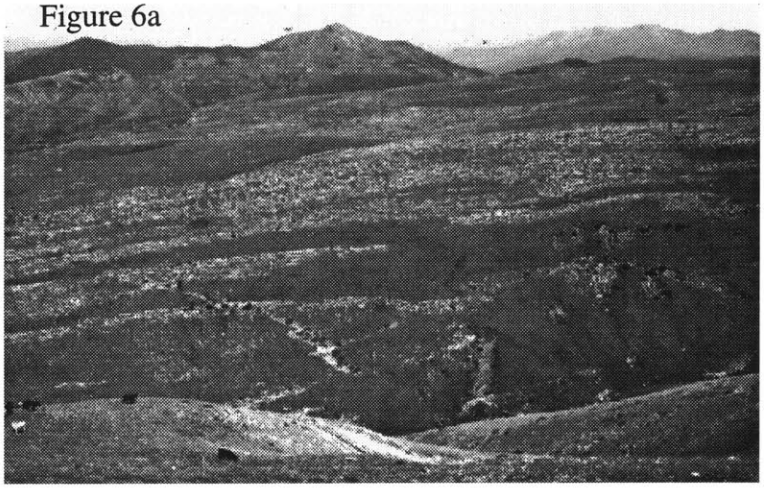

Figure 6b


SW
NE
Figure 6c

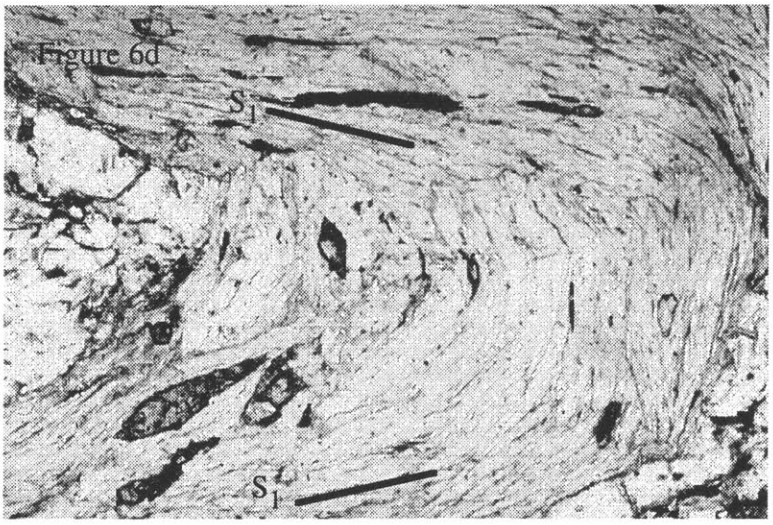
Figure 6d
S_1
S_1

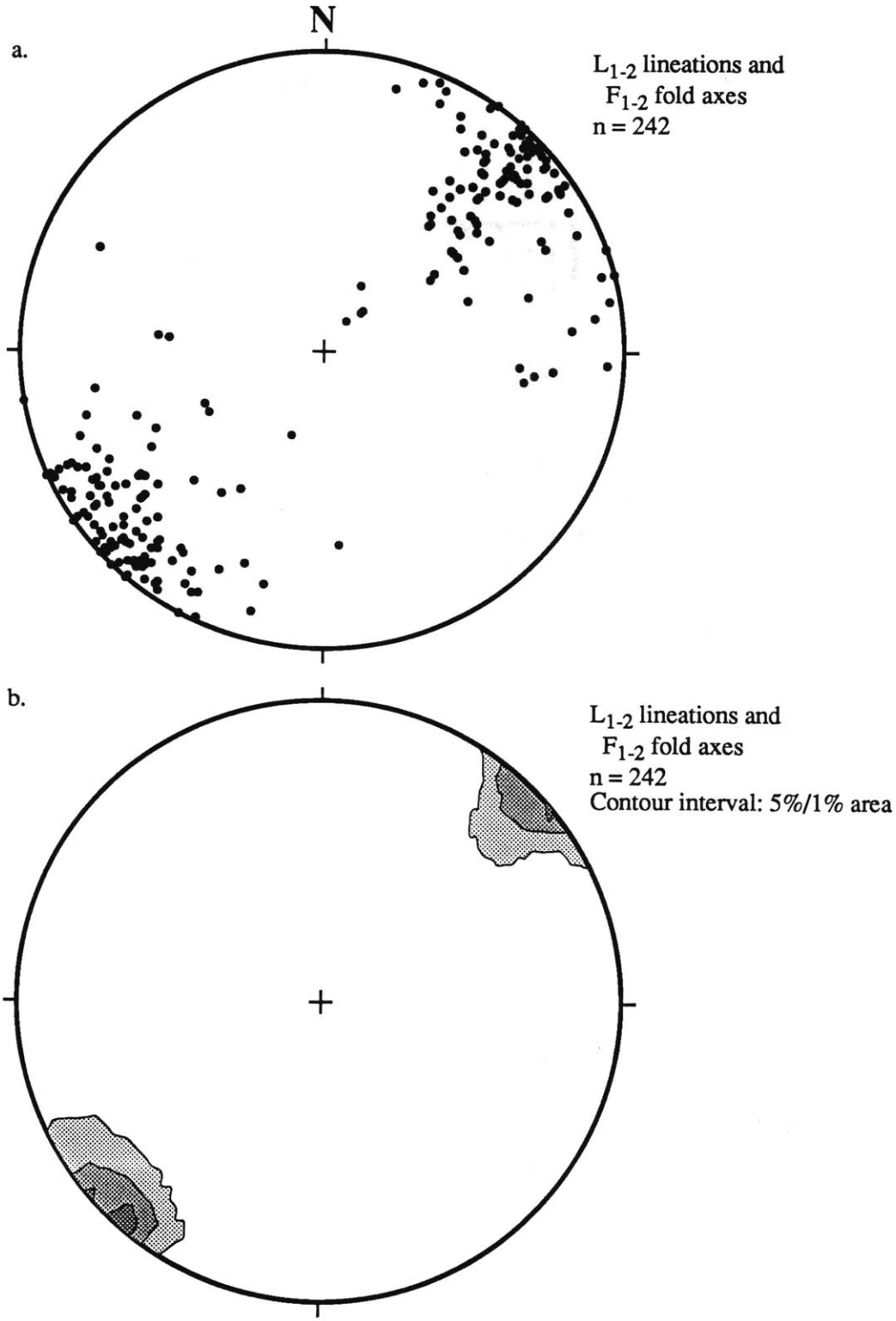
a.
N
L_{1-2} lineations and
F_{1-2} fold axes
n = 242
b.
L_{1-2} lineations and
F_{1-2} fold axes
n = 242
Contour interval: 5%/1% area

Figure 7

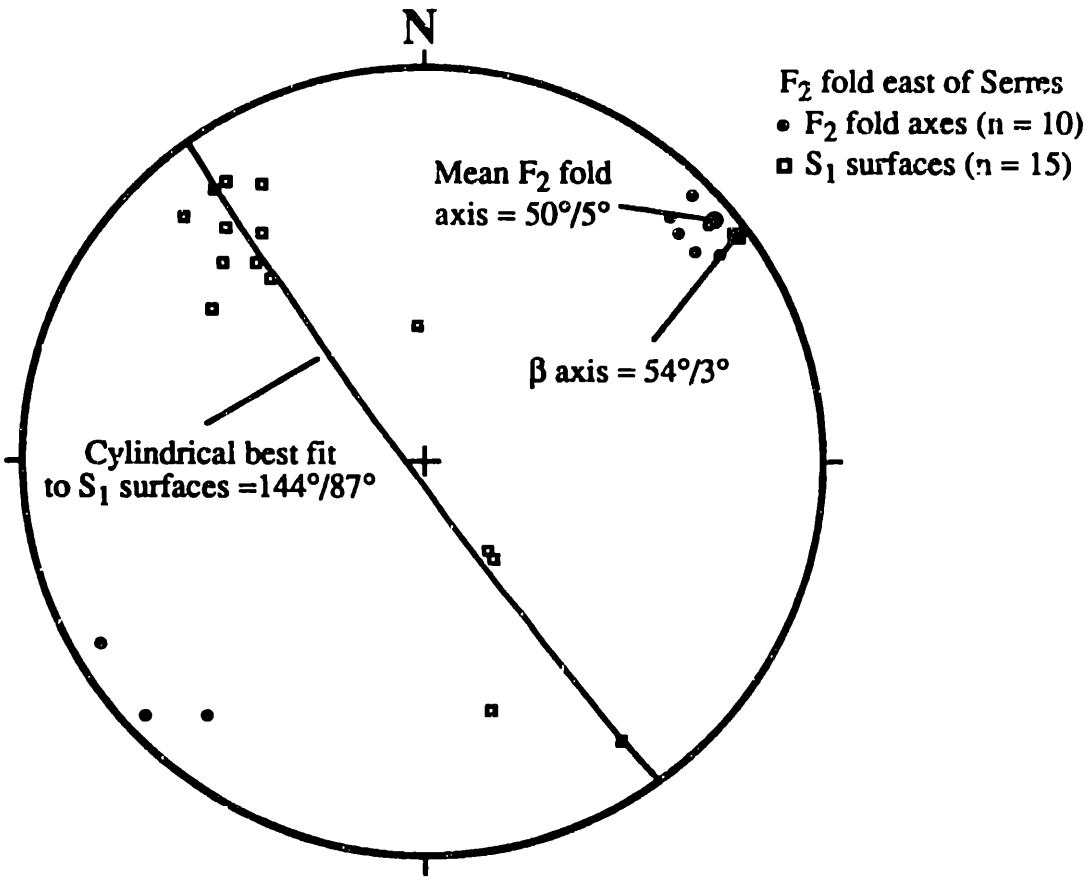
N
F_2 fold east of Serres
• F_2 fold axes (n = 10)
▫ S_1 surfaces (n = 15)
Mean F_2 fold axis = 50°/5°
β axis = 54°/3°
Cylindrical best fit to S_1 surfaces =144°/87°

Figure 8

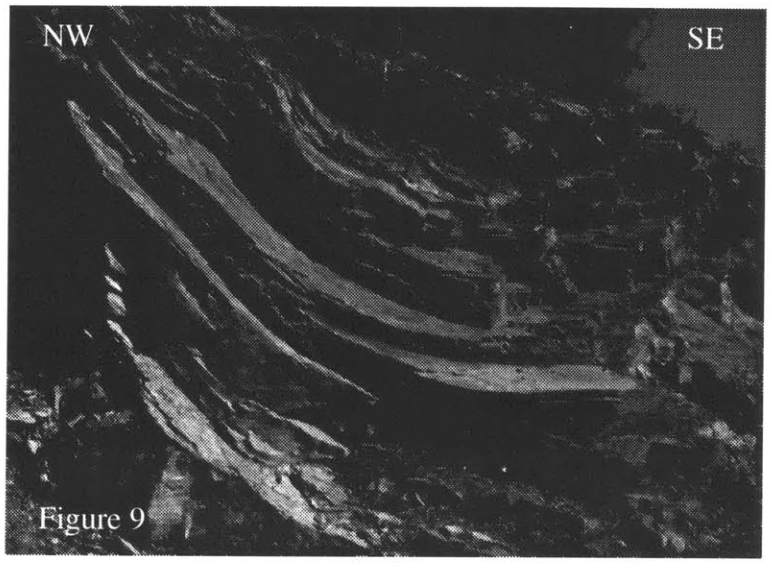

Figure 9

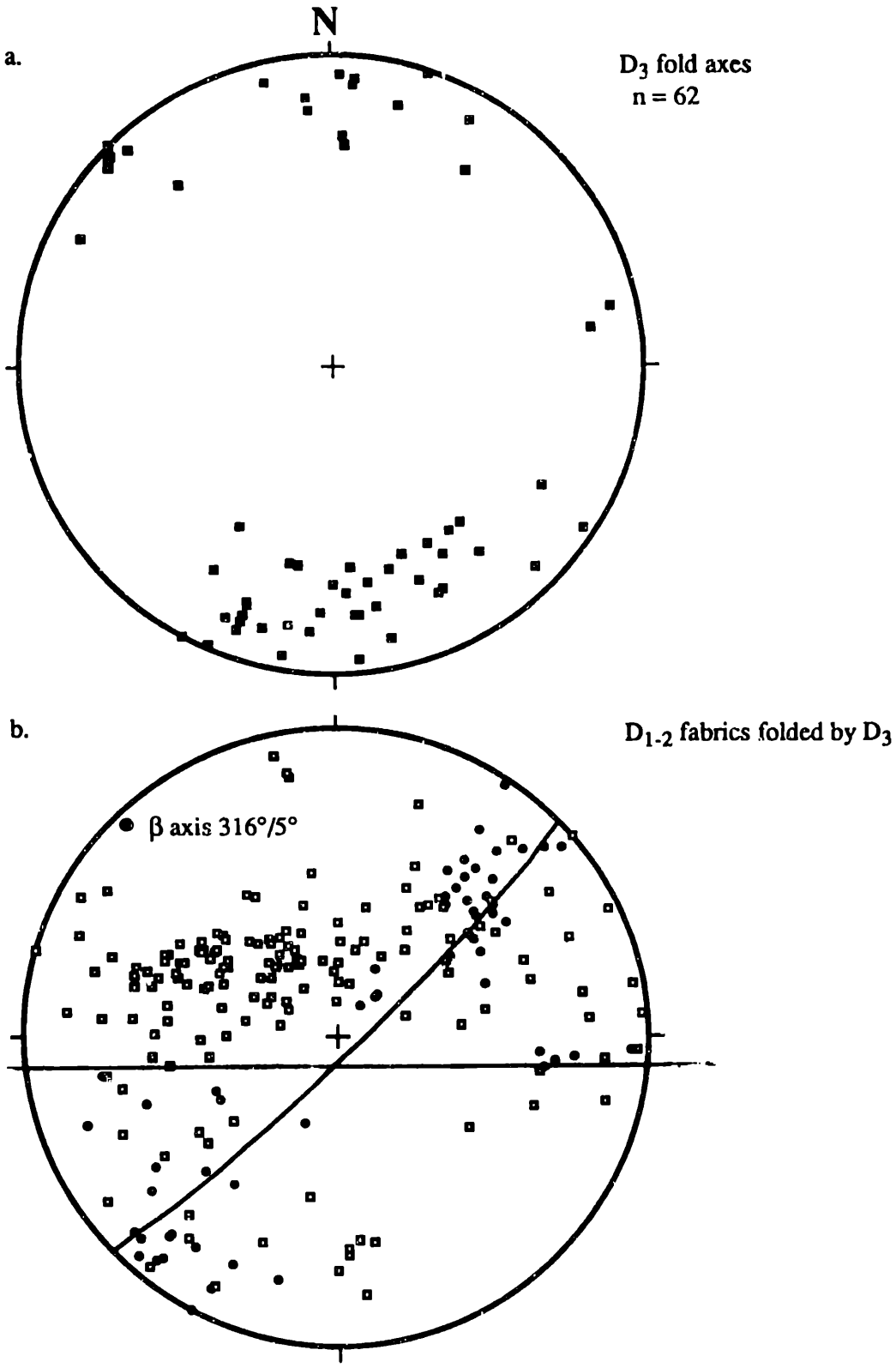

Figure 10

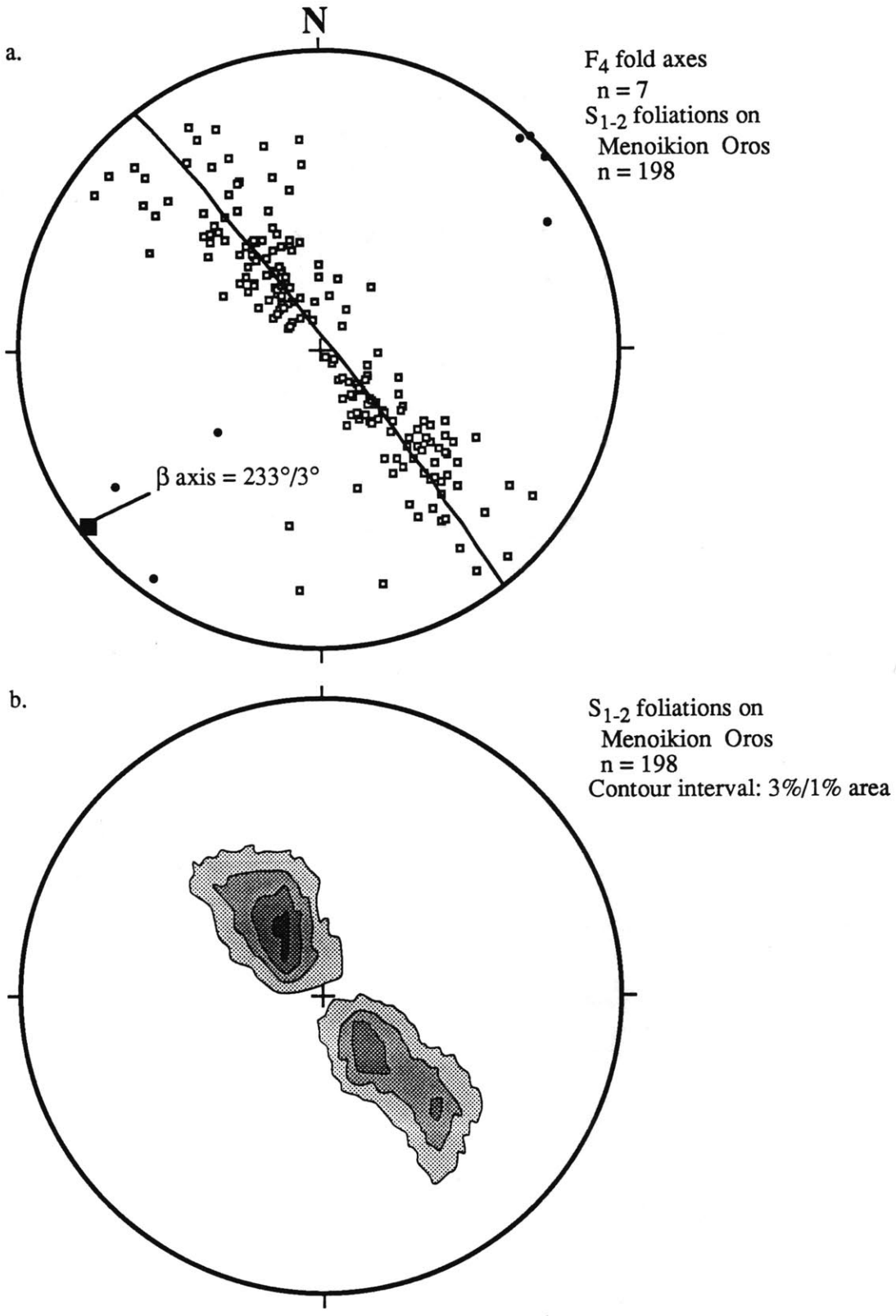

F_4 fold axes
n = 7
S_{1-2} foliations on
Menoikion Oros
n = 198

S_{1-2} foliations on
Menoikion Oros
n = 198
Contour interval: 3%/1% area

Figure 11

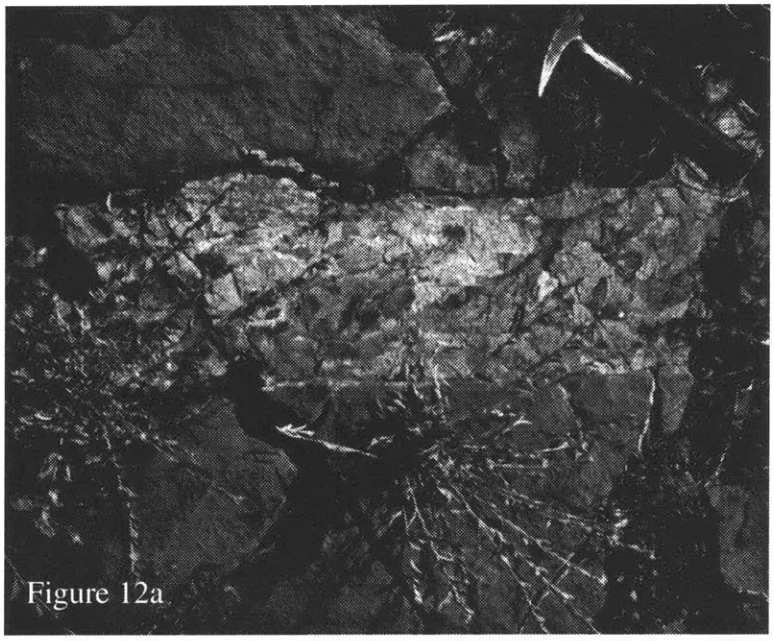

Figure 12a

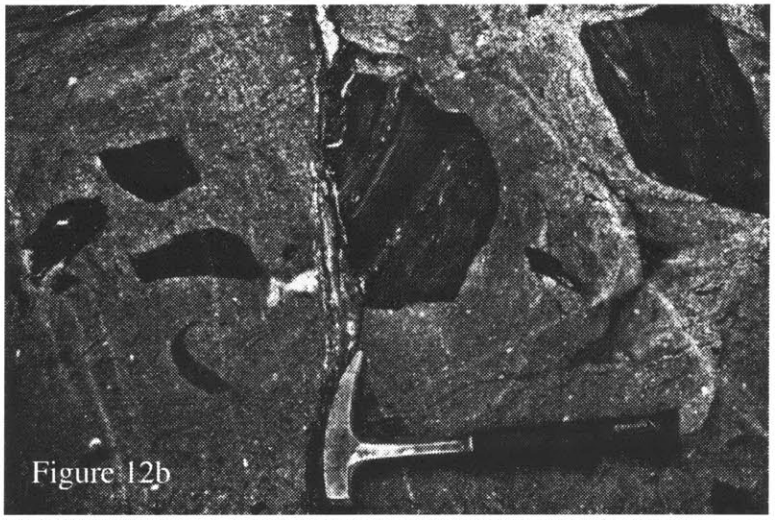

Figure 12b

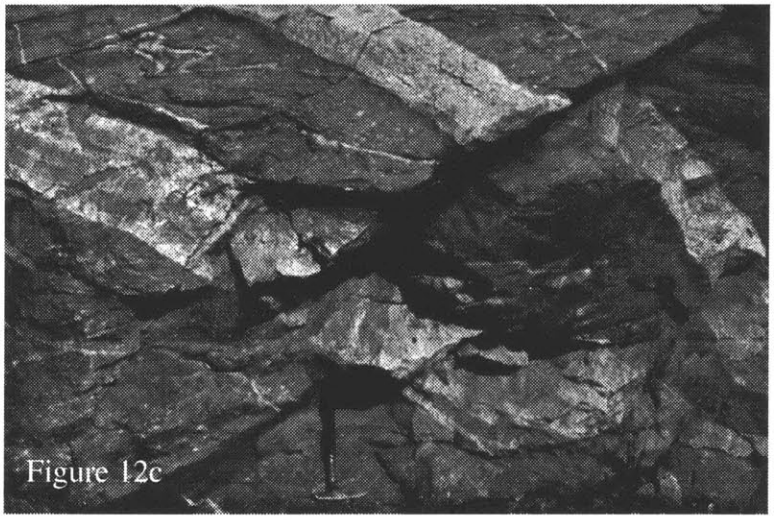

Figure 12c

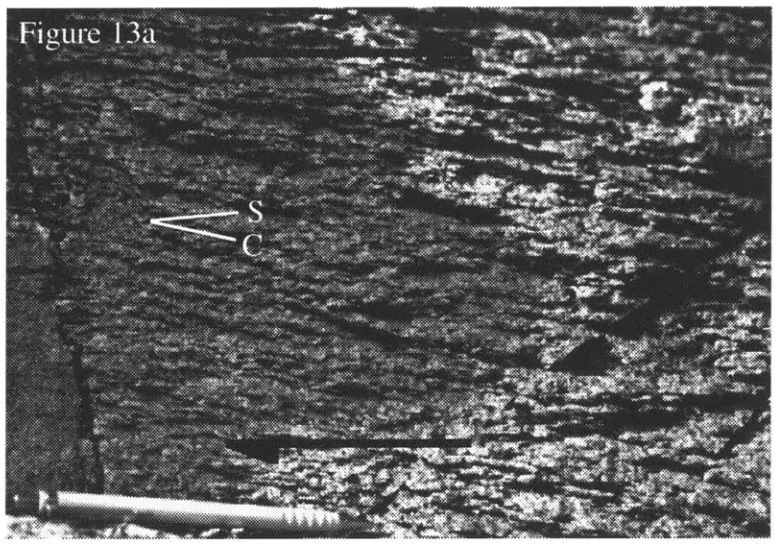
Figure 13a
S
C

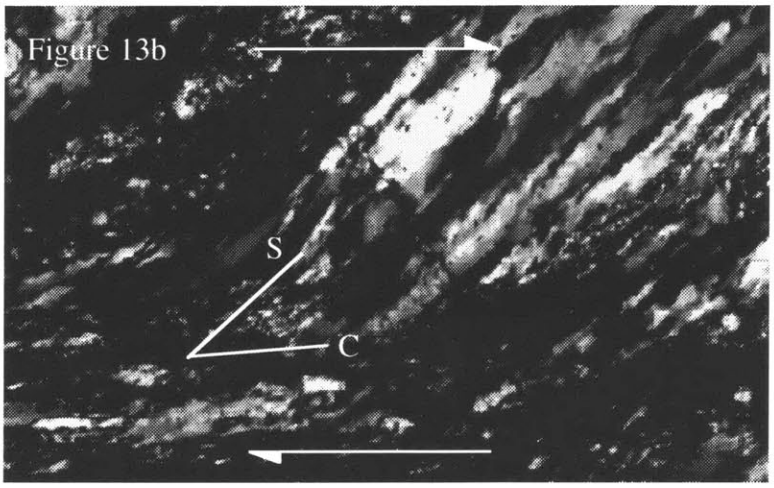
Figure 13b
S
C

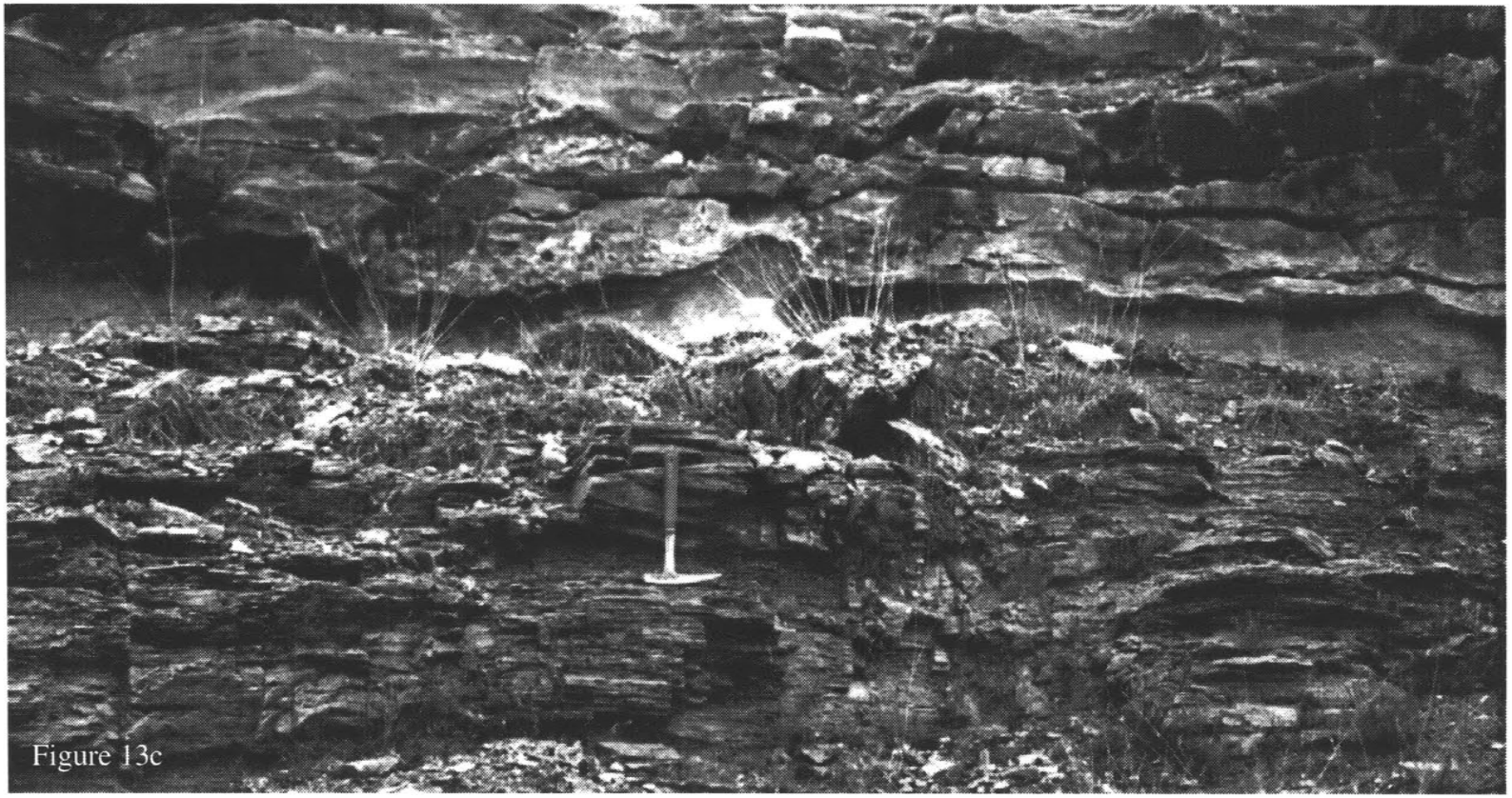

Figure 13c

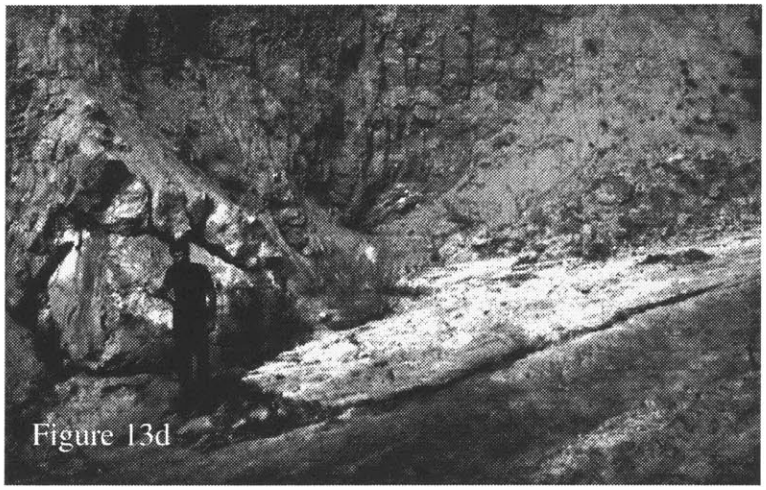

Figure 13d

Figure 13e

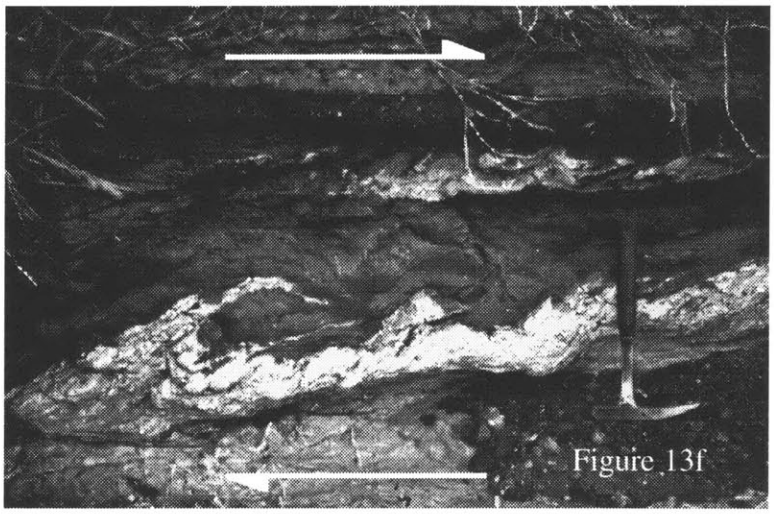

Figure 13f

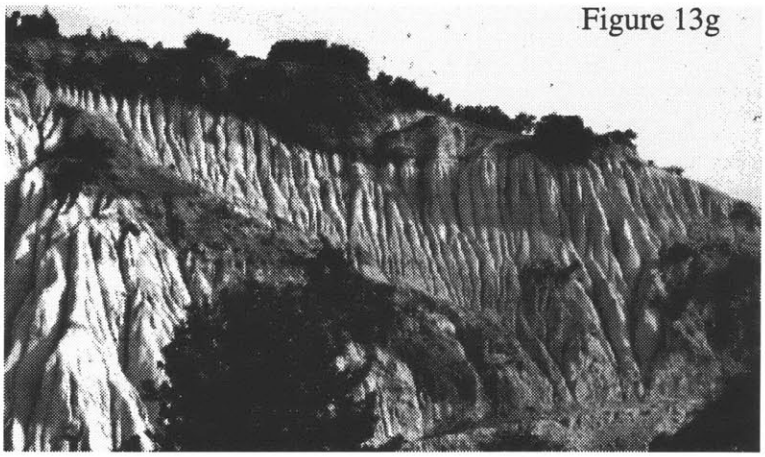

Figure 13g

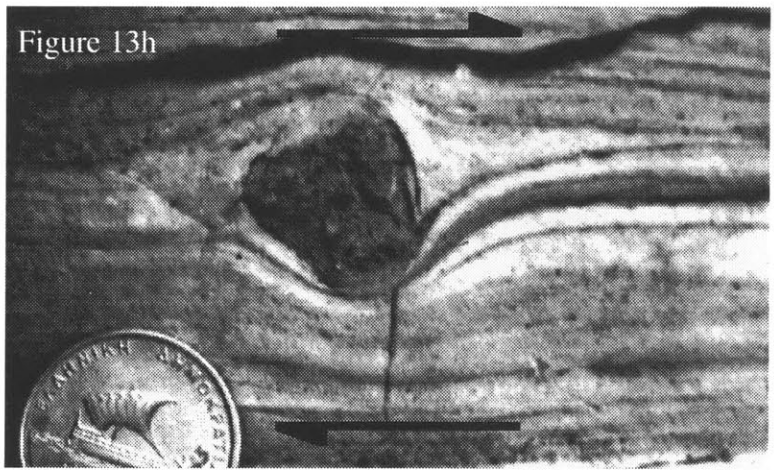

Figure 13h

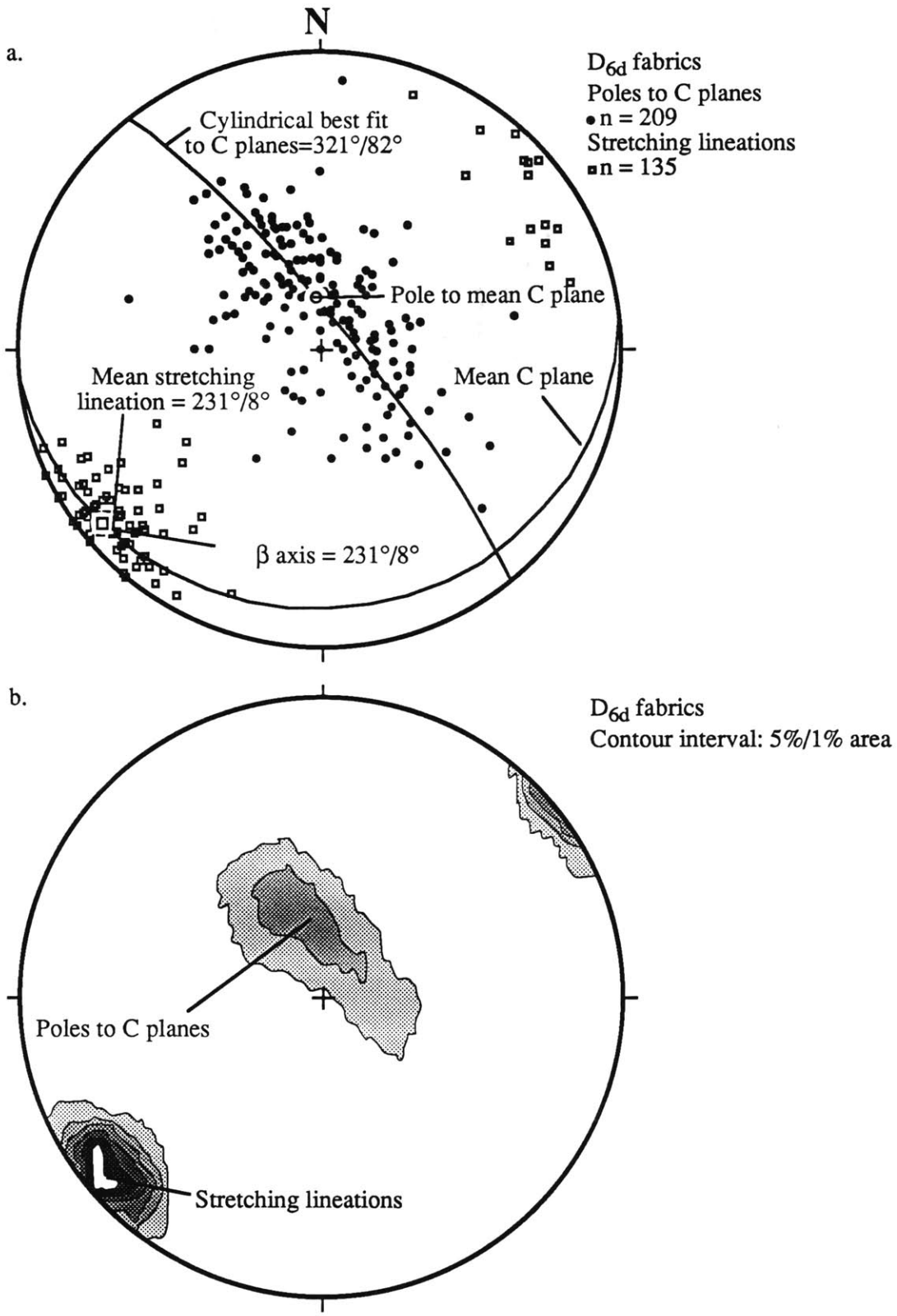
a.
N
Cylindrical best fit
to C planes=321°/82°
Pole to mean C plane
Mean stretching
lineation = 231°/8°
Mean C plane
β axis = 231°/8°
D6d fabrics
Poles to C planes
• n = 209
Stretching lineations
▪ n = 135
b.
D6d fabrics
Contour interval: 5%/1% area
Poles to C planes
L
Stretching lineations

Figure 14

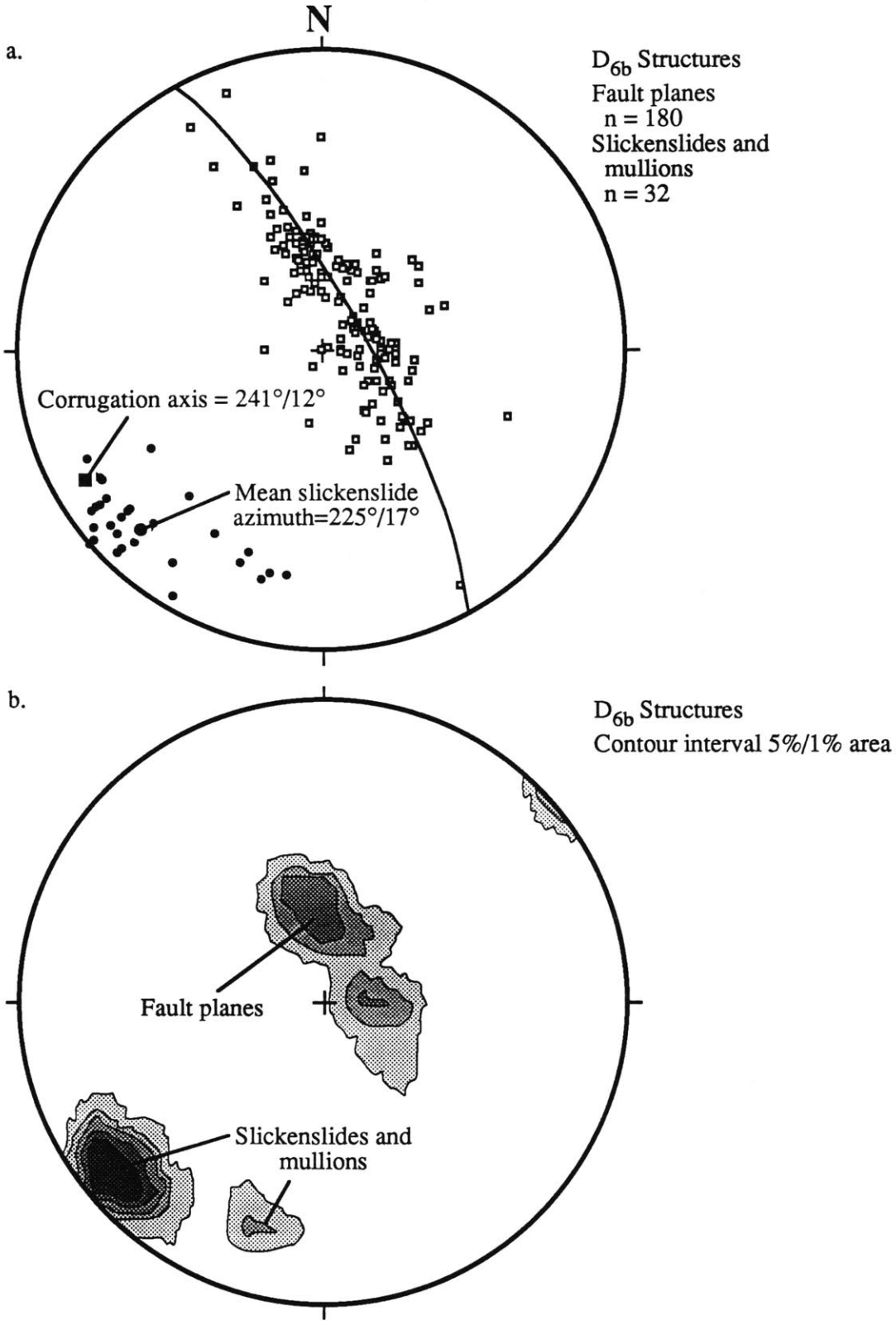
a.
N
D_{6b} Structures
Fault planes
n = 180
Slickenslides and
mullions
n = 32
Corrugation axis = 241°/12°
Mean slickenslide
azimuth=225°/17°
b.
D_{6b} Structures
Contour interval 5%/1% area
Fault planes
Slickenslides and
mullions

Figure 15

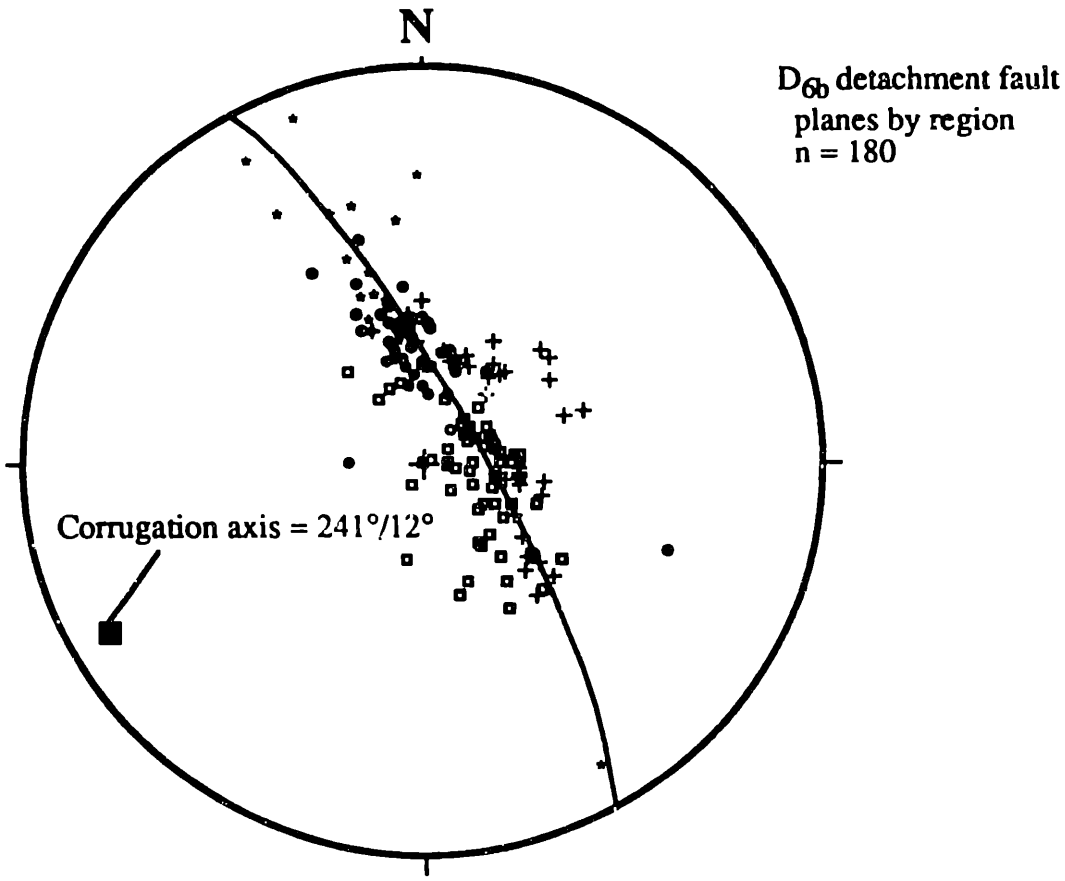
N
D_{6b} detachment fault planes by region n = 180
Corrugation axis = 241°/12°

Figure 16

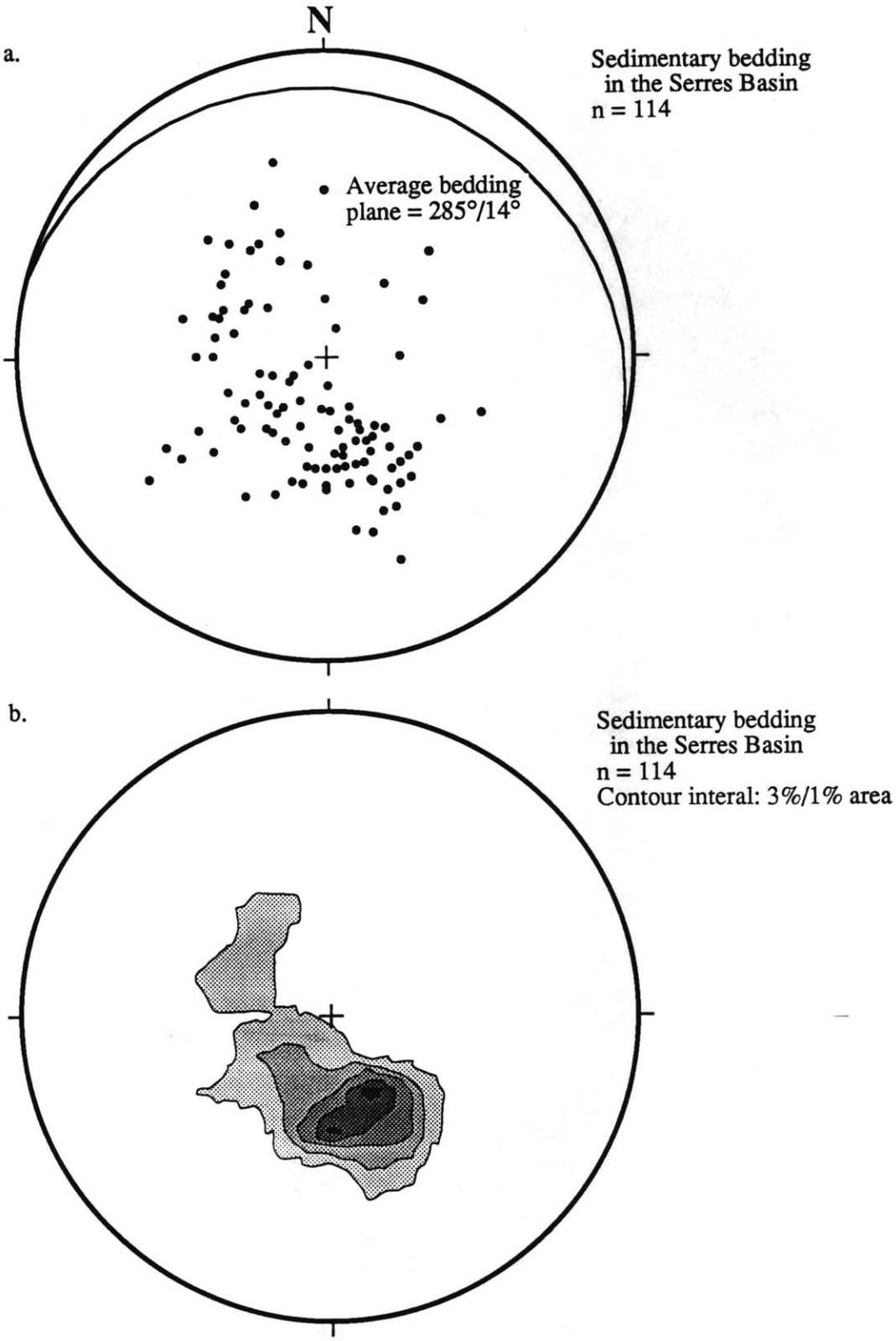
a.
N
Sedimentary bedding
in the Serres Basin
n = 114
Average bedding
plane = 285°/14°
b.
Sedimentary bedding
in the Serres Basin
n = 114
Contour interal: 3%/1% area

Figure 17

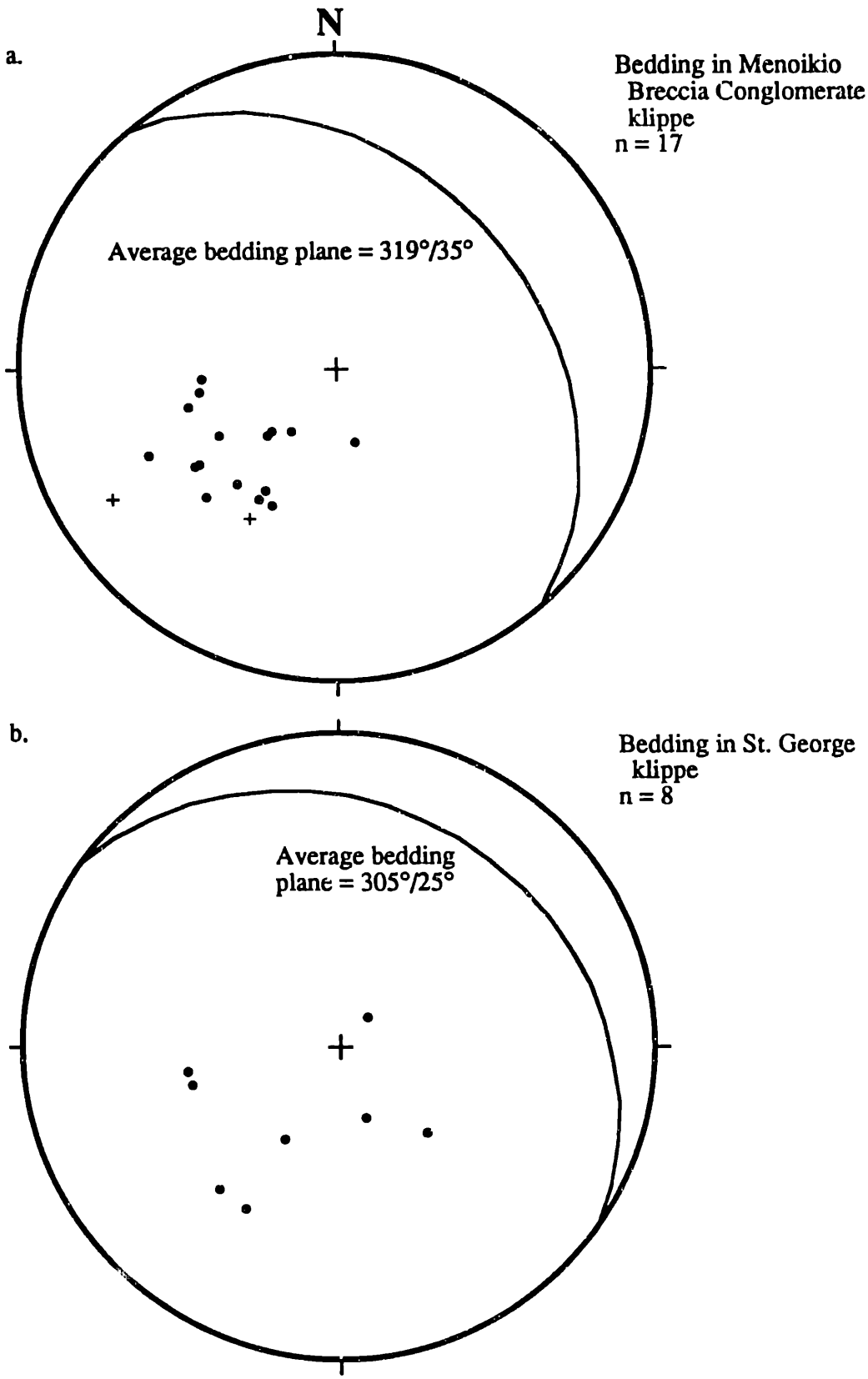
a.
N
Bedding in Menoikio Breccia Conglomerate klippe
n = 17
Average bedding plane = 319°/35°
b.
Bedding in St. George klippe
n = 8
Average bedding plane = 305°/25°

Figure 18

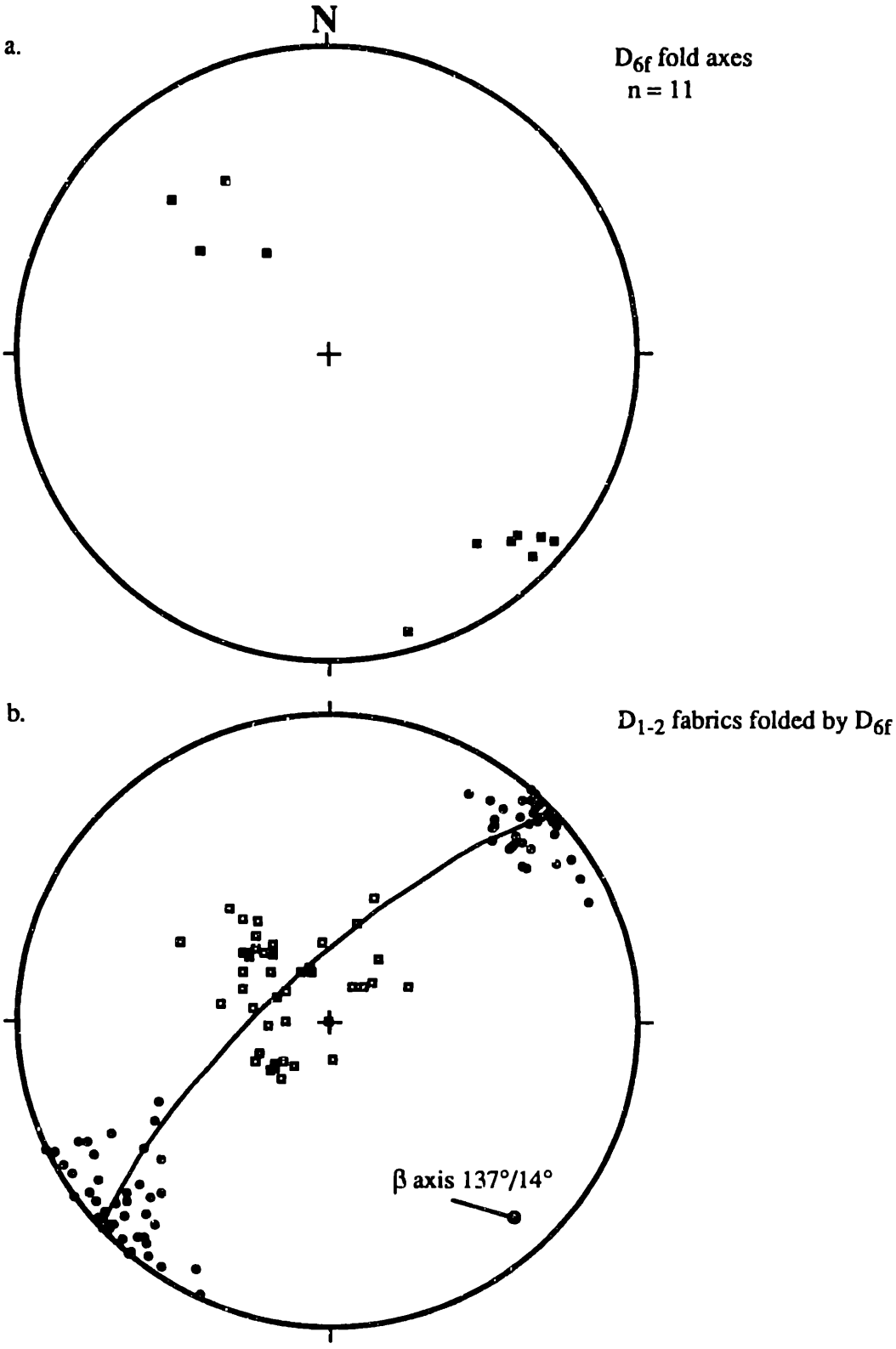

Figure 19

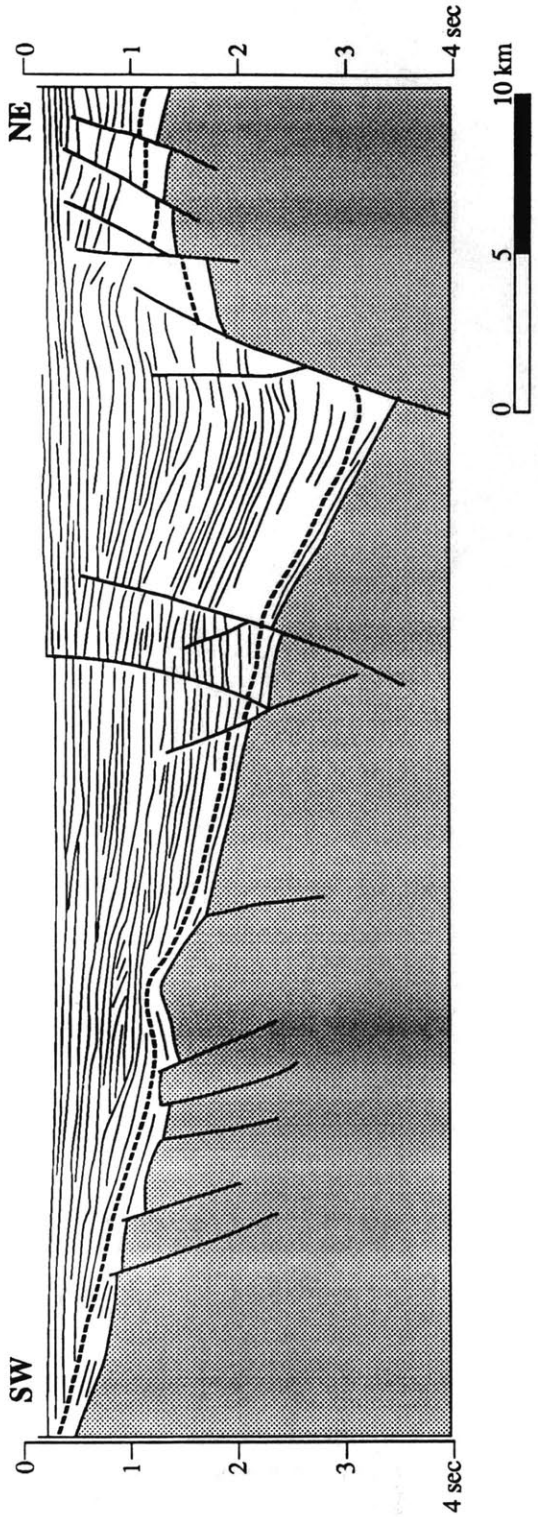

Figure 20

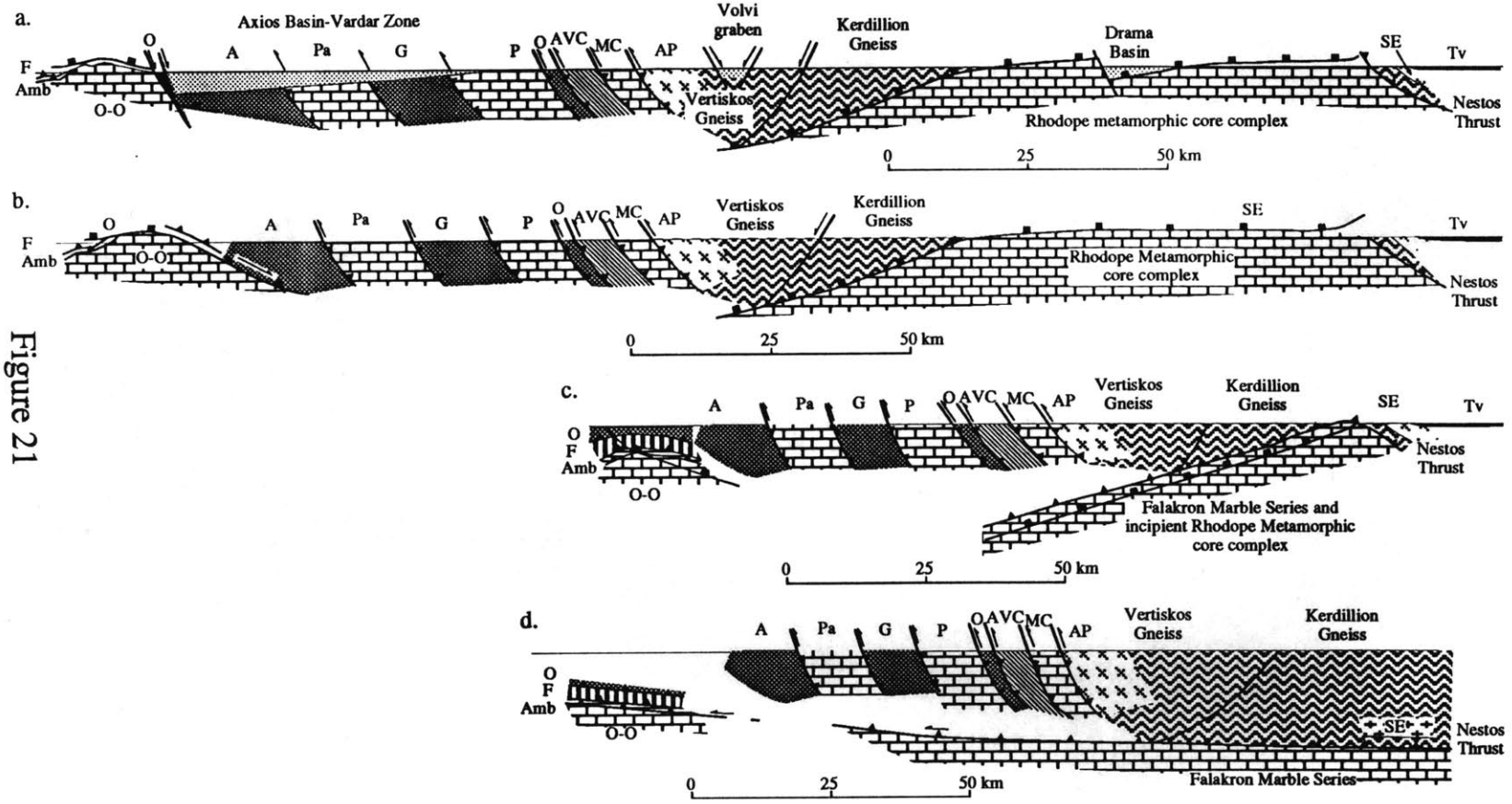
a.
Axios Basin-Vardar Zone
Volvi graben
Kerdillion Gneiss
Drama Basin
SE
Tv
F
Amb
O
A
Pa
G
P
O
AVC
MC
AP
O-O
Vertiskos Gneiss
Nestos Thrust
Rhodope metamorphic core complex
0
25
50 km
b.
Vertiskos Gneiss
Kerdillion Gneiss
SE
Tv
Rhodope Metamorphic core complex
Nestos Thrust
c.
Vertiskos Gneiss
Kerdillion Gneiss
SE
Tv
Nestos Thrust
Falakron Marble Series and incipient Rhodope Metamorphic core complex
d.
Vertiskos Gneiss
Kerdillion Gneiss
SE
Nestos Thrust
Falakron Marble Series

Figure 21

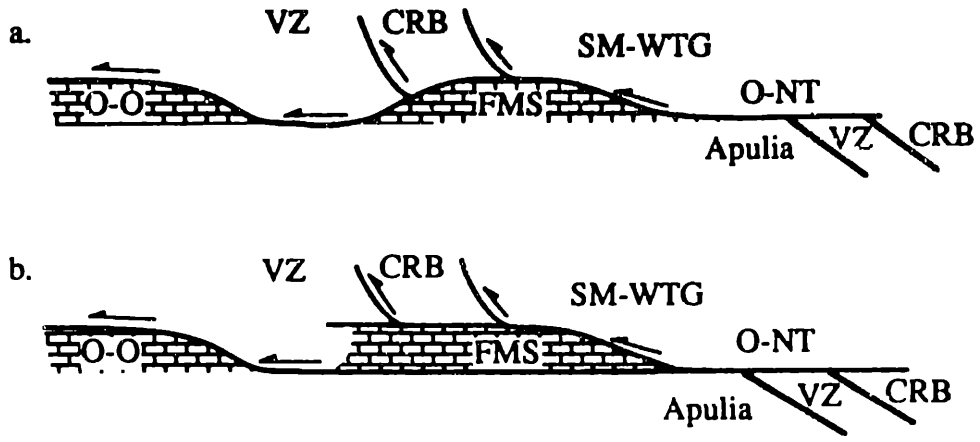

No scale implied

Figure 22

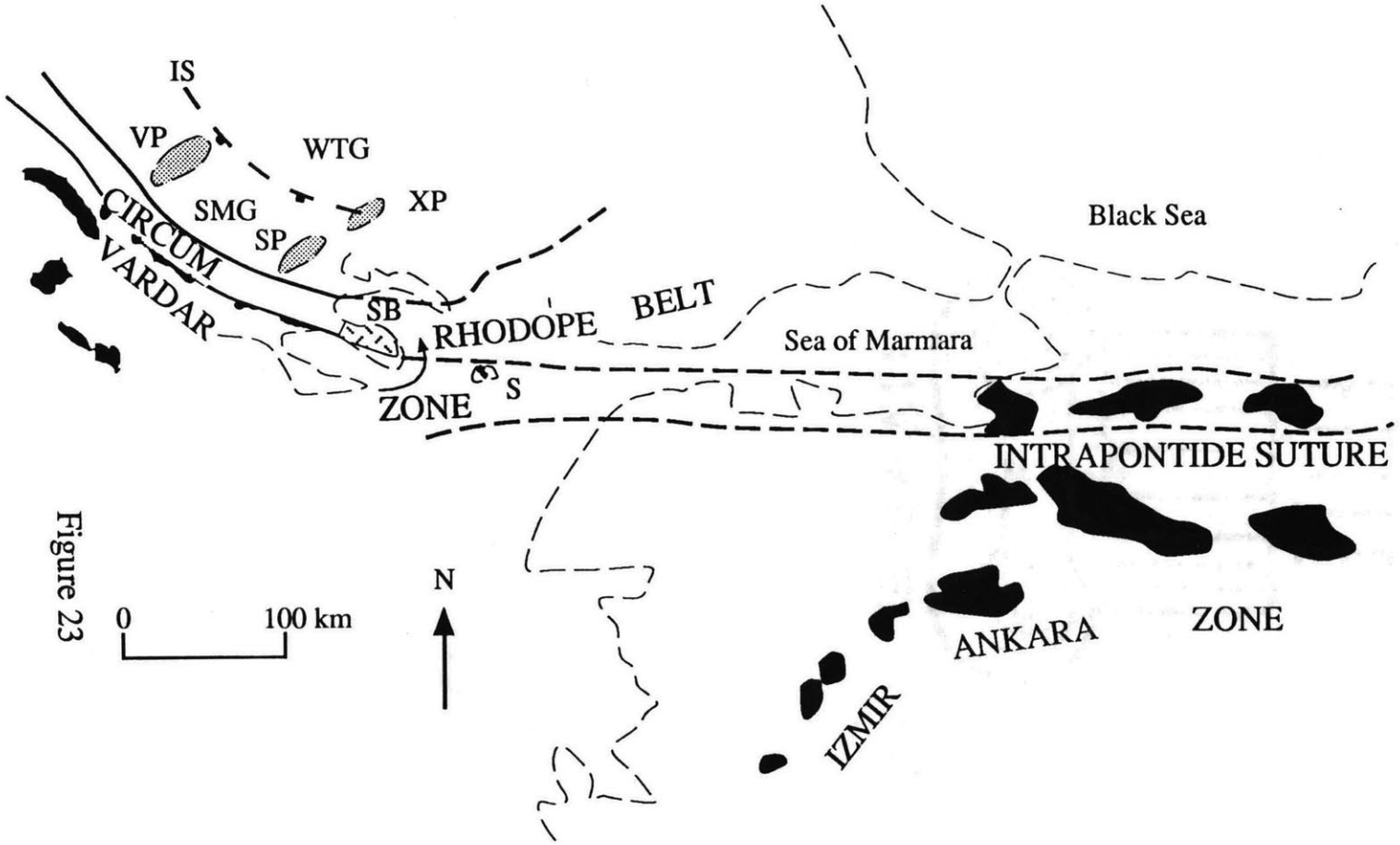
IS
VP
WTG
SMG
XP
SP
CIRCUM
VARDAR
SB
RHODOPE
BELT
ZONE
S
Black Sea
Sea of Marmara
INTRAPONTIDE SUTURE
ANKARA
ZONE
IZMIR
N
0
100 km

Figure 23

CHAPTER 4: TIMING OF MIOCENE EXTENSION IN THE NORTH AEGEAN: CONSTRAINTS FROM U-PB AND $^{40}AR/^{39}AR$ GEOCHRONOLOGY OF THE VRONDOU PLUTON AND THE NORTHERN RHODOPE METAMORPHIC CORE COMPLEX, NORTHERN GREECE

ABSTRACT

U-Pb and $^{40}Ar/^{39}Ar$ geochronology of the Vrondou pluton and the northern Rhodope metamorphic core complex place important constraints on the timing of pluton intrusion, the initiation of detachment faulting, the thermal evolution of the core complex during detachment faulting, and the rate of detachment faulting over time. Upper Oligocene $^{40}Ar/^{39}Ar$ hornblende cooling ages from the eastern Vrondou pluton and the Elaion stock and lowermost Miocene U-Pb titanite and $^{40}Ar/^{39}Ar$ hornblende ages from the central Vrondou pluton are interpreted to indicate two episodes of pluton intrusion. Initiation of tectonic denudation by the Strymon Valley detachment fault is inferred from 16 Ma biotite cooling ages whose closure temperature roughly overlaps with approximate conditions of mylonitization. Tectonic denudation and cooling of the Vrondou pluton and northern Rhodope metamorphic core complex are recorded by the biotite cooling ages and 9 to 16 Ma K-feldspar cooling ages. Spatial variations in K-feldspar cooling ages are interpreted to reflect the top-to-the-southwest denudation of the core complex at a rate of 2.3 ± 0.1 km/m.y. K-feldspar cooling ages overlap slightly with the oldest syn-extensional sediments in the Serres Basin, suggesting the earliest deposits were derived from the exposed eastern core complex before unroofing was complete.

INTRODUCTION

Throughout Cenozoic time in the Eastern Mediterranean, convergence between the European and African plates has been accommodated by northeastward subduction in the

Hellenic arc beneath Greece and Anatolia (Figure 1). During earliest Miocene time, retreat of the Hellenic subduction zone and outward bowing of the arc initiated extension in the back-arc region (future Aegean Sea) (e.g., *Le Pichon and Angelier* [1979]). The earliest stage of this extension is manifested by the formation of metamorphic core complexes and the exhumation of rocks from mid-crustal depths (e.g., *Lister et al.* [1984]; *Schermer et al.* [1990]; *Dinter and Royden* [1993]). The early "core complex style" extension is especially well developed and well exposed in the Rhodope metamorphic core complex, where the total magnitude of Tertiary extension has not been sufficient to submerge the extended region. Plutons intruded into the footwall of the Rhodope metamorphic core complex thermally reset isotopic systematics in the middle Tertiary, prior to the onset of regional-scale detachment faulting. This study seeks to constrain the timing of pluton intrusion, the initiation of detachment faulting, and the rate of extension and tectonic denudation in the northern Rhodope metamorphic core complex by applying U-Pb and $^{40}Ar/^{39}Ar$ geochronology to one of these intrusives, the Vrondou pluton, and metamorphic rocks in the core complex footwall.

GEOLOGIC FRAMEWORK OF THE RHODOPE METAMORPHIC CORE COMPLEX AND PREVIOUS GEOCHRONOLOGIC STUDIES

The Rhodope metamorphic core complex is exposed in the footwall of the Strymon Valley detachment fault, a regionally developed, low-angle normal fault that juxtaposes amphibolite-facies gneisses of the Serbo-Macedonian Range and syn-extensional supradetachment basins against footwall marbles, schists, and gneisses of the Falakron Marble Series and Tertiary plutons (Figure 2). The eastern geographic boundary of the core complex is the southwest-vergent Nestos Thrust, an Eocene (?) Alpine structure responsible for the emplacement of the amphibolite-facies West Thracian Gneiss Complex over the greenschist-facies Falakron Marble Series [*Papanikolaou and Panagopoulos*, 1981; *Kilias and Mountrakis*, 1990; *Dinter*, 1994].

In the northern Rhodope metamorphic core complex, the Vrondou pluton and the Falakron Marble Series are exposed in two kilometer-scale corrugations of the Strymon Valley detachment fault (Figure 3). Several phases of deformation attributed to Alpine compression have been recognized in the footwall; all are cross-cut by the pluton or dikes associated with it [Chapter 3]. The low angle Strymon Valley detachment fault cuts across Alpine structures and is characterized by a progression from ductile to brittle fabrics, typical of metamorphic core complexes (e.g., *Coney* [1980]; *Armstrong* [1982]; *Davis and Lister* [1988]; *Lister and Davis* [1988]). Motion on the Strymon Valley detachment fault initiated during the early Miocene and continued until the Pliocene [*Dinter and Royden*, 1993]. Post-detachment normal and east- to northeast-trending right-lateral strike-slip faults cut both the footwall and the supradetachment basins.

The oldest syn-extensional sediments in the hanging wall of the Strymon Valley detachment fault are typically terrigenous cobble to boulder conglomerates and coarse sandstones with clasts derived from the footwall of the Strymon Valley detachment fault. The oldest mammal fauna recovered from these syn-detachment sediments are ~15.5 Ma from the Bulgarian Sandanski Graben [*Kojumdgieva et al.*, 1982]. The oldest recovered faunal assemblages from the Serres Basin are 9.8 Ma [*Armour-Brown et al.*, 1977]. In the Serres Basin, the youngest sediments disrupted by the detachment fault are of Pliocene age [*Armour-Brown et al.*, 1977; *Karistineos and Georgiades-Dikeoulia*, 1985].

The Vrondou pluton and Elaion stock are I-type, metaluminous, mesozonal, medium-grained granitic bodies intruded into the lower and middle Falakron Marble Series during widespread Oligocene to Lower Miocene magmatism in northeastern Greece and southern Bulgaria [*Innocenti et al.*, 1984; *Eleftheriadis and Lippolt*, 1984; *Lilov et al.*, 1987; *Kotopouli and Pe-Piper*, 1989; *Kolocotroni and Dixon*, 1991; *Koukouvelas and Pe-Piper*, 1991; *Jones et al.*, 1992]. They range in composition from granite and granodiorite to monzonite with gradational contacts between the various phases [*Theodorikas*, 1983]. Minor enclaves of gabbro and dioritic xenoliths have been reported from the eastern

Vrondou pluton [*Theodorikas*, 1983]. The Vrondou pluton and Elaion stock are geochemically indistinguishable and are also chemically similar to the Xanthi, Granitis, Panorama, and Philippi intrusives and the Paranestion volcanics [*Kotopouli and Pe-Piper*, 1989; *Kolocotroni and Dixon*, 1991; *Jones et al.*, 1992]. The chemical composition of these plutons and their extrusive equivalents suggest they are formed in either a subduction-related or post-collisional environment [*Kotopouli and Pe-Piper*, 1989]. It has recently been suggested that this widespread magmatism in the north Aegean region is related to the extensional collapse of overthickened Rhodope crust [*Kolocotroni and Dixon*, 1991; *Koukouvelas and Pe-Piper*, 1991; *Jones et al.*, 1992; *Dinter et al.*, 1995].

Previous studies of the Vrondou pluton have included extensive geochemical work but only limited geochronology. K-Ar geochronology on hornblende and biotite has yielded ages of 29 ± 1 to 33 ± 2 Ma and 30 ± 3 Ma, respectively [*Marakis*, 1969; *Dürr et al.*, 1978]. A Rb-Sr whole-rock isochron gives the same age (30 Ma) (N. Kolocotroni, pers. comm., 1992). Preliminary $^{40}Ar/^{39}Ar$ dating has yielded biotite and K-feldspar cooling ages between 10 and 18 Ma (N. Kolocotroni, pers. comm., 1992). The adjacent Granitis and Panorama stocks yield K-Ar biotite ages of 28.2 ± 0.5 Ma and 26.8 ± 0.5 Ma respectively [*Meyer*, 1968].

In the southern part of the Rhodope metamorphic core complex, the mylonitized Symvolon pluton was intruded syn-extensionally during earliest Miocene time (~22 Ma) (Figure 2) [*Dinter et al.*, 1995]. Contacts with the country rock are typically highly sheared and no contact aureole is preserved. Biotite and K-feldspar K-Ar and $^{40}Ar/^{39}Ar$ cooling ages from the pluton ranging from 11.1 ± 0.2 to 17.8 ± 0.8 are interpreted to date the tectonic unroofing of the Rhodope metamorphic core complex [*Harre*, 1968; *Kokkinakis*, 1980; *Dinter et al.*, 1995].

There are only limited constraints on the age of either the protolith or metamorphism of the Falakron Marble Series. A single poorly preserved coral from the Falakron Series requires its protolith to be post-Cambrian [*Meyer et al.*, 1963]; structural relations with the

West Thracian Gneiss Complex and Serbo-Macedonian Gneisses suggest that Alpine structural fabrics are of Eocene age [*Dinter*, 1994]. A Rb-Sr whole rock isochron for paragneisses from the base of the Falakron Series in the southern Rhodope metamorphic core complex gives a late Paleozoic age (260 ± 5 Ma) [*Del Moro et al.*, 1990]. An early Triassic Rb-Sr age on white mica has been reported from a Hercynian pegmatite orthogneiss from the island of Thassos [*Wawrzenitz et al.*, 1994]. Paragneisses from the Falakron Marble Series yield Rb-Sr biotite-whole rock and muscovite-whole rock ages of ~12 Ma and 18 to 22 Ma respectively [*Del Moro et al.*, 1990].

STRUCTURAL ASPECTS OF THE STRYMON VALLEY DETACHMENT FAULT

The Strymon Valley detachment fault is a regionally-corrugated detachment fault characterized along its length by discrete, well-exposed, shallowly dipping fault planes overlying ductile fabrics formed during the early stages of its motion. Alpine metamorphic foliations, lineations, and fold axes in the footwall are warped into parallelism with the detachment fault to a depth of several hundred meters below the fault plane. The southern, western, and northwestern margins of the Vrondou pluton and the Elaion stock are sheared to form a shallowly dipping mylonitic fabric subparallel to the overlying brittle detachment fault. The degree of mylonitization generally decreases structurally downward from the margin of the pluton to its undeformed interior. The mylonitized zone has a structural thickness of up to 1 km. The intensity of mylonitization varies along the trace of the detachment fault. Ductile fabrics are well developed on the northwestern and southern margins of the Vrondou pluton and in the Elaion stock. In contrast, the western nose of the Vrondou pluton is characterized by intense brittle deformation superimposed on poorly developed ductile fabrics. Stretching lineations in the granite mylonite are generally close to a well-defined, gently southwest-plunging mean orientation of 231°/8°, but vary as much as 30° from the mean orientation (Figure 3 inset). The corrugation axis of mylonitic

foliations coincides with the mean stretching lineation. Both ductile and brittle structural fabrics associated with the Strymon Valley detachment fault consistently indicate top-to-the-southwest sense of shear.

Thin-section analyses of foliated granites from the mylonitized northern and southern margins of the Vrondou pluton and the Elaion stock show that the degree of deformation ranges from proto-mylonite to mylonite to ultramylonite. An S-C fabric *[Berthé et al.*, 1979] is generally well developed. S-surfaces are defined by broken and rotated feldspar porphyroclasts, quartz subgrain aggregates, and a preferred grain shape orientation in quartz subgrains. C-planes are defined by monocrystalline and polycrystalline quartz ribbons (e.g., *Simpson and De Paor* [1991]), aligned biotite crystals, tails of sigmoidal feldspar porphyroclasts, insoluble residue, and local formation of white mica. Quartz is precipitated in brittle fractures in some broken feldspar porphyroclasts. Quartz grains typically show undulatory extinction. Temperatures of mylonitization are estimated to be approximately 300° to 350° C (± 50°) based on textural relations (e.g., preferred grain shape orientation in quartz subgrains, rigid feldspar porphyroclast behavior, mechanical twinning and patchy undulatory extinction in feldspar grains, and precipitation of quartz in fractures in feldspar porphyroclasts) [*Simpson and De Paor*, 1991]. Textures indicative of higher temperature mylonitization (e.g., myrmekite development, recrystallized feldspar neoblasts, and preferred grain shape orientation in feldspar) were not observed.

SAMPLE SELECTION AND PREPARATION/ ANALYTICAL PROCEDURES AND DATA REDUCTION

In order to address the timing of emplacement of the Vrondou pluton and the tectonic denudation of the Rhodope metamorphic core complex by the Strymon Valley detachment fault, samples from a range of locations were collected for dating and thin section analysis. Approximately 60 hand specimens (approximately 250 g each) of fresh,

undeformed granites, intrusive dikes, and S-C granite mylonites were collected from the Vrondou pluton, its deformed margins, and the Elaion stock. A single large (~12 kg) sample (93-127) of undeformed hornblende granite containing five co-existing datable mineral phases (zircon, titanite, hornblende, biotite, and K-feldspar) was collected from the central Vrondou pluton to assure that ample quantities of titanite and zircon could be extracted for U-Pb analysis. From the pool of available hand specimens, three mylonitic samples representing the southern margin of the Vrondou pluton (91-132) and the Elaion stock (91-12, 91-113) were selected for $^{40}Ar/^{39}Ar$ analysis to complement the large granite sample. Two additional samples from a traverse of the Vrondou pluton were selected to examine the cooling history in the transport direction of the Strymon Valley detachment fault (93-135 and 94-95). Because muscovite is absent from the Vrondou pluton, a sample of muscovite-bearing gneiss (92-16) from the contact aureole of the Vrondou pluton was collected to further constrain the cooling history of the pluton. Muscovite and biotite separates were also prepared from the Falakron Marble Series (11-J-91 and 91-127 respectively) to compare the unroofing history of Mt. Menoikion to that of the Vrondou pluton. Sample locations are shown on Figure 3.

Samples were crushed, milled, and seived using standard equipment at the geochronologic facilities at Massachusetts Institute of Technology. Because of its large size, sample 93-127 was initially separated into several density fractions using a Wilfley table. The densest Wilfley fraction (approximately 0.5 kg total mass) was used for titanite and zircon separation; approximately 1 kg of the lighter Wilfley fractions were saved for K-feldspar, biotite, and hornblende separation.

U-Pb Analyses

Zircon and titanite were separated from the densest Wilfley fraction of sample 93-127 using a Frantz isodynamic separator and heavy liquids. The large volume of starting material allowed the recovery of ample titanite and zircon for U-Pb dating. The separates

of zircon and titanite were further subdivided into several fractions using the Frantz isodynamic separator. Zircon and titanite grains for U-Pb analysis were individually hand-picked in ethanol under a 60× picking scope from a weakly diamagnetic zircon fraction and the least magnetic titanite fraction. Grains were segregated into groups or "picks" so as to maximize similarities in crystal size, habit, color, and clarity, and to minimize visible inclusions. Zircon pick sizes were approximately 10 grains each. Estimated Pb concentrations as low as 2 ppm in titanite required larger volumes of titanite to be used in each pick. Two picks of approximately 100 grains each were prepared.

Zircon picks were air-abraded with pyrite for 23 hours following the technique developed by *Krogh* [1982] in an effort to reduce the effects of surfical lead loss. Pyrite and other contaminants were removed from the abraded grains by leaching for 10 minutes in 4N HNO_3 at ~60°C. Titanites, which are considerably more friable than zircons, were neither abraded nor leached. After leaching, each pick was washed in distilled water, dried in acetone, and spiked with a mixture of ^{205}Pb, ^{233}U, and ^{235}U tracer solution. The picks were then dissolved in a mixture of HF and HNO_3 in teflon bombs at 220°C for 48 hours. Pb and U were separated from the resulting solution using anion exchange chemistry [*Krogh*, 1973]. Total procedural blanks during the course of these analyses were 3.5 pg for Pb, and less than 1 pg for U. Total common Pb is reported for each analysis in Table 1. Pb was loaded on single rhenium filaments with silica gel and phosphoric acid. Isotopes of Pb were measured with a VG Sector-54 thermal ionization mass spectrometer using a Daly detector in ion counting mode, except for zircon pick 3 and titanite pick 2 which were measured in static mode using the Daly collector (^{204}Pb) and four Faraday collectors. Uranium was loaded with phosphoric acid and colloidal graphite on rhenium filaments and was measured as metal ions in static mode by utilizing three Faraday collectors and an average ^{235}U ion beam intensity of 2.5×10^{-13} amps. Errors in the $^{238}U/^{206}Pb$, $^{235}U/^{207}Pb$, and $^{207}Pb/^{206}Pb$ ratios were estimated using the method of *Ludwig* [1988a]. Linear regressions and calculations of intercepts and uncertainties

followed *Ludwig* [1988b]. Initial Pb composition estimates are based on the two-stage evolutionary model of *Stacey and Kramers* [1975] and age calculations were made using the decay constants 1.55125×10^{-10}/yr for ^{238}U and 9.8485×10^{-10}/yr for ^{235}U [*Steiger and Jäger*, 1977]. All age uncertainties are quoted at the 2σ confidence level.

$^{40}Ar/^{39}Ar$ analyses

Mineral separates for $^{40}Ar/^{39}Ar$ laser-fusion and furnace step-heating analyses were obtained from different size fractions using heavy liquids and a Frantz isodynamic separator and were further purified by hand removal of remaining impurities. Composite hornblende grains were broken up by vigorous saltation for 5 to 10 minutes in distilled water, sonically induced by a Cole-Parmer series 4710 ultrasonic homogenizer. The minimum purity of the hornblende, muscovite, biotite, and K-feldspar separates for $^{40}Ar/^{39}Ar$ analyses is estimated at 99%. Principal visible impurities in biotite, muscovite, and hornblende fractions were small intergrowths of chlorite, and in K-feldspar fractions, quartz and plagioclase.

Mineral separates were encased in aluminum foil and irradiated in a layered aluminum canister for seven to ten hours in the core of the McMaster University Nuclear Reactor Facility. Separates were prepared and irradiated in three packages, designated CLAIR 26, CLAIR 28, and CLAIR 30. Samples for laser-fusion and laser step-heating analyses averaged 50 grains in size. Samples for furnace step-heating analyses were larger. Interlaboratory standard Fish Canyon tuff sanidine (reference age of 27.84 Ma) [*Cebula et al.*, 1986] was included in each canister layer as a neutron flux monitor. The J values for packages CLAIR 26, CLAIR 28, and CLAIR 30 are 0.001638 ± 0.000008, 0.00166 ± 0.00002, and 0.00231 ± 0.00001 respectively.

All samples were analyzed at the Cambridge Laboratory for Argon Isotopic Research (CLAIR) facility at the Massachusetts Institute of Technology using a MAP 215-50 mass spectrometer. Laser-fusion analyses were conducted by exposing three-to five-

grain subsamples to the continuous emission of the argon-ion laser operating at approximately four watts for ten seconds. Laser incremental heating experiments were conducted by bathing approximately 60 grain subsamples with a defocussed beam for two minutes at successively higher laser output powers until all argon was released upon melting. Furnace samples were baked at successive temperature increments for five minutes in a double-vacuum resistance furnace and cooled to 200°C to 250°C between heating intervals. Model ages were calculated from the derived isotopic ratios assuming a decay constant of $5.81 \times 10^{-11} \pm 0.06 \times 10^{-11}$ yr^{-1} for the production of radiogenic ^{40}Ar from ^{40}K [*Steiger and Jäger*, 1977]. Additional details of laboratory procedures, description of facilities, and propagation of uncertainties can be found in *Hodges et al.* [1994].

Compiled age and sample data for argon analyses are given in Table 2; the raw data for incremental heating and laser analyses are given in Table 3. Release spectra and inverse isotope correlation diagrams for all samples are shown in Figures 5 to 13. Age estimates are based on linear regression analysis of inverse isotope correlation diagrams [*Roddick et al.*, 1980]. The mean squared weighted deviation (MSWD) of data from the best fit line was used to determine the choice of the regression treatment. If the calculated MSWD for a particular data set was within 2σ of the expected value of 1 [*Wendt and Carl*, 1991], then the regression treatment of *York* [1969] was used (hereafter referred to as a York 2 regression) which provides errors in fit parameters that are based largely on the magnitude of analytical uncertainties. Values of MSWD > $1+2\sigma$ were obtained for many samples, indicating that the scatter of data about a straight line was too large to be explained by analytical imprecision alone. In these cases, the regression treatment of *York* [1966] (hereafter referred to as a York 1 regression) was used which yields uncertainties based largely on data scatter. Samples prepared for laser-fusion analysis were divided into ten subsamples that were fused separately, yielding a model age for each subsample (assuming an atmospheric value for initial $[^{40}Ar/^{36}Ar]_0$ analogous to a conventional K-Ar age). If the

subsamples formed a linear array on an inverse isotope correlation diagram, the cooling age was calculated with a York 1 or York 2 regression. If not, a weighted mean model age with uncertainties was calculated from the multiple subsample analyses using the inverse of the variance in each subsample's model age as the weighting factor. All uncertainties are reported at the 2σ level.

Several of the K-feldspar samples analyzed by furnace step heating produced U-shaped release spectra. This type of behavior in K-feldspars is commonly interpreted to reflect the outgassing of two or more diffusion domains, which may have become closed to the escape of argon at different temperatures or may incorporate different components of excess argon [e.g., *Heizler and Harrison*, 1988; *Lovera et al.*, 1989; *Foster et al.*, 1990]. For each of the K-feldspar analyses that exhibited this behavior, cooling ages for both the low temperature (low-T) and high temperature (high-T) domains were determined by York 1 or York 2 regressions of the data on an inverse isotope correlation diagram. The cooling ages for high-T domains are typically less precise, owing to the difficulty of fitting a straight line to tightly clustered data.

Hornblendes from the Vrondou pluton were characterized by microprobe analysis of samples 91-12 and 94-95 at the JEOL microprobe facility at M.I.T. A sample from the same outcrop as 93-127 was also analyzed. Amphibole formulation based on 23 oxygen atoms [*Leake*, 1978] indicates that all hornblendes are calcic amphiboles with Si^{IV} averaging between 6.1 and 6.7, $Mg/(Mg+Fe^{II})$ averaging between 0.44 and 0.64, and $(Na+K)_A$ averaging between 0.38 and 0.46 for the various samples. Biotite from the Vrondou pluton has a Mg/(Mg+Fe) content of 51% to 58% in quartz monzonite samples [*Theodorikas*, 1983]. K-feldspars are typically K-Na binary solid solution series with χ_{Or} ranging from 87% to 97% in microcline [*Theodorikas*, 1983].

SAMPLE DESCRIPTION AND ANALYTICAL RESULTS

U-Pb Analyses

Euhedral to subhedral, pale yellow titanites are abundant accessory minerals in the Vrondou pluton and its mylonitized equivalents. They typically occur as discrete grains, up to 2 mm in length. In mylonites, they typically have their long axes oriented parallel to S- or C-planes. They are frequently broken with the subhedral fragments strung out along C-planes. Aligned and broken grains suggest that crystallization occurred before the formation of the mylonitic fabric. Euhedral zircons are present as inclusions in biotite, hornblende, and feldspar phenocrysts. Imaging with a scanning electron microscope revealed eroded cores in most of the zircon grains.

$^{206}Pb/^{238}U$, $^{207}Pb/^{235}U$, and $^{207}Pb/^{206}Pb$ ages obtained in 2 titanite and 4 zircon analyses from sample 93-127 are summarized in Table 1 and plotted on a concordia diagram (Figure 4). $^{207}Pb/^{235}U$ and $^{207}Pb/^{206}Pb$ ages of both titanite and zircon fractions from the Vrondou pluton are poorly constrained because of the low initial concentration of ^{235}U in young intrusive rocks. The first titanite fraction is concordant with a $^{206}Pb/^{238}U$ age of 23.7 ± 0.1 Ma and a $^{207}Pb/^{235}U$ age of 24.1 ± 1.0 Ma. The second titanite fraction is reversely discordant with a $^{206}Pb/^{238}U$ age of 23.6 ± 0.1 Ma and a $^{207}Pb/^{235}U$ age of 21.6 ± 0.9 Ma. Although reverse discordance is typically explained by excess ^{206}Pb in high thorium phases such as monazite (e.g., *Schärer* [1984]), the $^{208}Pb/^{206}Pb$ ratios of these titanites indicate they are not thorium enriched relative to each other or the zircons. It is more likely that the reverse discordance results from incomplete dissolution during the analysis and the second titanite fraction should be rejected.

Four zircon fractions yield $^{206}Pb/^{238}U$ ages between 27.6 ± 0.1 Ma and 39.5 ± 0.1 Ma and $^{207}Pb/^{235}U$ ages between 28.2 ± 0.1 Ma and 50.9 ± 0.2 Ma (Table 1). The discordant zircon fractions are interpreted to reflect derivation of the Vrondou magma from a heterogeneous source and/or the assimilation of heterogeneous crust during pluton emplacement. Zircon fractions 1, 2, and 4 fall close to concordia and define a linear array

subparallel to concordia. Because the array is subparallel to concordia, the lower concordia intercept is poorly defined and can be given little geologic significance.

$^{40}Ar/^{39}Ar$ Analyses

Tertiary intrusive rocks and mylonitized equivalents

91-12

Sample 91-12 is a medium-grained granite proto-mylonite collected from the Elaion stock approximately 400 m below the projection of the Strymon Valley detachment fault (Figure 3). It is composed of approximately 60% plagioclase and K-feldspar (microcline), 20% quartz, 13% hornblende, 3% biotite, 1% titanite, 1% epidote, 1% chlorite, and 1% magnetite. Accessory minerals include zircon and apatite. The fabric is poorly defined and there is no preferred crystallographic orientation. Hornblende is typically intergrown with biotite.

Hornblende from the 80-120 mesh size fraction (120 μm to 180 μm) was analyzed by furnace step heating (Table 3.1). The release spectrum for this sample is irregular and a meaningful plateau could not be identified (Figure 5a). The data form a linear array on an inverse isotope correlation diagram yielding a York 2 isochron age of 29.0 ± 0.7 Ma with an initial $[^{40}Ar/^{36}Ar]_0 = 300 \pm 20$, indistinguishable from the modern atmospheric value (Figure 5b).

91-113

Sample 91-113 is a fine to medium-grained, S-C granite mylonite collected from the Elaion stock approximately 100 m below the projection of the Strymon Valley detachment fault (Figure 3). It is composed of approximately 50% plagioclase and K-feldspar, 20% quartz, 10% chlorite, 10% hornblende, 3% titanite, 3% epidote, 2% biotite, and 2% magnetite. Accessory minerals include zircon and apatite. S and C planes have been brought into a parallel foliation through extreme shearing. This foliation is defined by

compositional zonation, quartz ribbons, flattened feldspar grains, chlorite foliation, attenuated magnetite aggregates, and undissolved residue. K-feldspar occurs as broken porphyroclasts up to 2 mm long and commonly exhibits mechanical twinning. Hornblende grains form subhedral blocky porphyroclasts up to 0.5 mm across. Biotite has a retrograde reaction to chlorite and is present as incompletely reacted relict grains, surrounded by chlorite.

Hornblende and K-feldspar from the 80-100 mesh size fraction (150 μm to 180 μm) were separated from sample 91-113 for dating by $^{40}Ar/^{39}Ar$ laser fusion. Because biotite could not be easily separated from chlorite, it was not analyzed. Ten hornblende subsamples yield model ages between 30.0 ± 0.9 Ma and 50 ± 1 Ma and a mean model age of 39.5 ± 0.4 Ma (Table 3.2). Ten K-feldspar subsamples yield model ages between 7.3 ± 0.8 Ma and 11 ± 1 Ma and a mean model age of 9.6 ± 0.2 Ma (Table 3.3). On an inverse isotope correlation diagram, the K-feldspar data cluster together precluding a more detailed isochron analysis (Figure 6).

91-132

Sample 91-132 is a medium-grained S-C granite mylonite collected from the southern margin of the Vrondou pluton approximately 700 m below the projection of the Strymon Valley detachment fault (Figure 3). It is composed of ~ 70% plagioclase and K-feldspar (microcline), 25% quartz, and 5% biotite. Accessory minerals include hornblende, magnetite, titanite, zircon, and apatite. K-feldspar and plagioclase form porphyroclasts in a matrix of recrystallized quartz and insoluble residue. Both are altered to sericite with plagioclase grains typically being more heavily altered. K-feldspar occurs as roughly equidimensional grains approximately 2.5 mm across but also occurs as porphyroclasts up to 5 mm in length. Broken grains and mechanical twinning are common. Biotite grains are about 0.5 mm in length and are aligned parallel to the C-foliation plane.

K-feldspar and biotite from the 80-100 mesh size fraction (150 μm to 180 μm) from sample 91-132 were analyzed by $^{40}Ar/^{39}Ar$ methods. Analytic results for furnace step-heating of K-feldspar are given on Table 3.4 and shown graphically in Figures 7a and 7b. The first heating increment produced gas with an old age of about 15 Ma, interpreted to result from excess argon. Ages then drop to a minimum age of about 10 Ma for several heating increments and then climb to a second relatively flat near-plateau at about 16 Ma. On an inverse isotope correlation diagram, steps 2 to 6 yield a York 2 regression age of 9.7 ± 0.1 Ma with an initial $[^{40}Ar/^{36}Ar]_0 = 300 \pm 50$, indistinguishable from atmospheric composition. Heating increments 9 to 15 produced over 55% of the total released gas and form a second linear array on an inverse isotope correlation diagram. A York 2 regression through these data gives an age of 9.5 ± 0.1 Ma with a poorly constrained initial $[^{40}Ar/^{36}Ar]_0 = 900 \pm 300$.

Laser-fusion analyses of 10 biotite subsamples yielded model ages between 11 ± 10 Ma and 20 ± 3 Ma (Table 3.5). On an inverse isochron diagram, a York 1 regression yields an age of 16 ± 3 Ma and an initial $[^{40}Ar/^{36}Ar]_0$ very close to atmospheric (300 ± 30) (Figure 7c).

93-127

Sample 93-127 is a medium-grained hornblende granite collected from near the summit of the Vrondou pluton (Figure 3). It is composed of ~60% plagioclase and K-feldspar, 25% quartz, 8% hornblende, 6% biotite, and 1% titanite. Accessory phases include magnetite, apatite, zircon, and chalcopyrite. K-feldspar occurs as microcline with grains up to 5 mm across. Hornblende crystals form euhedral to subhedral prisms up to 2 mm long intergrown with biotite grains up to 2 mm across.

K-feldspar, biotite, and hornblende from sample 93-127 were analyzed by $^{40}Ar/^{39}Ar$ methods. K-feldspar from the 80-100 mesh size fraction (150 μm to 180 μm) was analyzed by furnace step heating (Table 3.6, Figures 8a and 8b). The initial heating

increment released gas with an old age of 24 Ma interpreted to result from excess argon. The release spectrum then drops to a minimum at about 12 Ma for steps 2 through 9 and then climbs to ages of about 15 Ma. Regressing steps 2 to 6 on an inverse isotope correlation diagram gives a York 2 age of 12.7 ± 0.1 Ma with an initial $[^{40}Ar/^{36}Ar]_0 = 290 \pm 90$, equal to modern air. Argon released from the high-T diffusion domain (steps 10-14) yields a York 2 regression age of 13.6 ± 0.1 with an initial $[^{40}Ar/^{36}Ar]_0 = 520 \pm 50$.

Laser-fusion analyses of fifteen biotite subsamples from the 35-60 mesh size fraction (250 μm to 500 μm) produced model ages between 14 ± 1 Ma and 17.2 ± 0.9 Ma (Table 3.7). Due to laser misalignment, five subsamples were incompletely fused during initial analysis (4, 6, 7, 8, and 9). After the misalignment was corrected, these five subsamples were completely fused (producing analyses 15, 14, 13, 12, and 11, respectively). Because different biotite grains were fused in each of the two sets of analyses, these data are interpreted as ten independent analyses on smaller subsamples of biotite. The fifteen biotite analyses form a linear array on an inverse isochron plot (Figure 8c) yielding a York 1 regression age of 16.4 ± 0.6 Ma with an initial $[^{40}Ar/^{36}Ar]_0$ of 260 ± 20.

Laser-fusion analyses of ten hornblende subsamples from the 80-100 mesh size fraction (150 μm to 180 μm) produced model ages between 19 ± 1 Ma and 24 ± 1 Ma (Table 3.8). The analyses form a fairly linear array on an inverse isochron plot (Figure 8d) with a York 1 regression age of 22 ± 2 Ma and an initial $[^{40}Ar/^{36}Ar]_0$ of 260 ± 50, indistinguishable from modern atmospheric composition.

Sample 93-135

Sample 93-135 is a medium-grained hornblende quartz monzonite (proto-mylonite ?) collected from the western portion of the Vrondou pluton (Figure 3). It is composed of about 55% plagioclase and K-feldspar (microcline), 15% quartz, 10% hornblende, 10% chlorite, 3% titanite, 3% magnetite, and 2% epidote. Accessory phases include apatite and

zircon. K-feldspar occurs as microcline with grains up to 2.5 mm across. Plagioclase grains are as large as 1.5 mm. Some feldspar grains are broken and mechanically twinned. Hornblende crystals form euhedral to subhedral prisms up to 2 mm long and are extensively reacted to form chlorite. All original biotite has been altered to chlorite.

K-feldspar from the 80-100 mesh size fraction (150 μm to 180 μm) was analyzed by furnace step-heating in 14 increments to constrain the low temperature cooling history of the western Vrondou pluton (Table 3.9, Figures 9a and 9b). The initial two heating increment released gas with anomalously old ages (> 40 Ma) interpreted to result from excess argon. The release spectrum then drops to a minimum between 9 and 12 Ma for steps 3 through 8 and then climbs to ages of about 14 Ma. Regressing steps 3 to 6 on an inverse isotope correlation diagram gives a York 2 age of 9.4 ± 0.2 Ma with an initial $[^{40}Ar/^{36}Ar]_0 = 350 \pm 40$. A York 2 regression through heating steps 7 to 14 yields an age of 10.7 ± 0.2 Ma with an initial $[^{40}Ar/^{36}Ar]_0 = 520 \pm 50$.

Sample 94-95

Sample 94-95 is a medium-grained hornblende quartz monzonite collected from the eastern Vrondou pluton (Figure 3). It is composed of approximately 60% plagioclase and K-feldspar, 15% quartz, 20% hornblende, 2% magnetite, and less than 1% each of titanite, biotite, and epidote. Accessory phases include zircon and apatite. K-feldspar occurs as microcline with grains up to 3 mm across. Twinned plagioclase grains are as large as 1.5 mm and often show a strong zonation from core to rim. Hornblende crystals form large subhedral poikilitic crystals up to 3 mm in length containing plagioclase, K-feldspar, titanite, and magnetite. Biotite grains are small (up to 0.2 mm) and are always intergrown with hornblende crystals.

K-feldspar from the 80-100 mesh size fraction (150 μm to 180 μm) was analyzed by furnace step-heating in 14 increments to constrain the low temperature cooling history of the eastern Vrondou pluton (Table 3.10, Figures 10a and 10b). The volume of gas

released in the first three heating increments was at the level of the blank, yielding no meaningful data. The next five heating increments release only 10% of the gas, with ages increasing from 8 Ma to 14 Ma. The remaining 6 heating increments all released volumetrically significant amounts of gas with ages increasing to 18 Ma. An inverse isotope correlation diagram (Figure 10b) does not show evidence for the degassing of a low temperature diffusion domain such as was observed in the other K-feldspar heating experiments. A York 1 regression through heating steps 9 to 14 yields an age of 16 ± 1 Ma with a poorly constrained initial $[^{40}Ar/^{36}Ar]_0 = 800 \pm 500$.

Hornblende from the 80-100 mesh size fraction (150 μm to 180 μm) was analyzed by furnace step heating to determine the high temperature cooling history of the eastern part of the Vrondou pluton (Table 3.11). Over 90% of the gas was released in the three highest temperature increments, defining a plateau age of 30.1 ± 0.2 Ma (Figure 10c). The data also form a linear array on an inverse isotope correlation diagram (Figure 10d). A York 2 isochron regressed through the data yields an age of 30.0 ± 0.4 Ma with an initial $[^{40}Ar/^{36}Ar]_0 = 310 \pm 100$, equal to atmospheric composition.

Falakron Marble Series

11-J-91

Sample 11-J-91 is a medium-grained, type-II S-C mylonitic muscovite schist collected from the uppermost portion of the Falakron Marble Series southeast of Mt. Menoikion, approximately 200 m below the Strymon Valley detachment fault and more than 5 km from exposed Tertiary intrusives. It is the furthest south and east sample that has been analyzed from the northern Rhodope metamorphic core complex. It is composed of approximately 50% quartz, 30% muscovite, and 20% plagioclase (albite) and K-feldspar. Accessory phases include detrital zircon, monazite, and rutile grains. The main foliation is defined by aligned muscovite laths, quartz ribbons, and sigmoidal plagioclase porphyroclasts tails. Muscovite "fish" are up to 0.7 mm in length.

Muscovite from the 60-80 size fraction (180 μm to 250 μm) was analyzed by furnace step heating in 10 heating steps, yielding an irregular release spectrum with model ages ranging from 20 to 30 Ma (Figure 11a). The initial four heating increments probably reflect excess argon in the sample. An inverse isotope correlation diagram is shown in Figure 11b. York 1 regressions through the data have little geological significance.

Sample 91-127

Sample 91-127 is a medium-grained biotite gneiss collected from near the top of Mt. Menoikion approximately 400 m below the projection of the Strymon Valley detachment fault and between 2 and 4 km from the unexposed portions of the Elaion stock (Figure 3). It is composed of ~ 60% quartz and feldspar, 20% biotite, 10% epidote, 5% muscovite, and 5% calcite. Garnet, titanite, and apatite are present as accessory mineral phases. A weak foliation defined by compositional zonation and small (up to 0.25 mm), aligned biotite laths can be observed in thin section.

Ten biotite subsamples from the 100-120 mesh size (125 μm to 150 μm) were analyzed by laser fusion, yielding model ages between 15 ± 1 Ma and 17.8 ± 0.6 Ma with a mean model age of 16.3 ± 0.2 Ma (Table 3.13). An inverse isotope correlation diagram provides no additional information because the data are clustered along the $^{39}Ar/^{40}Ar$ axis (Figure 12).

Sample 92-16

Sample 92-16 was collected from the lowest part of the Falakron Marble Series approximately 100 m from a major apophysis of the Vrondou pluton and 1 km from its main body. It is composed of about 35% plagioclase and K-feldspar, 30% biotite, 25% quartz, 5% garnet, 2% muscovite, and 2% chlorite. Accessory minerals include opaque ore minerals (ilmenite ?) and fibrolitic sillimanite. A weak foliation is defined by aligned biotite (up to 0.5 mm long) and muscovite (up to 0.3 mm long) laths and quartz ribbons.

Muscovite from the 60-80 mesh size fraction (180 μm to 250 μm) was analyzed by laser step heating in 10 increments (Table 3.14). The irregular release spectrum is shown in Figure 13a. On an inverse isotope correlation diagram (Figure 13b) a York 2 isochron regression through the final four heating steps (representing 65% of the released gas) yields an age of 19.3 ± 0.4 Ma with an initial $[^{40}Ar/^{36}Ar]_0 = 200 \pm 100$.

DISCUSSION

Closure temperature

U-Pb dating of zircon and titanite, coupled with $^{40}Ar/^{39}Ar$ dating of hornblende, muscovite, biotite, and K-feldspar, help to elucidate the Tertiary thermal and tectonic history of the northern part of the Rhodope metamorphic core complex. Although a nominal closure temperature of 600° ± 50° C is assumed for Vrondou pluton titanites [*Ghent et al.*, 1988], this value may somewhat underestimate the true titanite closure temperature which is probably strongly grain size dependent. *Mezger et al.* [1991] estimated closure temperatures of 540° C and 670° C for grains 0.75 and 10 mm in length, respectively, at a cooling rate of 10° C/m.y. Vrondou pluton titanites fall within this size range, predictably yielding an older age than hornblende from the same sample. Closure temperatures for hornblende, muscovite, and biotite were calculated using the approach of *Dodson* [1973] with an assumed cooling rate of 50° C/m.y. and experimental diffusion parameters [*Robbins*, 1972; *Harrison*, 1981; *Harrison et al.*, 1985]. Closure temperatures for hornblende, muscovite, and biotite calculated in this manner are 520° ± 50° C, 420° ± 50° C, and 330° ± 50° C, respectively, and are comparable to the range of nominal closure temperatures for these systems [*McDougall and Harrison*, 1988].

Because K-feldspar is an anhydrous mineral that remains essentially stable during an incremental heating experiment, it is possible to model the argon release as a thermally activated volume diffusion, obtaining closure temperatures for individual samples [*Berger and York*, 1981]. For the three K-feldspar analyses that exhibited multiple argon

components on an inverse isotope correlation diagram (91-132, 93-127, and 93-135), a unique closure temperature was calculated for the low-temperature domain. The closure temperature was derived using the approach of *Dodson* [1973] with values of D_0/l^2 and E calculated from a linear regression of the low temperature step-heating data on an Arrhenius diagram (Figure 14a-c). (D_0 is the diffusion coefficient at infinitely high temperature, l is the characteristic diffusion dimension, and E is the activation energy.) Closure temperatures calculated in this manner ranged from 100° ± 20° C to a poorly constrained 200° ± 100° C (Table 4). Although the higher temperature increments of a K-feldspar release spectrum have been used with sophisticated models to calculate cooling histories (e.g., *Lovera et al.* [1989]; *Lovera et al.* [1991]; *Arnaud et al.* [1993]), the numerous heating steps and temperature cycling necessary for such an analysis were not attempted in this study. A nominal closure temperature of 150° ± 50° C was used for K-feldspar laser-fusion mean model ages (sample 91-113) and for K-feldspar samples that did not clearly exhibit multiple diffusion domain behavior (sample 94-95) [*McDougall and Harrison*, 1988].

The geochronologic data are summarized on a temperature-time diagram in Figure 15. The $^{40}Ar/^{39}Ar$ data record continuous cooling of the Vrondou pluton at rates ranging from 30° C/m.y. to 70° C/m.y. The data also record spatial variation in cooling ages which can be interpreted in the context of southwest-directed simple shear along the Strymon Valley detachment fault.

Intrusion of the Vrondou pluton: a composite body?

The earliest phase of intrusive activity in the northern Rhodope metamorphic core complex is indicated by Upper Oligocene $^{40}Ar/^{39}Ar$ hornblende cooling ages (29.0 ± 0.7 Ma and 30.0 ± 0.4 Ma) from the Elaion stock and the eastern Vrondou pluton. These data corroborate Upper Oligocene K-Ar and Rb-Sr cooling ages reported from the Vrondou pluton [*Marakis*, 1969; *Dürr et al.*, 1978; N. Kolocotroni, pers. comm., 1991] and are

comparable to cooling ages reported for other plutons intruded into the Rhodope metamorphic core complex. In the strictest interpretation, these data represent the cooling of the eastern Vrondou pluton and the Elaion stock through the hornblende closure temperature of ~520° C. However, given the presence of widespread igneous activity in northeastern Greece and southern Bulgaria during Oligocene time and the probable rapid initial cooling experienced by a pluton intruded into a cooler country rock, it is unlikely that these cooling ages are more than a few million years younger than the actual emplacement age of the eastern Vrondou pluton and Elaion stock.

A concordant U-Pb titanite age of 23.7 ± 0.1 Ma from sample 93-127 from the central Vrondou pluton, corroborated by a $^{40}Ar/^{39}Ar$ hornblende cooling age of 22 ± 2 Ma, suggests that what has been traditionally considered as the Vrondou pluton may be a composite body formed by at least two separate pulses of intrusive activity separated by several million years. However, these data can be interpreted alternatively as cooling ages of an Oligocene central Vrondou pluton that cooled slower than the eastern Vrondou pluton. This alternate interpretation is considered less likely because it requires the central Vrondou pluton to have been maintained at a temperature above the closure temperatures of titanite and hornblende for at least six million years after its intrusion, inconsistent with simple models of conductive pluton cooling. Lower Miocene U-Pb zircon ages have been reported from the Symvolon pluton in the southern Rhodope metamorphic core complex [*Dinter et al.*, 1995] and shallow intrusive stocks in the Serbo-Macedonian Range [*Frei*, 1992], indicating magmatism was ongoing in the north Aegean region in the lowermost Miocene and a younger pulse of intrusive activity in the Vrondou pluton would not be an isolated event. Because the data are multiply interpretable, the geologic significance of a composite Vrondou pluton should not be overstated.

A boundary between two intrusive phases was not delineated during the course of this study. Previous workers have described compositional variations within the pluton as gradational [*Theodorikas*, 1983]. From his limited description, hornblende samples used

in *Marakis'* [1969] geochronologic study appear to have been collected from the eastern portion of the Vrondou pluton, which is represented in this study by sample 94-95. Interpreting the data in the context of a composite pluton, the eastern Vrondou pluton and the Elaion stock comprise an older Oligocene intrusive phase and the central and western Vrondou pluton form a younger uppermost Oligocene to lowermost Miocene intrusive phase. *Theodorikas* [1983] made a similar interpretation of two intrusive phases forming the Vrondou pluton, identifying an early eastern low-silica intrusive pulse and a later western intermediate-silica intrusive pulse.

Recent work in the Rhodope Mountains and the Serbo-Macedonian Range suggests that mid Tertiary pluton emplacement occurred in an extensional setting [*Koukouvelas and Pe-Piper*, 1990; *Frei*, 1992; *Dinter et al.*, 1995]. This has been most satisfactorily demonstrated for the Symvolon pluton where textural and structural evidence suggest that it was intruded into a northeast-trending zone of pure-shear extension (the Symvolon Shear Zone) [*Dinter et al.*, 1995]. While it is possible that the intrusion of the Vrondou pluton is syn-extensional, all of the mylonitic structural fabrics along its margins can be attributed to the early ductile phase of motion on the Strymon Valley detachment fault. Unlike the Symvolon pluton, where there is convincing textural evidence for syn-extensional intrusion, the eastern and central portion of the Vrondou pluton are completely undeformed. Northeast dipping lineations are rare in the Vrondou pluton; almost all ductile fabrics are sub-parallel to the overlying Strymon Valley detachment fault. Sense-of-shear indicators are consistently top-to-the-southwest, unlike those observed in the Symvolon pluton which show a bimodal shear sense [*Dinter*, 1994]. Finally, high temperature mylonitic fabrics were not observed in the margins of the Vrondou pluton; mylonitic textures indicate formation at temperatures in the range of 300° to 350° C, which occur several million years after extension along the Symvolon Shear Zone (see below).

The early cooling history of the Vrondou pluton is indicated by segments 1a and 1b in Figure 15. Segment 1a tracks the cooling of the eastern Vrondou pluton from the

solidus (~700°C [*Theodorikas*, 1983]) to the closure temperature in hornblende (520° C) at an assumed rate > 50° C/m.y. Segment 1b tracks the cooling of the central Vrondou pluton from the solidus through the closure temperature of titanite (taken to be 600° C) at 23.7 ± 0.1 Ma to the closure temperature of hornblende (520° C) at 22 ± 2 Ma at a rate of about 40° C/m.y. These two segments are interpreted to reflect the fairly rapid cooling of one or more intrusive phases after their intrusion into the cooler country rock. If the closure temperature of titanite is significantly overestimated, slower cooling of the central Vrondou pluton would be implied, more consistent with a single Oligocene phase of intrusion.

The Upper Oligocene (30 - 24 Ma) thermal history of the Vrondou pluton and the northern Rhodope metamorphic core complex is poorly constrained and must be inferred from cooling ages from the Falakron Marble Series. Close to the Vrondou pluton, muscovite and biotite cooling ages (samples 92-16 and 91-127) indicate either maintenance of temperature conditions above the muscovite and biotite closure temperatures throughout the Late Oligocene or complete re-equilibration during a second phase of intrusive activity. Away from the Vrondou pluton, muscovite ages (sample 11-J-91) are interpreted to indicate complete isotopic re-equilibration during an Oligocene thermal event, followed by either slow cooling until Miocene time or partial re-equilibration during a second thermal pulse. Figure 15 shows two inferred cooling paths for this period, reflecting conditions close to the Vrondou pluton (segment 2a) and in the Falakron Marble Series (segment 2a'). Segment 2b tracks the cooling of the central Vrondou pluton from the closure temperature in hornblende to the closure temperature of muscovite at a rate of about 40° C/m.y. The thermal histories of the eastern Vrondou pluton, central Vrondou pluton, and northern Rhodope metamorphic core complex converge above the closure temperature of biotite.

Middle Miocene mylonitization of the Vrondou pluton and the tectonic denudation of the Rhodope metamorphic core complex

After the intrusion of the Vrondou pluton and its rapid initial cooling, the cooling history of the Rhodope metamorphic core complex is controlled by tectonic denudation by the Strymon Valley detachment fault. An expected rapid acceleration of the cooling rate cannot be clearly defined on the temperature-time diagram (Figure 15), probably because the onset of extension occurred before the complete decay of the thermal pulse generated by the intrusion of the Vrondou pluton. Because the earliest motion on the Strymon Valley detachment fault is associated with the formation of greenschist-grade granite mylonite along the margins of the Vrondou pluton and the Elaion stock, the timing of detachment initiation can be roughly constrained by superimposing estimates of mylonitization conditions on the temperature-time diagram. Unfortunately, the conditions of mylonitization are poorly known and are likely to vary around the Vrondou pluton. Taking the upper range of conditions implied by the textural fabrics observed in thin section (less than about 400° C), implies detachment faulting initiated between 16 and 20 Ma (Figure 15, segment 3).

Tectonic denudation of the northern Rhodope metamorphic core complex is recorded by cooling between the biotite and K-feldspar closure temperatures at rates between 30° C/m.y. and 60° C/m.y. as indicated by segments 4a, 4b, and 4b' on Figure 15, reflecting conditions for the eastern, central, and western Vrondou pluton, respectively. Continued motion on the Strymon Valley detachment fault brought the Vrondou pluton and the Rhodope metamorphic core complex to the surface by Late Miocene time. Paleontologic data indicate that the Vrondou pluton and Rhodope metamorphic core complex were at the surface supplying material into the supradetachment Serres Basin by Late Miocene time (between 9.8 Ma and 6 Ma) [*Armour-Brown et al.*, 1977; *Karistineos and Georgiades-Dikeoulia*, 1985]. The oldest conglomerates in the Serres Basin contain clasts of the Vrondou pluton, including breccia sheets of mylonitic granite sourced from

active fault scarps. K-feldspar ages from the southwestern part of the core complex overlap slightly with fossil ages, suggesting the earliest deposits in the Serres Basin were sourced from the exposed eastern part of the core complex before unroofing was complete.

Calculation of detachment rate

Variation of $^{40}Ar/^{39}Ar$ K-feldspar cooling ages can be attributed to a sample's relative position in the transport direction of the Strymon Valley detachment fault (231° SW). K-feldspar cooling ages projected perpendicularly into a southwest cross section show a clear age progression from northeast to southwest with samples younging to the southwest at a rate of 0.44 ± 0.02 Ma/km (Figure 16). This age progression is interpreted to reflect the top-to-the-southwest denudation of the Rhodope metamorphic core complex and can be converted into a displacement rate on the detachment fault assuming a linear relationship exists between fault displacement and cooling of the footwall through the K-feldspar closure temperature. If this linear relationship holds, the transport rate along the northern segment of the Strymon Valley detachment fault is 2.3 ± 0.1 km/m.y., less than half of the 6.0 km/m.y calculated by *Dinter et al.* [1995] along the southern segment of the detachment fault. An age progression was not apparent in biotite cooling ages, but the limited number of analyses from the Vrondou pluton and the large uncertainties do not exclude the existence of such an age progression.

It is important to recognize potential uncertainties in the calculated rate of detachment faulting. The K-feldspar regression does not take into account the different closure temperatures for each K-feldspar analysis. However, rapid cooling rates in the core complex suggest this may be a second order effect. Individual ages are not changed significantly by incorporating differences in closure temperature into the data. In addition, the calculated detachment rate is only a statistical fit to the data; the best-fit line in Figure 16 was calculated assuming that all of uncertainty in the slope of the line results from the uncertainty in each sample's cooling age, rather than the spread of the data about a line

(essentially a York 2 regression). A satisfactory visual fit to the data can be obtained with a displacement rate between 1.5 and 3.5 km/m.y. Despite these potential uncertainties, this estimate of displacement rate is comparable to the average displacement rate calculated by dividing the width of the core complex (~40 km) by the approximate duration of detachment faulting (~16 to 4 Ma), yielding a rate of approximately 3.3 km/m.y.

REFERENCES

Armour-Brown, A., H. de Bruijn, C. Maniati, G. Siatos, and P. Neisen, 1977, The geology of the Neogene sediments north of Serrai and the use of rodent faunas for biostratigraphic control, *in* G. Kallergis, ed., Colloquium on the Geology of the Aegean Region, VI, Proceedings, Athens, Institute of Geological and Mining Research, v. 2, p. 615-622.

Armstrong, R.L., 1982, Cordilleran metamorphic core complexes – From Arizona to southern Canada, *Annual Reviews of Earth and Planetary Sciences*, v. 10, p. 129-154.

Arnaud, N.O., M. Brunel, J.M. Cantagrel, and P. Tapponnier, 1993, High cooling and denudation rates at Kongur Shan, Eastern Pamir (Xinjiang, China) revealed by $^{40}Ar/^{39}Ar$ Alkali feldspar thermochronology, *Tectonics*, v. 12, p. 1335-1346.

Berger, G.W., and D. York, 1981, Geothermometry from $^{40}Ar/^{39}Ar$ dating experiments, *Geochimica and Cosmochimica Acta*, v. 45, p. 795-811.

Berthe, D., P. Choukroune, and P. Jegouzo, 1979, Orthogneiss, mylonite, and non coaxial deformation of granites: The example of the South Armorican Shear Zone, *Journal of Structural Geology*, v. 1, p. 31-42.

Cebula, G.T., M.J. Kunk, H.H. Mehnert, C.W. Naeser, J.D. Obradovich, and J.F. Sutter, 1986, The Fish Canyon Tuff, a potential standard for the ^{40}Ar-^{39}Ar and fission-track dating methods, *Terra Cognita*, v. 6, p. 139-140.

Coney, P.J., 1980, Cordilleran metamorphic core complexes: An overview, *Geological Society of America Memoir* 153, p. 7-31.

Davis, G.A., and G.S. Lister, 1988, Detachment faulting in continental extension: Perspectives from the Southwestern U.S. Cordillera, *in* S.P. Clark, B.C. Burchfiel, and J. Suppe, eds., Processes in Continental Lithospheric Deformation, Boulder, CO, Geological Society of America Memoir 218, p. 133-159.

Del Moro, A., K. Kyriakopoulos, A. Pezzino, P. Atzori, and A. Lo Giudice, 1990, The metamorphic complex associated to the Kavala plutonites: An Rb-Sr geochronological,

petrological and structural study, Proceedings of the 2nd Hellenic-Bulgarian Symposium, Thessaloniki, 1989, Geologica Rhodopica, v. 2, p. 143-152.

Dinter, D.A., and L. Royden, 1993, Late Cenozoic extension in northeastern Greece: Strymon Valley detachment and Rhodope metamorphic core complex, *Geology*, v. 21, p. 45-48.

Dinter, D.A., 1994, Tectonic evolution of the Rhodope metamorphic core complex, Northeastern Greece [Ph.D. Thesis], Massachusetts Institute of Technology, Cambridge, MA, 320 pp.

Dinter, D.A., A.M. Macfarlane, W. Hames, C. Isachsen, and L. Royden, 1995, U-Pb and $^{40}Ar/^{39}Ar$ geochronology of the Symvolon granodiorite: Implications for the thermal and structural evolution of the Rhodope metamorphic core complex, northeastern Greece, in press, *Tectonics*.

Dodson, M.H., 1973, Closure temperature in cooling geochronological and petrological systems, *Contributions to Mineralogy and Petrology*, v. 40, p. 259-274.

Dürr, St., R. Altherr, J. Keller, M. Okrusch, and E. Seidel, 1978, The median Aegean crystalline belt: Stratigraphy, structure, metamorphism, magmatism, *in* Alps, Apennines, and Hellenides–geodynamic investigation along geotraverses by an international group of geoscientists, Inter-union Commission on Geodynamics, Scientific Report 38, H. Cloos, D. Roeder, and K. Schmidt eds., Schweizerbart, Stuttgart, p. 455-477.

Eleftheriadis, G. and H.J. Lippolt, 1984, Altersbestimmungen zum oligozänen vulkanismus der Süd-Rhodopen/Nord Griechenland, *Neues Jahrbuch für Geologie und Paläontologie, Monatshefte*, v. 3, p. 179-191.

Foster, D.A., T.M. Harrison, P. Copeland, and M.T. Heizler, 1990, Effects of excess argon with large diffusion domains on K-feldspar ages spectra, *Geochimica and Cosmochimica Acta*, v. 54, p. 1699-1708.

Frei, R., 1992, Isotope (Pb, Rb-Sr, S, O, C, U-Pb) geochemical investigations on Tertiary intrusives and related mineralizations in the Serbomacedonian Pb-Zn, Sb+Cu-Mo metallogenetic province in northern Greece [Ph.D. Thesis], ETH, Zurich, Switzerland, 231 pp.

Ghent, E.D., M.Z. Stout, and R.R. Parrish, 1988, Determination of metamorphic pressure-temperature-time (PTt) paths, in E.G. Nisbet and C.M.R. Fowler eds., Short Course on Heat, Metamorphism, and Tectonics, Saint Johns's, Mineralogical Association of America, p. 155-188.

Harre, W., F. Kockel, H. Kreuzer, H. Lenz, P. Müller, and H.W. Walther, 1968, Über Rejuvenationen im Serbo-Mazedonischen Massiv (Deutung radiometrischer Alterbestimmungen), Proceedings of the 23rd International Geological Congress, Prague, p. 223-236.

Harrison, T.M., 1981, Diffusion of ^{40}Ar in hornblende, *Contributions to Mineralogy and Petrology*, v. 78, p. 324-331.

Harrison, T.M., I. Duncan, and I. McDougall, 1985, Diffusion of ^{40}Ar in biotite: Temperature, pressure, and compositional effects, *Geochimica et Cosmochimica Acta*, v. 49, p. 2461-2468.

Heizler, M.T., and T.M. Harrison, 1988, Multiple trapped argon isotope components revealed by $^{40}Ar/^{39}Ar$ isochron analysis, *Geochimica and Cosmochimica Acta*, v. 52, p. 1295-1303.

Hodges, K.V., W.E. Hames, W. Olszewski, B.C. Burchfiel, L.H. Royden, and Z. Chen, 1994, Thermobarometric and $^{40}Ar/^{39}Ar$ geochronologic constraints on the Eohimalayan metamorphism in the Dinggyê area, southern Tibet, *Contributions to Mineralogy and Petrology*, v. 117, p. 151-163.

Innocenti, F., N. Kolios, P. Manetti, R. Mazzuoli, G. Peccerillo, F. Rita, and L. Villari, 1984, Evolution and geodynamic significance of the Tertiary orogenic volcanism in northeastern Greece, *Bulletin Volcanologique*, v. 47, p. 25-37.

Jones, C.E., J. Tarney, J.H. Baker, and G. Gerouki, 1992, Tertiary granitoids of Rhodope, northern Greece: Magmatism related to extensional collapse of the Hellenic Orogen, *Tectonophysics*, v. 210, p. 295-314.

Karistineos, N.K., and E. Georgiades-Dikeoulia, 1986, The marine transgression in the Serres Basin, *Annales Géologiques des Pays Helléniques*, v. 33, p. 221-232.

Kilias, A., and D. Mountrakis, 1990, Kinematics of the crystalline sequences in the western Rhodope massif, *in* S. Konstantinos ed., Geologica Rhodopica, Proceedings of the 2nd Hellenic-Bulgarian Symposium, Thessaloniki, 1989, v. 2, Thessaloniki, Aristotle University Press, p. 100-116.

Kojumdgieva, E., I. Nikolov, P. Nedjalkov, and A. Busev, 1982, Stratigraphy of the Neogene in Sandanski graben, *Geologica Balcanica*, v. 12, p. 69-81.

Kokkinakis, A., 1980, Altersbeziehungen zwischen Metamorphosen, mechanischen, Deformationen und Intrusionen am Sudrand des Rhodope-Massivs (Makedonien, Griechenland), *Geologische Rundschau*, v. 69, p. 726-744.

Kolocotroni, C., and J.E. Dixon, 1991, The origin and emplacement of the Vrondou granite, Serres, N.E. Greece, *Bulletin of the Geological Society of Greece*, v. 25, p. 469-483.

Kotopouli, C.N. and G. Pe-Piper, 1989, Geochemical characteristics of felsic intrusive rocks within the Hellenic Rhodope: A comparative study and petrogenetic implications, *Neues Jahrbuch für Mineralogie, Abhandlungen*, v. 161, p. 141-169.

Koukouvelas, I., and G. Pe-Piper, 1991, The Oligocene Xanthi pluton, northern Greece: A granodiorite emplaced during regional extension, *Journal of the Geological Society, London*, v. 148, p. 749-758.

Krogh, T.E., 1973, A low-contamination method for hydrothermal decomposition of zircon and extraction of U and Pb for isotopic age determinations, *Geochimica et Cosmochimica Acta*, v. 37, p. 485-494.

Krogh, T.E., 1982, Improved accuracy of U-Pb zircon ages by the creation of more concordant systems using an air abrasion technique, *Geochimica et Cosmochimica Acta*, v. 46, p. 637-649.

Leake, B.A., 1978, Nomenclature of amphiboles, *American Mineralogist*, v. 63, p. 1023-1052.

Le Pichon X., and J. Angelier, 1979, The Hellenic Arc and Trench system: A key to the neotectonic evolution of the eastern Mediterranean area, *Tectonophysics*, v. 60, p. 1-42.

Lilov, P., Y. Yanev, and P. Marchev, 1987, K/Ar dating of the eastern Rhodope Paleogene magmatism, *Geologica Balcanica*, v. 17, p. 49-58.

Lister, G.S., G. Banga, and A. Feenstra, 1984, Metamorphic core complexes of Cordilleran type in the Cyclades, Aegean Sea, Greece, *Geology*, v. 12, p. 221-225.

Lister, G.S., and G.A. Davis, 1989, The origin of metamorphic core complexes and detachment faults formed during Tertiary continental extension in the northern Colorado River region, U.S.A., *Journal of Structural Geology*, v. 11, p. 65-94.

Lovera, O.M., F.M. Richter, and T.M. Harrison, 1989, The $^{40}Ar/^{39}Ar$ thermochronometry for slowly cooled samples having a distribution of diffusion domain sizes, *Journal of Geophysical Research*, v. 94, p. 17,917-17,935.

Lovera, O.M., F.M. Richter, and T.M. Harrison, 1991, Diffusion domains determined by ^{39}Ar released during step heating, *Journal of Geophysical Research*, v. 96, p. 2057-2069.

Ludwig, K.R., 1988a, PBDAT for MS-DOS: A computer program for IBM-PC compatibles for processing raw Pb-U-Th isotope data, U.S. Geological Survey Open File Report 88-542.

Ludwig, K.R., 1988b, ISOPLOT for MS-DOS: A plotting and regression program for radiogenic-isotope data, for IBM-PC compatible computers, U.S. Geological Survey Open File Report 88-557.

Marakis, G.I., 1969, Geochronologic studies of some granites from Macedonia, *Annales Géologiques des Pays Helléniques*, v. 21, p. 121-152.

Martin, L., 1987, Structure et evolution recente de la mer Egee: Apports d'une etude par sismique reflexion [Ph. D. Thesis], Universite Pierre et Marie Curie, Paris, 324 p.

McDougall, I. and T.M. Harrison, 1988, *Geochronology and Thermochronology by the $^{40}Ar/^{39}Ar$ Method*, New York, Oxford University Press, 212 p.

Meyer, W., 1968, Zur Alterstellung des Plutonismus im Südteil der Rila-Rhodope-Masse (Nordgriechenland), *Geologica et Paleontologica*, v. 2, p. 86-96.

Meyer, W., A. Pilger, F. Birk, and H. Jordan, 1963, Zur Geologie des Gebietes zwischen Strymon und Nestos (Rhodopen-Massiv) in Griechisch-Makedonien, *Neues Jahrbuch für Geologie und Paläontologie, Abhandlungen*, v. 118, p. 272-280.

Mezger, K., C.M Rawnsley, S.R. Bohlen, and G.N. Hanson, 1991, U-Pb garnet, sphene, monazite, and rutile ages: Implications for the duration of high-grade metamorphism and cooling histories, Adirondack Mts., New York, *Journal of Geology*, v. 99, p. 415-428.

Papanikolaou, D., and A. Panagopoulos, 1981, On the structural style of Southern Rhodope, Greece, *Geologica Balcanica*, v. 11 p. 13-22.

Robbins, G.A., 1972, Radiogenic argon diffusion in muscovite under hydrothermal conditions [M.S. Thesis], Brown University, Providence, RI.

Roddick, J.C., R.A. Cliff, and D.C. Rex, 1980, The evolution of excess argon in alpine biotites – a $^{40}Ar/^{39}Ar$ analysis, *Earth and Planetary Science Letters*, v. 48, p. 945-960.

Schärer, U., 1984, The effect of initial ^{230}Th disequilibrium on young U-Pb ages: The Makalu case, Himalaya, *Earth and Planetary Science Letters*, v. 67, p. 191-204.

Schermer, E.R., D.R. Lux, and B.C. Burchfiel, 1990, Temperature-time history of subducted continental crust, Mt. Olympos region, Greece, *Tectonics*, v. 9, p. 1165-1195.

Simpson, C., and D. De Paor, 1991, Deformation and kinematics of high strain zones, *Geological Society of America Short Course Notes*.

Stacey, J.S., and J.D. Kramers, 1975, Approximation of terrestrial lead isotope evolution by a two-stage model, *Earth and Planetary Science Letters*, v. 26, p. 207-221.

Steiger, R.H., and E. Jäger, 1977, Subcommission on geochronology: Convention on the use of decay constants in geo- and cosmochronology, *Earth and Planetary Science Letters*, v. 36, p. 359-362.

Theodorikas, S., 1983, The mineralogy, petrology and geochemistry of the Serres-Drama granitic complex, Northern Greece, Aristotle University of Thessaloniki, Faculty of Science, School of Geology, Scientific Annals, Thessaloniki, v. 22, n. 28, 415 p.

Wawrzenitz, N., A. Baumann, and G. Nollau, 1994, Miocene uplift of mid-crustal rocks in the Rhodope metamorphic core complex, caused by late Alpine extension of previously thickened crust (Thassos Island, Pangaeon Complex, northern Greece), 7th Congress of the Geological Society of Greece, Thessaloniki, May 25-27, 1994, abstracts, p. 74-75.

Wendt, I., and C. Carl, 1991, The statistical distribution of the mean squared weighted deviation, *Chemical Geology*, v. 86, p. 275-285.

York, D., 1966, Least squares fitting of a straight line, *Canadian Journal of Physics*, v. 44, p. 1079-1086.

York, D., 1969, Least squares fitting of a straight line with correlated errors, *Earth and Planetary Science Letters*, v. 5, p. 320-324.

Table 1. U-Pb zircon and titanite data from sample 93-127 from the Vrondou pluton, northern Greece

Fraction	Weight	Concentrations		Total	Atomic ratios								Ages (Ma)			
		U	Pb*	Common	^{206}Pb†	^{208}Pb§	^{206}Pb§	Error	^{207}Pb§	Error	^{207}Pb§	Error	^{206}Pb	^{207}Pb	^{207}Pb	corr.
	(μg)	(ppm)	(ppm)	Pb (pg)	^{204}Pb	^{206}Pb	^{238}U	(%)	^{235}U	(%)	^{206}Pb	(%)	^{238}U	^{235}U	^{206}Pb	coef.
Zircon 1	23.2	1975.4	8.7	16.5	939.0	0.150	0.00429	0.16	0.02819	0.30	0.04765	0.24	27.6	28.2	82.1	0.615
Zircon 2	14.4	1622.9	7.5	4.0	14179.5	0.164	0.00442	0.27	0.02898	0.33	0.04757	0.18	28.4	29.0	78.1	0.826
Zircon 3	14.9	1598.1	10.2	12.3	1076.5	0.143	0.00615	0.19	0.05138	0.27	0.06059	0.17	39.5	50.9	624.7	0.766
Zircon 4	5.9	2695.2	15.7	16.0	490.8	0.121	0.00579	0.33	0.03896	0.76	0.04878	0.65	37.2	38.8	137.4	0.534
Titanite 1	130	478.9	2.0	322.4	64.5	0.255	0.00368	0.45	0.02401	3.96	0.04730	3.60	23.7	24.1	64.6	0.804
Titanite 2	120	683.4	2.7	413.6	65.4	0.222	0.00366	0.42	0.02154	4.13	0.04262	3.78	23.6	21.6	-189.5	0.852

* Radiogenic Pb.

† Measured ratio corrected for fractionation only; Pb fractionation correction is 0.1% ± 0.03% per amu.

§ Corrected for fractionation, spike, blank, and initial common Pb; U blank = 1 pg ± 50%; Pb blank = 3.5 pg ± 50%. Initial common Pb composition is calculated from *Stacey and Kramers* [1975] by using the interpreted age of the sample. Errors are reported in percent at the 2σ confidence interval.

Table 2. $^{40}Ar/^{39}Ar$ ages and sample characteristics, Vrondou pluton, Elaion stock, and Falakron Marble Series, northern Rhodope metamorphic core complex, northern Greece

Sample	Rock Type	Mineral	Grain size (μm)	Heating method	Steps†	Age (Ma)	Fit
91-12	Granite proto-mylonite	Hbl	125-180	furnace step-heat[2]	10	29.0 ± 0.7	II
91-113	Granite mylonite	Hbl	150-180	laser fusion[1]	10	39.5 ± 0.4	M
"	"	Kfs	150-180	laser fusion[1]	10	9.6 ± 0.2	M
91-132	Granite mylonite	Kfs	150-180	furnace step-heat[1]	16	9.7 ± 0.1	II*
"	"	"	"	"	"	9.5 ± 0.1	II*
"	"	Bt	150-180	laser fusion[1]	10	16 ± 3	I
93-127	Granite	Kfs	150-180	furnace step-heat[1]	14	12.7 ± 0.1	II*
"	"	"	"	"	"	13.6 ± 0.1	II*
"	"	Bt	250-500	laser fusion[1]	15	16.4 ± 0.6	I
"	"	Hbl	150-180	laser fusion[1]	10	22 ± 2	I
93-135	Quartz monzonite	Kfs	150-180	furnace step-heat[2]	14	9.4 ± 0.2	II*
"	"	"	"	"	"	10.7 ± 0.2	II*
94-95	Quartz monzonite	Kfs	150-180	furnace step-heat[3]	14	16 ± 1	I*
"	"	Hbl	150-180	furnace step-heat[3]	10	30.0 ± 0.4	II*
11-J-91	Muscovite schist	Ms	180-250	furnace step-heat[3]	10	20 - 30	none
91-127	Biotite gneiss	Bt	125-150	laser fusion[1]	10	16.3 ± 0.2	M
92-16	Garnet biotite schist	Ms	180-250	laser step-heat[2]	10	19.3 ± 0.4	II*

Abbreviations: Bt = biotite, Hbl = hornblende, Kfs = K-feldspar, Ms = muscovite.

† Number of heating increments for furnace and laser step-heat analyses; number of 3- to 5-grain subsamples for laser-fusion analyses.

[1] J = 0.001638 ± 0.000008. [2] J = 0.00166 ± 0.00002. [3] J = 0.00231 ± 0.00001.

Ages were calculated using fitting algorithms designated in "Fit" column: I – least-squares linear regression [*York*, 1966]; II – least-squares linear regression with correlated errors [*York*, 1969]; M – mean model age; none – ages reflect spread of model ages for all gas increments. * Indicates age calculated using data subset (see Table 3 for details).

Multiple entries for 91-132, 93-127, and 93-135 K-feldspar samples reflect interpretation of multiple Ar domains (see text).

Table 3.1. $^{40}Ar/^{39}Ar$ Furnace Analytical Data for Sample 91-12, Hornblende

T(K)	$^{39}Ar/^{40}Ar$	$^{36}Ar/^{40}Ar$	^{39}Ar (%)	$^{40}Ar^{*}$ (%)	K/Ca	Age (Ma) (± 2σ)
1100	0.0184	0.00270	5.5	20.2	0.96	32.5 ± 0.7
1150	0.0700	0.00151	7.2	55.4	0.37	23.6 ± 0.5
1175	0.0698	0.00101	8.9	70.1	0.30	29.8 ± 0.7
1200	0.0722	0.00100	11.2	70.5	0.31	29.0 ± 0.7
1225	0.0713	0.00139	14.7	58.9	0.24	24.6 ± 0.6
1250	0.0734	0.00112	21.9	66.9	0.14	27.1 ± 0.6
1275	0.0860	0.00051	44.0	85.0	0.11	29.4 ± 0.7
1300	0.1006	0.00024	68.4	92.9	0.11	27.4 ± 0.6
1350	0.0856	0.00038	77.1	88.9	0.11	30.9 ± 0.7
1550	0.0872	0.00034	100.0	89.9	0.10	30.6 ± 0.7

York 2 regression age = 29.0 ± 0.7 Ma (MSWD = 1.2). $[^{40}Ar/^{36}Ar]_0 = 310 \pm 20$.
J = 0.00166 ± 0.00002. All steps used in regression. All steps of 5 minute duration.
$^{40}Ar^{*}$ (%) – percentage of measured ^{40}Ar derived from natural decay of ^{40}K.

Table 3.2. $^{40}Ar/^{39}Ar$ Laser Fusion Analytical Data for Sample 91-113, Hornblende

Subsample	$^{39}Ar/^{40}Ar$	$^{36}Ar/^{40}Ar$	$^{39}Ar_K$ ($\times 10^{-15}$)	$^{40}Ar^{*}$ (%)	K/Ca	Age (Ma) (± 2σ)
1	0.0735	0.00084	0.776	75.2	0.17	30.0 ± 0.9
2	0.0454	0.00077	0.455	77.2	0.10	50 ± 2
3	0.0417	0.00105	0.329	69.0	0.10	48 ± 2
4	0.0504	0.00091	0.464	73.2	0.13	42 ± 2
5	0.0536	0.00085	0.565	75.0	0.10	41 ± 1
6	0.0532	0.00082	0.840	75.8	0.11	42 ± 2
7	0.0614	0.00113	0.253	66.7	0.10	32 ± 2
8	0.0524	0.00104	0.549	59.3	0.10	39 ± 1
9	0.0457	0.00108	0.402	68.0	0.09	43.5 ± 0.8
10	0.0671	0.00072	0.345	78.8	0.12	34 ± 2

Mean model age = 39.5 ± 0.4. J value: 0.001638 ± 0.000008.
$^{39}Ar_K$ – moles of irradiation-produced ^{39}Ar released during laser fusion.
$^{40}Ar^{*}$ (%) – percentage of measured ^{40}Ar derived from natural decay of ^{40}K.

Table 3.3. $^{40}Ar/^{39}Ar$ Laser Fusion Analytical Data for Sample 91-113, K-feldspar

Subsample	$^{39}Ar/^{40}Ar$	$^{36}Ar/^{40}Ar$	$^{39}Ar_K$ ($\times 10^{-15}$)	$^{40}Ar^*$ (%)	K/Ca	Age (Ma) ($\pm 2\sigma$)
1	0.2104	0.00121	1.439	64.4	24.9	9.0 ± 0.5
2	0.1974	0.00102	1.724	69.9	10.8	10.4 ± 0.4
3	0.2036	0.00141	0.891	58.3	8.3	8 ± 1
4	0.1701	0.00127	0.868	62.4	11.0	10.8 ± 0.8
5	0.2228	0.00153	1.153	54.8	16.9	7.3 ± 0.8
6	0.1939	0.00135	0.756	60.1	16.1	9 ± 1
7	0.1802	0.00112	1.088	66.8	10.1	10.9 ± 0.8
8	0.1453	0.00156	0.600	53.8	9.1	11 ± 1
9	0.2326	0.00101	1.283	70.1	35.6	8.9 ± 0.7
10	0.2123	0.00110	0.928	67.3	18.0	9 ± 1

Mean model age = 9.6 ± 0.2. J value: 0.001638 ± 0.000008.
$^{39}Ar_K$ – moles of irradiation-produced ^{39}Ar released during laser fusion.
$^{40}Ar^*$ (%) – percentage of measured ^{40}Ar derived from natural decay of ^{40}K.

Table 3.4. $^{40}Ar/^{39}Ar$ Furnace Analytical Data for Sample 91-132, K-Feldspar

T(K)	$^{39}Ar/^{40}Ar$	$^{36}Ar/^{40}Ar$	^{39}Ar (%)	$^{40}Ar^*$ (%)	K/Ca	Age (Ma) ($\pm 2\sigma$)
800	0.0702	0.00219	5.6	35.2	12.3	14.7 ± 0.1
850 +	0.1568	0.00173	6.6	49.0	14.3	9.2 ± 0.1
900 +	0.1373	0.00180	8.2	46.8	13.5	10.0 ± 0.1
950 +	0.2108	0.00106	11.4	68.7	9.3	9.6 ± 0.1
1000 +	0.2383	0.00066	15.5	80.4	10.9	9.9 ± 0.1
1050 +	0.2487	0.00062	20.7	81.7	16.3	9.7 ± 0.1
1100	0.2449	0.00059	26.4	82.4	141.8	9.9 ± 0.1
1150	0.2343	0.00042	31.4	87.4	20.0	11.0 ± 0.1
1200 *	0.2158	0.00031	35.6	90.8	100.9	12.2 ± 0.1
1250 *	0.1952	0.00059	39.9	82.5	103.3	12.4 ± 0.1
1300 *	0.1792	0.00056	44.7	83.4	116.4	13.7 ± 0.1
1350 *	0.1721	0.00049	50.8	85.7	136.1	14.6 ± 0.1
1400 *	0.1663	0.00050	58.3	85.4	152.3	15.1 ± 0.1
1450 *	0.1496	0.00053	71.7	84.3	398.4	16.6 ± 0.2
1500 *	0.1445	0.00064	91.2	81.2	679.4	16.5 ± 0.2
1700	0.1397	0.00086	100.0	74.5	108.4	15.7 ± 0.2

York 2 regression age (Low-T domain) = 9.7 ± 0.1 Ma (MSWD = 0.1). $[^{40}Ar/^{36}Ar]_0 = 300 \pm 50$.
York 2 regression age (High-T domain) = 9.5 ± 0.1 Ma (MSWD = 2.2). $[^{40}Ar/^{36}Ar]_0 = 900 \pm 300$.
J = 0.001638 ± 0.000008. Steps used in regressions are marked with plus sign for Low-T domain and with asterisk for High-T domain. All steps of 5 minute duration.
$^{40}Ar^*$ (%) – percentage of measured ^{40}Ar derived from natural decay of ^{40}K.

Table 3.5. $^{40}Ar/^{39}Ar$ Laser Fusion Analytical Data for Sample 91-132, Biotite

Subsample	$^{39}Ar/^{40}Ar$	$^{36}Ar/^{40}Ar$	$^{39}Ar_K$ ($\times 10^{-15}$)	$^{40}Ar^*$ (%)	K/Ca	Age (Ma) ($\pm 2\sigma$)
1	0.0498	0.00269	0.501	20.4	30.6	12 ± 3
2	0.0537	0.00221	0.251	34.6	13.5	19 ± 4
3	0.0215	0.00311	0.146	8.1	9.1	11 ± 10
4	0.0842	0.00205	0.537	39.4	236.0	14 ± 3
5	0.0505	0.00252	0.911	25.5	25.6	14.9 ± 0.5
6	0.0569	0.00269	0.117	20.5	28.1	11 ± 10
7	0.0571	0.00247	0.658	27.1	20.7	14 ± 4
8	0.0650	0.00242	1.293	28.6	34.1	12.9 ± 0.5
9	0.0671	0.00187	0.404	44.8	22.5	20 ± 3
10	0.0495	0.00254	0.826	24.8	55.7	15 ± 2

York 1 regression age = 16 ± 3 Ma. $[^{40}Ar/^{36}Ar]_0$ = 290 ± 30. J value: 0.001638 ± 0.000008.
$^{39}Ar_K$ – moles of irradiation-produced ^{39}Ar released during laser fusion.
$^{40}Ar^*$ (%) – percentage of measured ^{40}Ar derived from natural decay of ^{40}K.

Table 3.6. $^{40}Ar/^{39}Ar$ Furnace Analytical Data for Sample 93-127, K-Feldspar

T(K)	$^{39}Ar/^{40}Ar$	$^{36}Ar/^{40}Ar$	^{39}Ar (%)	$^{40}Ar^*$ (%)	K/Ca	Age (Ma) ($\pm 2\sigma$)
800	0.0534	0.00192	2.4	43.2	52.0	23.8 ± 0.2
850 +	0.2085	0.00045	3.5	86.7	25.1	12.3 ± 0.1
900 +	0.1348	0.00142	5.2	58.0	12.2	12.7 ± 0.1
950 +	0.1915	0.00060	8.6	82.3	76.9	12.7 ± 0.1
1000 +	0.2213	0.00046	12.7	86.4	94.5	11.5 ± 0.1
1050 +	0.2243	0.00010	17.5	97.0	111.6	12.7 ± 0.1
1100	0.2227	0.00020	22.9	94.1	57.4	12.4 ± 0.1
1150	0.2196	0.00011	28.1	96.7	122.2	13.0 ± 0.1
1200	0.2157	0.00019	32.9	94.4	64.4	12.9 ± 0.1
1250 *	0.2105	0.00005	37.8	98.5	113.9	13.8 ± 0.1
1300 *	0.1998	0.00018	43.1	94.6	123.6	13.9 ± 0.1
1400 *	0.1735	0.00040	55.5	88.1	79.0	14.9 ± 0.1
1500 *	0.1613	0.00049	89.0	85.4	0.0	15.6 ± 0.2
1700 *	0.1570	0.00054	100.0	84.1	72.6	15.8 ± 0.2

York 2 regression age (Low-T domain) = 12.7 ± 0.1 Ma (MSWD = 0.1). $[^{40}Ar/^{36}Ar]_0$ = 290 ± 90.
York 2 regression age (High-T domain) = 13.6 ± 0.1 Ma (MSWD = 0.2). $[^{40}Ar/^{36}Ar]_0$ = 520 ± 50.
J = 0.001638 ± 0.000008. Steps used in regressions are marked with plus sign for Low-T domain and with asterisk for High-T domain. All steps of 5 minute duration.
$^{40}Ar^*$ (%) – percentage of measured ^{40}Ar derived from natural decay of ^{40}K.

Table 3.7. $^{40}Ar/^{39}Ar$ Laser Fusion Analytical Data for Sample 93-127, Biotite

Subsample	$^{39}Ar/^{40}Ar$	$^{36}Ar/^{40}Ar$	$^{39}Ar_K$ ($\times 10^{-15}$)	$^{40}Ar^*$ (%)	K/Ca	Age (Ma) ($\pm 2\sigma$)
1	0.1332	0.00101	4.581	70.2	36.2	15.5 ± 0.3
2	0.0979	0.00165	1.210	51.3	95.5	15.4 ± 0.8
3	0.1530	0.00051	1.275	85.0	344.6	16.3 ± 0.7
4	0.1333	0.00074	1.491	78.1	22.5	17.2 ± 0.9
5	0.1419	0.00084	1.741	75.1	4.4	15.6 ± 0.3
6	0.1088	0.00158	0.905	53.3	405.6	14.4 ± 0.8
7	0.1134	0.00147	3.425	56.5	74.6	14.7 ± 0.4
8	0.0951	0.00180	0.650	46.9	429.0	14 ± 2
9	0.1154	0.00141	2.077	58.3	186.4	14.9 ± 0.7
10	0.1225	0.00128	6.266	62.1	64.9	14.9 ± 0.2
11 (9)**	0.1590	0.00075	1.947	78.0	63.8	14.4 ± 0.4
12 (8)**	0.1542	0.00064	2.819	81.0	37.7	15.5 ± 0.2
13 (7)**	0.1325	0.00097	2.051	71.2	21.0	15.8 ± 0.8
14 (6)**	0.1335	0.00101	0.954	70.2	428.4	15.4 ± 0.5
15 (4)**	0.1398	0.00107	1.123	68.5	72.5	14 ± 1

York 1 regression age = 16.4 ± 0.6. $[^{40}Ar/^{36}Ar]_0 = 260 \pm 20$. J value: 0.001638 ± 0.000008.
$^{39}Ar_K$ – moles of irradiation-produced ^{39}Ar released during laser fusion.
$^{40}Ar^*$ (%) – percentage of measured ^{40}Ar derived from natural decay of ^{40}K.
** See text for discussion.

Table 3.8. $^{40}Ar/^{39}Ar$ Laser Fusion Analytical Data for Sample 93-127, Hornblende

Subsample	$^{39}Ar/^{40}Ar$	$^{36}Ar/^{40}Ar$	$^{39}Ar_K$ ($\times 10^{-15}$)	$^{40}Ar^*$ (%)	K/Ca	Age (Ma) ($\pm 2\sigma$)
1	0.086	0.00123	0.673	63.7	0.11	22 ± 2
2	0.104	0.00107	0.860	68.5	0.12	19 ± 1
3	0.095	0.00097	0.617	71.3	0.12	22 ± 2
4	0.107	0.00078	0.684	76.9	0.11	21 ± 1
5	0.102	0.00105	0.512	68.9	0.11	19.9 ± 0.9
6	0.109	0.00059	1.047	82.5	0.11	22 ± 1
7	0.103	0.00065	0.918	80.7	0.12	23 ± 1
8	0.071	0.00168	0.754	50.5	0.12	21 ± 1
9	0.105	0.00082	0.957	75.8	0.11	21.3 ± 0.7
10	0.107	0.00044	0.720	86.9	0.11	24 ± 1

York 1 regression age = 22 ± 2. $[^{40}Ar/^{36}Ar]_0 = 260 \pm 50$. J value: 0.001638 ± 0.000008.
$^{39}Ar_K$ – moles of irradiation-produced ^{39}Ar released during laser fusion.
$^{40}Ar^*$ (%) – percentage of measured ^{40}Ar derived from natural decay of ^{40}K.

Table 3.9. $^{40}Ar/^{39}Ar$ Furnace Analytical Data for Sample 93-135, K-Feldspar

T(K)	$^{39}Ar/^{40}Ar$	$^{36}Ar/^{40}Ar$	^{39}Ar (%)	$^{40}Ar^{*}$ (%)	K/Ca	Age (Ma) (± 2σ)
800	0.0027	0.00239	0.1	29.4	1.0	299 ± 6
850	0.0460	0.00128	2.7	62.1	25.7	40.0 ± 0.9
900 +	0.2038	0.00078	4.3	77.0	54.9	11.3 ± 0.3
950 +	0.1234	0.00177	8.7	47.8	51.7	11.6 ± 0.3
1000 +	0.2462	0.00075	14.4	77.8	73.9	9.4 ± 0.2
1050 +	0.2707	0.00039	19.2	88.6	79.2	9.8 ± 0.2
1100 *	0.2567	0.00028	23.3	91.7	71.1	10.7 ± 0.2
1150 *	0.2530	0.00038	26.6	88.7	104.0	10.5 ± 0.2
1200 *	0.2614	0.00010	29.5	97.0	79.4	11.1 ± 0.3
1250 *	0.2332	0.00045	32.7	86.8	85.6	11.1 ± 0.3
1300 *	0.2025	0.00064	37.0	81.1	133.1	12.0 ± 0.3
1400 *	0.1637	0.00092	50.4	72.8	73.4	13.3 ± 0.3
1500 *	0.1570	0.00085	87.9	74.8	277.1	14.2 ± 0.3
1700 *	0.1653	0.00071	100.0	79.1	212.3	14.3 ± 0.3

York 2 regression age (Low-T domain) = 9.4 ± 0.2 Ma (MSWD = 0.4). $[^{40}Ar/^{36}Ar]_0 = 350 \pm 40$.
York 2 regression age (High-T domain) = 10.7 ± 0.2 Ma (MSWD = 2.0). $[^{40}Ar/^{36}Ar]_0 = 520 \pm 50$.
J = 0.00166 ± 0.00002. Steps used in regressions are marked with plus sign for Low-T domain and with asterisk for High-T domain. All steps of 5 minute duration.
$^{40}Ar^{*}$ (%) – percentage of measured ^{40}Ar derived from natural decay of ^{40}K.

Table 3.10. $^{40}Ar/^{39}Ar$ Furnace Analytical Data for Sample 94-95, K-Feldspar

T(K)	$^{39}Ar/^{40}Ar$	$^{36}Ar/^{40}Ar$	^{39}Ar (%)	$^{40}Ar^{*}$ (%)	K/Ca	Age (Ma) (± 2σ)
800 †	—	—	—	—	—	—
850 †	—	—	—	—	—	—
900 †	—	—	—	—	—	—
950	0.3252	0.00106	0.4	68.6	20.5	8.8 ± 0.1
1000	0.2943	0.00081	1.0	76.0	16.6	10.7 ± 0.1
1050	0.2669	0.00042	2.0	87.7	33.1	13.6 ± 0.2
1100	0.2671	0.00043	3.6	87.4	33.2	13.6 ± 0.2
1150	0.2540	0.00045	6.2	86.7	30.7	14.2 ± 0.2
1200 *	0.2448	0.00019	30.3	94.2	35.6	16.0 ± 0.2
1250 *	0.2571	0.00006	40.6	98.2	59.7	15.8 ± 0.2
1300 *	0.2497	0.00002	45.1	99.4	87.3	16.5 ± 0.2
1400 *	0.2301	0.00011	60.3	96.8	61.6	17.4 ± 0.2
1500 *	0.2096	0.00023	90.8	93.2	96.1	18.4 ± 0.2
1700 *	0.2061	0.00035	100.0	89.6	94.1	18.0 ± 0.2

† Volume of gas released indistinguishable from blank.
York 1 regression age = 16 ± 1 Ma. $[^{40}Ar/^{36}Ar]_0$ = 800 ± 500. J = 0.00231 ± 0.00001.
Steps used in regressions are marked with asterisk. All steps of 5 minute duration.
$^{40}Ar^{*}$ (%) – percentage of measured ^{40}Ar derived from natural decay of ^{40}K.

Table 3.11. $^{40}Ar/^{39}Ar$ Furnace Analytical Data for Sample 94-95, Hornblende

T(K)	$^{39}Ar/^{40}Ar$	$^{36}Ar/^{40}Ar$	^{39}Ar (%)	$^{40}Ar^{*}$ (%)	K/Ca	Age (Ma) (± 2σ)
1100 *	0.0311	0.00265	0.6	21.8	0.2	28.9 ± 0.4
1150 *	0.0650	0.00183	0.9	45.8	0.2	29.1 ± 0.4
1175 *	0.0790	0.00150	1.3	55.8	0.1	29.2 ± 0.4
1200	0.0778	0.00045	1.8	86.6	0.1	45.8 ± 0.6
1225 *	0.0870	0.00115	2.6	66.1	0.1	31.3 ± 0.4
1250 *	0.1024	0.00080	4.0	76.2	0.1	30.7 ± 0.4
1275	0.1191	0.00014	8.8	95.9	0.1	33.2 ± 0.4
1300 *	0.1278	0.00022	31.0	93.6	0.1	30.2 ± 0.4
1350 *	0.1342	0.00010	65.4	97.0	0.1	29.9 ± 0.4
1550 *	0.1256	0.00027	100.0	91.9	0.1	30.2 ± 0.4

York 2 regression age = 30.0 ± 0.4 Ma (MSWD = 0.1). $[^{40}Ar/^{36}Ar]_0$ = 310 ± 100.
Steps used in regression are marked with asterisk. Plateau age (steps 8-10) = 30.1 ± 0.2 Ma.
J = 0.00231 ± 0.00001. All steps of 5 minute duration.
$^{40}Ar^{*}$ (%) – percentage of measured ^{40}Ar derived from natural decay of ^{40}K.

Table 3.12. $^{40}Ar/^{39}Ar$ Furnace Analytical Data for Sample 11-J-91, Muscovite

T(K)	$^{39}Ar/^{40}Ar$	$^{36}Ar/^{40}Ar$	^{39}Ar (%)	$^{40}Ar^{*}$ (%)	K/Ca	Age (Ma) (± 2σ)
900	0.1256	0.00025	0.9	92.5	25.0	30.4 ± 0.4
950	0.1498	0.00113	1.2	66.7	30.8	18.4 ± 0.2
1000	0.1267	0.00013	1.7	96.1	35.7	31.3 ± 0.4
1050	0.1196	0.00050	2.4	85.2	551.8	29.4 ± 0.4
1100	0.1220	0.00119	3.5	64.7	167.3	22.0 ± 0.3
1050	0.1303	0.00106	14.7	68.6	380.0	21.8 ± 0.3
1200	0.1358	0.00043	50.0	87.3	1033.9	26.6 ± 0.3
1250	0.1478	0.00041	64.5	87.8	1017.4	24.6 ± 0.3
1350	0.1413	0.00024	93.5	92.9	613.7	27.2 ± 0.3
1550	0.1375	0.00007	100.0	98.0	47.3	29.4 ± 0.4

Regression age not calculated. J = 0.00231 ± 0.00001. All steps of 5 minute duration.
$^{40}Ar^{*}$ (%) – percentage of measured ^{40}Ar derived from natural decay of ^{40}K.

Table 3.13. $^{40}Ar/^{39}Ar$ Laser Fusion Analytical Data for Sample 91-127, Biotite

Subsample	$^{39}Ar/^{40}Ar$	$^{36}Ar/^{40}Ar$	$^{39}Ar_K$ ($\times 10^{-15}$)	$^{40}Ar^{*}$ (%)	K/Ca	Age (Ma) (± 2σ)
1	0.1475	0.00038	0.558	88.9	178.8	18 ± 2
2	0.1406	0.00057	0.781	83.3	9.5	17 ± 1
3	0.1367	0.00095	0.714	71.9	64.2	15.5 ± 0.5
4	0.1488	0.00071	0.760	79.0	120.6	15.6 ± 0.9
5	0.1327	0.00081	0.504	75.9	98.6	16.8 ± 0.8
6	0.1531	0.00024	0.808	92.8	99.9	17.8 ± 0.6
7	0.1579	0.00068	0.537	80.0	235.3	14.9 ± 0.7
8	0.1340	0.00084	0.859	75.1	76.5	16.5 ± 0.8
9	0.1543	0.00076	0.689	77.7	48.6	15 ± 1
10	0.1566	0.00038	0.579	88.7	254.1	16.7 ± 0.5

Mean model age = 16.3 ± 0.2. J value: 0.001638 ± 0.000008.
$^{39}Ar_K$ – moles of irradiation-produced ^{39}Ar released during laser fusion.
$^{40}Ar^{*}$ (%) – percentage of measured ^{40}Ar derived from natural decay of ^{40}K.

Table 3.14. $^{40}Ar/^{39}Ar$ Laser Step Heating Analytical Data for Sample 92-16, Muscovite

Increment (Ampers)	$^{39}Ar/^{40}Ar$	$^{36}Ar/^{40}Ar$	^{39}Ar (%)	$^{40}Ar^{*}$ (%)	K/Ca	Age (Ma) (± 2σ)
11.5	0.0791	0.00118	4.6	65.2	5.0	24.5 ± 0.6
12.5	0.1138	0.00101	9.9	70.3	12.4	18.4 ± 0.4
13.0	0.1135	0.00051	14.9	84.8	54.0	22.3 ± 0.5
13.5	0.1119	0.00004	19.5	98.9	92.1	26.3 ± 0.6
14.0	0.1084	0.00066	25.3	80.5	115.3	22.1 ± 0.5
14.5	0.1293	0.00011	33.9	96.7	171.8	22.3 ± 0.5
15.0 *	0.1043	0.00138	43.2	59.3	125.3	16.9 ± 0.4
16.0 *	0.1177	0.00126	62.2	62.9	390.8	15.9 ± 0.4
18.0 *	0.1316	0.00067	85.0	80.1	59.3	18.2 ± 0.5
25.0 *	0.1412	0.00041	100.0	87.9	304.7	18.6 ± 0.4

York 2 regression age = 19.3 ± 0.4 Ma (MSWD = 0.4). $[^{40}Ar/^{36}Ar]_0 = 200 \pm 100$.
J = 0.00231 ± 0.00001. Steps used in regressions are marked with asterisk.
All steps of 2 minute duration.
$^{40}Ar^{*}$ (%) – percentage of measured ^{40}Ar derived from natural decay of ^{40}K.

Table 4. Calculated closure temperatures for K-feldspars

Sample	Increments	$\ln(D_0/l^2)$ (s^{-1})	E (kJ/mol)	T_c (°C)
91-132	5 (850 K - 1050 K)	2.2 ± 0.6	106 ± 5	100 ± 20
93-127	5 (850 K - 1050 K)	4 ± 1	119 ± 8	130 ± 40
93-135	4 (900 K - 1050 K)	7 ± 4	140 ± 30	200 ± 100

Values for kinetic parameters ln (D_0/l^2) and E (where D_0 is the diffusion coefficient at infinitely high temperature, l is the characteristic diffusion dimension, and E is the activation energy) were calculated by simple linear regression of kinetic parameters for low temperature heating steps (identified in the "Increments" column) as discussed in the text. Closure temperatures (T_c) were calculated from the kinetic parameters following the methods of *Dodson* [1973] assuming a cooling rate of 50° C/m.y. Uncertainties are based on regression statistics and are reported at the 2σ confidence level.

FIGURE CAPTIONS

Figure 1. Regional tectonic map of southeastern Europe and the northeastern Mediterranean region. RCF – Rhodope continental fragment (horizontal lines), RMP – Rhodope metamorphic province (vertical lines), RMCC – Rhodope metamorphic core complex, NAT – North Aegean Trough. From *Dinter* [1994].

Figure 2. Generalized geology of the Rhodope metamorphic core complex. From *Dinter* [1994] and *Martin* [1987].

Figure 3. Simplified geologic map of the northern Rhodope metamorphic core complex. Sample locations are shown by numbered dots. Upper inset shows regional tectonic zones of the Hellenides (EH – External Hellenides; m – Tertiary molasse basin; PZ – Pelagonian zone; AZ – Axios Zone; CRB – Circum Rhodope belt; Rmcc – Rhodope metamorphic core complex). Box indicates location of main figure. Lower inset shows lower hemisphere equal area stereonet diagram of ductile mylonitic fabrics formed by the Strymon Valley detachment fault. See Figure 2 for location.

Figure 4. Concordia plot of U-Pb zircon and titanite analyses from sample 93-127 from the central Vrondou pluton.

Figure 5. Geochronologic results for sample 91-12. $^{40}Ar/^{39}Ar$ release spectra (a) and inverse isotope correlation diagram (b) for furnace step-heating analysis of hornblende. For all isotope correlation diagrams and release spectra, numbers correspond to the sequence of release increments. Filled symbols are those used in the regression analyses, the results of which are indicated by solid lines. "Air" refers to the $^{36}Ar/^{40}Ar$ ratio of the modern atmosphere and is included for reference.

Figure 6. Geochronologic results for sample 91-113. Inverse isotope correlation diagram for 10 laser-fusion analyses of K-feldspar.

Figure 7. Geochronologic results for sample 91-132. $^{40}Ar/^{39}Ar$ release spectra (a) and inverse isotope correlation diagram (b) for furnace step-heating analysis of K-feldspar. The upper regression line is the best fit to steps 2-6 (filled symbols). The

lower line is the best fit to steps 9-15 (shaded symbols). Inverse isotope correlation diagram (c) for 10 laser-fusion analyses of biotite.

Figure 8. Geochronologic results for sample 93-127. $^{40}Ar/^{39}Ar$ release spectra (a) and inverse isotope correlation diagram (b) for furnace analysis of K-feldspar. The upper regression line in (b) is the best fit to steps 2-6 (filled symbols). The lower line is the best fit to steps 10-14 (shaded symbols). Inverse isotope correlation diagram for 15 laser-fusion analyses of biotite (c) and 10 laser-fusion analyses of hornblende (d).

Figure 9. Geochronologic results for sample 93-135. $^{40}Ar/^{39}Ar$ release spectra (a) and inverse isotope correlation diagram (b) for furnace analysis of K-feldspar. The upper regression line in (b) is the best fit to steps 3-6 (filled symbols). The lower line is the best fit to steps 7-14 (shaded symbols).

Figure 10. Geochronologic results for sample 94-95. $^{40}Ar/^{39}Ar$ release spectra (a) and inverse isotope correlation diagram (b) for furnace analysis of K-feldspar. The regression line is the best fit to steps 9-14 (filled symbols). $^{40}Ar/^{39}Ar$ release spectra (c) and inverse isotope correlation diagram (d) for furnace analysis of hornblende.

Figure 11. Geochronologic results for sample 11-J-91. $^{40}Ar/^{39}Ar$ release spectra (a) and inverse isotope correlation diagram (b) for furnace analysis of muscovite.

Figure 12. Geochronologic results for sample 91-127. Inverse isotope correlation diagram for 10 laser-fusion analyses of biotite.

Figure 13. Geochronologic results for sample 92-16. $^{40}Ar/^{39}Ar$ release spectra (a) and inverse isotope correlation diagram (b) for laser step heating of muscovite.

Figure 14. Arrhenius diagram for K-feldspar from sample 91-132 (a), 93-127 (b), and 93-135 (c). Solid squares indicate data used in the regression.

Figure 15. Interpreted time-temperature plot for the northern Rhodope metamorphic core complex. Symbols correspond to best estimates of cooling age plotted against closure temperature. Closure temperatures for titanite, hornblende, muscovite, and biotite (600° ± 50° C, 520° ± 50° C, 420° ± 50° C, and 330° ± 50° C) are nominal

estimates for a cooling rate of 50° C/m.y. When possible, closure temperatures for K-feldspars are estimated from the step-heating experiment (Table 4); otherwise a nominal closure temperature of 150° C was used. Shaded box indicates ball-park estimate of mylonitization conditions (see text). Numbers indicate segments of inferred cooling path: 1a, 2a, 4a – Eastern Vrondou pluton; 1b, 2b, 3, 4b – Central Vrondou pluton; 2a′ – Falakron Marble Series; 4b′ – Western Vrondou pluton.

Figure 16. K-feldspar cooling ages with uncertainties plotted as a function of position along the transport direction of the Strymon Valley detachment fault with best-fit linear regression to K-feldspar data. Samples projected onto cross section shown in Figure 3.

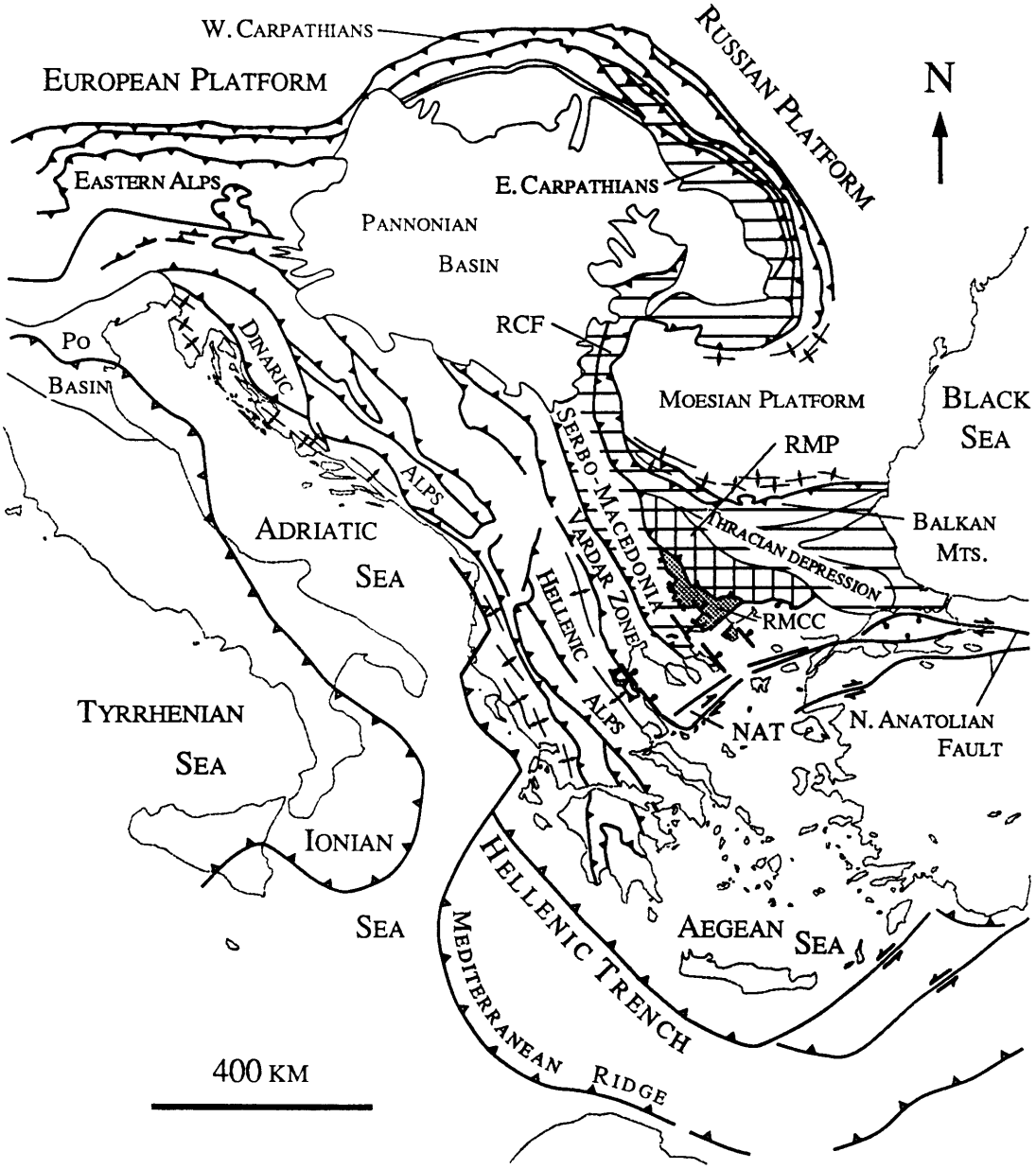
W. CARPATHIANS
EUROPEAN PLATFORM
RUSSIAN PLATFORM
N
EASTERN ALPS
E. CARPATHIANS
PANNONIAN
BASIN
RCF
PO
BASIN
DINARIC
ALPS
MOESIAN PLATFORM
BLACK
SEA
SERBO-MACEDONIA
RMP
VARDAR ZONE
THRACIAN DEPRESSION
BALKAN
MTS.
ADRIATIC
SEA
HELLENIC
ALPS
RMCC
TYRRHENIAN
SEA
NAT
N. ANATOLIAN
FAULT
IONIAN
SEA
HELLENIC TRENCH
AEGEAN SEA
MEDITERRANEAN RIDGE
400 KM

FIGURE 1

N
CENTRAL PIRIN PLUTON
SANDANSKI GRABEN
TESHOVO PLUTON
WEST THRACIAN
GNEISS COMPLEX
SMOLJAN ANDESITES
NESTOS THRUST
PARANESTION
ANDESITES
KERKINI MTNS.
KATO-NEVROKOPION
BASIN
ELATAIA-SKALOTE
GRANITES
FALAKRON MTNS.
VRONDOU PLUTON
ACHLADOCHORIAN BASIN
SIDEROKASTRO BASIN
FIGURE 3
MENOIKION
MTNS.
Drama
XANTHI PLUTON
Xanthi
SERRES BASIN
RHODOPE METAMORPHIC CORE COMPLEX
Serres
SERBO-
MACEDONIAN
GNEISS COMPLEX
STRYMON BASIN
Strymon Valley detachment
DRAMA BASIN
LEKANIS MTNS.
ANGITIS
Angitis fault
BASIN
Kavala-Xanthi
fault
Kavala
MT. PANGAION
SYMVOLON PLUTON
Transport direction of
hanging wall
AKROPOTAMOS
BASIN
AEGEAN
SEA
Vertiskos
gneiss
series
Kerdilion
gneiss
PRINOS-KAVALA BASIN
Thasos detachment
3.0
2.0
series
0
30 km

Figure 2

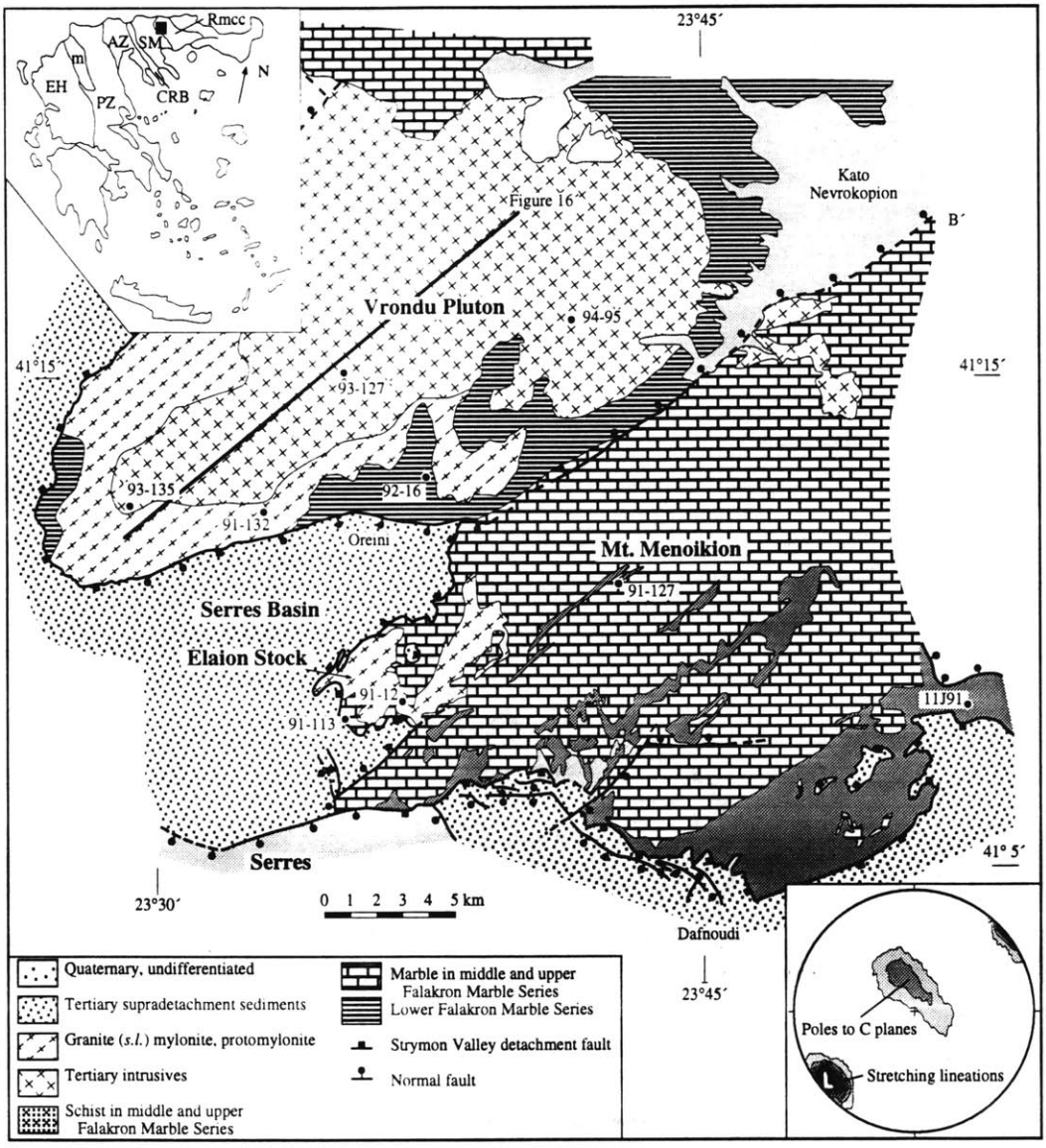
Rmcc
AZ
SM
m
EH
PZ
CRB
N
23°45′
Figure 16
Kato
Nevrokopion
B′
Vrondu Pluton
94-95
41°15′
93-127
93-135
92-16
91-132
Oreini
Mt. Menoikion
91-127
Serres Basin
Elaion Stock
91-12
91-113
11J91
41° 5′
Serres
23°30′
0 1 2 3 4 5 km
Dafnoudi
23°45′
Quaternary, undifferentiated
Tertiary supradetachment sediments
Granite (s.l.) mylonite, protomylonite
Tertiary intrusives
Schist in middle and upper Falakron Marble Series
Marble in middle and upper Falakron Marble Series
Lower Falakron Marble Series
Strymon Valley detachment fault
Normal fault
Poles to C planes
L
Stretching lineations

Figure 3

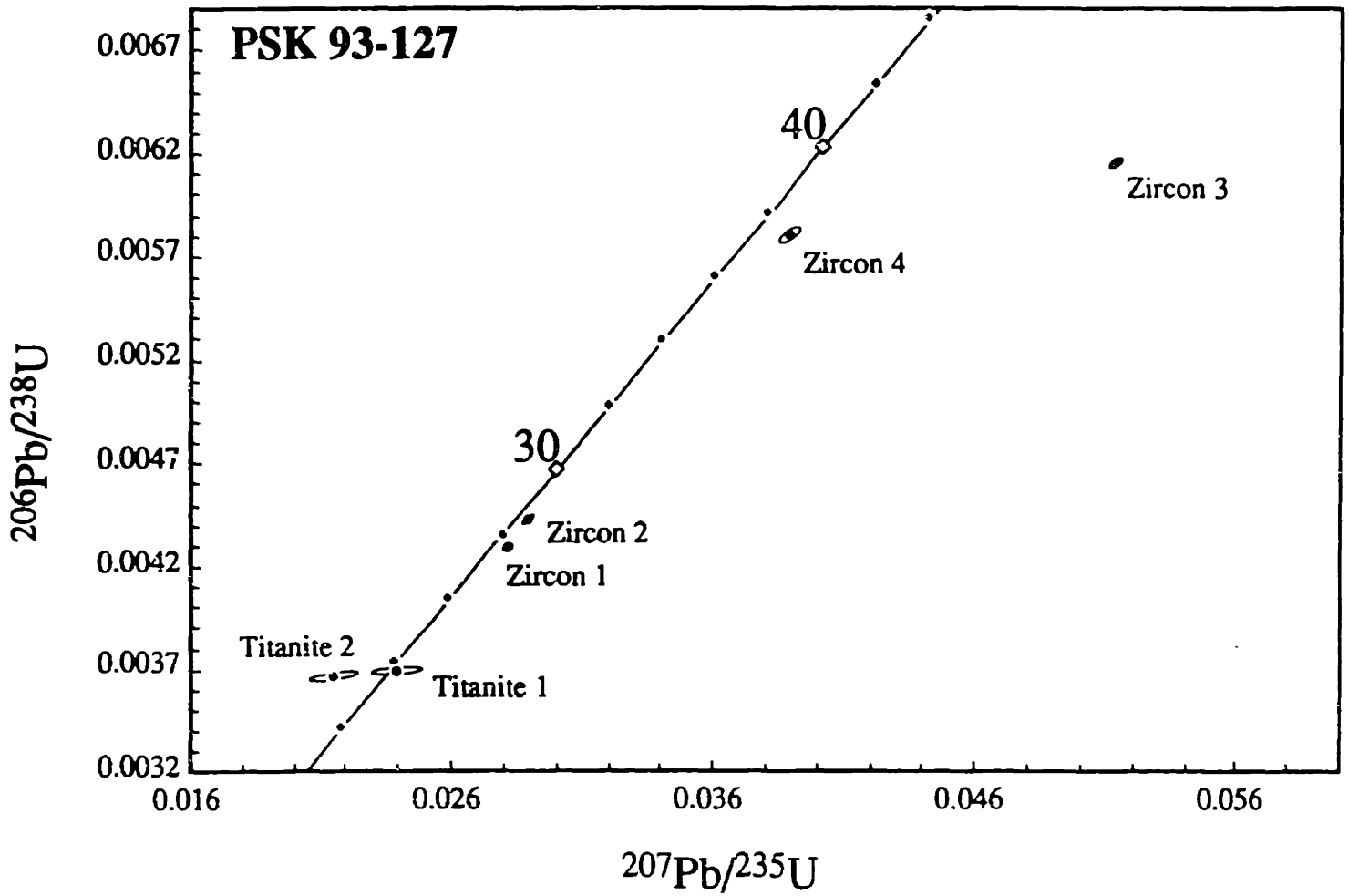
PSK 93-127
0.0067
0.0062
0.0057
0.0052
0.0047
0.0042
0.0037
0.0032
0.016
0.026
0.036
0.046
0.056
40
30
Zircon 3
Zircon 4
Zircon 2
Zircon 1
Titanite 2
Titanite 1
206Pb/238U
207Pb/235U

Figure 4

a.

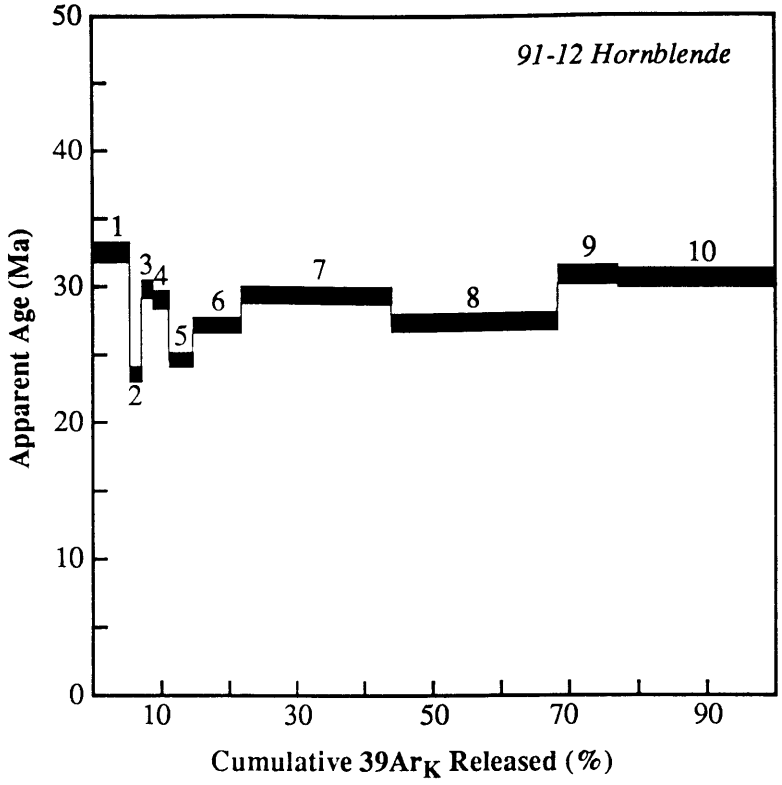
91-12 Hornblende
Apparent Age (Ma)
50
40
30
20
10
0
1
2
3
4
5
6
7
8
9
10
10
30
50
70
90
Cumulative 39Ar$_K$ Released (%)

b.

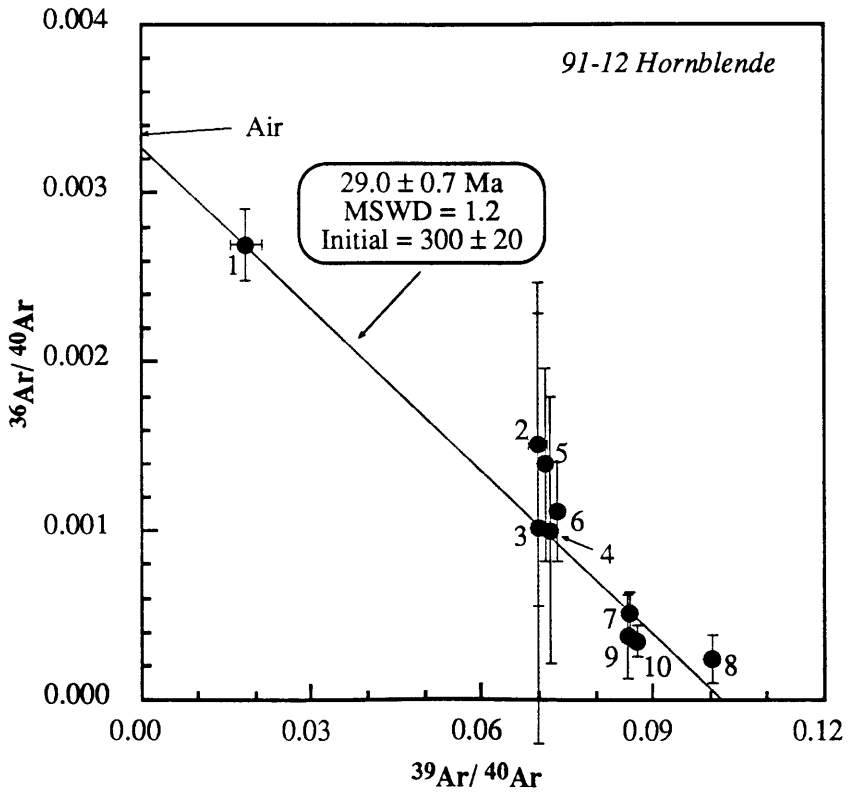
91-12 Hornblende
Air
29.0 ± 0.7 Ma
MSWD = 1.2
Initial = 300 ± 20
36Ar/40Ar
0.004
0.003
0.002
0.001
0.000
0.00
0.03
0.06
0.09
0.12
39Ar/40Ar
1
2
3
4
5
6
7
8
9
10

Figure 5

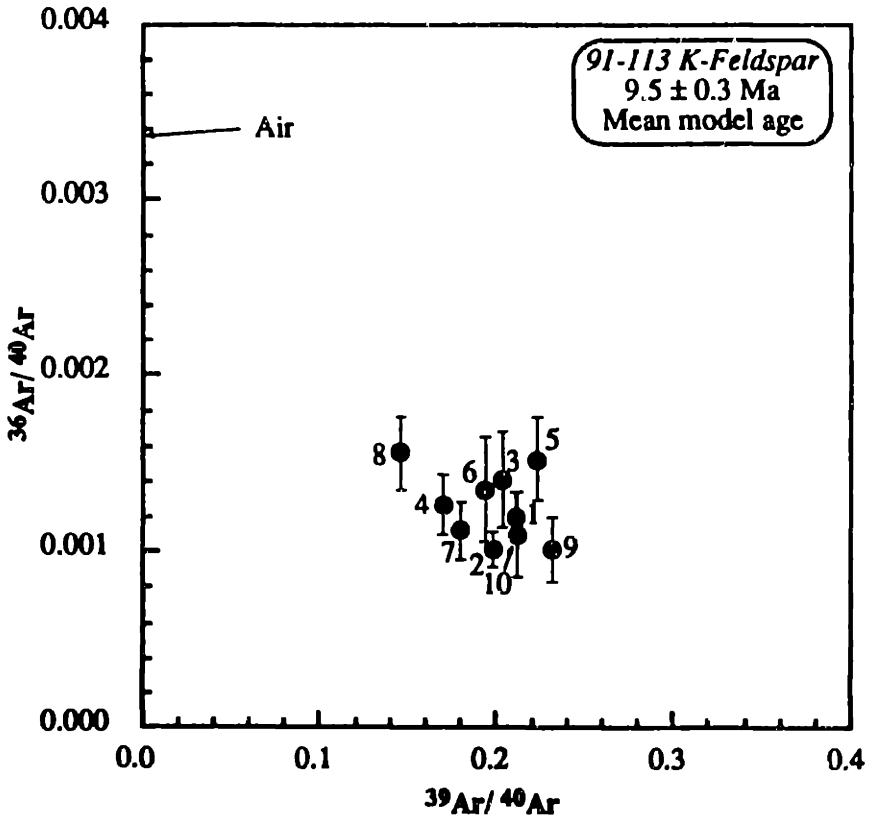
91-113 K-Feldspar
9.5 ± 0.3 Ma
Mean model age
Air
0.004
0.003
0.002
0.001
0.000
0.0
0.1
0.2
0.3
0.4
36Ar/40Ar
39Ar/40Ar
1
2
3
4
5
6
7
8
9
10

Figure 6

a.

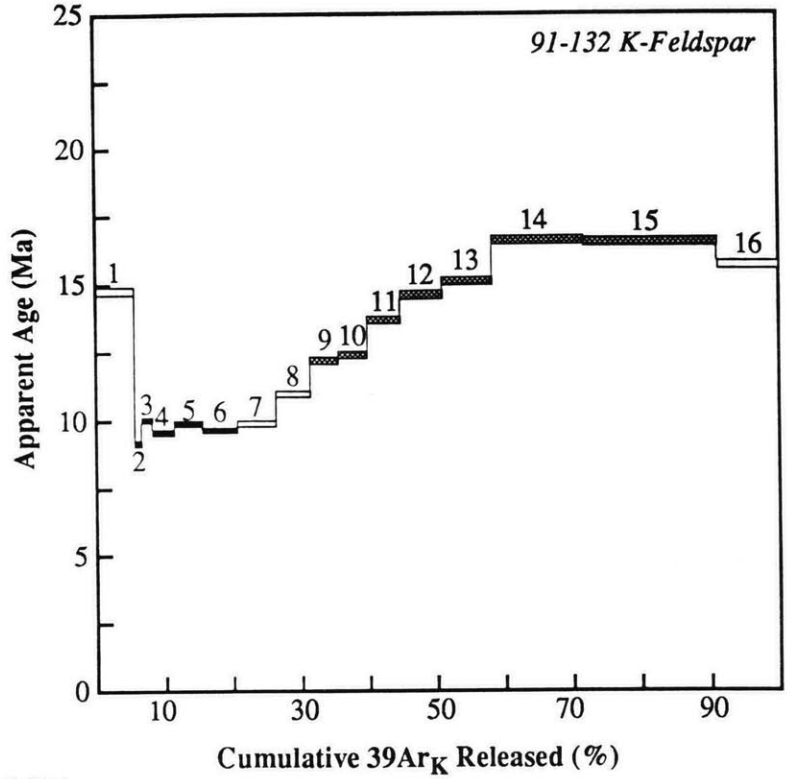
91-132 K-Feldspar
Apparent Age (Ma)
Cumulative 39Ar$_K$ Released (%)
25
20
15
10
5
0
10
30
50
70
90
1
2
3
4
5
6
7
8
9
10
11
12
13
14
15
16

b.

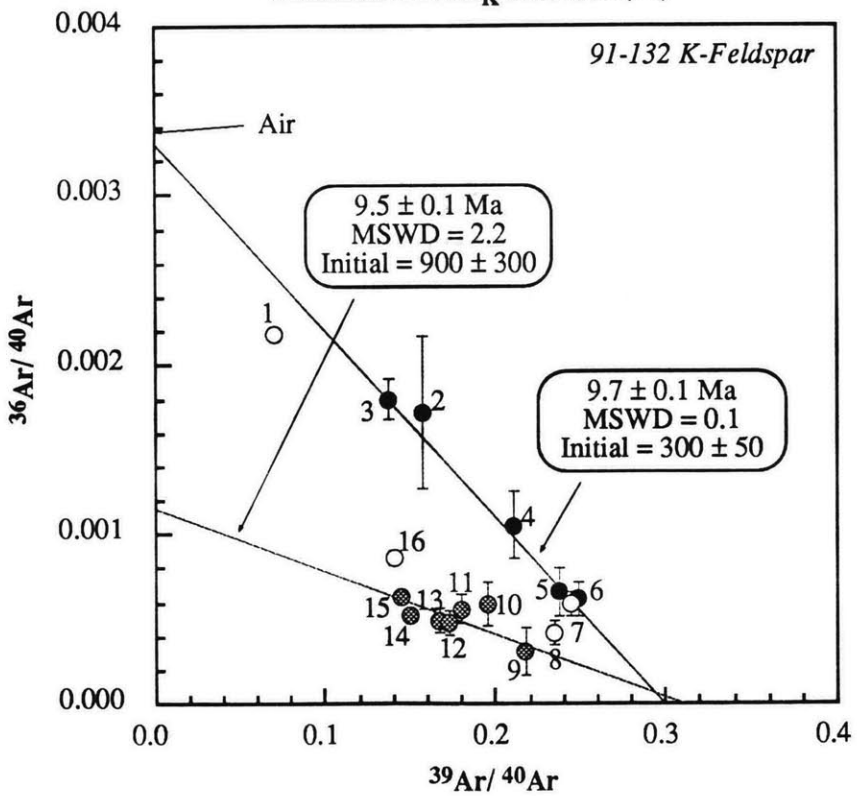
91-132 K-Feldspar
Air
9.5 ± 0.1 Ma
MSWD = 2.2
Initial = 900 ± 300
9.7 ± 0.1 Ma
MSWD = 0.1
Initial = 300 ± 50
36Ar/ 40Ar
39Ar/ 40Ar
0.004
0.003
0.002
0.001
0.000
0.0
0.1
0.2
0.3
0.4
1
2
3
4
5
6
7
8
9
10
11
12
13
14
15
16

Figure 7

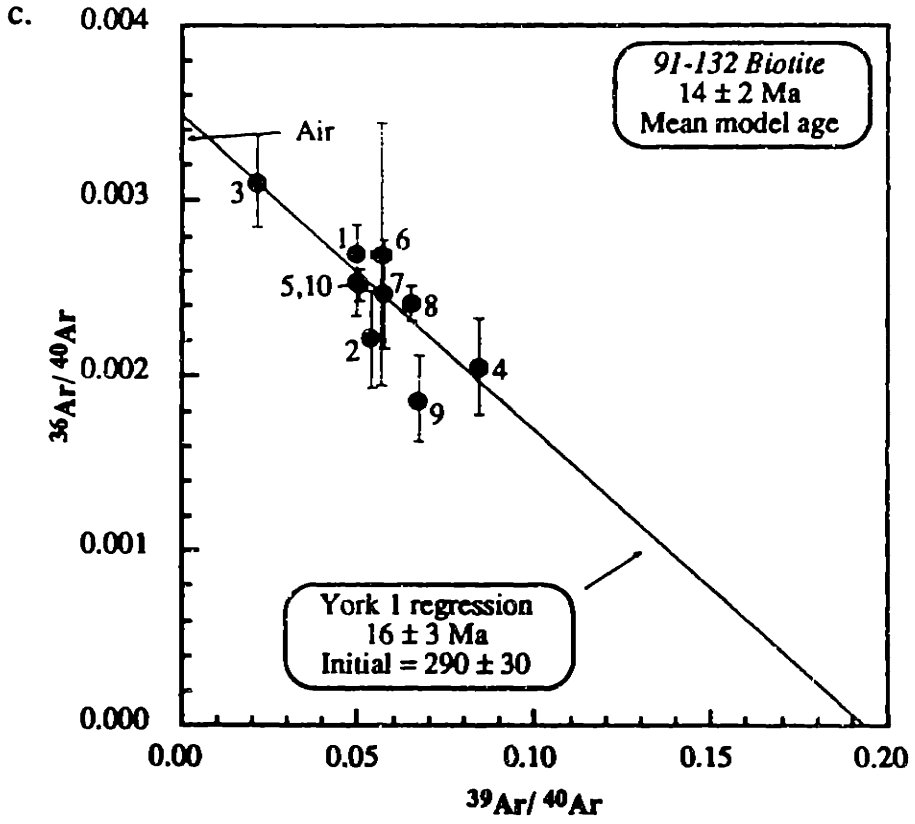
c.
0.004
0.003
0.002
0.001
0.000
$^{36}Ar/^{40}Ar$
0.00
0.05
0.10
0.15
0.20
$^{39}Ar/^{40}Ar$
91-132 Biotite
14 ± 2 Ma
Mean model age
Air
3
1
6
5,10
7
8
2
4
9
York 1 regression
16 ± 3 Ma
Initial = 290 ± 30

Figure 7

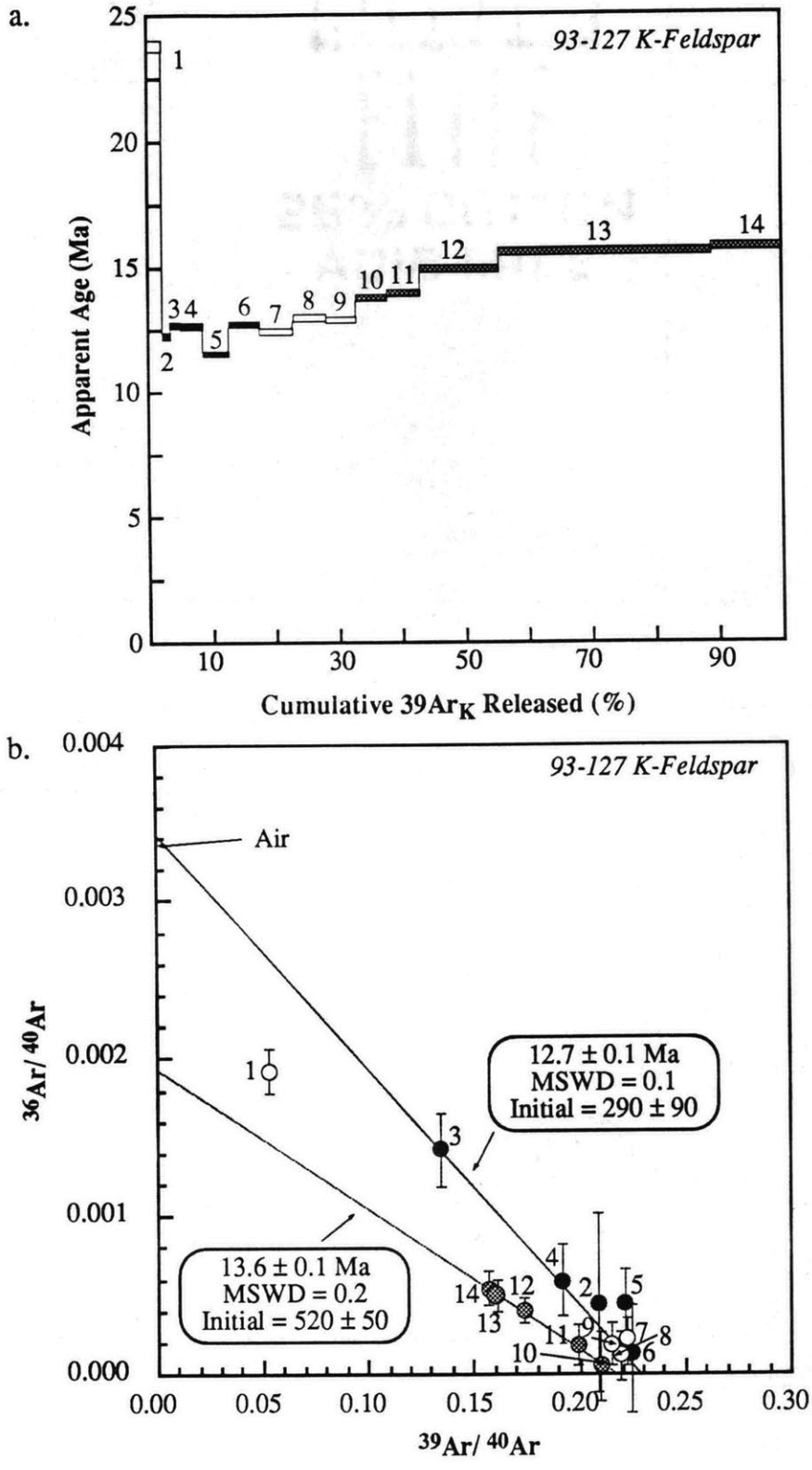
a.
93-127 K-Feldspar
Apparent Age (Ma)
Cumulative 39Ar$_K$ Released (%)
b.
93-127 K-Feldspar
Air
12.7 ± 0.1 Ma
MSWD = 0.1
Initial = 290 ± 90
13.6 ± 0.1 Ma
MSWD = 0.2
Initial = 520 ± 50
36Ar/ 40Ar
39Ar/ 40Ar

Figure 8

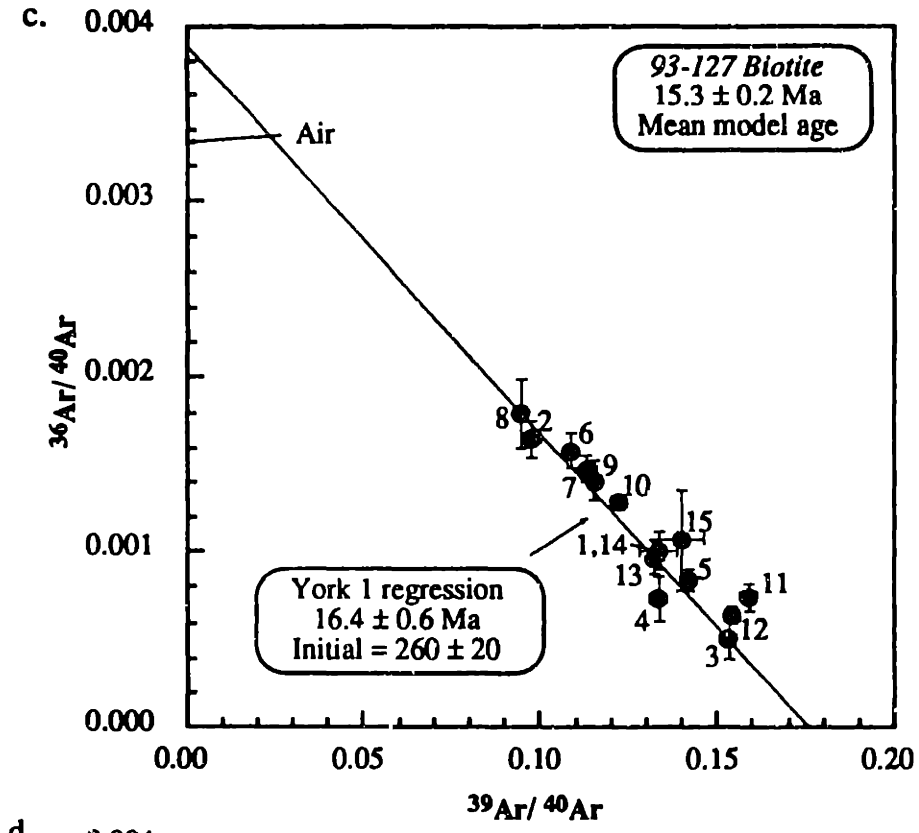
c.
93-127 Biotite
15.3 ± 0.2 Ma
Mean model age
Air
York 1 regression
16.4 ± 0.6 Ma
Initial = 260 ± 20
0.004
0.003
0.002
0.001
0.000
0.00
0.05
0.10
0.15
0.20
36Ar/ 40Ar
39Ar/ 40Ar

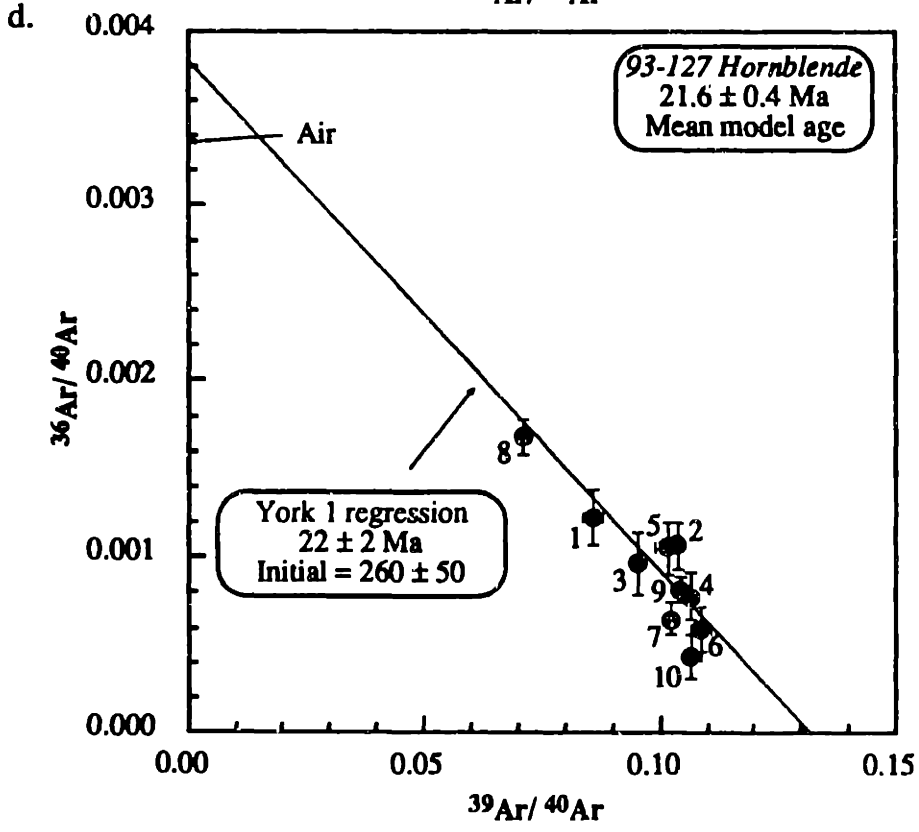
d.
93-127 Hornblende
21.6 ± 0.4 Ma
Mean model age
Air
York 1 regression
22 ± 2 Ma
Initial = 260 ± 50
0.004
0.003
0.002
0.001
0.000
0.00
0.05
0.10
0.15
36Ar/ 40Ar
39Ar/ 40Ar

Figure 8

a.

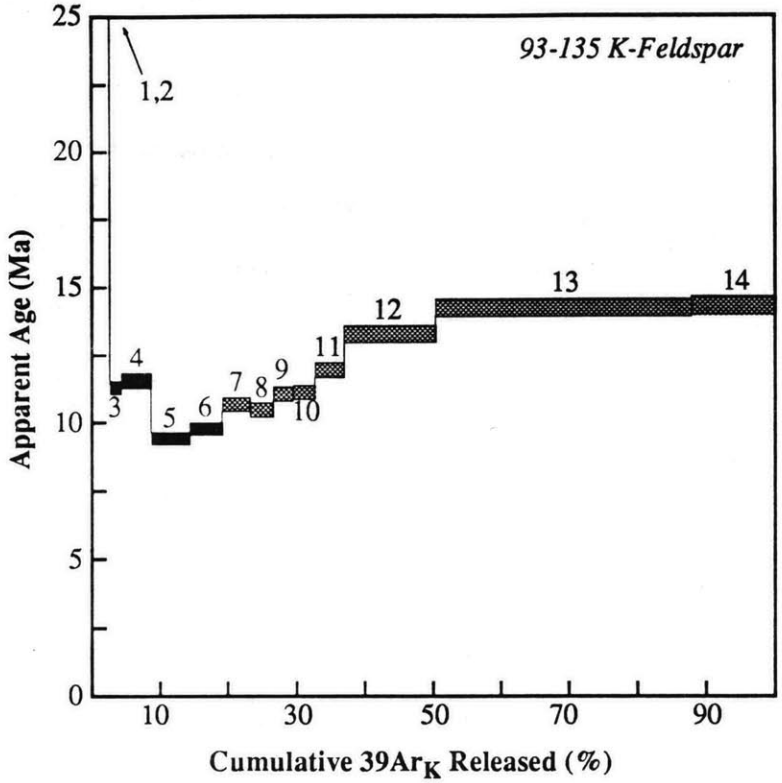
93-135 K-Feldspar
Apparent Age (Ma)
Cumulative 39Ar$_K$ Released (%)
1,2
3
4
5
6
7
8
9
10
11
12
13
14

b.

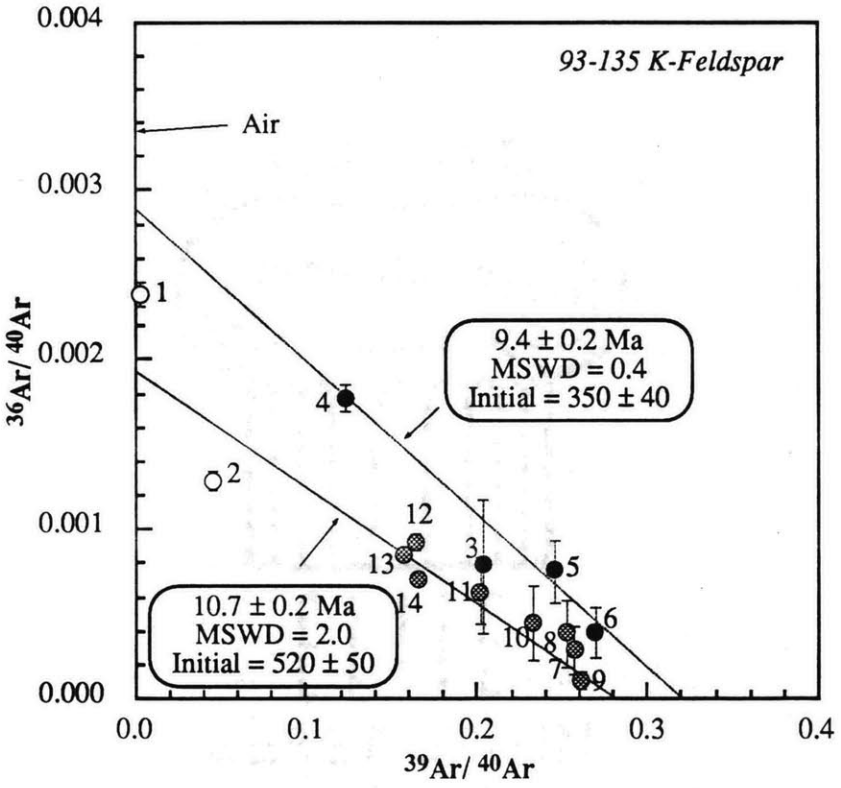
93-135 K-Feldspar
Air
9.4 ± 0.2 Ma
MSWD = 0.4
Initial = 350 ± 40
10.7 ± 0.2 Ma
MSWD = 2.0
Initial = 520 ± 50
36Ar/ 40Ar
39Ar/ 40Ar

Figure 9

a.

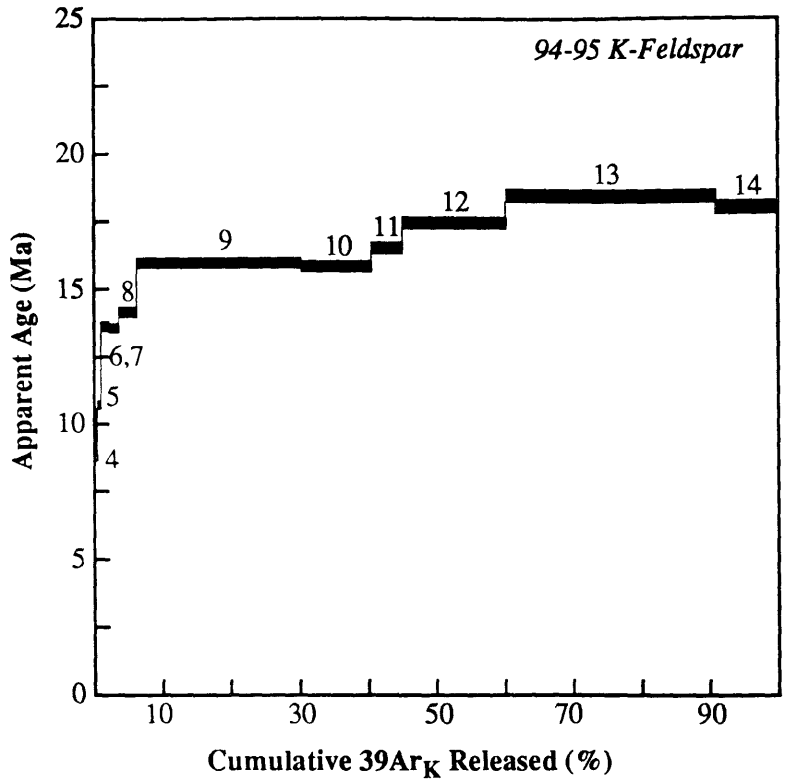
94-95 K-Feldspar
Apparent Age (Ma)
Cumulative 39Ar$_K$ Released (%)
25
20
15
10
5
0
10
30
50
70
90
4
5
6,7
8
9
10
11
12
13
14

b.

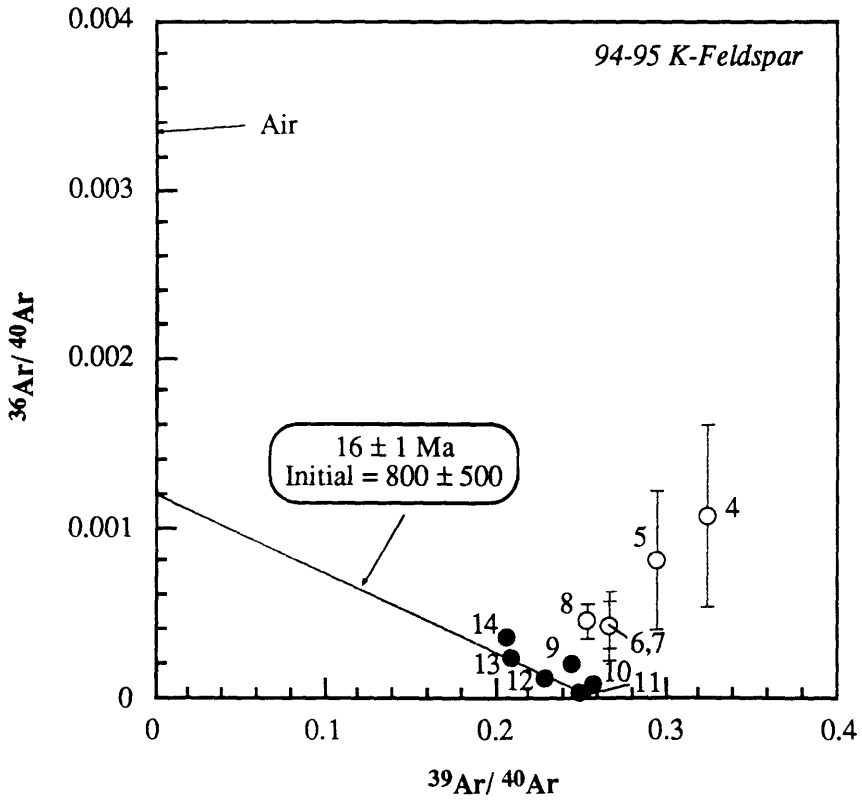
94-95 K-Feldspar
Air
16 ± 1 Ma
Initial = 800 ± 500
36Ar/40Ar
39Ar/40Ar
0.004
0.003
0.002
0.001
0
0.1
0.2
0.3
0.4
4
5
6,7
8
9
10
11
12
13
14

Figure 10

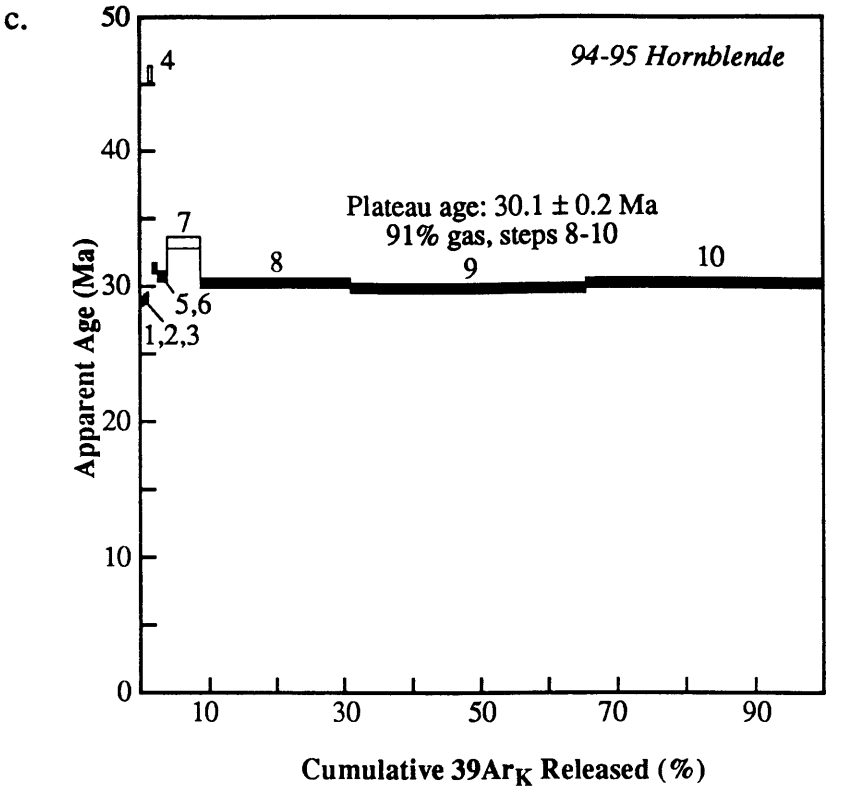
c.
94-95 Hornblende
Plateau age: 30.1 ± 0.2 Ma
91% gas, steps 8-10
Apparent Age (Ma)
Cumulative 39Ar$_K$ Released (%)
d.
94-94 Hornblende
Air
30.0 ± 0.4 Ma
MSWD = 0.1
Initial = 300 ± 100
36Ar/40Ar
39Ar/40Ar

Figure 10

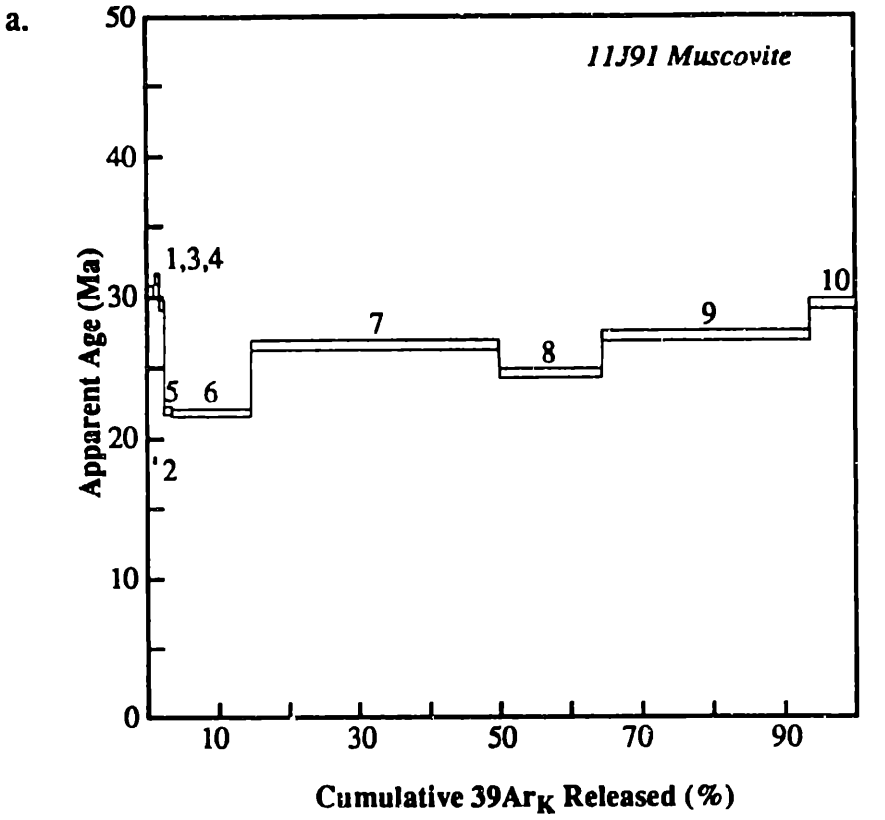
a.
11J91 Muscovite
Apparent Age (Ma)
50
40
30
20
10
0
1,3,4
2
5
6
7
8
9
10
10
30
50
70
90
Cumulative 39Ar$_K$ Released (%)

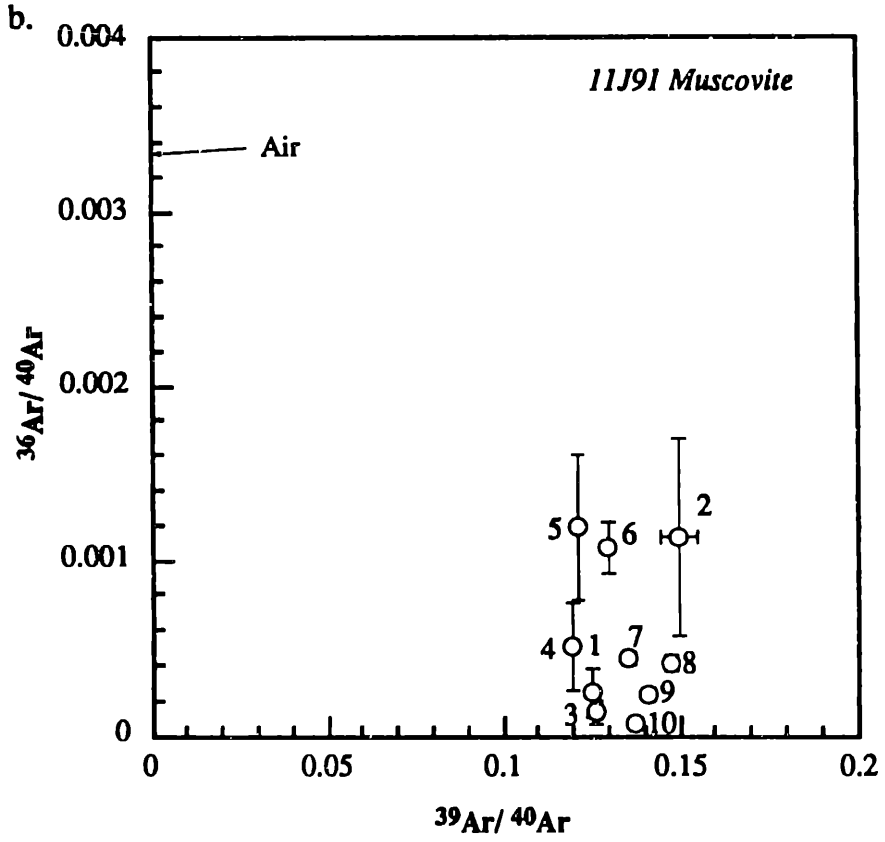
b.
11J91 Muscovite
Air
36Ar/40Ar
0.004
0.003
0.002
0.001
0
0
0.05
0.1
0.15
0.2
39Ar/40Ar
1
2
3
4
5
6
7
8
9
10

Figure 11

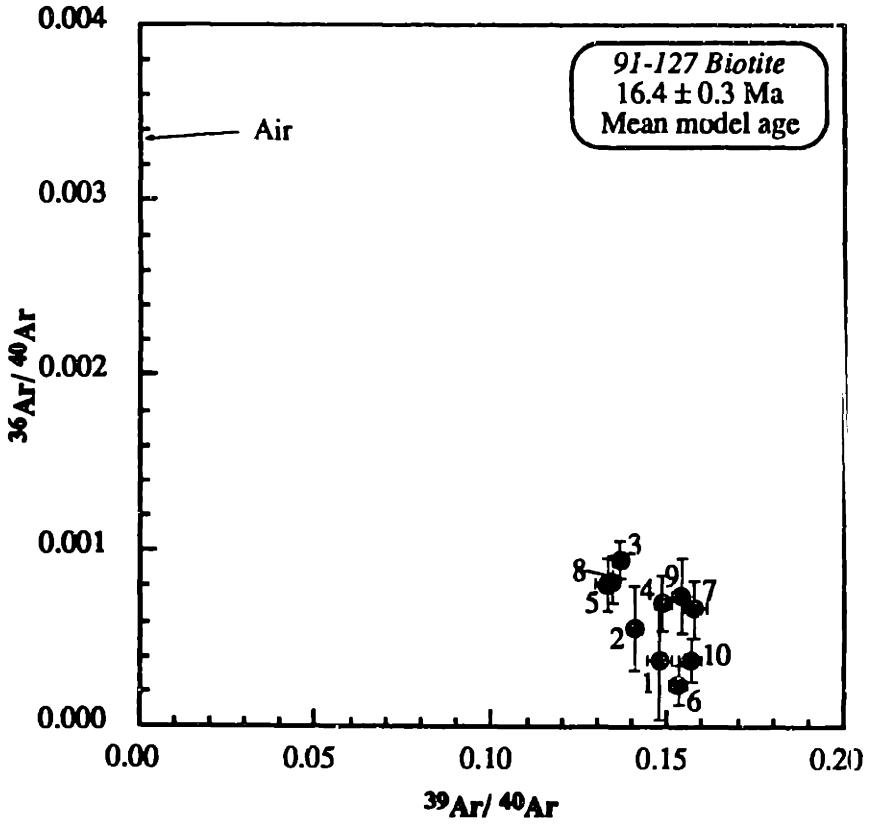
0.004
0.003
0.002
0.001
0.000
$^{36}Ar/^{40}Ar$
Air
91-127 Biotite
16.4 ± 0.3 Ma
Mean model age
3
8
9
4
7
5
2
10
1
6
0.00
0.05
0.10
0.15
0.20
$^{39}Ar/^{40}Ar$

Figure 12

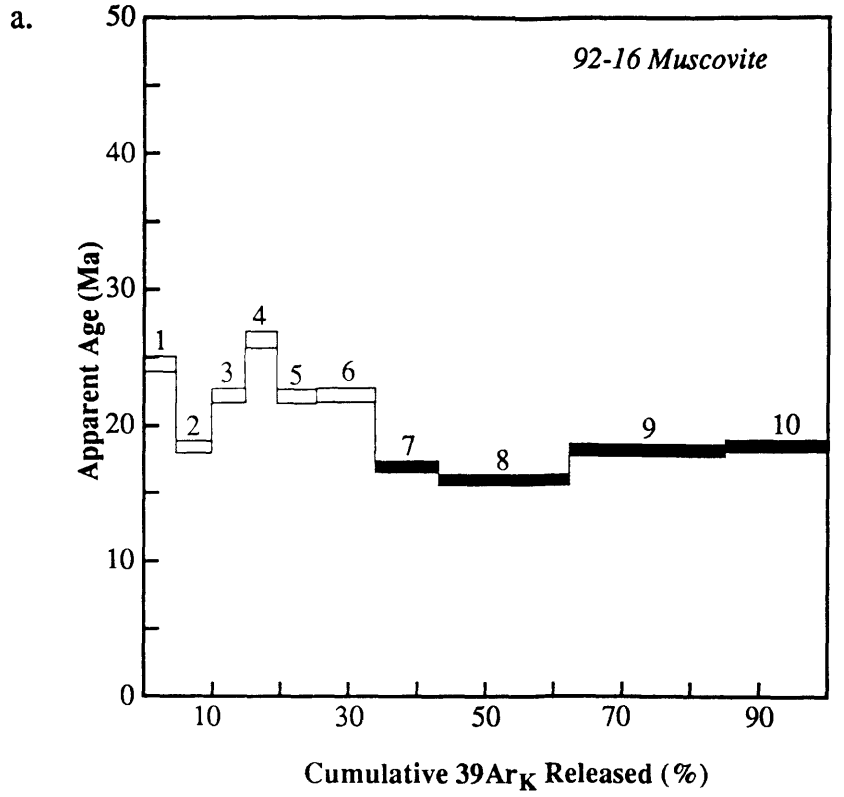
a.
92-16 Muscovite
Apparent Age (Ma)
50
40
30
20
10
0
1
2
3
4
5
6
7
8
9
10
10
30
50
70
90
Cumulative 39Ar$_K$ Released (%)

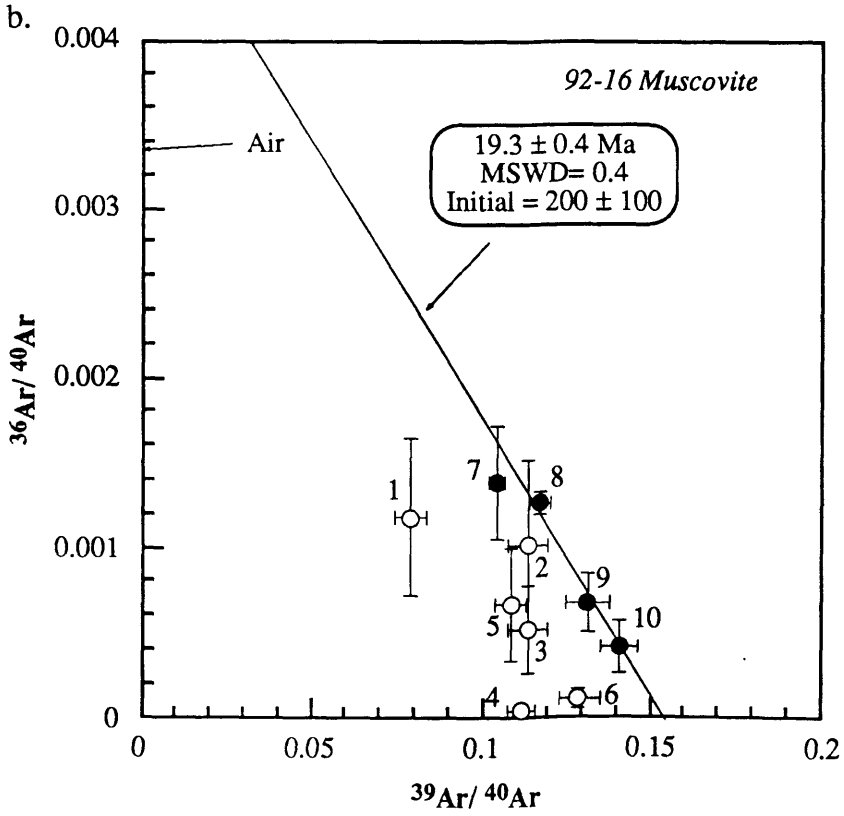
b.
92-16 Muscovite
Air
19.3 ± 0.4 Ma
MSWD= 0.4
Initial = 200 ± 100
36Ar/ 40Ar
0.004
0.003
0.002
0.001
0
1
2
3
4
5
6
7
8
9
10
0
0.05
0.1
0.15
0.2
39Ar/ 40Ar

Figure 13

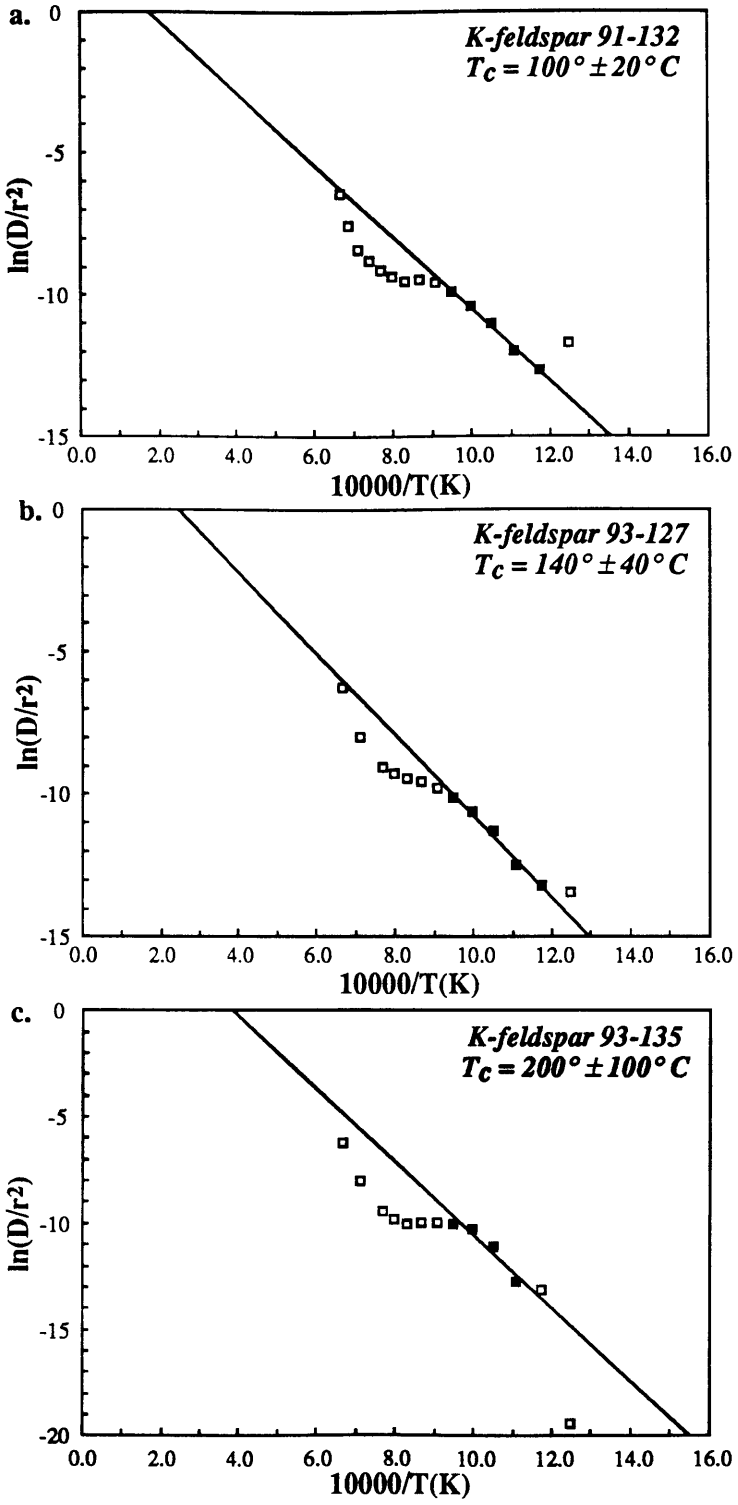
a.
K-feldspar 91-132
$T_c = 100° \pm 20° C$
ln(D/r²)
10000/T(K)
b.
K-feldspar 93-127
$T_c = 140° \pm 40° C$
ln(D/r²)
10000/T(K)
c.
K-feldspar 93-135
$T_c = 200° \pm 100° C$
ln(D/r²)
10000/T(K)

Figure 14

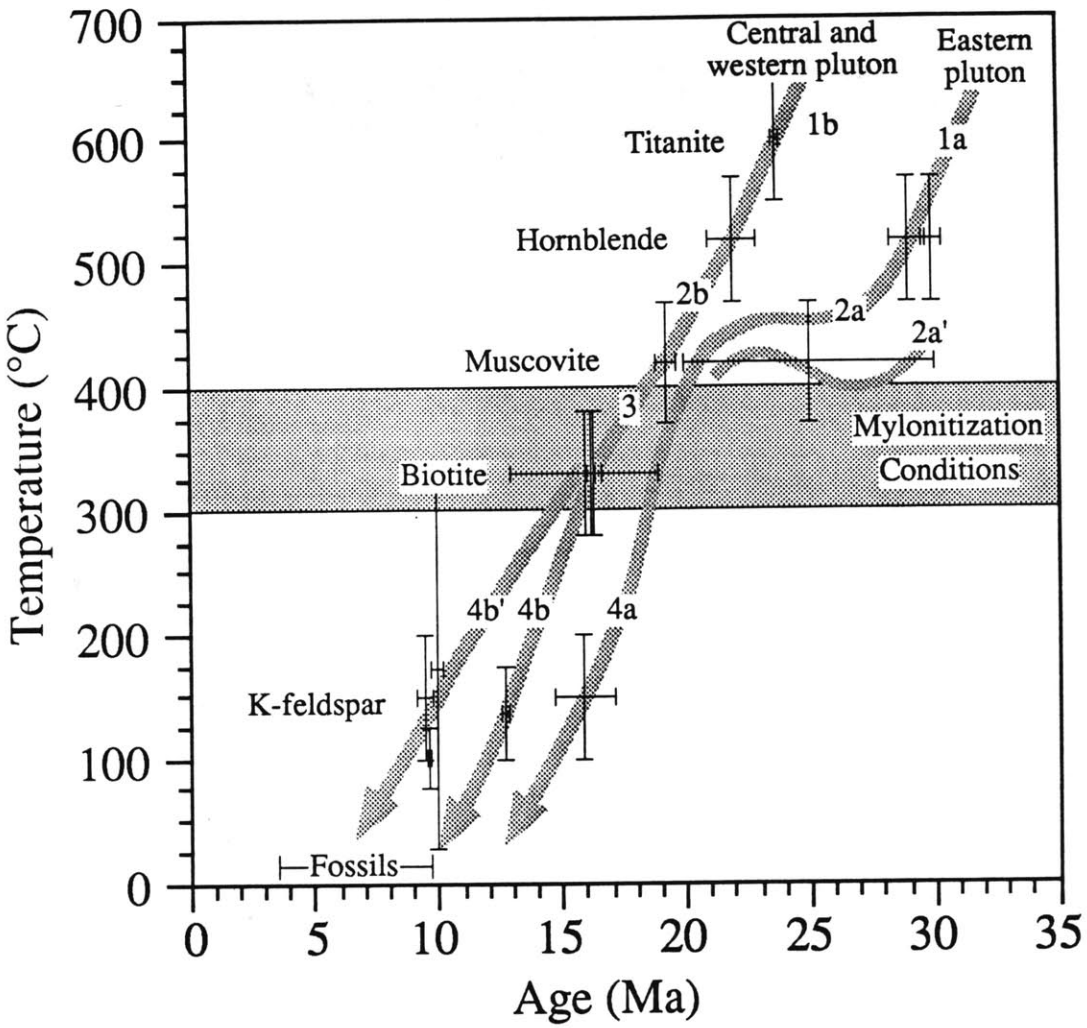
Temperature (°C)
Age (Ma)
Central and western pluton
Eastern pluton
Titanite
Hornblende
Muscovite
Biotite
K-feldspar
Fossils
Mylonitization Conditions
1b
1a
2b
2a
2a'
3
4b'
4b
4a

Figure 15

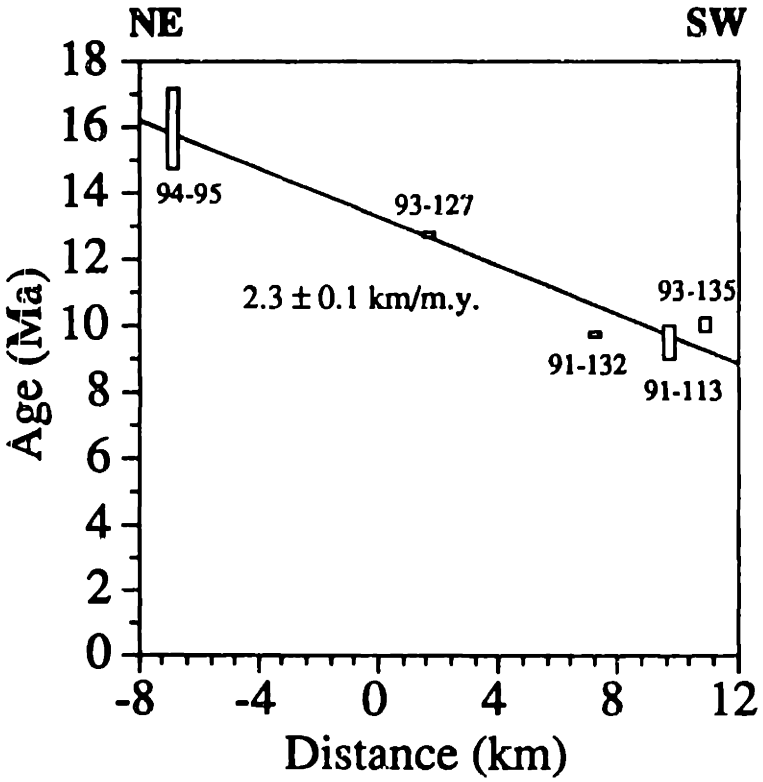
NE
SW
18
16
14
12
10
8
6
4
2
0
Age (Ma)
94-95
93-127
2.3 ± 0.1 km/m.y.
93-135
91-132
91-113
-8
-4
0
4
8
12
Distance (km)

Figure 16

CHAPTER 5: CRUSTAL TILTING OF THE RHODOPE METAMORPHIC CORE COMPLEX, NORTHERN GREECE: CONSTRAINTS FROM ALUMINUM-IN-HORNBLENDE GEOBAROMETRY

ABSTRACT

In the northern Rhodope metamorphic core complex, the Vrondou pluton and the Elaion stock are Mid Tertiary intrusives exposed in kilometer-scale structural corrugations of the Strymon Valley detachment fault. Regional structural relations suggest the Strymon Valley detachment fault initiated at a steeper angle than its presently shallow dip and that it has significant along-strike structural relief. To quantify these observations, aluminum-in-hornblende geobarometry was applied to a suite of samples collected parallel and perpendicular to the direction of hanging wall transport. The results indicate that a 0.16 ± 0.15 kbar/km (2σ confidence level) emplacement gradient exists in the direction of hanging wall transport and the Elaion stock was emplaced at pressures about 2 kbar less than the central and western Vrondou pluton. These apparent emplacement gradients are interpreted to reflect crustal-scale uplift and rotation in the footwall of a detachment fault with an original dip as great as 40° and significant along-strike structural relief. These data highlight the role of isostatic uplift in the evolution of low-angle normal fault systems and show the potential utility of the aluminum-in-hornblende barometer to constrain the three-dimensional pre-detachment geometry of core complexes containing intrusive rocks of an appropriate composition.

INTRODUCTION

Since their recognition, one of the outstanding unanswered questions about low angle normal faults has been: are low-angle normal faults initiated at low angles, or are they rotated into their orientation from steeper dips? Arguments from numerous geologic and geophysical disciplines have been used both for and against the initiation of normal faults at

low angles. One technique that has yet to find widespread application to this question is geothermobarometry, perhaps because most thermobarometers rely on metamorphic assemblages which, in core complexes, typically record pressures and temperatures from earlier unrelated deformation. However, igneous geobarometers, such as the aluminum-in-hornblende barometer [*Hammarstrom and Zen*, 1986; *Hollister et al.*, 1987; *Johnson and Rutherford*, 1989; *Schmidt*, 1992] offer the potential to determine paleodepths in core complexes that contain intrusive rocks of an appropriate composition emplaced before detachment fault initiation (e.g., *Holm et al.* [1992]). Recent calibration of the aluminum-in-hornblende barometer has improved significantly and it has been used satisfactorily in a number of studies to quantify vertical structural offset of granitic intrusives (e.g., *Vynall and McSween* [1990]; *Coleman and Parrish* [1991]; *Tobisch et al.* [1993]). It is possible that in a well-exposed core complex containing a significant aerial distribution of intrusives of the appropriate composition, the three-dimensional pre-extension geometry, and thereby the original detachment fault geometry, could be constrained by applying the barometer to a suite of samples parallel and perpendicular to the extension direction.

The Rhodope metamorphic core complex [*Dinter and Royden*, 1993; Chapter 3], a Mid to Late Tertiary core complex in northern Greece, offers an excellent setting to apply the aluminum-in-hornblende barometer to constrain the pre-extensional core complex geometry, addressing the question of original detachment fault dip as well as examining along-strike structural relief on the bounding Strymon Valley detachment fault. In the northern part of the core complex, the Vrondou pluton and Elaion stock are exposed in kilometer-scale structural corrugations of the detachment fault (Figure 1). They are mesozonal, medium-grained, granitic bodies that intrude the middle and lower units of the Falakron Marble Series and cross-cut Alpine structural fabrics. They are composed predominantly of quartz monzonite, granite, and granodiorite with gradational contacts between the various phases [*Theodorikas*, 1983]. Geochemically the Vrondou pluton and Elaion stock are indistinguishable, suggesting they were formed from the same magma

body [*Kolocotroni and Dixon*, 1991]. $^{40}Ar/^{39}Ar$ hornblende cooling ages of 29 to 30 Ma from the eastern Vrondou pluton and Elaion stock are thought to approximate the timing of intrusion [Chapter 4]. Younger U-Pb titanite and $^{40}Ar/^{39}Ar$ hornblende ages (22 to 24 Ma) from the central Vrondou pluton are interpreted to reflect a second, later pulse of magmatism, although slow cooling of a single Oligocene pluton cannot be excluded [Chapter 4]. The margins of both bodies were sheared to form an S-C granite mylonite during Middle Miocene ductile motion on the Strymon Valley detachment fault [Chapter 4]. The mean stretching lineation and the corrugation axis of mylonitic foliation planes coincide (S231°W/ 8° SW) defining a shallowly dipping, top-to-the-southwest transport vector for the hanging wall during ductile motion on the detachment fault (Figure 1 inset).

Regional intrusive relationships support an initial southwest dip to the Strymon Valley detachment fault, but hint that it may have initiated at a steeper dip than is evidenced by shallowly plunging structural fabrics now observed in its footwall. Pre-detachment Oligocene-Miocene plutons intruded at mesozonal depths are found along the southwestern boundary of the core complex; contemporaneous epizonal intrusives and volcanics are present near the suspected breakaway zone [*Eleftheriadis and Lippolt*, 1984; *Koukouvelas and Pe-Piper*, 1991; *Kolocotroni and Dixon*, 1991; *Dinter et al.*, 1995]. Given the present width of the core complex, an average detachment fault dip of at least 10° is required to unroof these plutons from mid-crustal depths.

In the northern Rhodope metamorphic core complex, the Strymon Valley detachment fault cuts down-section to the northwest, exposing successively deeper levels of the Falakron Marble Series [Chapter 3]. The detachment fault reaches its shallowest structural level in the southern part of Figure 1 and cuts down-section again to the southeast where it exposes the Symvolon pluton and the basal part of the Falakron Marble Series. The magnitude of structural relief is probably at least 6 km [Chapter 3] but may approach the thickness of the Falakron Marble Series, estimated to exceed 10 km [*Kronberg*, 1969].

SAMPLES AND ANALYTIC TECHNIQUES

Four samples of hornblende-bearing granite and quartz monzonite collected along a 14 km southwest-trending traverse of the Vrondou pluton were analyzed to quantify variations in emplacement depth parallel to the direction of hanging wall transport. An additional sample from the Elaion stock, 11 km southeast of the Vrondou pluton traverse, was analyzed to determine pre-detachment conditions perpendicular to the extension direction (sample lithologies are summarized in Appendix 1). All samples contain the critical mineral assemblage (quartz, plagioclase, K-feldspar, hornblende, biotite, titanite, and magnetite) for the use of the aluminum-in-hornblende geobarometer. In all samples, hornblende occurs as subhedral to euhedral crystals with grain boundaries in physical contact with all major mineral phases. Polished thin sections of the five samples were analyzed at the JEOL microprobe facility at the Massachusetts Institute of Technology. Operating conditions were maintained at an accelerating voltage of 10 kV and a beam current of 10 nA with a beam size of 10 μm. Mineral standards were used in the calibration process.

Amphibole chemical formulas were calculated from the individual analyses on the basis of 23 oxygen atoms and 13 cations excluding Ca, Na, and K (13eCNK) [*Robinson et al.*, 1982] using algorithms described in *Spear and Kimball* [1984] (Table 1). The 13 cation formulation calculates ferrous and ferric iron by charge balance and is appropriate for calcic amphiboles [*Robinson et al.*, 1982]. Alternative methods for calculating ferrous and ferric iron generally produced non-ideal amphibole stoichiometries and were rejected. Calculations based on 23 oxygen atoms and 15 cations excluding Na and K (15eNK) were successful for some analyses, yielding slightly higher total aluminum (Al^T) and silicon content and lower Fe^{3+} content. However, there is usually less than 1% difference in calculated Al^T between the two methods which is negligible relative to inter- and intra-crystal variation within a sample and relative to uncertainty in the geobarometer calibration.

Analyses reported on Table 1 reflect the average and 2σ uncertainty of 5 to 16 amphibole rim points evaluated from each sample.

Compositional zonation is not evident in either thin section or in microprobe traverses across hornblende grains. Although some grains show minor evidence for late alteration during unroofing of the core complex, only fresh, unaltered euhedral crystals were analyzed during this study. A plot of $Mg/(Mg+Fe^{2+})$ vs. Al^T (Figure 2) for a traverse across a single grain indicates core and rim compositions are identical (within uncertainty), down-playing the likelihood of subsolidus reactions affecting hornblende composition.

BAROMETRY RESULTS

A number of empirical and experimental calibrations of the aluminum-in-hornblende barometer have been developed [*Hammarstrom and Zen*, 1986; *Hollister et al.*, 1987; *Johnson and Rutherford*, 1989; *Schmidt*, 1992] and it is not clearly evident which is the most appropriate for the Vrondou pluton. For the range of total aluminum content observed in the Vrondou hornblendes, the maximum and minimum emplacement pressures are bracketed by the experimental calibrations of *Johnson and Rutherford* [1989] ($P(kbars) = -3.46 + 4.23Al^T$) and *Schmidt* [1992] ($P(kbars) = -3.01 + 4.76Al^T$) (Table 2). The calibration of *Schmidt* [1992] yields pressures which are higher by 1.0 to 1.4 kbar. Although both barometer calibrations yield pressures that are generally consistent with the regional metamorphic conditions (i.e., greenschist facies), quantitative independent geobarometry has not been applied to the Falakron Marble Series. The barometer was also applied to published hornblende microprobe data from four samples of granite, granodiorite, and quartz monzonite from the eastern Vrondou pluton (Figure 1) [*Theodorikas*, 1983; *Theodorikas*, 1986]. Because this study is mainly interested in relative emplacement pressures between samples rather than absolute pressure, the systematic uncertainty in the barometer calibrations can be neglected. Uncertainties

presented in Table 2 are the calculated from intra-sample Al^T variation and are quoted at the 2σ level.

The data show a systematic increase in emplacement pressure along a southwest-trending transect in the direction of hanging wall transport (Figure 3a). Although the absolute emplacement pressures are significantly affected by the choice of barometer calibration, the apparent emplacement gradient is relatively insensitive to the calibration choice because both calibrations have a similar dependence on the total aluminum content. The best statistical regression through the data yields an average southwest emplacement gradient of 0.16 ± 0.15 kbar/km (using the *Schmidt* [1992] calibration), assuming the uncertainty in the slope of the line results from the uncertainty in each data point, rather than the spread of the data about a line. The large uncertainty in the emplacement gradient results from the propagation of 2σ uncertainties through the calculations. If uncertainties at the 1σ confidence level are propagated instead, the 1σ uncertainty in the emplacement gradient is only 0.03 kbar/km. The single analysis from the Elaion stock yields an intermediate pressure. Intra-sample variation is typically small with the exception of sample 91-67, which contains two distinct amphibole populations. The pressures calculated for the first population are within the range of expected pressures given the metamorphic assemblages in the Falakron Marble Series; the second population predicts anomalously high pressures, suggesting they are either xenocrysts or early crystals formed during the magma's ascent.

DISCUSSION

The 0.16 kbar/km emplacement gradient along the length of the Vrondou pluton quantifies the differential removal of overburden and is interpreted to reflect tectonic denudation by the Strymon Valley detachment fault. Attributing all of the unroofing to the detachment fault predicts a low to intermediate initial fault dip. This implies that the Vrondou pluton and the Rhodope metamorphic core complex represent a tilted crustal

section in the footwall of a regional detachment fault. Recent paleomagnetic work on the Vrondou pluton provides additional evidence for post-intrusional tilting, indicating as much as 18° of tilting to the northeast about a subhorizontal north to northwest trending axis [*Atzemoglou et al.*, 1994] if the alternative Oligocene paleopole for Eurasia is accepted [*Westphal*, 1993].

Although it is possible that the apparent variation in emplacement pressures could be explained by structural deformation in the footwall unrelated to detachment faulting, there is no evidence for structures of sufficient magnitude (approximately 6 km of vertical separation) to explain the geobarometric results. Pre-detachment intracore shear zones have not been recognized within the Vrondou pluton; thick mylonite zones characteristic of shear zones in the Rhodope metamorphic core complex are associated exclusively with the Strymon Valley detachment fault. Structural fabrics consistently have a top-to-the-southwest sense of shear, opposite to that required to offset the eastern pluton downward relative to the central and western pluton. The existence of an intracore shear zone between the Vrondou pluton and the Elaion stock cannot be excluded on the grounds of structural data, but pervasive southwest-trending, shallowly plunging stretching lineations found throughout the core complex would require a predominantly oblique (sub-horizontal) sense of relative motion. Large-magnitude post-detachment faults in the north Aegean region are typically characterized by the formation of Plio-Quaternary sedimentary basins and the development of significant topographic relief; neither is observed between the eastern and western Vrondou pluton. Post-detachment normal faulting is known to displace the Serres Basin (and the Elaion stock) downwards relative to the Vrondou pluton, but the magnitude of vertical offset is relatively minor (< 1 km [Chapter 3]).

A northeast-southwest reconstruction of the northern Rhodope metamorphic core complex based on regional intrusive relationships and the results of the geobarometry is shown in Figure 3c, highlighting the apparent emplacement gradient that is interpreted to reflect the magnitude of tectonic denudation by the Strymon Valley detachment fault. The

reconstruction suggests that the initial detachment dip may have been significantly steeper (up to 40°) than present structural fabrics imply. Along strike, the increasing width of the Rhodope metamorphic core complex and the decreasing emplacement depth of Tertiary intrusives (the Elaion stock) suggest that the average initial detachment fault dip decreases to the southeast.

The restored cross section is interpreted to indicate the present exposure of the Rhodope metamorphic core complex represents a crustal block that has been significantly tilted from its original orientation during tectonic denudation by the Strymon Valley detachment fault. This progressive syn-extensional tilting rotates structural fabrics formed during detachment faulting, perhaps accounting for the steeper average dip on late brittle fabrics as compared to earlier ductile fabrics [Chapter 3]. This rotation of the Rhodope metamorphic core complex is comparable to crustal block rotations reported from the footwall of other detachment faults (e.g., *Wernicke and Axen* [1988]; *Fryxell et al.* [1992]). It is suspected that flexural isostatic rebound is responsible for rotating the detachment fault and structural fabrics associated with it during the extensional process (c.f., *Buck* [1988]; *Yin* [1991]; *Kaufman and Royden* [1994]). The apparent rotation of structural fabrics and the paleomagnetic data precludes isostatic uplift occurring by subvertical simple shear (e.g., *Selverstone et al.* [1993]).

The projection of the emplacement pressure of the Elaion stock onto the southwest-trending transect of the Vrondou pluton (Figure 3a) implies that the Elaion stock was emplaced at pressures approximately 2 kbar less than the central and western Vrondou pluton. This apparent emplacement pressure difference is consistent with the gross metamorphic stratigraphy in the northern Rhodope metamorphic core complex and is interpreted to result from significant along-strike structural relief on the Strymon Valley detachment fault. Such an interpretation implies that kilometer-scale corrugations of the Strymon Valley detachment fault are completely dwarfed by the regional structural relief on the detachment fault, calling the interpretation of these corrugations as primary features of

the detachment fault into question [*Dinter*, 1994]. While it is possible that these corrugations are second-order structures formed by a curvi-planar detachment fault with regional structural relief, it seems unlikely that second-order features on the detachment fault would be preserved as the primary regional topographic expression in the Rhodope metamorphic core complex while significant first-order structural relief on the detachment fault produces no topographic expression. It is suspected that these corrugations are not primary warps of the detachment fault plane but are formed during extension by a combination of flexural isostatic uplift and compression perpendicular to the extension direction (e.g., *Yin* [1991]; *Mancktelow and Pavlis* [1994]). However, without more thorough analysis of pre-detachment conditions in the footwall, a mechanism for the formation of these corrugations remains speculative.

CONCLUSIONS

This study demonstrates the utility of aluminum-in-hornblende barometry for constraining footwall geometries in core complexes that contain pre-detachment intrusive rocks of an appropriate composition. Successful application of the barometer to pre-detachment Tertiary intrusives in the northern Rhodope metamorphic core complex has identified variations in emplacement depth which are interpreted to reflect the geometry of the Strymon Valley detachment fault cutting across these intrusives. These emplacement gradients indicate that the Strymon Valley detachment fault initiated as a low- to intermediate-angle normal fault, but rotation of the fault and its ductile and brittle fabrics has occurred following (or during) tectonic denudation. The geobarometry also suggests that significant along-strike structural relief on the Strymon Valley detachment fault dwarfs the modern km-scale corrugations reflected by alternating footwall highs and supradetachment basins. Additional aluminum-in-hornblende geobarometry on Tertiary intrusives exposed throughout the Rhodope metamorphic core complex offers the potential to constrain the three-dimensional pre-detachment geometry on a regional scale.

APPENDIX: SAMPLE DESCRIPTIONS

Sample 91-12: Medium-grained granite proto-mylonite (?) collected from the Elaion stock approximately 400 m below the projection of the Strymon Valley detachment fault. It is composed of approximately 60% plagioclase and K-feldspar (microcline), 20% quartz, 13% hornblende, 3% biotite, 1% titanite, 1% epidote, 1% chlorite, and 1% magnetite. Accessory minerals include zircon and apatite. The fabric is poorly defined and there is no preferred crystallographic orientation. Large feldspars (up to 5 mm) show intense mechanical twinning. Quartz is typically neoblastic with a maximum grain size of 0.1 mm. Euhedral to subhedral hornblende crystals are up to 0.5 mm across. Biotite is typically intergrown with hornblende and is commonly altered to chlorite. All amphibole microprobe analyses are all classified as magnesio-hornblende (9). In amphiboles, $1.320 < Al^T < 1.477$.

Sample 91-67: Medium-grained hornblende granite collected from 2 km southwest of the summit of the Vrondou pluton. It is composed of ~60% plagioclase and K-feldspar, 25% quartz, 8% hornblende, 6% biotite, and 1% titanite. Accessory phases include ore minerals (magnetite, chalcopyrite), zircon, and apatite. K-feldspar occurs as microcline with grains up to 5 mm across. Twinned plagioclase grains are as large as 8 mm. Quartz occurs as subgrains 0.25 to 0.5 mm across which exhibit minor dynamic recrystallization. Quartz shows undulose extinction and local myrmekitic intergrowth with feldspar. Hornblende crystals form euhedral to subhedral prisms up to 2 mm long. They occur as independent crystals and intergrown with biotite grains up to 2 mm across. Amphibole microprobe analyses are classified as magnesio-hornblende (3), edenitic hornblende (2), and magnesian hastingsite (2). In amphiboles, $1.511 < Al^T < 1.813$ (grain 1) and $2.300 < Al^T < 2.406$ (grains 2 and 3).

Sample 91-68: Medium-grained hornblende quartz monzonite collected at the summit of the Vrondou pluton. It is composed of ~75% plagioclase and K-feldspar, 15% quartz, 4% hornblende, 4% biotite, and 1% titanite. Accessory phases include magnetite, zircon, and apatite. K-feldspar occurs as microcline with grains up to 2 mm across. Zoned plagioclase grains are as large as 2 mm. Mechanical twinning is common in feldspars. Quartz grains up to 2 mm across show undulose extinction and local myrmekitic intergrowth with feldspar. Hornblende crystals form euhedral to subhedral prisms up to 2 mm in length. Biotite grains are up to 2 mm across. All amphibole microprobe analyses are classified as magnesio-hornblende (12). In amphiboles, $1.003 < Al^T < 1.524$.

Sample 93-132: Medium-grained hornblende quartz monzonite collected from the western Vrondou pluton. It is composed of ~65% plagioclase and K-feldspar (microcline), 15% quartz, 15% hornblende, 1% biotite, 1% chlorite, 1% epidote, 1% magnetite, and 1% titanite. Accessory phases include zircon and apatite. K-feldspar occurs as microcline with grains up to 2.5 mm across. Some feldspar grains are mechanically twinned. Quartz occurs as subgrains up to 0.5 mm across which show minor dynamic recrystallization. Quartz grains show undulose extinction and local myrmekitic intergrowth with feldspar. Hornblende crystals form euhedral to subhedral prisms up to 1.5 mm long. They occur as independent crystals and intergrown with biotite. Biotite grains are up to 0.75 mm across and commonly show a retrograde reaction to chlorite. Amphibole microprobe analyses are classified as magnesian hastingsitic hornblende (10), magnesio-hornblende (3), and Tschermakitic hornblende (3). In amphiboles, $1.685 < Al^T < 1.964$.

Sample 94-95: Medium-grained hornblende quartz monzonite collected from the eastern Vrondou pluton. It is composed of approximately 60% plagioclase and K-feldspar, 15% quartz, 20% hornblende, and 2% magnetite, and less than 1% each of titanite, biotite, and epidote. Accessory phases include zircon and apatite. K-feldspar occurs as microcline with grains up to 3 mm across. Twinned plagioclase grains are as large as 1.5 mm and often show a strong zonation from core to rim. Quartz occurs as subgrains 0.25 to 0.5 mm across which show minor dynamic recrystallization. Quartz grains show local myrmekitic intergrowth with feldspar. Hornblende crystals form large subhedral poikilitic crystals up to 3 mm in length containing plagioclase, K-feldspar, titanite, and magnetite. Biotite grains are small (up to 0.2 mm) and are always intergrown with hornblende crystals. Amphibole microprobe analyses are classified as magnesio-hornblende (13), edenitic hornblende (1), and magnesian hastingsitic hornblende (1). In amphiboles, $1.434 < Al^T < 1.977$.

Sample 110 (Theodorikas, 1986): Granite. Amphibole microprobe analyses are classified as magnesio-hornblende (11), edenite (3) and actinolitic hornblende (1). In amphiboles, $0.927 < Al^T < 1.376$.

Sample 119 (Theodorikas, 1986): Quartz monzonite. Amphibole microprobe analyses are classified as magnesio-hornblende (13) and edenite (1). In amphiboles, $0.980 < Al^T < 1.305$.

Sample 213 (*Theodorikas*, 1986): Granodiorite. Amphibole microprobe analyses are classified as magnesio-hornblende (10), edenite (6) and edenitic hornblende (6). In amphiboles, $1.013 < Al^T < 1.662$.

Sample 239 (*Theodorikas*, 1986): Quartz monzonite. Amphibole microprobe analyses are classified as magnesio-hornblende (8), actinolitic hornblende (5) and actinolite (2). In amphiboles, $0.850 < Al^T < 1.262$.

REFERENCES

Atzemoglou, A., D. Kondopoulou, S. Papamarinopoulos, and S. Dimitriadis, 1994, Paleomagnetic evidence for block rotations in the western Greek Rhodope, *Geophysical Journal International*, v. 118, p. 221-230.

Buck, R., 1988, Flexural rotation of normal faults, *Tectonics*, v. 7, p. 959-973.

Coleman, M.E., and R.R. Parrish, 1991, Eocene dextral strike-slip and extensional faulting in the Bridge River Terrane, Southwest British Columbia, *Tectonics*, v. 10, p. 1222-1238.

Dinter, D.A., and L. Royden, 1993, Late Cenozoic extension in northeastern Greece: Strymon Valley detachment and Rhodope metamorphic core complex, *Geology*, v. 21, p. 45-48.

Dinter, D.A., 1994, Tectonic evolution of the Rhodope metamorphic core complex, Northeastern Greece [Ph.D. Thesis], Massachusetts Institute of Technology, Cambridge, MA, 320 pp.

Dinter, D.A., A.M. Macfarlane, W. Hames, C. Isachsen, and L. Royden, 1995, U-Pb and $^{40}Ar/^{39}Ar$ geochronology of the Symvolon granodiorite: Implications for the thermal and structural evolution of the Rhodope metamorphic core complex, northeastern Greece, in press, *Tectonics*.

Eleftheriadis, G. and H.J. Lippolt, 1984, Altersbestimmungen zum oligozänen vulkanismus der Süd-Rhodopen/Nord Griechenland, *Neues Jahrbuch für Geologie und Paläontologie, Monatshefte*, v. 3, p. 179-191.

Fryxell, J.E., G.G. Salton, J. Selverstone, and B. Wernicke, 1992, Gold Butte crustal section, South Virgin Mountains, Nevada, *Tectonics*, v. 11, p. 1099-1120.

Hammarstrom, J.M., and E. Zen, 1986, Aluminum in hornblende: An empirical igneous geobarometer, *American Mineralogist*, v. 71, p. 1297-1313.

Hollister, L.S., G.C. Grissom, E.K. Peters, H.H. Stowell, and V.B. Sisson, 1987, Confirmation of the empirical correlation of Al in hornblende with pressure of solidification of calc-alkaline plutons, *American Mineralogist*, v. 72, p. 231-239.

Holm, D.K., J.K. Snow, and D.R. Lux, 1992, Thermal and barometric constraints on the intrusive history of the Black Mountains: Implications for timing, initial dip, and kinematics of detachment faulting in the Death Valley region, California, *Tectonics*, v. 11, p. 507-522.

Johnson, M.C., and M.J. Rutherford, 1989, Experimental calibration of the aluminum-in-hornblende geobarometer with application to Long Valley caldera (California) volcanic rocks, *Geology*, v. 17, p. 837-841.

Kaufman, P.S., and L.H. Royden, 1994, Lower crustal flow in an extensional setting: Constraints from the Halloran Hills region, eastern Mojave Desert, California, *Journal of Geophysical Research*, v. 99, p. 15,723-15,739.

Kolocotroni, C., and J.E. Dixon, 1991, The origin and emplacement of the Vrondou granite, Serres, N.E. Greece, *Bulletin of the Geological Society of Greece*, v. 25, p. 469-483.

Koukouvelas, I., and G. Pe-Piper, 1991, The Oligocene Xanthi pluton, northern Greece: A granodiorite emplaced during regional extension, *Journal of the Geological Society, London*, v. 148, p. 749-758.

Kronberg, P., 1969, Gliederung, Petrographie und Tektogenese des Rhodopen-Kristallins im Tsal-Dag, Simvolon, und Ost-Pangaon (Griechisch-Makedonien), *Geotektonische Forschungen*, v. 31, p. 1-49.

Mancktelow, N.S., and T.L. Pavlis, 1994, Fold-fault relationships in low-angle detachment systems, *Tectonics*, v. 11, p. 668-685.

Robinson, P., F.S. Spear, J.C. Schumacher, J. Laird, C. Klien, B.W. Evans, and B.L. Doolan, 1982, Amphiboles: Petrology and experimental phase relations *in* D.R. Veblen

and P.H. Ribbe, eds., Reviews in mineralogy, Volume 9B: Chelsa, Michigan, Mineralogical Society of America, p. 3-42.

Schmidt, M.W., 1992, Amphibole composition in tonalite as a function of pressure: An experimental calibration of the Al-in-hornblende barometer, *Contributions to Mineralogy and Petrology*, v. 110, p. 304-310.

Selverstone, J., G. Axen, and J. Bartley, 1993, P-T conditions of successive fracturing events during unroofing of an extensional mylonite zone: Constraints from oriented fluid inclusion planes, *Geological Society of America, Abstracts*, v. 25, p. 423.

Spear, F.S., and K.L. Kimball, 1984, RECAMP – a FORTRAN IV program for estimating Fe^{3+} contents in amphiboles, *Computers and Geosciences*, v. 10, p. 317-325.

Theodorikas, S., 1983, The mineralogy, petrology and geochemistry of the Serres-Drama granitic complex, Northern Greece [Ph.D. Thesis], Aristotle University of Thessaloniki, Faculty of Science, School of Geology, Scientific Annals, Thessaloniki, v. 22, n. 28, 415 p.

Theodorikas, S., 1986, Amphiboles from the Serres-Drama granitic complex, *Oriktos Ploutos*, v. 40, p. 33-50.

Tobisch, O.T., P.R. Renne, and J.B. Saleeby, 1993, Deformation resulting from regional extension during pluton ascent and emplacement, central Sierra Nevada, California, *Journal of Structural Geology*, v. 15, p. 609-628.

Vyhnal, C.R., and H.Y. McSween Jr., 1990, Constraints on Alleghanian vertical displacements in the southern Appalachian Piedmont, based on aluminum-in-hornblende barometry, *Geology*, v. 18, p. 938-941.

Wernicke, B., and G.J. Axen, 1988, On the role of isostasy in the evolution of normal fault systems, *Geology*, v. 16, p. 848-851.

Westphal, M., 1993, Did a large departure from the geocentric axial dipole hypothesis occur during the Eocene? Evidence from the magnetic Polar wander path of Eurasia, *Earth and Planetary Science Letters*, v. 117, p. 15-28.

Yin, A, 1991, Mechanism for the formation of domal and basinal detachment faults: A three dimensional analysis, *Journal of Geophysical Research*, v. 96, p. 14,577-14,594.

TABLE 1. AMPHIBOLE MICROPROBE ANALYSES FROM THE VRONDOU PLUTON AND ELAION STOCK

Sample*	VP-93-132 (16)	VP-91-67 (5)	VP-91-67 (2)	VP-91-68 (12)	VP-94-95 (15)	ES-91-12 (9)
			Weight percent oxides			
MgO	9.1 ± 0.6	10 ± 1	7.0 ± 0.9	11 ± 1	10 ± 1	11 ± 1
Al_2O_3	10.3 ± 0.8	10 ± 1	13.0 ± 0.8	8 ± 1	8 ± 1	8.2 ± 0.5
SiO_2	43 ± 1	44 ± 1	39.8 ± 0.8	45 ± 2	42 ± 2	45.5 ± 0.8
CaO	11.5 ± 0.2	11.6 ± 0.5	11.5 ± 0.4	10.7 ± 0.4	10.2 ± 0.6	11.3 ± 0.4
TiO_2	0.7 ± 0.5	1.0 ± 0.3	0.4 ± 0.2	0.6 ± 0.8	0.8 ± 0.6	1.2 ± 0.7
Cr_2O_3	0.03 ± 0.04	0.01 ± 0.03	0.1 ± 0.1	0.05 ± 0.06	0.04 ± 0.05	0.06 ± 0.05
MnO	0.69 ± 0.07	0.73 ± 0.09	0.86 ± 0.01	0.8 ± 0.1	0.8 ± 0.2	0.8 ± 0.2
FeO	20.0 ± 0.8	19 ± 1	21 ± 1	17 ± 1	16 ± 2	17 ± 2
Na_2O	1.4 ± 0.2	1.3 ± 0.1	1.45 ± 0.04	1.3 ± 0.4	1.4 ± 0.4	1.4 ± 0.5
K_2O	1.3 ± 0.2	1.1 ± 0.2	1.6 ± 0.2	0.8 ± 0.2	1.0 ± 0.2	1.0 ± 0.2
Total	97.9 ± 0.8	97.5 ± 0.6	96.9 ± 0.7	94 ± 1	90 ± 4	98 ± 1
			Cations per 23 oxygens			
Si	6.4 ± 0.1	6.6 ± 0.1	6.1 ± 0.1	6.8 ± 0.2	6.7 ± 0.2	6.7 ± 0.1
Al^{IV}	1.6 ± 0.1	1.4 ± 0.1	1.9 ± 0.1	1.2 ± 0.2	1.3 ± 0.2	1.3 ± 0.1
Al^{VI}	0.27 ± 0.06	0.3 ± 0.1	0.49 ± 0.05	0.2 ± 0.1	0.3 ± 0.2	0.12 ± 0.08
Fe^{3+}†	0.7 ± 0.2	0.6 ± 0.1	0.7 ± 0.1	0.9 ± 0.1	0.7 ± 0.2	0.7 ± 0.2
Ti	0.08 ± 0.06	0.11 ± 0.03	0.05 ± 0.02	0.1 ± 0.1	0.10 ± 0.07	0.14 ± 0.08
Cr	<0.01	<0.01	<0.01	<0.01	<0.01	<0.01
Mg	2.0 ± 0.1	2.2 ± 0.2	1.6 ± 0.3	2.5 ± 0.2	2.4 ± 0.3	2.5 ± 0.3
Fe^{2+}†	1.8 ± 0.2	1.7 ± 0.2	2.0 ± 0.3	1.3 ± 0.2	1.4 ± 0.3	1.4 ± 0.3
Mn	0.09 ± 0.01	0.09 ± 0.01	0.11 ± 0.00	0.10 ± 0.01	0.10 ± 0.03	0.10 ± 0.03
Ca	1.86 ± 0.03	1.9 ± 0.1	1.91 ± 0.07	1.74 ± 0.06	1.75 ± 0.06	1.78 ± 0.07
Na	0.42 ± 0.06	0.38 ± 0.04	0.43 ± 0.01	0.4 ± 0.1	0.4 ± 0.1	0.4 ± 0.1
K	0.24 ± 0.05	0.21 ± 0.03	0.32 ± 0.04	0.15 ± 0.05	0.21 ± 0.04	0.19 ± 0.03
X_{Fe3+}	0.29 ± 0.08	0.26 ± 0.06	0.26 ± 0.05	0.42 ± 0.06	0.3 ± 0.1	0.35 ± 0.07
X_{Mg}	0.53 ± 0.03	0.56 ± 0.04	0.45 ± 0.06	0.67 ± 0.06	0.64 ± 0.04	0.64 ± 0.06
Al^T	1.8 ± 0.2	1.7 ± 0.2	2.4 ± 0.2	1.3 ± 0.3	1.6 ± 0.3	1.43 ± 0.09

* Number in parentheses indicates number of replicate rim analyses averaged to yield value. Uncertainties are given at 2σ level.

† Ferrous and ferric iron calculated on the basis of 13 cations excluding Ca, Na, and K.

$X_{Fe3+} = Fe^{3+}/(Fe^{total})$. $X_{Mg} = Mg/(Mg + Fe^{2+})$.

TABLE 2. EMPLACEMENT PRESSURE ALONG THE LENGTH OF THE VRONDOU PLUTON

Sample†	Position (km)*	Al^T	Pressure[a] (kbar)	Pressure[b] (kbar)	Depth** (km)
VP-93-132 (16)	- 6.9	1.8 ± 0.2	6 ± 1	4.3 ± 0.8	16 - 22 (± 4)
VP-91-67 (5)	- 1.7	1.7 ± 0.2	5 ± 1	3.7 ± 0.8	14 - 19 (± 4)
VP-91-68 (12)	0.0	1.3 ± 0.2	3 ± 1	2.0 ± 0.8	8 - 12 (± 4)
VP-94-95 (15)	6.9	1.6 ± 0.3	5 ± 1	3 ± 1	12 - 17 (± 4)
VP-110 (15)	5.9	1.2 ± 0.3	3 ± 1	2 ± 1	6 - 10 (± 4)
VP-119 (14)	6.9	1.2 ± 0.3	3 ± 1	2 ± 1	6 - 10 (± 4)
VP-213 (22)	8.8	1.3 ± 0.4	3 ± 2	2 ± 2	8 - 11 (± 8)
VP-239 (13)	9.0	1.0 ± 0.4	2 ± 2	1 ± 2	3 - 8 (± 8)
ES-91-12 (9)	- 7.6	1.43 ± 0.09	3.8 ± 0.4	2.6 ± 0.4	10 - 14 (± 2)

† Number in parentheses after sample number indicates number of rim analyses averaged for total aluminum content. Average for sample 91-67 is for amphibole grain with lowest total aluminum content. Microprobe analyses for samples 110, 213, 119, and 239 are from *Theodorikas* [1986]

* Distance along a southwest-trending transect using the summit of the Vrondou pluton as an arbitrary reference point. Positive values are northeast of the summit.

[a] Pressure calculated from the aluminum-in-hornblende barometer calibration of *Schmidt* [1992]. Uncertainties incorporate only standard deviation of Al^T and are given at 2σ level.

[b] Pressure calculated from the aluminum-in-hornblende barometer calibration of *Johnson and Rutherford* [1989]. Uncertainties incorporate only standard deviation of Al^T and are given at 2σ level.

** Emplacement depth range calculated from pressure range assuming a crustal density of 2700 kg/m^3. Uncertainty is calculated from the larger of the two uncertainties in emplacement pressure.

FIGURE CAPTIONS

Figure 1. Simplified geologic map of the northern Rhodope metamorphic core complex, showing locations of analyzed samples. Location of figure shown in upper inset with regional tectonic zones of the Hellenides (EH – External Hellenides; m – Tertiary molasse basin; PZ – Pelagonian zone; AZ – Axios zone; CRB – Circum-Rhodope Belt; Rmcc – Rhodope metamorphic core complex). Lower inset – Lower hemisphere, equal area stereonet diagram of stretching lineations and poles to mylonitic foliations formed during ductile motion on the Strymon Valley detachment fault.

Figure 2. $Mg/(Mg+Fe^{2+})$ vs. Al^T for rim and core analyses of a single hornblende grain from Sample 91-67. Filled circles – rim compositions. Open circles – core compositions. Error bars show overlapping average and 2σ uncertainties for rim (r) and core (c) compositions.

Figure 3. (a) Emplacement pressure as a function of position along a southwest-trending transect of the Vrondou pluton (see Figure 1 for location). Open symbols reflect calculation of pressure using aluminum-in-hornblende calibration of *Schmidt* [1992]. Filled symbols use calibration of *Johnson and Rutherford* [1989]. Circles are data from the Vrondou pluton. Squares are data from the Elaion stock. Best-fit regression lines for Vrondou data are shown for both calibrations. (b) Present-day cross section through the Vrondou pluton parallel to the transport direction of the hanging wall. No vertical exaggeration. (c) Reconstructed cross section parallel to the extension direction on the Strymon Valley detachment fault using emplacement pressure calculated with the calibration of *Schmidt* [1992]. Heavy line is the inferred orientation of the Strymon Valley detachment fault. Light line indicates present-day level of exposure. Geobarometric results with 2σ uncertainties are given for each sample. Errors do not incorporate $\pm$ 0.6 kbar uncertainty in the geobarometer calibration. Because the reconstruction is based on a best-fit linear regression of data, some of the data fall above the present day level of exposure.

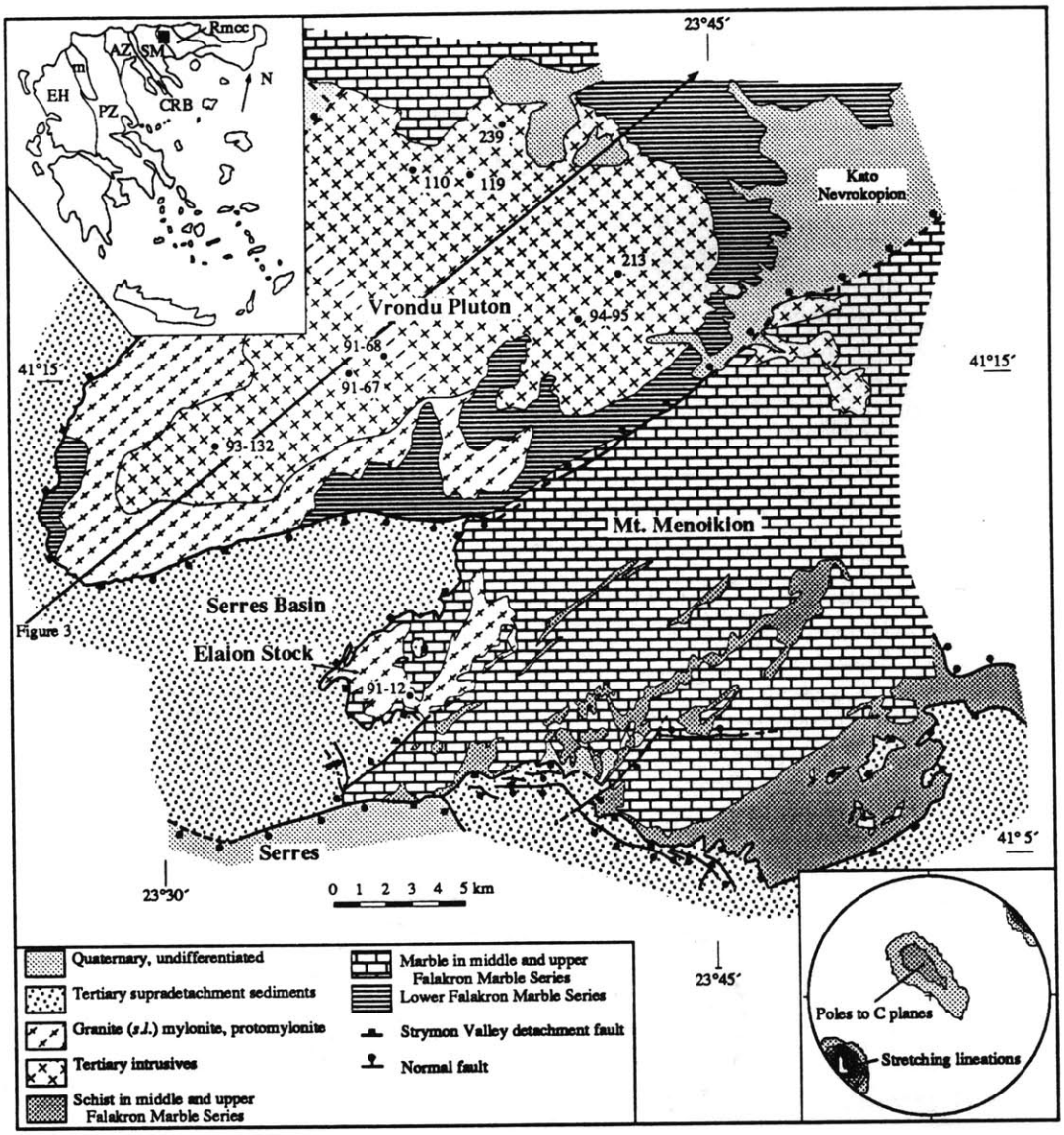
Rmcc
AZ
SM
EH
PZ
CRB
N
23°45′
239
110
119
213
94-95
Vrondu Pluton
91-68
91-67
93-132
41°15′
Kato Nevrokopion
Mt. Menoikion
Serres Basin
Figure 3
Elaion Stock
91-12
Serres
41° 5′
23°30′
0 1 2 3 4 5 km
23°45′
Quaternary, undifferentiated
Tertiary supradetachment sediments
Granite (s.l.) mylonite, protomylonite
Tertiary intrusives
Schist in middle and upper Falakron Marble Series
Marble in middle and upper Falakron Marble Series
Lower Falakron Marble Series
Strymon Valley detachment fault
Normal fault
Poles to C planes
Stretching lineations

Figure 1

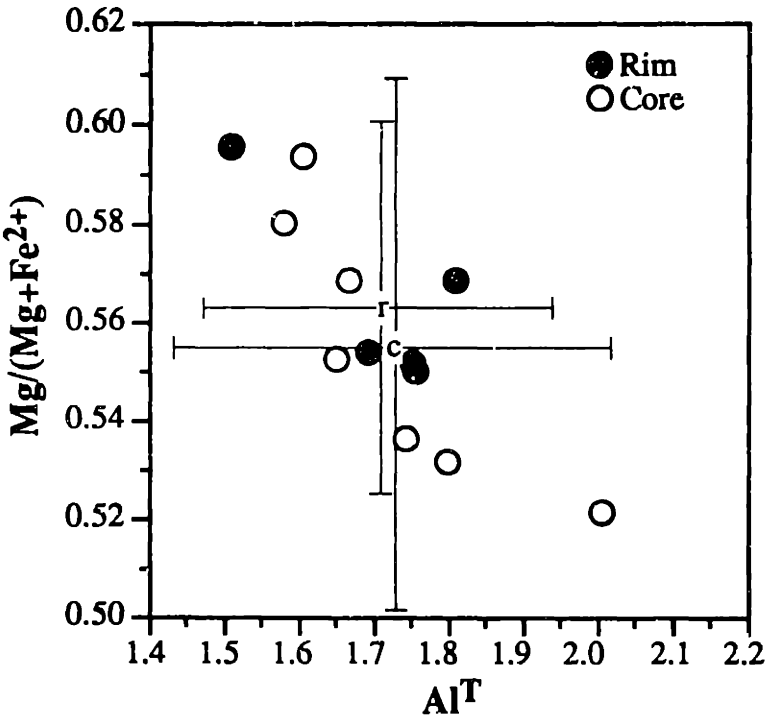
Rim
Core
r
c
0.62
0.60
0.58
0.56
0.54
0.52
0.50
Mg/(Mg+Fe2+)
1.4
1.5
1.6
1.7
1.8
1.9
2.0
2.1
2.2
AlT

Figure 2

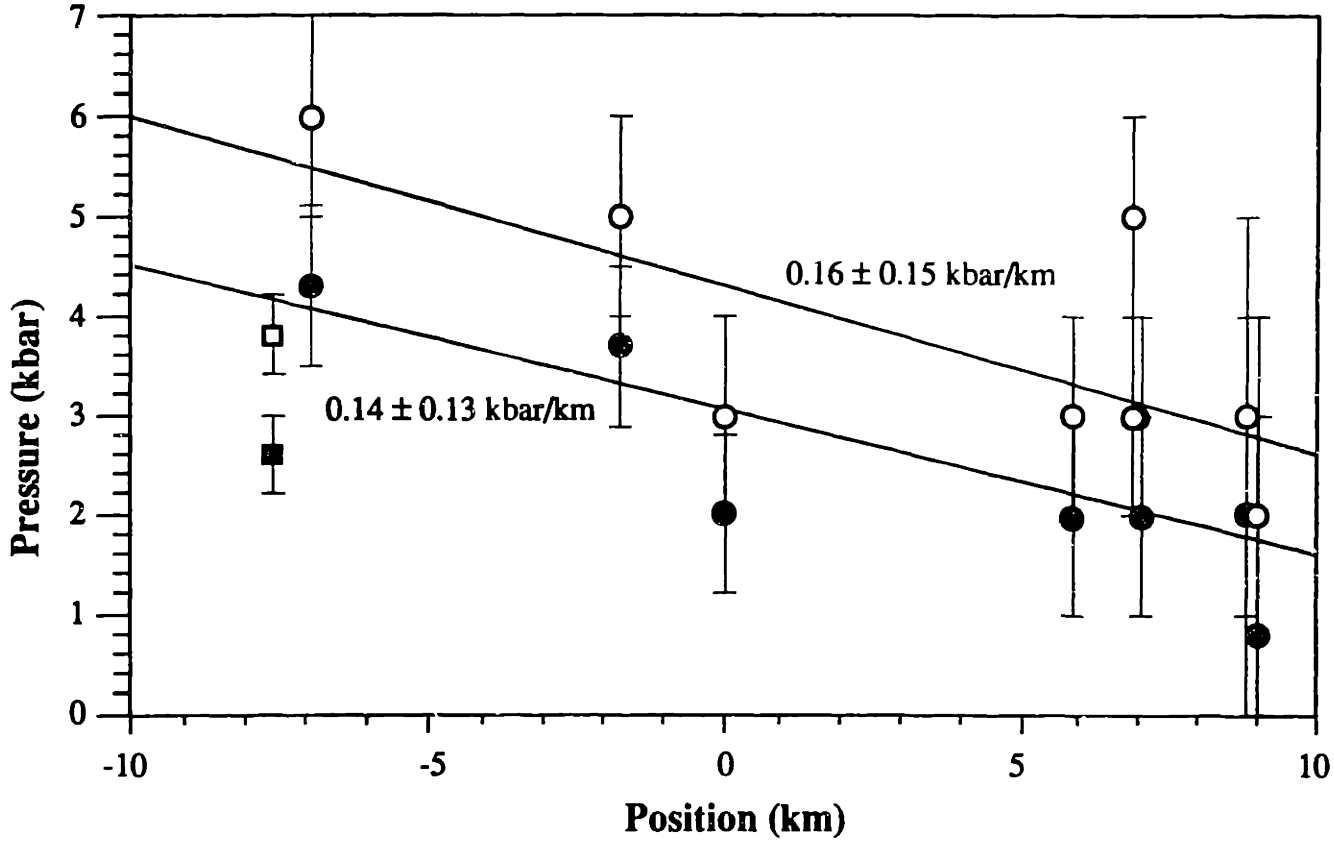
Pressure (kbar)
Position (km)
0.16 ± 0.15 kbar/km
0.14 ± 0.13 kbar/km
0
1
2
3
4
5
6
7
-10
-5
0
5
10

Figure 3a

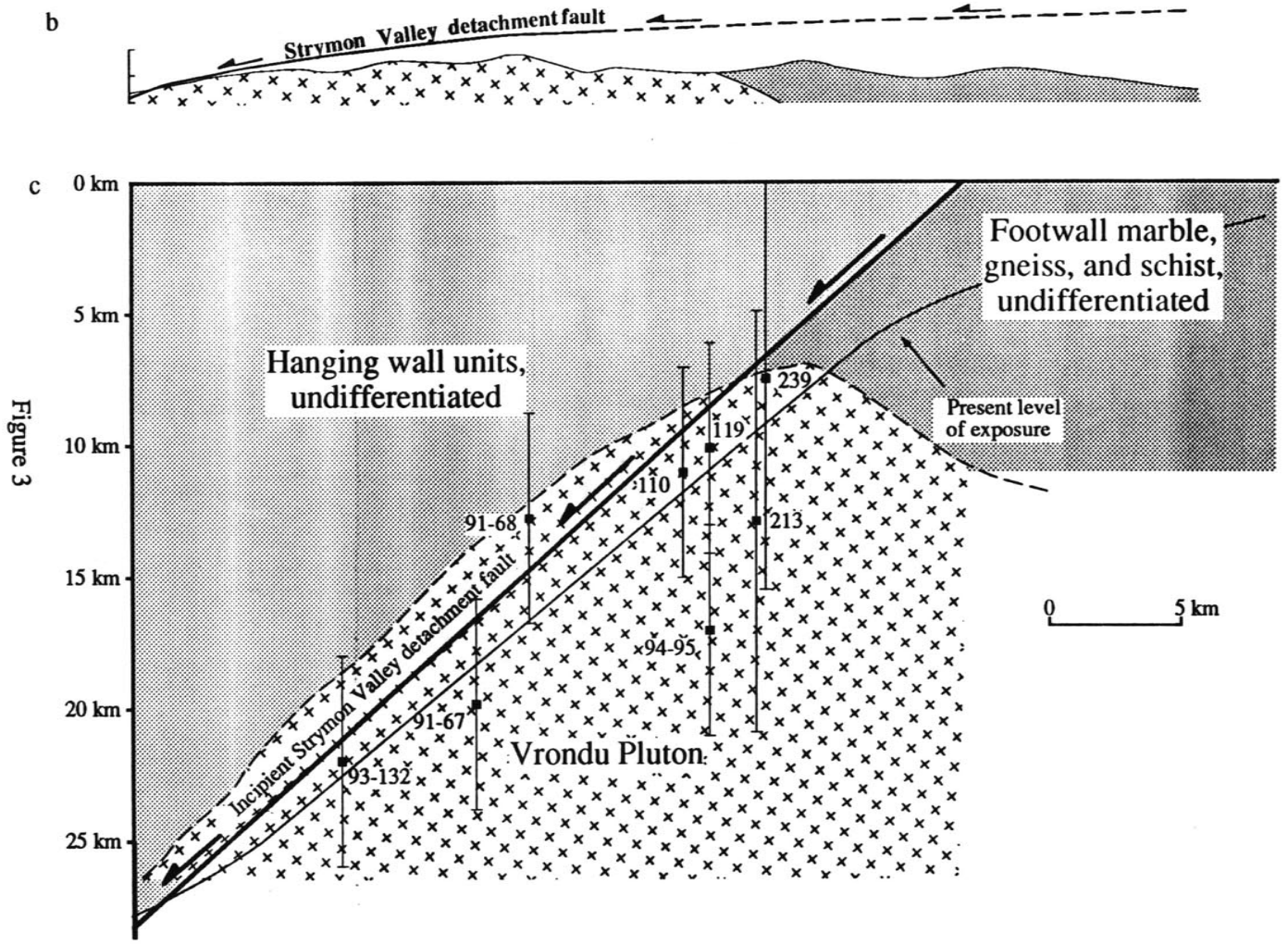
b
Strymon Valley detachment fault
c
0 km
5 km
10 km
15 km
20 km
25 km
Hanging wall units, undifferentiated
Footwall marble, gneiss, and schist, undifferentiated
Present level of exposure
239
119
110
213
91-68
94-95
91-67
93-132
Incipient Strymon Valley detachment fault
Vrondu Pluton
0
5 km

Figure 3

CHAPTER 6: CONCLUDING REMARKS

Although the Halloran Hills and the Rhodope metamorphic core complex are widely separated geographically, their common genesis in continental crustal extension makes it natural to draw comparisons between them. Both are Miocene to Recent extensional terranes formed in thickened continental crust in regions where there is significant interplay between magmatism and extension. Because they are young, geologic features with low preservation potential (e.g., Quaternary lake beds, geomorphologic surfaces) are not completely erased and can be used to draw important conclusions about the extensional process. Some generalized comparisons between the two regions tie them together and show how a better understanding of the detachment faulting process emerges from an integrated approach to geologic problems.

The role of isostasy and lower crustal flow in the Rhodope metamorphic core complex

In the Halloran Hills, post-tectonic uplift of Quaternary lake beds is attributed to lower crustal flow in response to tectonic loads emplaced in the crust during extension [Chapter 2]. The analytic model developed in Chapter 2 implies the lower crust of the Halloran Hills region has a density close to that of the upper crust and flows over time scales of millions of years. Comparable crustal properties would be anticipated for the Rhodope metamorphic core complex, based on its similar regional tectonic setting.

The well-exposed, present-day geometry of the Strymon Valley detachment fault [Chapter 3; *Dinter*, 1994], coupled with estimates of its original geometry [Chapter 5] strongly suggest that lower crustal flow has occurred on a regional scale in the Rhodope metamorphic core complex. The magnitude of tectonic denudation in the Rhodope metamorphic core complex almost requires the flow of the lower crust, or at least isostatic compensation by material not significantly denser than the upper crust. In the transport direction, the amount of hanging wall material that has been tectonically removed increases

from 0 km at the breakaway zone to at least 15 km along the western boundary of the exposed core complex. If isostatic compensation by a material with mantle density were occurring, there would be a significant topographic depression (on the order of 3 km deep) along the western boundary of the core complex (e.g., *Block and Royden* [1990]). In fact, the opposite is true: the 1.5 to 2 km high mountains of Menoikion, Vrondou, Pangaion, and Symvolon form some of the highest topography in the Rhodopes, implying that loads emplaced by extension are isostatically supported by material with a density comparable to that of the upper crust.

In the Rhodope metamorphic core complex, flow of the lower crust over finite time scales is also implied by Tertiary marine formations now exposed at high elevations. Syn- to post-detachment uplift (of strata) can be quantified in those few locations where shallow marine sediments of known or suspected age are found. Although some of the uplift may be attributed to an isostatic response to erosion (e.g., *England and Molnar* [1990]), the amount of erosion in the core complex is relatively small and this effect is probably minor. Possible uplift resulting from crustal unloading during the formation of the Drama and Strymon Basins is unquantified. The observation of post-detachment uplift in both the Halloran Hills and the Rhodope metamorphic core complex suggests that similar crustal-scale processes (i.e., lower crustal flow) could have occurred in both regions.

Shallow marine limestone lenses in the Menoikio Breccia Conglomerate permit it to be used as a datum to estimate uplift of the Rhodope metamorphic core complex relative to sea level (Figure 1). *Dinter* [1994] calculates an uplift rate for this formation of ~0.43 mm/yr, assuming that all of its uplift (present maximum elevation of ~1500 m) occurred continuously since the cessation of motion on the Strymon Valley detachment fault at 3.5 Ma. Because uplift probably occurred synchronously with detachment faulting, this represents the maximum uplift rate. Estimates of the minimum uplift rate are limited by uncertainty of the unit's age. Assuming that the Menoikio Breccia Conglomerate correlates

to the oldest units in the Serres Basin (9.8 Ma), the minimum bound on uplift rate is 0.15 mm/yr.

The hanging wall klippe of the shallow marine St. George Formation exposed at elevations up to 840 m on the eastern margin of the Serres Basin provides a second datum for estimating the magnitude and rate of uplift in the northern Rhodope metamorphic core complex (Figure 1). These sediments were deposited near sea level at approximately the Miocene-Pliocene boundary, ~5 Ma [*Karistineos and Georgiades-Dikeoulia*, 1986], when sea level was as much as 100 m higher than present [*Haq et al.*, 1988]. Their present elevation requires a minimum of 740 m of uplift of the eastern Serres Basin relative to sea level since 5 Ma, equal to an minimum average uplift rate of 0.14-0.15 mm/yr.

Post-detachment uplift rates have been calculated for the southern part of the Rhodope metamorphic core complex. *Dinter* [1994] reports undeformed Upper Pliocene or Quaternary wave-cut platforms at elevations of 290 m on the southwest flank of Mt. Pangaion. Although the age of these is not known, it is unlikely that they are younger than the last pre-glacial high-stand (approximately 1.1 Ma [*Haq et al.*, 1988]). Assuming maximum Plio-Quaternary sea level fluctuations of 60 m [*Haq et al.*, 1988] and a maximum age of 3.5 Ma for these platforms, the minimum rate of uplift is 0.06 mm/yr.

The three estimates for uplift in the Rhodope metamorphic core complex are shown with their uncertainties in Figure 2a. The magnitude of uplift increases with increasing age of the formation or geomorphologic feature. Uncertainties reflect potential eustatic fluctuations (assumed to be up to 100 m for the Miocene formations and 60 m for the Plio-Quaternary terraces), displacement on the Strymon Valley detachment fault, and uncertainties in the age of the formation or feature. It is interesting that average uplift rate also increases with increasing age of the formation or feature used to calculate the uplift rate (Figure 2b). The uplift rates on Figure 2b are calculated from the present elevation of the feature and ignore potential structural and eustatic effects. The minimum uplift rate is calculated by assuming continuous uplift since deposition or formation of the unit or

geomorphologic feature. The true maximum uplift rate is unconstrained because uplift timing is uncertain (e.g., if all uplift occurred in the Holocene, uplift rates would be enormous). The maximum uplift rates for the Menoikio Breccia Conglomerate and the St. George klippe shown in Figure 2b assume constant uplift since 3.5 Ma, the approximate time of cessation of motion on the Strymon Valley detachment fault. The maximum uplift rate for the Plio-Quaternary terraces assumes constant uplift since the last pre-glacial sea level maximum at approximately 1.1 Ma [*Haq et al.*, 1988].

Although it is speculative to make broad generalizations about laterally distant parts of the Rhodope metamorphic core complex, the data indicate significant post-tectonic uplift has occurred in the Rhodope metamorphic core complex, consistent with numerical models of lower crustal flow in extended regions [*Kaufman and Royden*, 1994]. The apparent decrease through time of the uplift rate is also consistent with these models. The uplift rates estimated for the Rhodope metamorphic core complex are roughly comparable to relative Quaternary uplift rates in the Halloran Hills region. Because there is no absolute datum in the Halloran Hills (e.g., sea level), uplift must be determined relative to an arbitrary datum (taken to be Valley Wells). Quaternary lake sediments exposed on the flanks of the Halloran Hills and south of the Kingston Range (60 m above and 120 m below the lake beds at Valley Wells, respectively) yield average Quaternary uplift rates between 0.12 and 0.24 mm/yr. The modelled average uplift rate with respect to Valley Wells since the cessation of detachment faulting is a function of position and assumed lower crustal viscosity (see Figures 8 and 9, Chapter 2), but is usually about an order of magnitude less (0.01 to 0.07 mm/yr) than the average rate of uplift in the Rhodope metamorphic core complex, possibly reflecting the greater crustal thinning in the Rhodopes.

If there has been significant flow of the lower crust during and following the formation of the Rhodope metamorphic core complex, several general predictions can be made about its potential regional impact. The flow of lower crust from east of the

breakaway zone towards the western core complex along the pressure gradient produced by tectonic denudation would be expected to uplift the western part of the core complex relative to the eastern part, reduce east-west topographic gradients, and smooth regional crustal thickness variations. Uplift of the western core complex has occurred as described above, but it is not clear if this is due to east-west tilting or regional uplift of the Rhodopes (e.g., *Psilovikos* [1986]; *Zagorchev* [1992]). A reduction of topographic gradients in the Rhodope metamorphic core complex is implied by an overall upward fining of supradetachment sediments in the Serres Basin. In the southeastern Serres Basin, coarse boulder conglomerates and marble breccia sheets give way to fine-grained sands, silts, and marls [Chapter 3; *Karistineos and Georgiades-Dikeoulia* [1986]). If detailed study of clast provenance were to reveal derivation of material from east of breakaway zone (as is observed in the Halloran Hills [*Friedmann et al.*, 1994]), the case for regional tilting would be greatly strengthened. Significant variations in crustal thickness across the Rhodope metamorphic core complex are not evident in regional gravity maps or seismic tomography of the north Aegean region (e.g., *Spakman* [1990]; *Morelli* [1990]) but it is likely that the scale of observations in these experiments is too coarse to image crustal-scale features.

The role of plutons on detachment fault geometry

In both the Halloran Hills and the Rhodope metamorphic core complex, there is an intimate relationship between pluton intrusion and detachment faulting. In the Halloran Hills, the epizonal Kingston Peak pluton was intruded across the active Kingston Range-Halloran Hills detachment fault, pinning the northern segment of the fault [*Davis et al.*, 1993]. Continued extension was accommodated by motion on the unpinned Halloran Hills segment of the detachment fault. In the Rhodope metamorphic core complex, the Strymon Valley detachment fault follows plutonism closely in time and space. The pre-detachment Vrondou and Symvolon plutons are both exposed in structural corrugations of the detachment fault.

Along the western boundary of the core complex, gross metamorphic stratigraphy and aluminum-in-hornblende geobarometry imply that the Strymon Valley detachment fault has significant along-strike structural relief and cuts down-section to expose both the Vrondou and Symvolon plutons [Chapter 3; Chapter 5]. It is unclear if the detachment fault cuts deeply into either pluton's interior, or if it opportunistically localizes near the pluton-country rock interface. In the northern Rhodope metamorphic core complex, the lower and middle Falakron Marble Series are in intrusive contact with the Vrondou pluton on all of its margins, suggesting the detachment does not cut deeply into the pluton's interior. (However, it is possible that the lower Falakron Marble Series exposed on the western end of the Vrondou pluton (Figure 1) could be an isolated roof pendant.) Because the footwall of the core complex is submerged south of the Symvolon pluton, it is uncertain if the detachment fault is behaving similarly in the southern Rhodope metamorphic core complex. Several small, isolated outcrops of the Falakron Marble Series are exposed along the length of its southern flank, which suggest the detachment fault may not cut deeply into the Symvolon pluton's interior.

If the detachment fault is localized along the pluton-country rock interface, then it would seem that the plutons are acting as mid-crustal stress guides. A likely explanation for this behavior is that the granitic plutons are much stronger than the marbles and schists of the Falakron Marble Series at the time of detachment faulting, as would be expected from a comparison of the typical yield strengths of quartz and marble based rheologies (e.g., *Carter and Tsenn* [1987]). The thermal pulse originating from an intrusive pluton would exacerbate this strength contrast, further weakening the country rock immediately around the pluton. The strength profile for the mid-crust into which a granitic pluton has intruded marbles and marble-bearing schist would have a rheologically weak zone sandwiched between two stronger zones (Figure 3) superficially resembling the strength profile for the lower continental crust. The rheologically weakest part of the mid-crust would be at the interface between the two lithologies, forming a natural site for detachment

fault localization. If so, then most of the relative displacement across the detachment fault may have been accommodated by the weak Falakron Marble Series, implying that the thick mylonitized margins of the plutons might represent only a minor amount of the overall displacement on the detachment fault.

If these interpretations are correct, a further similarity can be drawn between the Halloran Hills and the Rhodope metamorphic core complex: granitic plutons, even though recently emplaced, are significantly stronger than the country rocks into which they are intruded. In the two areas, detachment faults were either pinned by a pluton or localized along its interface with the country rock, implying that on a crustal scale, it is harder to deform an isotropic granitic pluton than to take advantage of zones of crustal weaknesses.

Possible regional causes of detachment faulting in the Rhodope metamorphic core complex

One of the important questions to address in the Rhodope metamorphic core complex is what is the driving force behind the extensional process? Several important factors that may influence detachment initiation are weakening of the crust by regional magmatism, collapse of an overthickened continental crust, and relaxation of regional compressional stresses. Many workers have emphasized that plutonism and core complex formation are intimately related in time and space (e.g., *Coney* [1980]; *Gans et al.* [1989]; *Lister and Baldwin* [1993]). It is clear that extensive magmatism in northeastern Greece and southern Bulgaria preceded detachment faulting in the Rhodope metamorphic core complex [*Innocenti et al.*, 1984; *Eleftheriadis and Lippolt*, 1984; *Lilov et al.*, 1987; *Jones et al.*, 1992], but it is not clear what role plutonism has on detachment fault initiation. In both the northern and southern Rhodope metamorphic core complex, detachment fault initiation post-dates pluton intrusion by at least eight to ten million years [*Dinter et al.*, 1995; Chapter 4].

A simple analytical expression for a conductively cooling, two-dimensional pluton shows that the thermal pulse generated by an intrusion with dimensions comparable to the

Vrondou or Symvolon pluton decays fairly quickly. For a rectangular pluton of width w intruded between depths z_1 and z_2, with its center at $x = a/2$ (where $a >> w$) the solution to the heat flow equation is

$$T(x,z,t) = \zeta z + \frac{\Delta T}{4}\left[erf\left(\frac{2x - a + w}{4\sqrt{\alpha t}}\right) - erf\left(\frac{2x - a - w}{4\sqrt{\alpha t}}\right)\right]\left[erf\left(\frac{z - z_1}{2\sqrt{\alpha t}}\right) - erf\left(\frac{z - z_2}{2\sqrt{\alpha t}}\right)\right]$$

for boundary conditions $T(x,z,t) = 0$ at $z = 0$ and $dT/dx = 0$ at $x = 0$ and $x = a$. ΔT is the temperature increase of the intrusion above the ambient linear geothermal gradient ζ.

The temperature-time history for a pluton with the approximate dimensions of the Vrondou pluton is shown in Figure 4. The cooling curves indicate that although Oligocene magmatism may have generated significant heat, weakening the Rhodope crust (and possibly forming rheologically weak zones within the crust), most of the thermal anomaly generated by an Oligocene pluton would have decayed by Miocene time. Although the extensive Oligocene magmatism in the Rhodopes may not initiate detachment faulting by itself, it may be a manifestation of a regional-scale thermal event within the upper mantle. If so, the crust may be weakened by the gradual diffusion of heat from the mantle, possibly causing detachment initiation several million years after the magmatic precursor.

The collapse of overthickened continental crust, such as is found in the Rhodopes [*Makris*, 1978], is thought to be a major cause of core complex formation (e.g., *Bird* [1989]; *Buck* [1991]; *England and Houseman* [1989]). In the Rhodopes much of the crustal thickening occurred during Alpine compression, which in the internal Hellenides and Rhodopes lasted until Eocene time [*Schermer*, 1990; *Dinter*, 1994; *Tsankov et al.*, in prep.; Chapter 3]. Oligocene magmatism may have further thickened the Rhodope crust. Compression in the Hellenides continued throughout the Tertiary, but in general, the locus of active thrusting propagated arc-ward from the Rhodopes to the external Hellenides. North of the Rhodopes in Bulgaria, there is evidence for extensional faulting beginning in the late Middle Eocene and continuing through the Oligocene and Miocene in the Sub-

Balkan Grabens and the Thracian depression [*Tsankov et al.*, in prep.; Nakov, pers. comm., 1992]. This extensional faulting may signal the relaxation of regional compressional stresses that had held the overthickened Rhodope crust together. With the relaxation of these stresses, the Rhodope crust began extending, possibly initiating extensive Oligocene magmatism at the same time (e.g., *Kotopouli and Pe-Piper* [1989]; *Jones et al.* [1992]). Extensive magmatism, and perhaps a regional-scale thermal event in the mantle, would heat and further weaken the overthickened crust, perhaps accelerating the extensional process. Although extension was actively ongoing in the Thracian depression during the Late Eocene and Oligocene, to the south (i.e., in the incipient Rhodope metamorphic core complex), extension did not initiate until the Miocene. It is possible that the regional compressive stresses were maintained between the southern Rhodopes and the Hellenic arc until the Miocene. After the relaxation of these stresses holding the warm thick Rhodope crust together, extension initiated, forming the Rhodope metamorphic core complex.

REFERENCES

Bird, P., 1991, Lateral extrusion of lower crust from under high topography, in the isostatic limit, *Journal of Geophysical Research*, v. 96, p. 10,275-10,286.

Block, L., and L.H. Royden, 1990, Core complex geometries and regional scale flow in the lower crust, *Tectonics*, v. 9, p. 557-567.

Buck, W.R., 1991, Modes of continental lithospheric extension, *Journal of Geophysical Research*, v. 96, p. 20,161-20,178.

Carter, N.L., and M.C. Tsenn, 1987, Flow properties of continental lithosphere, *Tectonophysics*, v. 136, p. 27-63.

Coney, P.J., 1980, Cordilleran metamorphic core complexes: An overview, *Geological Society of America Memoir* 153, p. 7-31.

Davis, G.A., T.K. Fowler, K.M. Bishop, T.C. Brudos, S.J. Friedmann, D.W. Burbank, M.A. Parke, and B.C. Burchfiel, 1993, Pluton pinning of an active Miocene detachment fault system, eastern Mojave Desert, California, *Geology*, v. 21, p. 627-630.

Dinter, D.A., 1994, Tectonic evolution of the Rhodope metamorphic core complex, Northeastern Greece [Ph.D. Thesis], Massachusetts Institute of Technology, Cambridge, MA, 320 pp.

Dinter, D.A., A.M. Macfarlane, W. Hames, C. Isachsen, and L. Royden, 1995, U-Pb and $^{40}Ar/^{39}Ar$ geochronology of the Symvolon granodiorite: Implications for the thermal and structural evolution of the Rhodope metamorphic core complex, northeastern Greece, in press, *Tectonics*.

Eleftheriadis, G. and H.J. Lippolt, 1984, Altersbestimmungen zum oligozänen vulkanismus der Süd-Rhodopen/Nord Griechenland, *Neues Jahrbuch für Geologie und Paläontologie, Monatshefte*, v. 3, p. 179-191.

England, P., and G. Houseman, 1989, Extension during continental convergence, with application to the Tibetan Plateau, *Journal of Geophysical Research*, v. 94, p. 17,561-17,579.

England, P., and P. Molnar, 1990, Surface uplift, uplift of rocks, and exhumation of rocks, *Geology*, v. 18, p. 1173-1177.

Friedmann, S.J., G.A. Davis, T.K. Fowler, T. Brudos, M. Parke, D.W. Burbank, and B.C. Burchfiel, 1994, Stratigraphy and gravity-glide elements of a Miocene supradetachment basin, Shadow Valley, East Mojave Desert, 1994 G.S.A. Cordilleran Section Guide Book, p. 302-318.

Gans, P.B., G.A. Mahood, and E.R. Schermer, 1989, Syn-extensional magmatism in the Basin and Range province; a case study from the eastern Great Basin, *Geological Society of America Special Paper* 233, 60 pp.

Haq, B.U., J. Hardenbol, and P.R. Vail, 1988, Mesozoic and Cenozoic chronostratigraphy and cycles of sea-level change, *in* Sea-Level Changes – an Integrated Approach, Society of Economic Paleontologists and Mineralogists Special Publication No. 42, C.K. Wilgus, B.S. Hastings, C.G.St.C. Kendall, H.W. Posamentier, C.A. Ross, and J.C. van Wagoner, eds., p. 71-109

Innocenti, F., N. Kolios, P. Manetti, R. Mazzuoli, G. Peccerillo, F. Rita, and L. Villari, 1984, Evolution and geodynamic significance of the Tertiary orogenic volcanism in northeastern Greece, *Bulletin Volcanologique*, v. 47, p. 25-37.

Jones, C.E., J. Tarney, J.H. Baker, and G. Gerouki, 1992, Tertiary granitoids of Rhodope, northern Greece: Magmatism related to extensional collapse of the Hellenic Orogen, *Tectonophysics*, v. 210, p. 295-314.

Karistineos, N.K., and E. Georgiades-Dikeoulia, 1986, The marine transgression in the Serres Basin, *Annales Géologiques des Pays Helléniques*, v. 33, p. 221-232.

Kaufman, P.S., and L. H. Royden, 1994, Lower crustal flow in an extensional setting: Constraints from the Halloran Hills region, eastern Mojave Desert, California, *Journal of Geophysical Research*, v. 99, p. 15,723-15,739.

Kotopouli, C.N. and G. Pe-Piper, 1989, Geochemical characteristics of felsic intrusive rocks within the Hellenic Rhodope: A comparative study and petrogenetic implications, *Neues Jahrbuch für Mineralogie, Abhandlungen*, v. 161, p. 141-169.

Lilov, P., Y. Yanev, and P. Marchev, 1987, K/Ar dating of the eastern Rhodope Paleogene magmatism, *Geologica Balcanica*, v. 17, p. 49-58.

Lister, G.S., and S.L. Baldwin, 1993, Plutonism and the origin of metamorphic core complexes, *Geology*, v. 21, p. 607-610.

Makris, J., 1978, The crust and upper mantle of the Aegean region from deep seismic soundings, *Tectonophysics*, v. 46, p. 269-284.

Morelli, C., 1990, The regional meaning of the Bouguer gravity anomalies in the Mediterranean, *Journal of Geodynamics*, v. 12, p. 123-136.

Psilovikos, A.A., 1986, Contribution to the geomorphology of the southwestern part of the Rhodope massif (Greek East Macedonia), *Geologica Balcanica*, v. 16(5), p. 21-32.

Schermer, E.R., D.R. Lux, and B.C. Burchfiel, 1990, Temperature-time history of subducted continental crust, Mt. Olympos region, Greece, *Tectonics*, v. 9, p. 1165-1195.

Spakman, W., 1990, Tomographic images of the upper mantle below central Europe and the Mediterranean, *Terra Nova*, v. 2, p. 542-553.

Tsankov, Ts., D. Angelova, R. Nakov, B.C. Burchfiel, and L.H. Royden, The sub-Balkan graben system of central Bulgaria, in prep.

Zagorchev, I.S., 1992, Neotectonics of the central parts of the Balkan Peninsula: Basic features and concepts, *Geologische Rundschau*, v. 83, p. 635-654.

FIGURE CAPTIONS

Figure 1. Simplified geologic map of the northern Rhodope metamorphic core complex. MBC – Menoikio Breccia Conglomerate at ~ 1500 m elevation; SGK – Klippe of calcareous sandstones and marls of the St. George Formation.

Figure 2. (a) Present elevation of sedimentary units or geomorphologic features formed at or near sea level plotted as a function of their age. Uncertainties in the age of the formation and range of elevations shown as shaded regions. Timing of sea level high-stands from *Haq et al.* [1988]. (b) Calculated uplift rate for sedimentary units and geomorphologic features. Shaded region gives uncertainty which reflects uncertainty in timing of uplift. Lower bound given by continuous uplift since deposition or formation (uplift rate = elevation/formation age). Timing of sea level high-stands from *Haq et al.* [1988].

Figure 3. Cartoon diagram of yield strength versus depth with an interface between two different rheologies (e.g., marble and granitic pluton or continental crust and mantle). Magnitude of yield strength envelope depends on crustal thermal structure and material properties.

Figure 4. (a) Thermal history (temperature-time plot) of the crust intruded by a pluton 10 km thick and 20 km wide at a depth of 15 km. Curves are for positions 2 and 4 km above the center of the pluton, at the pluton-country rock interface, and 2 km below the pluton-country rock interface (z = 11, 13, 15, and 17 km). The ambient geothermal gradient is assumed to be linear at 25° C/km. The initial temperature of the pluton was taken to be 425° C above the ambient geothermal gradient. Dotted lines indicate steady-state temperature at z = 11, 13, 15, and 17 km for a linear geothermal gradient of 25° C/km. (b) Cooling rate as a function of time for above positions and initial conditions.

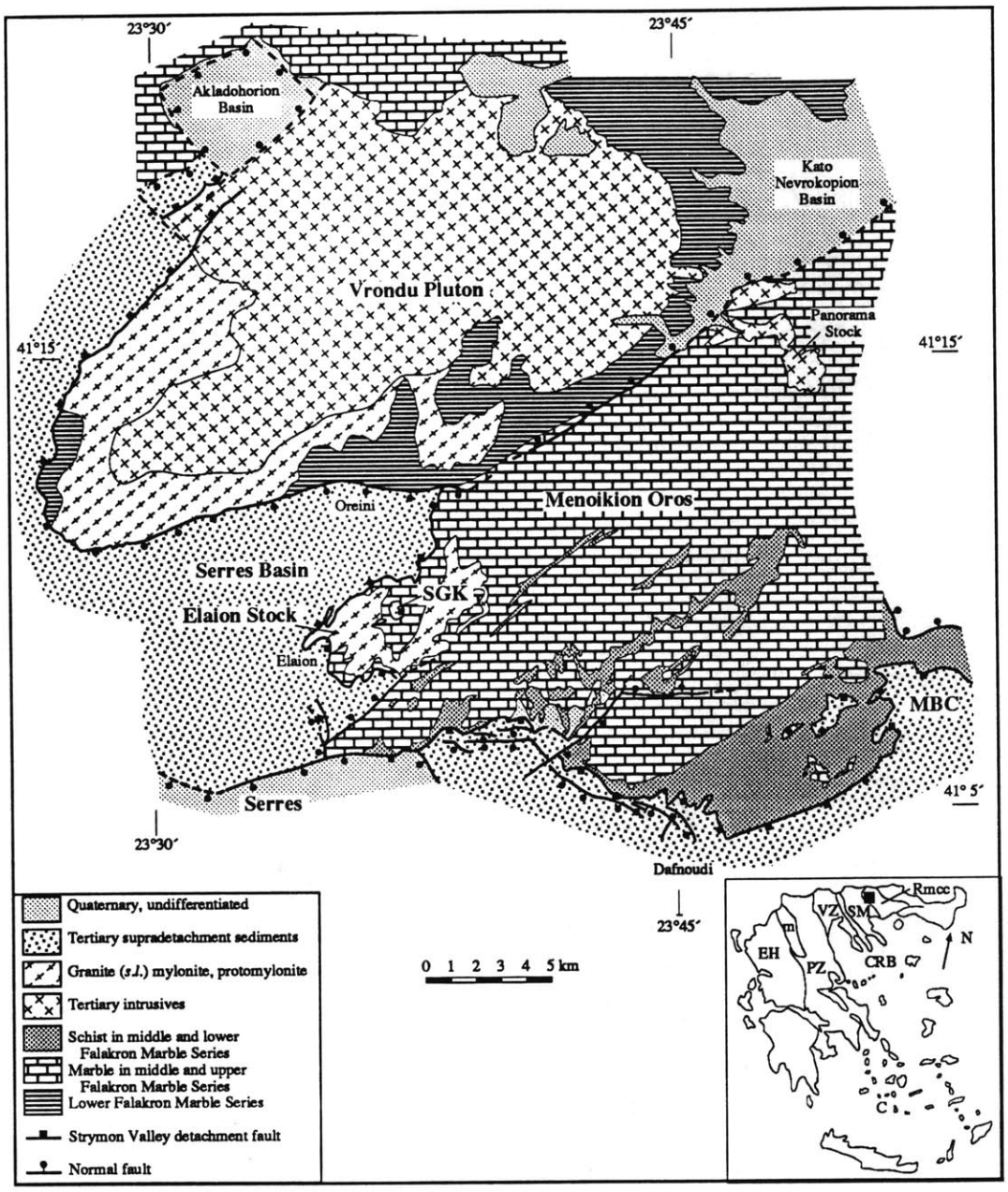
23°30′
23°45′
Akladohorion Basin
Kato Nevrokopion Basin
Vrondu Pluton
Panorama Stock
41°15′
Oreini
Menoikion Oros
Serres Basin
SGK
Elaion Stock
Elaion
MBC
41° 5′
Serres
Dafnoudi
Quaternary, undifferentiated
Tertiary supradetachment sediments
Granite (s.l.) mylonite, protomylonite
Tertiary intrusives
Schist in middle and lower Falakron Marble Series
Marble in middle and upper Falakron Marble Series
Lower Falakron Marble Series
Strymon Valley detachment fault
Normal fault
0 1 2 3 4 5 km
Rmcc
VZ
SM
EH
PZ
CRB
N
C

Figure 1

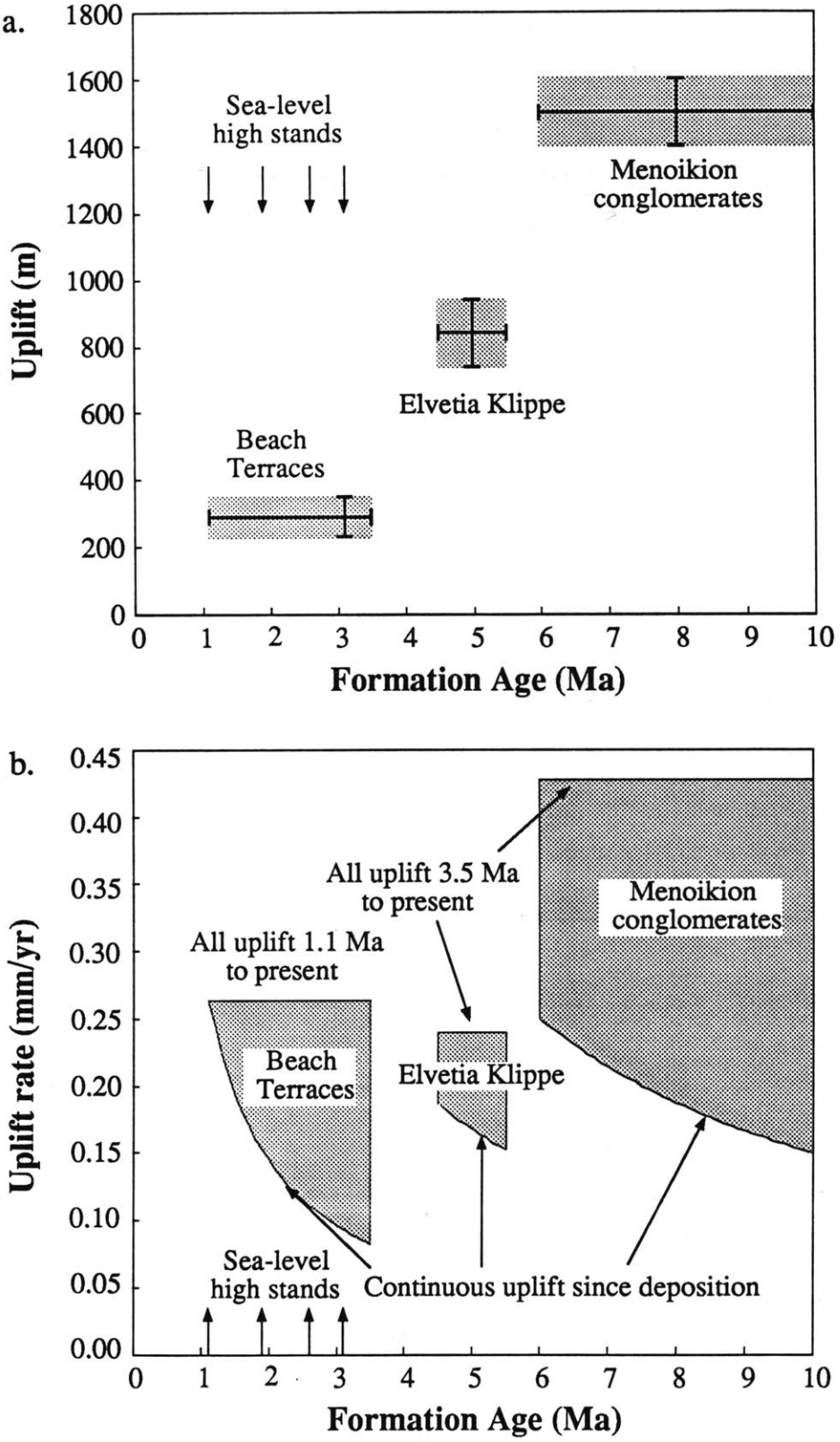
a.
Uplift (m)
1800
1600
1400
1200
1000
800
600
400
200
0
Sea-level
high stands
Menoikion
conglomerates
Elvetia Klippe
Beach
Terraces
0 1 2 3 4 5 6 7 8 9 10
Formation Age (Ma)
b.
Uplift rate (mm/yr)
0.45
0.40
0.35
0.30
0.25
0.20
0.15
0.10
0.05
0.00
All uplift 3.5 Ma
to present
Menoikion
conglomerates
All uplift 1.1 Ma
to present
Beach
Terraces
Elvetia Klippe
Sea-level
high stands
Continuous uplift since deposition
0 1 2 3 4 5 6 7 8 9 10
Formation Age (Ma)

Figure 2

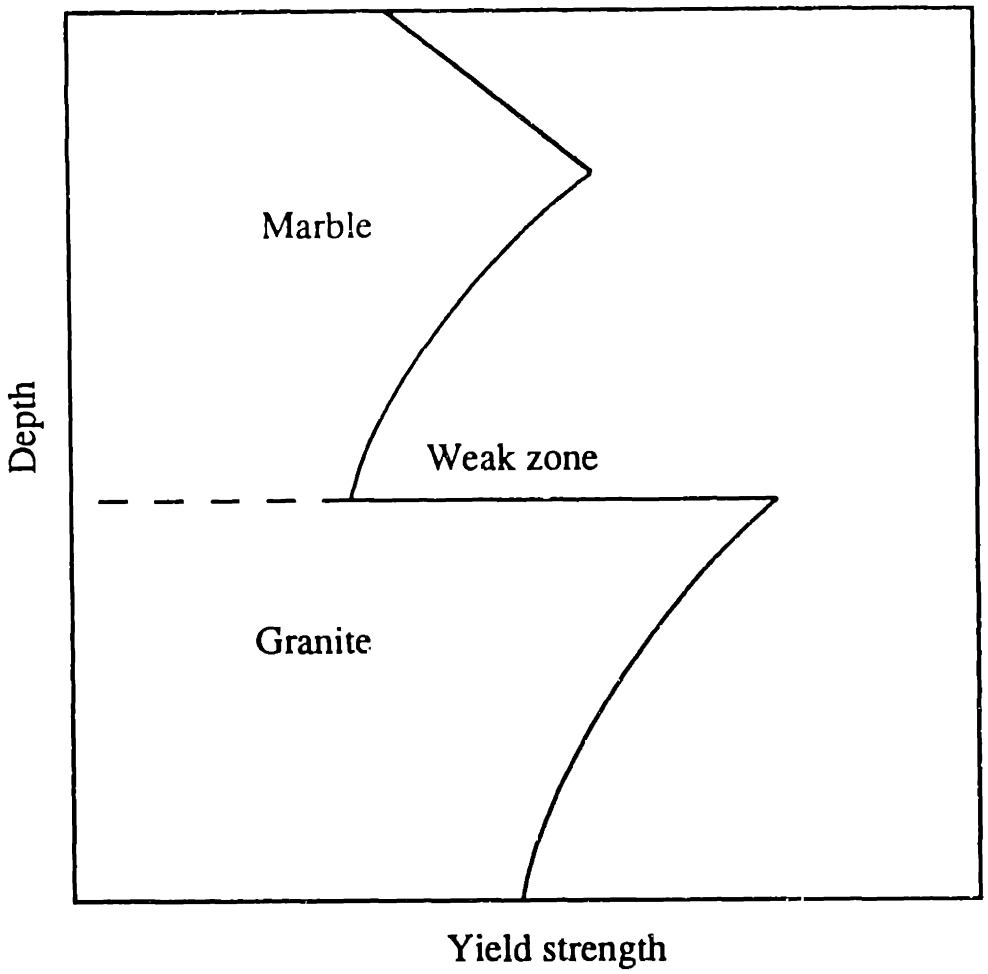

Figure 3

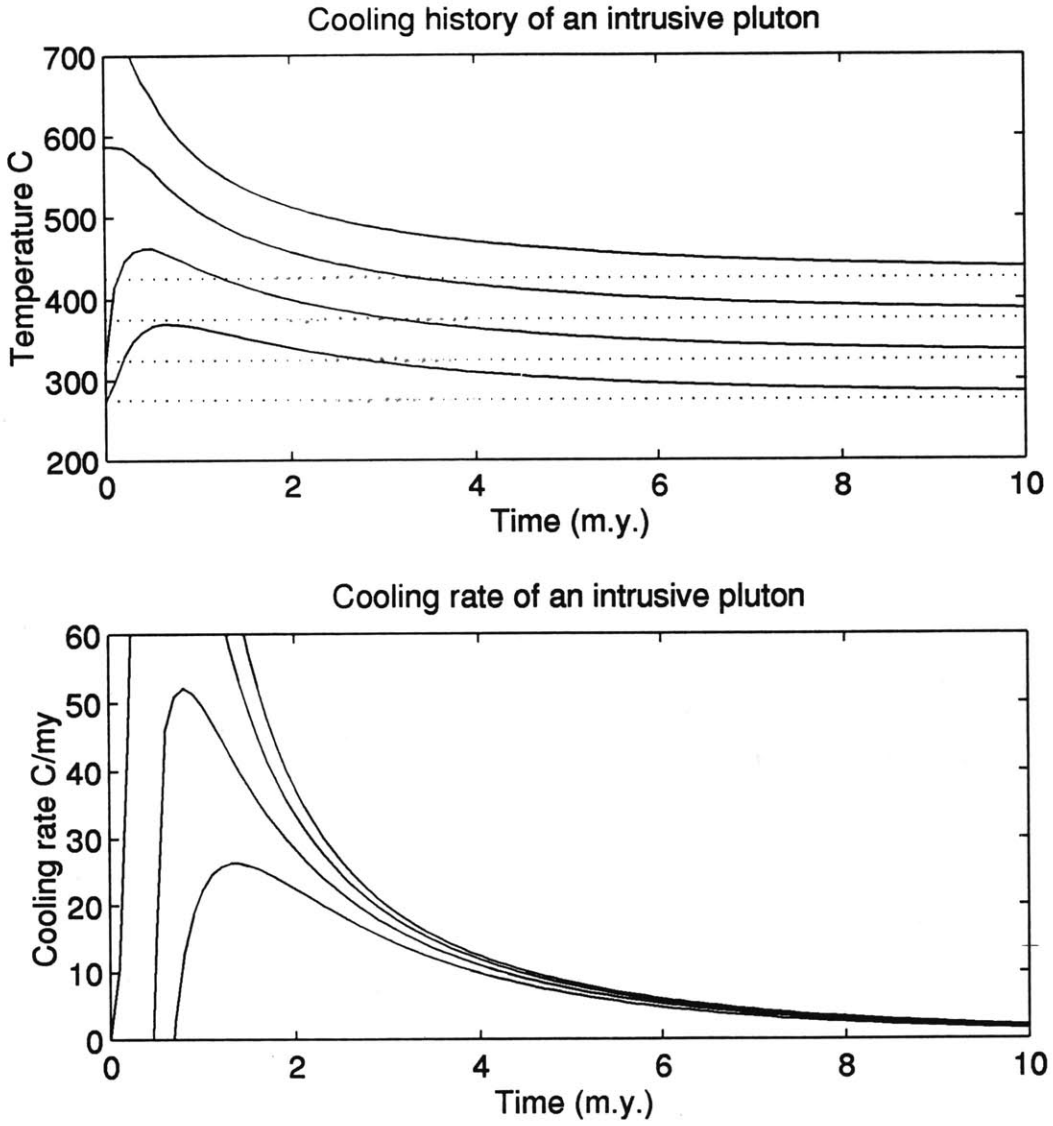
Cooling history of an intrusive pluton
Temperature C
700
600
500
400
300
200
0
2
4
6
8
10
Time (m.y.)
Cooling rate of an intrusive pluton
Cooling rate C/my
60
50
40
30
20
10
0
0
2
4
6
8
10
Time (m.y.)

Figure 4

Cross sections of the Northwest Rhodope Metamorphic Core Complex, Eastern Macedonia, Greece

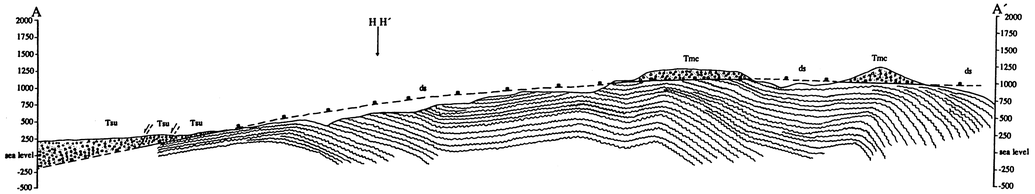

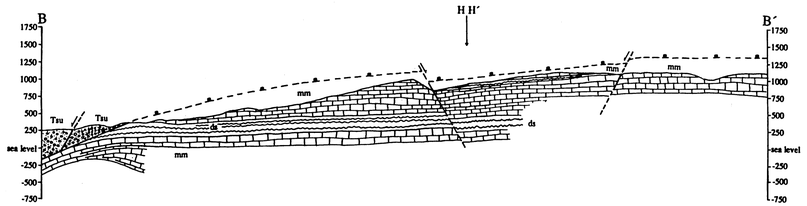

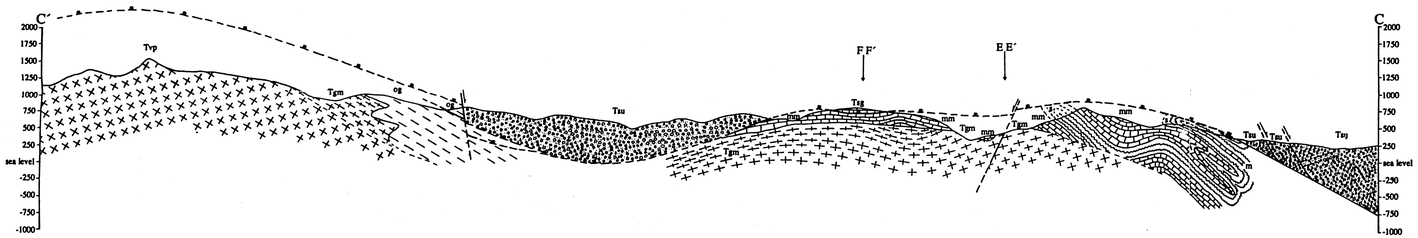

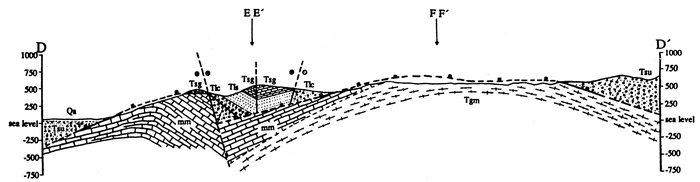

Scale 1:41,667

1 0 1 2 3 4 km

All elevations in meters

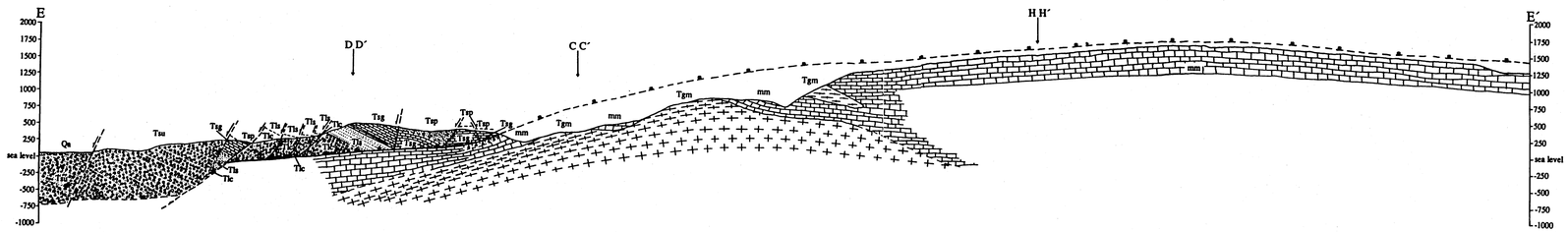

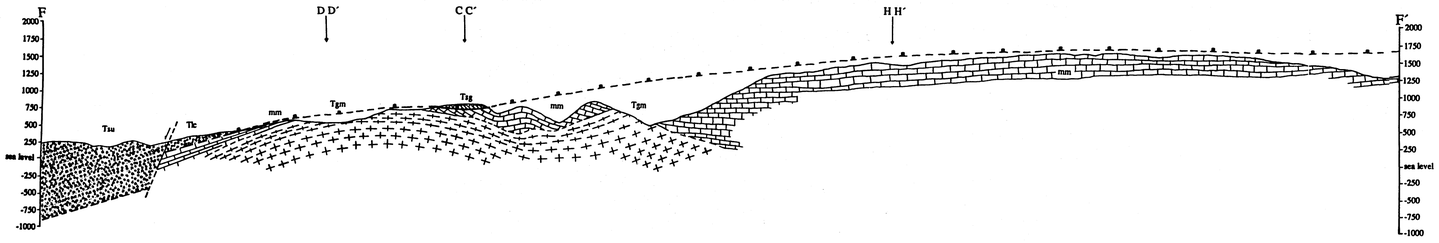

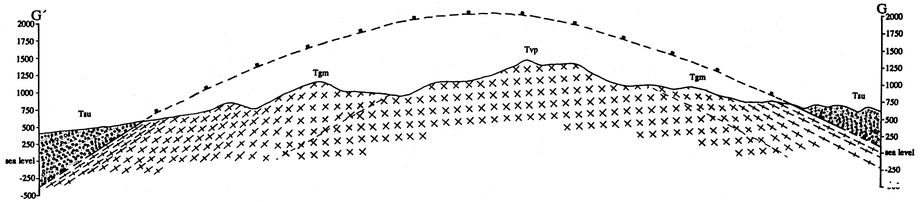

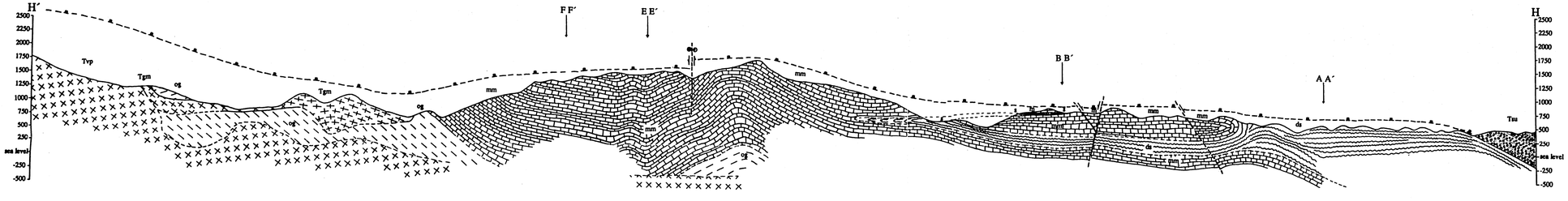

Geologic Map of the Northwestern Rhodope Metamorphic Core Complex, Vrondu and Menoikion Mountains, Eastern Macedonia, Greece

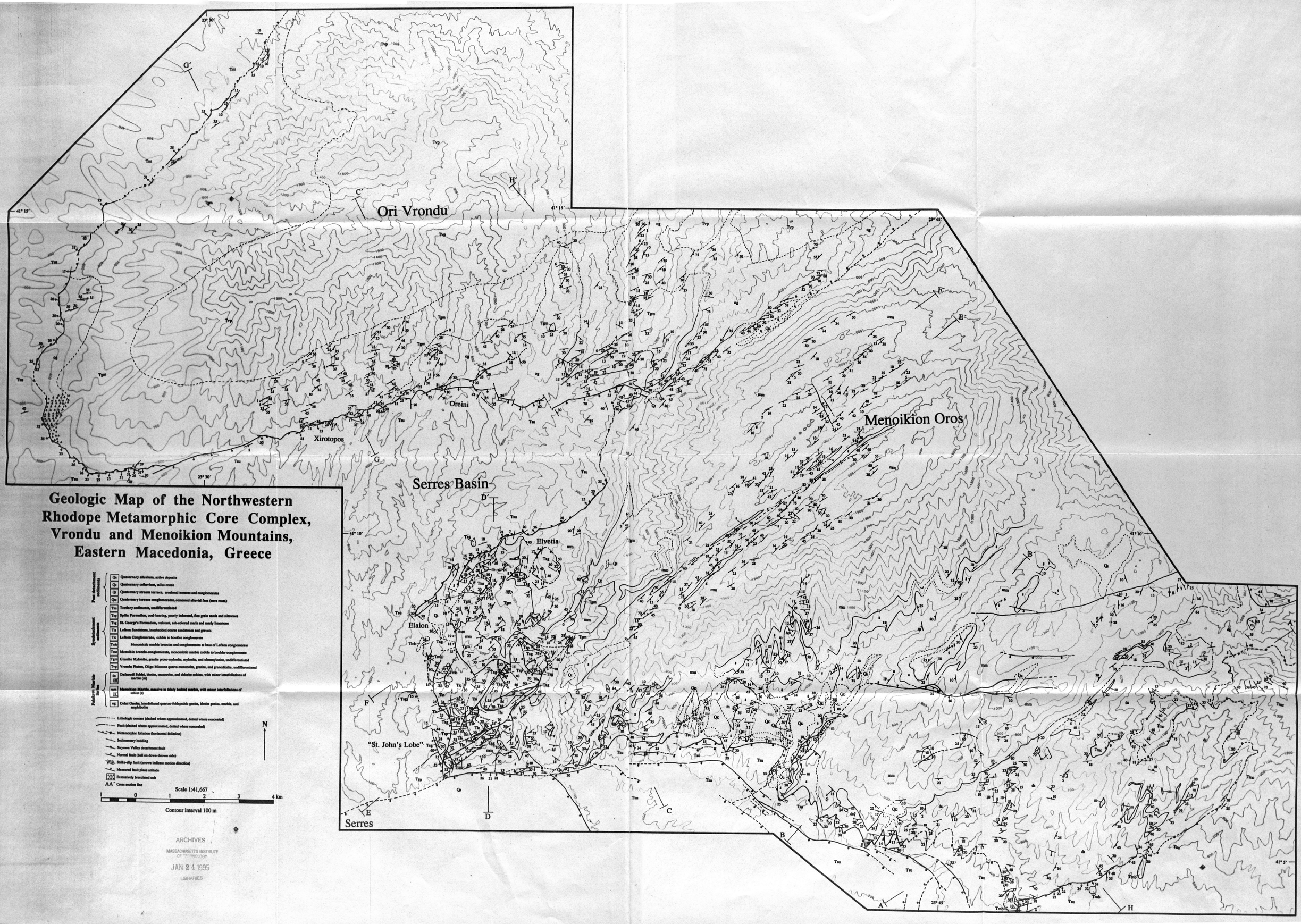

Post detachment sediments
- Qs Quaternary alluvium, active deposits
- Qc Quaternary colluvium, talus cones
- Q Quaternary stream terrace, erosional terraces and conglomerates
- Qtc Quaternary terrace conglomerates, cemented alluvial fans (terra rossa)

Syndetachment sediments
- Tu Tertiary sediments, undifferentiated
- Tsp Sphin Formation, coal-bearing, poorly indurated, fine grain sands and siltstones
- Tst St. George's Formation, resistant, ash-colored snails and marly limestones
- Tl Lefkon Sandstone, interbedded coarse sandstones and gravels
- Tcl Lefkon Conglomerate, cobble to boulder conglomerate
- Tmb Monocimicic marble breccias and conglomerates at base of Lefkon conglomerate
- Tmk Menoikio breccio-conglomerate, monomictic marble cobble to boulder conglomerate
- Tgn Granite Mylonite, granite proto-mylonite, mylonite, and ultramylonite, undifferentiated
- Tvp Vrondu Pluton, Oligo-Miocene quartz-monzonite, granite, and granodiorite, undifferentiated

Paleozoic Marble Schist
- ds Dafnoudi Schist, biotite, muscovite, and chlorite schists, with minor interbeddings of marble (ds)
- m Menoikion Marble, massive to thinly bedded marble, with minor interbeddings of schist (s)
- og Orini Gneiss, interfoliated quarzo-feldspathic gneiss, biotite gneiss, marble, and amphibolite

- Lithologic contact (dashed where approximated, dotted where concealed)
- Fault (dashed where approximated, dotted where concealed)
- Metamorphic foliation (horizontal foliation)
- Sedimentary bedding
- Strymon Valley detachment fault
- Normal fault (ball on down-thrown side)
- Strike-slip fault (arrows indicate motion direction)
- Measured fault plane attitude
- Extensively brecciated unit
- AA´ Cross section line

N

Scale 1:41,667

1 0 1 2 3 4 km

Contour interval 100 m